Stony Brook University

OFFICIAL COPY

The official electronic file of this thesis or dissertation is maintained by the University Libraries on behalf of The Graduate School at Stony Brook University.

© All Rights Reserved by Author.

Characterization of Structural Defects in Wide Band-Gap Compound Materials for Semiconductor and Opto-Electronic Applications

A Dissertation Presented

by

Ouloide Yannick Goue

to

The Graduate School

in Partial Fulfillment of the

Requirements

for the Degree of

Doctor of Philosophy

in

Materials Science and Engineering

Stony Brook University

May 2016

Stony Brook University

The Graduate School

Ouloide Yannick Goue

We, the dissertation committee for the above candidate for the

Doctor of Philosophy degree, hereby recommend

acceptance of this dissertation.

Michael Dudley – Dissertation Advisor
Professor, Department of Materials Science and Engineering

Balaji Raghothamachar - Chairperson of Defense
Research Assistant Professor, Department of Materials Science and Engineering

Jonathan Sokolov
Professor, Department of Materials Science and Engineering

Anwar Hossain
Ph.D., Research Scientist, Radiation Detector and Nonproliferation R&D Group
Brookhaven National Laboratory

This dissertation is accepted by the Graduate School

Charles Taber
Dean of the Graduate School

Abstract of the Dissertation

Characterization of Structural Defects in Wide Band-Gap Compound Materials for Semiconductor and Opto-Electronic Applications

by

Ouloide Yannick Goue

Doctor of Philosophy

in

Materials Science and Engineering

Stony Brook University

2016

Single crystals of binary and ternary compounds are touted to replace silicon for specialized applications in the semiconductor industry. However, the relative high density of structural defects in those crystals has hampered the performance of devices built on them. In order to enhance the performance of those devices, structurally perfect single crystals must be grown. The aim of this thesis is to investigate the interplay between crystal growth process and crystal quality as well as structural defect types and transport property. To this end, the thesis is divided into two parts.

The first part provides a general review of the theory of crystal growth (chapter I), an introduction to the materials being investigated (chapter II and III) and the characterization techniques being used (chapter IV).

- In chapter I, a brief description of the theory of crystal growth is provided with an eye towards the driving force behind crystal nucleation and growth along with the kinetic

factors affecting crystal growth. The case of crystal growth of silicon carbide (SiC) by physical vapor transport (PVT) and chemical vapor deposition (CVD) is discussed. The Bridgman, travelling heater method (THM) and physical transport growth of cadmium zinc telluride (CZT) is also treated. In chapters II and III, we introduce the compound materials being investigated in this study. While a description of their crystal structure and properties is provided, the issues associated with their growth are discussed. In chapter IV, a description of the characterization techniques used in these studies is presented. These techniques are synchrotron X-ray topography (SXRT), transmission electron microscopy, transmission infrared microscopy (TIM), micro-Raman spectroscopy (μRS) and light microscopy. Extensive treatment of SXRT technique is also provided.

In the second part, the experimental results obtained in the course of these studies are presented and discussed. These results are divided into three subsections.

- The development of a new technique for the production of large and high quality silicon carbide single crystal boule is proposed. This technique herein referred to as Large Tapered Crystal (LTC) growth consists of two steps: growth of long SiC rod crystal by solvent-laser heated floating zone (Solvent-LHFZ) and lateral expansion of a seed by hot wall chemical vapor deposition (HWCVD). Solvent-LHFZ was successful as SiC rod crystals, replicating the polytype structure of the starting seed, were achieved at a growth rate varying from 4 to 100μm/hr. However, SXRT revealed the presence of an inhomogeneous strain in the grown crystal rod. This was further confirmed by SEM images, which showed the platelet-like morphology of the growth front with pockets in which iron (Fe)-rich material from the Fe solvent is trapped. It was furthermore observed

that at high Fe to Si ratio (~1.9), no growth was achieved. HWCVD enlargement was also successful as SiC boules, replicating the polytype structure of the starting seed, were achieved at growth rate of about 180μm/hr. The boules had a faceted hexagonal morphology with a strain-free surface marked by steps. Combination of SXRT, TEM and μRS revealed the presence of stacking disorder in the seed (3C, 4H and 15R-SiC) that replicated in the homoepitaxial layer. The formation of the observed stacking disorder is attributed to the low energy difference between stacking configurations on the growth surface as proposed by Takahashi and Ohtani.

- The influence of structural defect type and distribution on minority carrier lifetime in 4H-SiC epilayers was investigated. Structural defect type and distribution map was obtained using SXRT, whereas minority carrier lifetime map was obtained using μPCD. Decrease in carrier lifetime observed from μPCD map was associated with specific structural defects such as low angle grain boundaries (LAGBs), stacking faults (SFs), interfacial dislocations (IDs), half loop arrays (HLAs) as well as basal plane dislocations (BPDs) pinned at TSDs. While the effect of morphological defects was mitigated, combination of defects such as microcracks, overlapping triangular defects and BPD half loops were observed to reduce carrier lifetime. Furthermore, regions of high dislocation density were associated with low carrier lifetime.
- Finally, the effect of cadmium (Cd) overpressure on the quality of cadmium zinc telluride crystal ingots was investigated for two set of samples (set 1 and 2). Overall, high resistivity single crystals were achieved. Evaluation of the crystal quality by SXRT revealed that under certain Cd overpressures and growth conditions, the quality of the grown boule improved. Similarly, transmission infrared (IR) microscopy showed a

correlation between the size/density and distribution of Te inclusions/precipitates and Cd overpressure. The size of Te inclusions was observed to decrease as a function of Cd overpressure as predicted from partial pressure data for stoichiometric melt. The best improvement in crystalline quality were observed for samples from set 1at a Cd reservoir of 785 °C and for set 2 samples for a Cd reservoir at 825 °C. This difference in Cd reservoir temperature for stoichiometric growth between set 1 and set 2 was attributed to other factors such as rate of cooling of Cd reservoir, rate of cooling of the crystal along with control of the melt interface. The summary of these results and the implication of this growth approach for producing high quality CZT single crystals are discussed.

The heavens declare the glory of
God; the skies proclaim the work
of his hands. (Psalm 19:1)

To only GOD be the Glory

Table of Contents

List of Figures xi

List of Tables xv

List of Abbreviations xvi

List of Symbols xxii

Acknowledgments xxvii

Publications xxix

Part I: Theory and Characterization Techniques 1

Chapter I: Introduction to Crystal Growth Theory 2

I.1 Motivation 2

I.2 Theory of Crystal Growth 4

I.2.1 Driving force 4

I.2.2 Kinetic considerations 6

I.3 Growth of SiC 9

I.3.1 Physical vapor transport 9

I.3.2 Chemical vapor deposition 11

I.4 Growth of CZT 13

I.4.1 Melt growth 13

I.4.2 Vapor growth 18

I.5 Summary 19

References 20

Chapter II: Introduction to Silicon Carbide 24

II.1 History 24

II.2 Crystal structure and material potential 25

II.2.1 Crystal structure 25

II.2.2 Material potential 27

II.3 Challenges in the growth of silicon carbide 29

II.3.1 Point defects 31

II.3.2 Linear defects 32

II.3.3 Planar defects 37

II.3.4 Volume defects 40

II.3.5 Doping 41
II.4 Motivation 43
References 46
Chapter III: Introduction to Cadmium Zinc Telluride 53
III.1 Overview 53
III.2 Crystal structure and material potential 53
III.2.1 Crystal Structure 53
III.2.2 Material potential 55
III.3 Challenges in the growth of cadmium zinc telluride 57
III.4 Summary 60
References 62
Chapter IV: Characterization Techniques 64
IV.1 Overview 64
IV.2 Theory of X-ray topography 64
IV.3 Experimental Techniques 79
IV.3.1 Synchrotron X-ray topography geometries 79
IV.3.2 Raman spectroscopy 80
IV.3.3 Transmission electron microscopy 81
IV.3.4 Transmission infrared microscopy 82
IV.3.5 Light microscopy 84
References 85
Part II: Experimental Results 87
Chapter V: Development of Large Tapered Crystal Growth Technique 88
V.1 Overview 88
V.2 Motivation 88
V.3 Brief description of LTC technique 91
V.4 Solvent-Laser heated floating zone (Solvent-LHFZ) 93
V.4.1 Experiment 94
V.4.2 Results and discussions 96
V.4.3 Summary 100
V.5 Lateral Expansion by hot wall chemical vapor deposition (HWCVD) 100
V.5.1 Experiment 101

V.5.2 Results and discussions 103
V.5.2.1 Lateral growth expansion of 4H/6H-SiC m-plane pseudo fiber crystals 103
V.5.2.2 Structural defect behavior in laterally grown 6H-SiC a/m-plane seed crystals by Hot wall CVD 105
V.5.2.3 Summary 113
V.6 Conclusion 114
References 116
Chapter VI: Correlation of Lifetime Mapping of 4H-SiC Epilayers with Structural Defects Using Synchrotron X-ray Topography 119
VI.1 Overview 119
VI.2 Motivation 119
VI.3 Experiment 122
VI.4 Results and discussion 123
VI.4.1 Lifetime measurements 123
VI.4.2 Synchrotron X-ray Topography 126
VI.4.3 Effect of structural and morphological defects on carrier lifetimes 134
VI.5 Conclusion 138
References 139
Chapter VII: Characterization of CZT Single Crystals Grown by Vertical Bridgman Method under Different Cadmium Overpressures 142
VII.1 Introduction 142
VII.2 Experiment 143
VII.3 Results and discussion 144
VII.4 Conclusion 152
References 153
Chapter VIII: Summary and Future Work 155

List of Figures

Figure 1.1. Diagram of free energy as a function of radius of nucleus (a) [11], relation between supersaturation and radius of nucleus (b) ... 6
Figure 1.2. Illustration of the TLK assisted growth model. Atoms are represented by cubes. (T: terrace site, L: ledge site and K: kink site)... 7
Figure 1.4. Screw dislocation assisted growth ... 9
Figure 1.5. SiC phase diagram (a) and conventional experimental set up along with a plot of growth rate versus temperature gradient (b). Note that the growth rate is shown to be a linear function of the thermal gradient inside the growth chamber [21]. ... 10
Figure1.6. Temperature field along with temperature-pressure profile inside a SiC PVT growth chamber ... 11
Figure 1.7. Atomic process and temperature profile versus gas flow for CVD homoepitaxial growth of SiC. Note the presence of steps on the substrate surface due to off-axis orientation of the substrate ... 12
Figure 1.8. Conventional three-zone furnace for vertical Bridgman growth along with temperature profile ... 15
Figure 1.9. Schematic of the THM technique (a), and Temperature versus composition projection of Cd0.9Zn0.1Te1±δ solidus ... 16
Figure 1.10. CdTe-ZnTe pseudo binary phase diagram... 17
Figure 2.1. Tetrahedrons showing the building blocks of silicon carbide crystals. Note that the tetrahedron on the right is obtained by rotating the one on the left around its c-axis by 180° ... 26
Figure 2.2. Stacking sequence of (a) 2H, (b) 3C, (c) 4H and (d) 6H-SiC polytypes, projected along [11-20] direction ... 26
Figure 2.3. Illustration of different types of point defects ... 31
Figure 2.4. Schematic of edge (a), and screw (b) dislocations ... 32
Figure 2.5. Schematic illustration of the splitting of a perfect BPD into Shockley partials ... 33
Figure 2.6. Diagram describing the formation mechanism of IDs and HLAs (a), and illustration of a single HLA (b)... 35
Figure 2.7. TEDs etch pits aligned along low angle grain boundaries (a), and transmission X-ray topograph showing defect contrast from TEDs, TSDs and micropipe (b)... 36
Figure 2.8. Intrinsic stacking fault (a), and Extrinsic stacking fault (b) ... 37
Figure 2.9. Diagram illustrating common domain misorientations in SiC. (a) misorientation free crystal, (b) twist boundary, (c) basal plane tilt boundary, and (d) prismatic plane tilt boundary ... 39
Figure 2.10. Evolution of diameter of commercially available SiC wafer ... 44
Figure 2.11. Evolution of micropipe density in SiC wafer ... 44
Figure 3.1. Unit cell structure of CZT (a), and atomic stacking sequence projected along [110] direction (b). Note that II indicate Cd or Zn atoms, while VI indicate Te atoms... 54
Figure 3.2. Typical CZT-based space telescope ... 57
Figure 4.1. Schematic diagram showing the effect of finite source dimension on resolution. g is the active reciprocal lattice vector. The angle bPg, which is the semiapex angle of the Bragg cone of revolution, is 90- θB. θB is the Bragg angle ... 65
Figure 4.2. Schematic of XRT in transmission geometry ... 66

Figure 4.3. Orientation contrast arising from misoriented regions: (a) monochromatic radiation (beam divergence <misorientation); (b) monochromatic radiation (beam divergence > misorientation); and (c) white beam radiation 67
Figure 4.4. Schematic diagram demonstrating primary extinction 69
Figure 4.5. Construction of the dispersion surface: (a) Spheres of radius k and k(1+χ/2) about origin O and the reciprocal lattice point H in reciprocal space showing the positions of Laue point L and Lorentz point L0; (b) Dispersion surface for σ and π polarization states 72
Figure 4.6. Dispersion surface construction showing the tie points excited by an incident wave in (a) the Laue geometry: One tie point on each branch (A on branch 1 and B on 2); (b) The Bragg geometry: Two tie points (A and B) on the same branch 74
Figure 4.7. Standing wavefields of (a) branch 1 and (b) branch 2, with a period corresponding to the spacing between the Bragg planes produced at the exact Bragg condition 75
Figure 4.8. Bormann fan bounded by the incident (AB) and diffracted (AC) beams showing the distribution of energy for an incident spherical wave that excites all tie points along the dispersion surface 76
Figure 4.9. (a) Formation of the three types of image under high strain gradients: 1- Direct image; 2- Dynamical image; 3- Intermediary image; (b) contrast formation under low strain gradients 77
Figure 4.10. SWBT transmission topograph (g = 10-10, λ = 0.75Å) recorded from an AlN single crystal under intermediate absorption conditions (μt = 8) showing the direct (1), dynamical (2), and intermediary (3) images of a dislocation 79
Figure 4.11. Transmission geometry (a), back reflection geometry (b), and Grazing geometry (c) 80
Figure 4.12. Conventional JEOL 2100F 82
Figure 4.13. Transmission infrared microscope 83
Figure 5.1. Synchrotron white beam X-ray transmission topograph of 4H-SiC substrate showing prismatic dislocations 90
Figure 5.2. Temperature dependence of critical resolved shear stress for 6H-SiC 90
Figure 5.3. Schematic description of Large Tapered Crystal Growth (LTC) Process 92
Figure 5.4. Long range optical images of melted source material seed crystal: (a) before wetting and (b) after wetting 94
Figure 5.5. Top-down view of solvent-LHFZ system schematic 95
Figure 5.6. X-ray transmission Laue diffraction pattern (a) recorded form the LHFZ portion of fiber sample (b) simulated Laue diffraction pattern and (c) SWBXT transmission topography 97
Figure 5.7. SEM images of a growth front of a solvent-LHFZ grown crystal (a) The hexagonal platelet growth fronts, (b) webbing between growth fronts, (c) defect creating pockets are completely webbed over and (d) a cross sectional area (created by FIB) showing Fe-rich inclusion 98
Figure 5.8. SIMS depth profile analysis of 4H-SiC layer grown using high C (at 16%) and low C (at 8%) source material grown at T_m+190°C for a 175 μm x 175 μm area taken in middle of C face 99
Figure 5.9. Schematic diagram showing the SiC unit cell with associated crystallographic planes and the orientation of the seed slivers (pseudo fibers) as cut from m-plane polished boule slices 101
Figure 5.10. Post growth results for the eight hour growth showing three m-plane fibers mounted on top of an uncoated graphite carrier. Two other control fibers protrude from the front of the carrier. Yellow 3C-SiC decorates the surface of the as-grown crystals 104

Figure 5.11. SEM of 4H/6H-SiC m-plane (fiber 1) after five hours of growth showing the hexagonal unit cell orientation on the end of the fiber (a), and 6H-SiC m-plane (fiber 2) after eight hours of growth showing some regions of 3C-SiC nucleated near either end of the fiber (b). Note the growth at the intersection of the m-planes dominates. The portion of fiber visible in the lower left of the SEM was used for mounting and exhibits almost no growth 104
Figure 5.12. SWBXT topograph of fiber 2 showing developing facets........ 105
Figure 5.13. SWBXT transmission topograph of (a) a-plane cut (sample 1) and (b) m-plane axial cut (sample 2) from as-grown crystals........ 106
Figure 5.14. SWBXT transmission topograph of a transverse (0001) slice along with sketch showing crystallographic directions. Note the bundles of dislocations running along the <1-100> directions 106
Figure 5.15. Schematic of transverse slice showing region of interest, seed and regions 1 through 6 (left), Raman map of region of interest along with color scale (right) 108
Figure 5.16. Raman spectra for regions marked 1 through 6 as shown in schematic of transverse slice above........ 108
Figure 5.17. Optical micrograph of sample 4 (left), and Raman mapped region (right) 109
Figure 5.18. Raman map of selected region on sample 4 and spectra at x=84.4μm (1), x=-375.1 μm (2) and x=372.1 μm (3)........ 110
Figure 5.19. HRTEM image of 6H-SiC axial slice (sample 2) showing 3C and 8H-SiC polytype........ 111
Figures 5.20. Bright field images showing dislocation loops (left), SFs (middle), and inclusion-like feature (right) 112
Figure 5.21. Stacking sequence in SF_2 showing the presence of partials dislocations (PDs), lattice distortion and shift in sequence form left to right........ 113
Figure 5.22. Atomistic surface model for 6H-SiC (1-100) surface........ 113
Figure 6.1. Illustration of step flow growth during CVD growth 120
Figure 6.2. Microwave photoconductance decay maps of sample 1 (a) and sample 2 (b)........ 124
Figure 6.3. Typical surface morphology of sample 1 (a) and sample 2 (b). Note that (a) and (b) are representative area of samples 1 and 2, respectively. 125
Figure 6.4. Photoluminescence decay time curve of sample 1 along with sample schematics........ 125
Figure 6.5. Photoluminescence decay time curve of sample 2 along with sample schematics........ 126
Figure 6.6. SWBXT transmission topographs for (-1-120) and (1-101) diffracting plane. Note that the scale is the same for both reflections 128
Figure 6.7. Formation mechanism of stacking fault associated with micropipe as suggested by Wu et al. 128
Figure 6.8. Nomarski micrograph of cross feature in facet a in (a) reflection on carbon face, (b) transmission on carbon face, (c) reflection on silicon face and (d) transmission on silicon face. Note the pit associated with micropipe at the center of the cross in red circle........ 129
Figure 6.9. (a) SMBXT of facet a, (b) SWBXT of facet a for g = 11-20, and (c) g = 1-101. Note red circle correspond to pits associated with micropipe at center of cross feature and blue rectangle shows isolated triangular stacking fault. 130
Figure 6.10. SWBXT transmission topographs for SF1 (a) and SF2 (b). Notice the red triangle in (b) highlighting the Franck fault........ 131
Figure 6.11. SWBXT of sample 2 for three different reflection vectors. The scale is identical for all three reflections........ 131

Figure 6.12. SMBXT of sample 2 for (11-28) reflection vector. Note the triangular defects and BPD half loops highlighted near the edge 132
Figure 6.13. Diagram describing formation of IDs and HLAs along with illustration of single HLAs (a), and schematic of IDs and HLAs originating from 3C inclusion. Note that h_c correspond to critical thickness at which screw type BPD (straight line from substrate) is forced to glide sideways at epilayer-substrate interface 132
Figure 6.14. Morphological defects of various size and shape 134
Figure 6.15. Correlation between stacking faults SF_1, SF_2, SF_3 and their μPCD map. Note that the μPCD map is overlaid on top of the SWBXT for each region encompassing the stacking faults 135
Figure 6.16. (11-20) SWBXT transmission image of four regions from sample 1 along with their corresponding μPCD map 135
Figure 6.17. Effect of parasitic particulates (PaDs) on carrier lifetime. Blue circles highlight linear defects that correspond to obtuse triangular defects at the apex of which lies wavy pit associated with micropipe 136
Figure 6.18. Effect of triangular defects, microcracks associated with triangular defects at edge of sample. Note the corresponding SMBXT images of highlighted regions from the μPCD map as well as optical micrograph of a region along the edges of sample 2. Also, the individual triangular defects appear to have no negative effect on lifetime........ 137
Figure 6.19. Illustration of the effect of IDs and HLAs on carrier lifetimes. Note the HLA originating from a 3C inclusion. Also, the μPCD lifetime map is overlaid on top of the SMBXT image........ 138
Figure 7.1. Schematic diagram showing boule from which sample 2g-36/1, 2g-36/2 and 2g-36/3 were cut. Direction of cut of axial slices is perpendicular to x-axis and direction of cut for transverse slices in perpendicular to z-axis. 144
Figure 7.2. SWBXT reflection topograph for samples grown using various Cd reservoir temperatures. Sample 2g-30 grown using 785 ^oC (a), sample 2g-31 grown using 800 ^oC (b), sample 2g-34 grown using 840-845 ^oC (c), sample 2g-36 grown using 785 ^oC (d), sample 2g-36/1 grown using 785 ^oC (e), and sample 2g-38 grown using 810 ^oC (f) 146
Figure 7.3. SWBXT reflection topograph of both faces of sample 2g-36/1. Note the change in contrast of the subgrain boundaries indicating the nature of the stress on each face........ 147
Figure 7.4. Back reflection Laue pattern showing the (2-10) surface orientation of the twin region, which is rotated 180o to the (111) plane normal with respect to the main grains 148
Figure 7.5. SWBXT reflection topograph of sample 2g-36/2 (a), and sample 2g-36/3 (b). The blue arrows indicate surface scratch from polishing, and the white arrows indicate Te inclusions 149
Figure 7.6. Distribution of Te inclusions with respect to Cd overpressure for sample 2g-30 with a Cd reservoir temperature of 785 ^oC (a), sample 2g-31 with a Cd reservoir temperature of 800 ^oC (b), sample 2g-34 with a Cd reservoir temperature of 840-845 ^oC (c), sample 2g-36 with a Cd reservoir temperature of 785 ^oC (d), sample 2g-36/1 with a Cd reservoir temperature of 785 ^oC (e), and sample 2g-38 with a Cd reservoir temperature of 810 ^oC (f). Note the bed of Te inclusions and the thin strip of Te inclusions respectively indicating the grain and the twin boundary in (e). 150
Figure 7.7. Variation in Te inclusions size and concentration with respect to Cd overpressure 151
Figure 7.8. Transmission infrared micrograph highlighting in yellow box the concentration of Te secondary phase particles near center of samples (a) for sample 2g-36/2 and (b) for sample 2g-36/3 152

List of Tables

Figure1.6. Temperature field along with temperature-pressure profile inside a SiC PVT growth chamber [23] 11
Table 2.1. Room temperature bandgap of the most common grown silicon carbide polytypes 28
Table 2.2. Comparison of the properties of common silicon carbide polytypes with other known conventional semiconductors [26] 29
Table 3.1. Physical properties of the principal compound semiconductors at T = 25 ˚C 56
Table 5.1. Un-sintered and sintered feed rod densities as determined by Archimedes' principal 95
Table 5.2. Summary of growth rate for different temperature and source material composition 97
Table 5.3. Summary of results Tm = temperature at which feed rod forms a melt, at % = atomic. Temperatures are not corrected for emissivity. Approximate Fe concentrations in the SiC crystal layers are listed 99
Table 5.4. Growth parameters for two separate growth runs. Fiber 1 was five hours in length. Fiber 2 was eight hours in length. Note that the intentional Si/C is 2.7 and 3.5 respectively. There is a substantial and unknown quantity of carbon contribution coming from the uncoated graphite sample carrier and carbon foam insulation 102
Table 7.1. Sample Id and corresponding Cd reservoir temperature for set 1 144
Table 7.2. Sample Id and corresponding Cd reservoir temperature for set 2 144

List of Abbreviations

Al	Aluminum
AlN	Aluminum Nitride
APBs	Anti-phase Boundaries
APCVD	Atmospheric Pressure Chemical Vapor Deposition
Ar	Argon
$B_{12}As_2$	Boron Arsenide
BM	Bridgman Method
BNL	Brookhaven National Laboratory
BP	Boron Phosphide
BPDs	Basal Plane Dislocations
BSF	Basal Plane Stacking Fault
C	Carbon
C	Czochralski
C_i	Carbon Interstitial
CCl_4	Carbon Tetrachloride
Cd	Cadmium
CdTe	Cadmium Telluride
CFN	Center for Functional Nanomaterial
C_3H_8	Propane
CH_4	Methane
C_2H_4	Ethylene
CO_2	Carbon Dioxide
CsI	Cesium Iodide

CVD	Chemical Vapor Deposition
CZT	Cadmium Zinc Telluride
DIC	Differential Interference Contrast
DPBs	Double Positioning Boundaries
DSSFs	Double Shockley Stacking Faults
DT	Dynamical Theory
EDS	Energy Dispersive Spectroscopy
ESF	Extrinsic Stacking Fault
eV	Electron volt
Fe	Iron
FCC	Face-Centered Cubic
FF	Franck Fault
FIB	Focus Ion Beam
FLA	Folded Longitudinal Acoustic
FLO	Folded Longitudinal Optic
FTA	Folded Transverse Acoustic
FTO	Folded Transverse Optic
FWHM	Full Width at Half Maximum
GaAs	Gallium Arsenide
GBs	Grain Boundaries
GaN	Gallium Nitride
Ge	Germanium
GRC	Glenn Research Center
H_2	Hydrogen
HAGB	High Angle Grain Boundary

HB	Horizontal Bridgman
HCl	Hydrogen Chloride
HEFT	High-Energy Focusing Telescope
HF	Hydrofluoric Acid
HgCdTe	Mercury Cadmium Telluride
HgI_2	Mercury Iodide
HLA	Half-Loop Array
HNO_3	Nitric Acid
H_2O_2	Hydrogen Peroxide
HPB	High Pressure Bridgman
HRTEM	High Resolution Transmission Electron Microscopy
H_2SO_4	Hydrogen Sulfate
HWCVD	Hot Wall Chemical Vapor Deposition
IDs	Interfacial Dislocations
IGSF	In-Grown Stacking Fault
IR	Infrared
ISF	Intrinsic Stacking Fault
K	Kink site
KOH	Molten Potassium
KT	Kinematical Theory
kV	kilovolt
L	Ledge site
LAGBs	Low Angle Grain Boundaries
LEDs	Light Emitted Diodes
LPB	Low Pressure Bridgman

LPCVD	Low Pressure Chemical Vapor Deposition
LTC	Large Tapered Crystal
MOS	Metal Oxide Semiconductor
MOSFETs	Metal Oxide Semiconductor Field Effect Transistors
MP	Micropipe
MTS	Methyltrichlorosilane
μPCD	Microwave Photoconductivity Decay
μRS	Micro-Raman Spectroscopy
NASA	National Aeronautics and Space Agency
N_2	Nitrogen
nm	Nanometer
NSLS	National Synchrotron Light Source
PaDs	Parasitic Depositions
PCD	Photoconductivity Decay
PDs	Partial Dislocations
PiN	Positive Intrinsic Negative
PL	Photoluminescence
PLD	Photoluminescence Decay
PSF	Prismatic stacking fault
PVT	Physical Vapor Transport
RAF	Repeat-A-Face
REDG	Recombination Enhanced Dislocation Glide
SB	Subgrain Boundary
SD	Screw Dislocation
SEM	Scanning Electron Microscopy

SFs	Stacking Faults
Si	Silicon
Si_i	Silicon Interstitial
SiC	Silicon Carbide
$SiCl_4$	Silicon Tetrachloride
SiH_4	Silane
SiH_2Cl_2	Dichlorosilane
Si-X	Halogenated Silicon Precursor
SIMS	Secondary Ion Mass Spectroscopy
SMBXT	Synchrotron Monochromatic X-ray Topography
Solvent-LHFZ	Solvent-Laser Heated Floating Zone
SRH	Shockley-Reed-Hall
SSF	Shockley Stacking Fault
SXRT	Synchrotron X-ray Topography
SWBXT	Synchrotron White Beam X-ray Topography
T	Terrace site
Te	Telluride
TEDs	Threading Edge Dislocations
TEM	Transmission Electron Microscopy
THM	Traveler heater method
TiBr	Titanium Bromine
TIM	Transmission Infrared Microscopy
TSD	Threading Screw Dislocation
VAM	Vertical ampoule method
VB	Vertical Bridgman

VGF	Vertical Gradient Freeze
V_c	Carbon Vacancy
V_{si}	Silicon Vacancy
WBG	Wide Band Gap
XRT	X-ray Topography
ZB	Zincblende
Zn	Zinc
ZnTe	Zinc Telluride

List of Symbols

a_1, a_2	lattice constant
A	Distance between nearest neighbor atoms
Å	Angstrom
α	Angle between BPD line direction and growth normal
α_0	Deviation parameter for incident wave
α_h	Deviation parameter for diffracted wave
abc$\alpha\beta\gamma$	Crystallographic lattice constants
b	Burgers vector
B	Magnetic induction
bPg	Semi-apex angle of the Bragg cone of revolution
c	Speed of light in vacuum
c	Lattice constant
C	X-ray source-specimen distance, polarization factor
C_s, C_m	Solid and melt concentration respectively
d, d_{hkl}	Interplanar spacing
D	Specimen-detector distance
D	Electric displacement
D_o	Electric displacement of incident beam
D_h	Electric displacement of diffracted beam
D_s	Surface diffusion constant
E	Electric field, line energy
E_b	Breakdown field
E_c	Conduction band

E_i	Initial energy state of a molecule
E_f	Final energy state of a molecule
E_g	Band gap
E_v	Valence band
ε_d	Migration barrier height
ξ_g	Extinction distance
ξ'_g	Extinction distance that accounts for deviation parameter
F	Structure factor
F_h	Structure factor for hkl
$F_{\bar{h}}$	Structure factor for $\overline{hkl}$
g	Active reciprocal lattice vector, diffraction vector
ΔG	Free energy barrier
G	Work required to form a stable cluster
h	Height of 2D nucleus, Planck's constant
h_c	Critical thickness
hkl	Reflecting plane
H	Magnetic field
I	Total amplitude
Io	Initial amplitude
J, J_o	Nucleation rate, constant dependent on surface free energy
κ	Distribution coefficient
k	Wavevector, thermal conductivity
k_o	Incident wavevector
k_h	Diffracted wavevector
kHz	Kilohertz

K_b	Boltzmann constant
$\mathbf{K_0}$	Incident X-ray beam
$\mathbf{K_h}$	Diffracted X-ray beam
$\boldsymbol{l}$	Dislocation line direction
L_s	Mean migration distance
μ	Microns, linear absorption coefficient
μ_c, μ_v	Crystalline and vapor phase chemical potential
μ_e	Electron mobility
μ_h	Hole mobility
μs	Microsecond
$\Delta\mu$	Chemical Potential
n	Integer number
n_1, n_2, n_3	Number of repeat unit in stacking sequence
nJ	Nanojoule
$\mathbf{n}$	Unit vector normal to the surface
N	Number of molecules
P, P_e	Vapor pressure, equilibrium vapor pressure
$\mathbf{P}$	Poynting vector
ΔP, ΔP_{crit}	Supersaturation, critical supersaturation
π	Pi
Φ_0	X-ray entrance angle
Φ_h	X-ray exit angle
φ_a	Interaction energy between nearest neighbor atoms
R, R_{crit}	Radius of nuclei, Critical radius of nuclei, amplitude ratio
R_e	Resolution

r_e	Electron radius
$\mathbf{R_h}$	Reciprocal lattice vector
r_i	Scattering center position
ρ_d	Dislocation density
S	X-ray source dimension
slm	Standard liter meter
σ	Surface Free Energy
t_k	Kinematical penetration depth
T	Temperature
T_g	Growth temperature
T_m	Melting temperature
T_o	Observed temperature
T_w	Working temperature
τ	Unit vector in the surface
τ_e	Electron lifetime
τ_h	Hole lifetime
τ_s	Mean lifetime
τ_r	Carrier lifetime
θ_B	Bragg angle
u	displacement vector
ν	Frequency of incident photon
ν'	Frequency of scattered phonon
$\boldsymbol{\nu}$	Frequency factor
V	Volume on nucleus, Rate of advance of a step
V_c	Unit cell volume

V_s	Saturated carrier velocity
W	Total evaporation energy
W	Elastic energy
x	Concentration
Z	Atomic number
$Z_{1/2}$	Lifetime limiting point defects
Ze	Dynamical penetration depth
λ	wavelength
χ_h	Dielectric susceptibility constant for h
$\chi_{\bar{h}}$	Dielectric susceptibility constant for $\overline{hkl}$
χ_0	Dielectric susceptibility constant for incident wavevector
η	Deviation parameter
ω	Rocking curve for asymmetric Bragg reflection
Ω	Rocking curve for symmetric Bragg reflection, Ohm
δd	dilation
δθ	Effective misorientation
δφ	Tilt in plane of incidence
Δθ	Rocking curve for Laue case

Acknowledgments

The appearance of my name only on the front of this thesis does not render justice to the many people who have contributed to its completion. I am indebted to all those people and would like to thank them for making my graduate experience memorable.

My first thank goes to my advisor, Professor Michael Dudley, for the opportunity to work in such an intellectually stimulating field as that of crystal growth of compound semiconductor material and their characterization. He has given me freedom over my projects, and chaperoned me to ensure that I do not falter in the process. He has imparted in me his enthusiasm for research and passion for the thought process that goes into it. I could not have imagined a more supportive advisor and mentor.

Next, I would like express my gratitude to Dr. Balaji Raghothamachar, who has acted as a co-advisor to me and is the chairperson of my committee. He has assisted me through my research with meaningful discussions and in developing a more efficient research method. His patience and encouragement have helped me endure and persevere through this dissertation. I am thankful to him for carefully reading and providing suggestions to enhance this thesis.

I would also like to sincerely acknowledge Professor Jonathan Sokolov and Dr. Anwar Hossain for agreeing to sit on my committee. Professor Sokolov has previously sat on my prelim committee. Special thanks to Dr. Hossain for his insightful discussions on the fabrication of cadmium zinc telluride (CZT) detectors and tips on efficiently polishing CZT wafers.

My further thank you goes to all my peers in the Laboratory of Synchrotron X-ray Topography. Particular thanks to Jianqiu Guo and Yu Yang for the stimulating discussions we had and the sleepless night recording X-ray topographs at the Advanced Photon Source at Argonne National Laboratory. I would like to credit Dr. Fangzhen Wu for showing me the way to transmission electron microscopy technique. My gratitude goes to Dr. Shayan Byrappa for taking me with him in the earliest stage of my graduate school career to teach me the art of synchrotron X-ray topography. He has gone on to provide comments on some of my published papers. I am also thankful to Dr. Huanhuan Wang for her candidness, which stimulated me in my research endeavor. I am very appreciative of the support and friendship all of you, Dr. Jun Gyu Kim, Tianyi Zhou, Shun Sun, Hao Wang, my brother Zheyu Li, Mr. and Mrs. Ding, Mengnan Zhou, Xuejing Wang, Fei Wang, Jianing Yan, Jinlong Li, Xaoling Yang, Wu Shuang, have provided. Your presence in this lab has fostered an atmosphere of conviviality.

Thank you to Brian Mc. Candless, my supervisor and mentor during my undergraduate research at the Institute of Energy Conversion at the University of Delaware. Your passion for self-learning and your bright mind have benefited me. I hope to walk in your footsteps.

Many friends have contributed to my balance during these years. I would like to recognize them. To my Brothers and Sisters in Christ (BASIC) family, I would like to say Thank you. Your prayers and fellowship have been comforting to me. Particular thanks to my brother Gene Kleine for being a voice of reason and truth to me. Further thanks to my good friend, Ms. Madhura Som, a friend from another mother. You have been mellow and sweet to me, yet tough on me with your pertinent and insightful questions/suggestions during our group study sessions. I owe you a lot for letting me pick up your brain.

Special thanks to my parents, Goue Thietemomin and Gueye Zaonde Temon Nahin Clementine, for their loving support and sacrifices in the course of my studies. Thank you to my older brother, Kouadio Yao Eric Marc, for having my best interest in mind. Thank you to my other siblings, Wilfried, Arnaud and Miremont, for genuine brotherhood. I would be ungrateful to forget you, Michael Perna (Uncle Mike). Thank you for designing the scheme that brought me to further my education in the United States. To you all I dedicate this dissertation. May you rejoice and give thanks.

In the end, I would like to acknowledge the partner institutions that provided samples and characterization facility for my studies. Thank you to NASA Glenn Research Center for the work on the Large Tapered Crystal (LTC) Growth technique. Thank you to the Naval Research Laboratory for the opportunity to investigate the relation between structural defects and transport properties of 4H- silicon carbide epitaxial layers. Thank you to NASA Marshal Space Flight Center for the studies on the effect of cadmium overpressure on the structural quality of cadmium zinc telluride single crystals. Thank you to Stony Brook University, the Materials Science and Engineering Department for opening me its doors and nurturing me academically and professionally.

Publications

1. **Ouloide Y. Goue**, Yu Yang, Jianqiu Guo, Balaji Raghothamachar, Michael Dudley, John Hostetler, Rachael L. Myers-Ward, Paul B. Klein and Kurt D. Gaskill, "Correlation of lifetime mapping of 4H-SiC epilayers with structural defects using synchrotron X-ray topography", Mat. Sci. Forum **858**, p 297-300 (2016)

2. Jianqiu Guo, Y. Yang, F. Wu, J.J. Sumakeris, R.T. Leonard, **Ouloide Y. Goue**, Balaji Raghothamachar, Michael Dudley, "Using ray tracing simulations for direct determination of Burgers vectors of threading mixed dislocations in 4H-SiC c-plane wafers grown by PVT method", Mat. Sci. Forum **858**, p 15-18 (2016)

3. **Ouloide Y. Goue**, Balaji Raghothamachar, Yu Yang, Jianqiu Guo, Michael Dudley, Kim Kisslinger, Andrew J. Trunek, Philip G. Neudeck, David J. Spry and Andrew A. Woodworth, "Study of defect structures in 6H-SiC a/m plane pseudofiber crystals grown by hot-wall CVD epitaxy", J. Electron. Mater. **45 (4)**, p 2078-2086 (2016)

4. Jianqiu Guo, Yu Yang, Fangzhen Wu, Joe Sumakeris, Robert Leonard, **Ouloide Y. Goue**, Balaji Raghothamachar and Michael Dudley, "Direct determination of Burgers vectors of threading mixed dislocations in 4H-SiC grown by PVT method", J. Electron. Mater. **45 (4)**, p 2045-2050 (2016)

5. Yu Yang, Jianqiu Guo, **Ouloide Y. Goue**, Balaji Raghothamachar, Michael Dudley, Gil Chung, Edward K. Sanchez, Jeff Quast, Ian Manning and Darren Hansen, "Experimental verification of the model for formation of double Shockley stacking faults in highly doped regions of PVT-grown 4H-SiC wafers", J. Cryst. Growth, First online (2016)

6. Jianqiu Guo, Yu Yang, Fangzhen Wu, Joe Sumakeris, Robert Leonard, **Ouloide Y. Goue**, Balaji Raghothamachar and Michael Dudley, "Synchrotron X-ray Topographic Study on Nature of Threading Mixed Dislocations in 4H-SiC Crystals Grown by PVT Method", J. Cryst. Growth, First online (2015)

7. Jianqiu Guo, Yu Yang, Fangzhen Wu, **Ouloide Y. Goue**, Balaji Raghothamachar and Michael Dudley, "Direct determination of Burgers vectors of threading mixed dislocations in 4H-SiC c-plane wafers grown by PVT method", ECS Transaction **69 (11)**, p 33-38 (2015)

8. Yu Yang, Jianqiu Guo, **Ouloide Y. Goue**, Huanhuan Wang, Fangzhen Wu, Balaji Raghothamachar, Michael Dudley, Gil Chung, J. Quast, Edward Sanchez, I. Manning and D. Hansen, "Double Shockley stacking fault formation in higher doping regions of PVT-grown 4H-SiC wafers", ECS **69 (11)**, p 39-46 (2015)

9. **Ouloide Y. Goue**, Balaji Raghothamachar, Michael Dudley, Andrew J. Trunek, Philip G. Neudeck, Andrew A. Woodworth, David J. Spry, "Structural characterization of lateral-

grown 6H-SiC a/m-plane seed crystals by hot wall CVD epitaxy", MRS Proceedings 1693, (2014)

Part I: Theory and Characterization Techniques

Chapter I: Introduction to Crystal Growth Theory

I.1 Motivation

Dr. Robert Laudise from Bell Labs once said "New materials are the lifeblood of solid state research and device technology. Contrary to what many believe, new materials are not usually discovered by device engineers, solid state theorists, or research managers; they are mostly discovered by crystal chemists who are crystal growers. Some physical phenomena are only exhibited in single crystals and can only be studied and understood in single crystals. Thus the crystal grower - especially if he develops a proficiency *in* relating structure, bonding and other chemo-physical considerations to properties of interest - is in a key position in determining the direction and success of solid state research and - ultimately - technology [1]."

The quintessence of this statement highlights two key points in the advancement of technology. One point promotes the importance of materials' discovery while the second emphasizes the role of characterization in either validating or improving the viability of the discovered materials for technological application. The meaning of materials in this thesis focuses on single crystals that are binary or ternary.

Single crystals, i.e. crystals, are class of material in which the elementary building blocks are arranged regularly in space to form a lattice structure with a high degree of symmetry. The elementary building blocks are atoms of a given element. The long-range atomic order that this class of material exhibits can be disturbed by the presence of irregularities called imperfections or defects. Ideally, single crystals should be perfect. This suggests that their atomic arrangement should not suffer from any imperfection. In reality, there is no such thing as a perfect crystal; not even in nature. The concept of perfect crystals is defined in theory as a mathematical abstraction to describe crystal lattice and run simulation. Experimentally, the concept of perfect crystals serves as a baseline against which the quality of a crystal is determined. So, a perfect crystal will be described as one in which the density of imperfections is about 1 per square centimeter.

Why are crystals not completely perfect? Growing a structurally perfect crystal requires a tremendous amount of energy, which is not attainable in practice because of thermodynamic constraints. These thermodynamic constraints promote the path of least energy during crystal growth. Imperfections help easily reach this path, and are thus useful in the growth of crystals. According to the theory of nucleation and growth, defects facilitate the growth of crystals as they

provide source for nucleation. In 1927, Kossel discovered that the growth of crystal was associated with the presence of kinks and steps on atomic surface [2]. Two decades later, Frank revealed that screw dislocations were associated with the formation of growth hillocks [3].

In addition, defects influence the properties of a crystal. In strengthening metal alloy crystals, solute impurities can be incorporated in a process called solid solution hardening to increase mechanical strength. Another strengthening mechanism of crystal alloys is through grain size reduction. In this process, the alloy is transformed into a mosaic of several smaller grains where the boundary caused by the slight misorientation of each grain with respect to other grains prevents the motion of dislocations and strengthens the metal alloy. It should be noted that each grain represents a crystal, and that a dislocation is a type of imperfection.

Imperfections can also be engineered or controlled to influence other properties of a crystal depending on the type of technological application. Impurities can be injected in a semiconductor crystal in the form of donors or acceptors to provide free carriers (i.e. electrons and holes) and improve its electronic properties. Donors and acceptors are foreign atoms that respectively give off electrons to the conduction band and holes to the valence band of semiconductors. When the free carriers are in the vicinity of other impurities (i.e. extended defects) related to the structural arrangement of the crystal, their diffusion length can be reduced, and their lifetime affected. The mechanism through which extended defects can reduce lifetime is addressed in chapter 5. However, it should be noted that engineering or controlling the distribution and type of extended defects could tailor carrier lifetime for certain technological applications. An instance of this is in high frequency devices where extended defects can potentially produce shorter lifetime, which can in turn prevent loss of power during switching cycles. Although crystal properties can benefit from impurities for specific technological application, their harmful effect should not be overshadowed.

During the last decade progresses have been made in the growth of high quality binary and ternary compound single crystals. These progresses have made possible a wealth of applications that were before unattainable. Applications that are geared towards harsh condition environment such as high temperature and irradiation have now become a reality. However, the lack of a uniform growth technology means that the conditions for growing structurally perfect single crystal vary for every compound. It becomes thus necessary to investigate all the stages of the crystal growth process since those stages determine the growth yield and crystal perfection. This

will entails the studies of the formation of crystal defects as well as the influence of those defects on the crystal properties. Such investigations will consolidate understanding of the crystal growth process, enable production of structurally perfect large single crystal, and help predict which type of application is suitable for certain types and density of defects.

The aim of this chapter is to briefly introduce key points regarding the theory of nucleation and crystal growth and address the two standard methods for the growth of silicon carbide (SiC) and cadmium zinc telluride (CZT) single crystals.

I.2 Theory of Crystal Growth

The advancement of modern technology heavily relies on the growth of high quality bulk single crystals, which are the base material for device fabrication. Their importance to our contemporary society can be traced back to World War II, where they were heavily used [4] for military applications as transducers in sonar and radar devices. Following the end of World War II, new applications of single crystals emerged with the discovery of the transistor effect in 1948. Today, devices built on single crystals are used in the automobile, electronic, data processing, telecommunication and space industries. The table below represents the percentage of application with respect to the total semiconductor market from 2006 to 2012.

These current applications have become possible thanks to progresses made in growing relatively large and high quality single crystals. However, macroscopic and microscopic defects associated with the growth conditions prevent us from harnessing the full potential of these single crystals. In this section, we first discuss the driving force and other related factors that affect crystal growth process, and address the case of vapor growth of silicon carbide and melt growth of cadmium zinc telluride. The reader can refer to references [5-9] for a detail treatment of the crystal growth theory.

I.2.1 Driving force

The growth of a crystal starts with the formation of nuclei through a process called nucleation. Nucleation is the first step in the transformation from one phase to another. It describes the process by which atoms or molecules of a parent phase self-assemble into a large enough cluster (i.e. nuclei) in the product phase to irreversibly grow into a macroscopically larger size. Two types of nucleation exist: homogeneous and heterogeneous. Homogeneous nucleation describes a nucleation process whereby no foreign substance act as nucleus. In this

case, the nucleation relies solely on the parent phases. When foreign substances are present in the parent phase, the nucleation process is said to be heterogeneous. Here, “foreign substances” refers to either chemical elements (e.g. dust particles or nuclei of the new phase) or physical condition (e.g. surface morphology or roughness).

The process of nucleation is energy driven as a free energy barrier ΔG must be overcome before the formation of large cluster that would irreversibly lead to crystal growth. In nature and experiments, the nucleation process is predominantly heterogeneous. This is so because heterogeneous nucleation has a lower energy barrier compared to homogeneous nucleation. This energy barrier can be described in term of the supersaturation. Supersaturation (ΔP) is the driving force of crystal nucleation and growth. It is defined as a difference in chemical potential ($\Delta\mu$) between the parent and daughter phases. For the case of sublimation growth, it is given as:

$\Delta\mu = \mu_v - \mu_c,$ (1), where μ_V and μ_C are for the vapor phase and crystalline phase, respectively.

The change in chemical potential is related to supersaturation by the relation:

$\Delta\mu = K_b T ln \frac{\Delta P}{P} \ and \ \Delta P = \frac{P - P_e}{P_e},$ (2), where, P is the vapor pressure, P_e is equilibrium vapor pressure, K_b is Boltzmann constant.

When the supersaturation reaches a critical value ΔP_{crit}, a stable nuclei forms and crystal growth becomes possible. Therefore, a critical size of the nuclei must exist at which supersaturation is reached. This critical size is derived from the equation of the work (G) required to form a stable cluster and is expressed in term of the radius of the nucleus by assuming it to be spherical.

$G = -N\mu + 4\pi R^2 \sigma \ and \ G_{crit} = -N\mu + 4\pi R_{crit}^2 \sigma,$ (3), where R, σ and N are respectively the radius of the nucleus, surface free energy and number of molecules. The subscript *crit* denotes the critical values.

For a volume V occupied by each molecule, N is rewritten as:

$N = \frac{4}{3V}\pi R^3 \ and \ N_{crit} = \frac{4}{3V}\pi R_{crit}^3,$ (4)

It follows from equations (3) and (4) that the work required to form a stable cluster is a function of the radius of the nucleus, with the critical radius being the point at which nucleation is achieved and crystal growth irreversible. Similarly, the radius of the nucleus can be expressed as a function of the supersaturation. Its expression is given in equation 5 [10].

$R = 2\sigma V K_b T ln \frac{\Delta P}{P},$ (5), where T is temperature.

A plot of G and ΔP versus R is shown in Figures 1.1. It can be seen that R_{crit} and G_{crit} move in the same direction, while ΔP moves in the opposite direction. This suggests that nucleation is more likely to occur at higher supersaturation. Another observation that could be drawn from equations (3) and (4) is the dependence of R_{crit} and G_{crit} on surface free energy σ. Simply put, the surface free energy describes the amount of energy required to create a new surface. As such, surface energy quantifies the energy necessary to break intermolecular bonds to form a new surface. This implies that any process that can influence this quantity will also affect the nucleation and growth process. Some of these factors are discussed with an eye on the kinetic considerations.

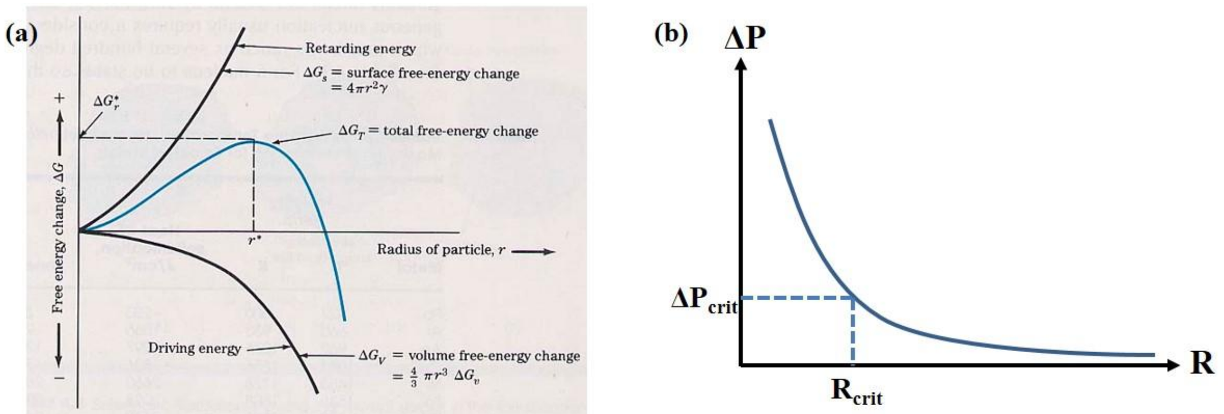

Figure 1.1. Diagram of free energy as a function of radius of nucleus (a) [11], relation between supersaturation and radius of nucleus (b)

I.2.2 Kinetic considerations

In introducing the driving force of crystal nucleation and growth, thermodynamic was considered and the nucleus was assumed spherical. This thermodynamic treatment of the driving force does not predict how fast growth occurs as well as the shape and morphology of the grown crystal. Crystals of well-defined shapes and morphology have been experimentally grown. It is thus important to understand what determines the grown crystals shape and morphology. This is answered in light of the kinetic of growth.

The kinetic of growth considers how fast nucleation and crystal growth occur. This is quantified by the rate of nucleation [12].

$$J = J_o \exp\left(\frac{-G}{K_b T}\right),$$ (6), where J_o is a constant that depends on the surface free energy σ.

The dependence of the growth rate on the surface free energy suggests that the interface at the growth front plays an important role in the crystal growth process. Crystal growth may be

mediated by the type of interface as well as dislocations at the interface. Two types of interfaces exist: *smooth* and *rough*. A *smooth* interface is one where the surface is regular and does not contain any steps, terraces, kinks or ledges. In comparison, a *rough* interface is one that contains surface irregularities such as steps, terraces or kinks.

Steps are raised partial layers of atomic dimension at the interface that flat regions called *terraces* separate. *Kinks* can be defined as atomic disruptions along the length of a step. A *ledge* is an atomic size protuberance along the length of a step. Kossel, Volmer and Stranski explained the crystal growth process on the basis of these surface irregularities [2, 13, 14]. According to them, crystal growth is a discrete process in which matter is adsorbed layer by layer on the crystal surface. More specifically, atoms arriving on the crystal surface migrate over the surface to locations, i.e. lattice sites, where they are incorporated. These lattice sites are illustrated in Figure 1.2 for the terrace-ledge-kink (TLK) model. It follows that only adatoms that reach a lattice site will become part of the growing crystal. This entails that the adatoms have a mean lifetime τ_s. The mean lifetime of an adatom can be expressed as a function of its mean migration distance L_s [15].

$\tau_s = \frac{L_s^2}{D_s} \; and \; L_s \approx Aexp\left[\frac{\varphi_{a-} \varepsilon_d}{2K_bT}\right],$ (7), where D_s is the surface diffusion constant, A is the distance between nearest neighbor atoms, φ_a is interaction energy between nearest neighbor atoms and ε_d is the migration barrier height.

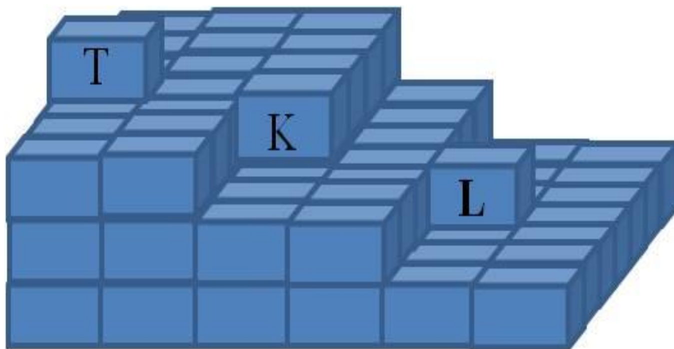

Figure 1.2. Illustration of the TLK assisted growth model. Atoms are represented by cubes. (T: terrace site, L: ledge site and K: kink site)

Adatoms are easily incorporated at kink sites compared to ledge and terrace sites because kink sites have a lower surface energy. This lower surface energy translates into a stronger binding energy between the adatoms and the growing crystal surface. Under ideal conditions, crystal growth will proceed by the advancement of steps as kink and ledge sites get filled up. When the step reaches its edge, further growth is only possible by the formation of 2D nuclei on

terrace sites. These nuclei will spread and coalesce to form layers according to a mechanism referred to as 2D nucleation. An illustration of 2D nucleation is shown in Figure 1.3.

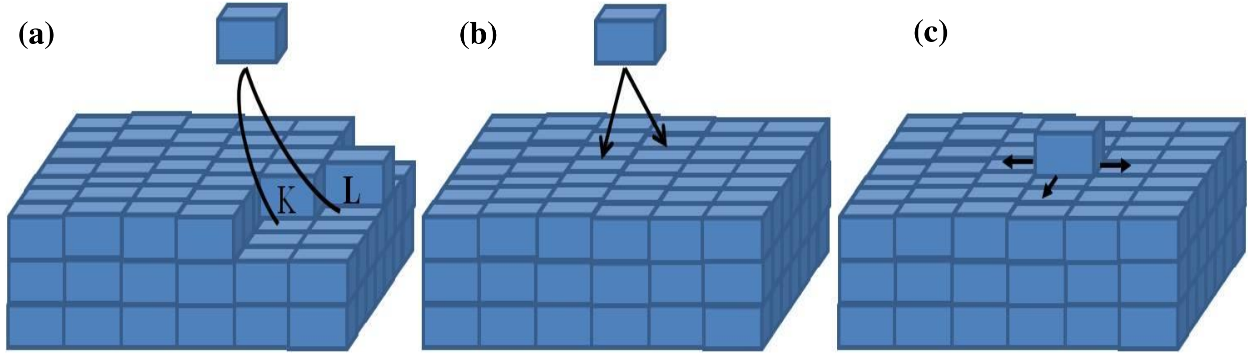

Figure 1.3. Illustration of 2D nucleation process. (a) Adatoms incorporate at kink and ledge sites, (b) adatom occupies a terrace site after steps has completely advanced to crystal edge, and (c) adatom on terrace surface becomes a 2D nucleus which expands in all directions

The rate of advance of a step and the energetic favoring 2D nucleation are given in equations 8 and 9 [16, 17]. Equation 9 assumes the 2D nucleus has radius R and height h.

$V = 2\frac{\Delta P}{P} L_s \nu \exp\left(\frac{-W}{K_b T}\right)$ (8), where $\boldsymbol{\nu}$ is a frequency factor and W is total evaporation energy.

$$\Delta G_{T-2D} = -\pi . \frac{hr^2}{V} \Delta\mu + 2\pi . rh\sigma \tag{9}$$

The critical size of the 2D nucleus is given in equation 10.

$$R_{crit} = \frac{\sigma . V}{K_b T ln\frac{\Delta P}{P}}, \tag{10}$$

While equations 8 and 9 may accurately predict that growth is favored at higher supersaturation, they do not explain the experimentally observed growth at lower supersaturation. In 1949, Franck posited that the continuous growth observed at lower supersaturation was achieved because of the presence of dislocations at the crystal surface [3]. These dislocations have a screw character and provide the source for steps of height equal to the projection of their Burgers vector. The definitions of Burgers vector and screw dislocations are provided in chapter 3. Works by Burton, Cabrera and Frank gives a detail insight into this dislocations assisted growth mechanism [16]. It should nonetheless be mentioned that this growth proceeds in the form of spiral around the dislocation. Figure 1.4 shows an illustration of this type of growth.

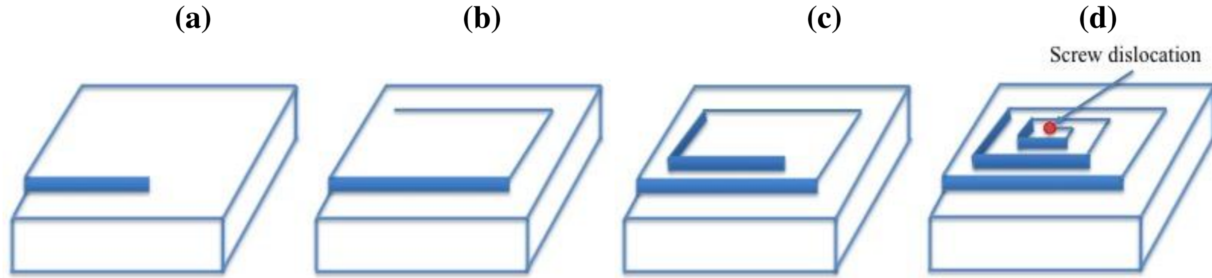

Figure 1.4. Screw dislocation assisted growth

Various methods of crystal growth exist depending on the type of phase transformation that takes place. The followings are the main type of phase transformation: solid-solid, vapor-solid, liquid-solid. Growth methods based on these types of phase transformation have been developed and refined over the years [18-20]. The use of a particular method for the growth of a given material is determined by the material's properties. In case two or more growth methods can be used, factor such as growth yield, practical feasibility and quality of grown crystal are considered in determining the most viable growth method. One compound material for which these criterions are used in determining a suitable growth method is silicon carbide. Because silicon carbide becomes unstable at temperature nearing its melting point, its growth from the melt is nearly impossible at reasonable temperature and pressure. Hence, SiC is grown by vapor technique. In comparison, it is more practical to grow cadmium zinc telluride from the melt because of the higher growth yield and relatively good crystal quality this method offers. In the subsequent sections, the growth of silicon carbide and cadmium zinc telluride are discussed.

I.3 Growth of SiC

The current industry standard for the production of bulk and thin film silicon carbide relies on vapor growth techniques. This section provides a brief overview of the two main vapor growth techniques used in the production of silicon carbide. These techniques are physical vapor transport (PVT) and chemical vapor deposition (CVD).

I.3.1 Physical vapor transport

In the *PVT* technique, a SiC powder inside a growth chamber is heated to a temperature typically exceeding 2200˚C at which silicon and carbon species from the SiC powder vapor are transported to a colder seed abetted by an axial temperature gradient. At the seed, the silicon and carbon species recombine to form a covalently bonded regular atomic arrangement, i.e. a SiC crystal. The ease with which the SiC crystal forms depends on the conditions inside the graphite

crucible. The phase diagram of SiC along with the conventional experimental setup of PVT growth is shown in Figures 1.5. The existence of the peritecticum in Figure 1.5a reveals the difficulty of growing SiC from the melt.

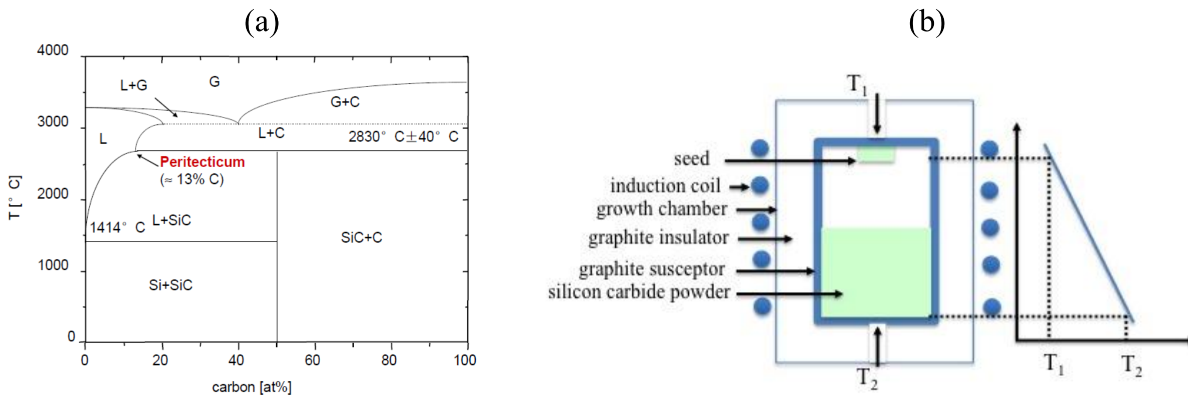

Figure 1.5. SiC phase diagram (a) and conventional experimental set up along with a plot of growth rate versus temperature gradient (b). Note that the growth rate is shown to be a linear function of the thermal gradient inside the growth chamber [21].

The factors affecting SiC crystal growth can be listed as follow: growth temperature, thermal gradient, convection and diffusion of silicon and carbon species. Optimization of these factors is necessary to improve growth conditions, and yield high crystal quality. It is important to highlight that these growth factors are all interdependent. According to T. Kimoto and J. A. Cooper, a suitable design of the growth chamber to control thermal gradient helps reduce the density of extended defects and avoid cracking in the grown SiC boule [22]. They further suggest that a larger radial thermal gradient lead to a convex growth front, while at smaller radial thermal gradient, the growth front is flatter. A typical temperature field inside a PVT growth chamber along with its corresponding temperature-pressure profile is shown in Figure 1.6.

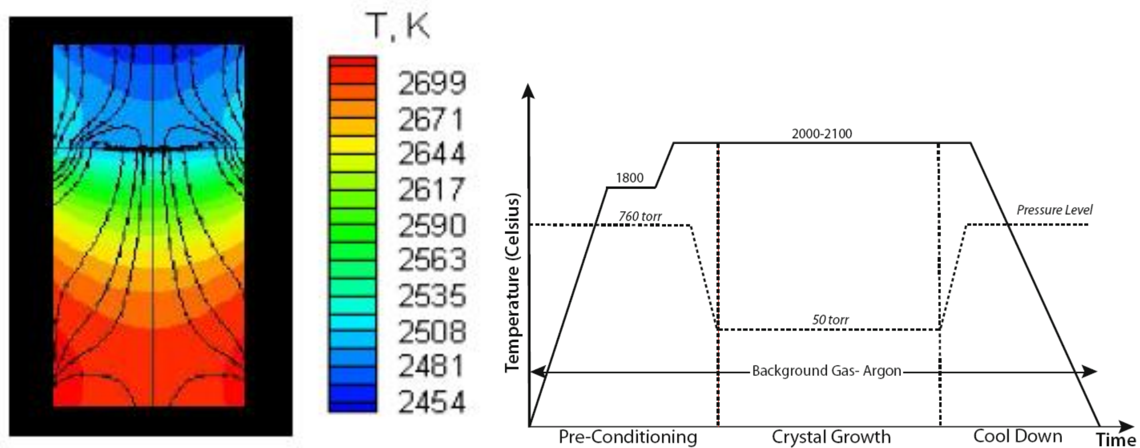

Figure1.6. Temperature field along with temperature-pressure profile inside a SiC PVT growth chamber [23]

The PVT technique is the preferred method for producing bulk SiC single crystal as it enables relatively large yield and polytype control. Despite its advantages, doping using PVT remains a challenge. While n-type doping has been achieved in PVT with relative ease by the addition of nitrogen [24], a lot of grounds have to be covered in order to achieve p-type doping or semi-insulation. A requisite to realize SiC device technology is to precisely control dopant incorporation and uniformity. Thus, in order to achieve control over doping, chemical vapor deposition is used.

I.3.2 Chemical vapor deposition

Chemical vapor deposition (CVD) is used to grow epitaxial layers with controlled doping for the realization of complex SiC devices. CVD operates in a manner similar to PVT with a few differences. The differences lie in the configuration of the reactor being used, the nature of the silicon and carbon precursor i.e. the process by which the Si and C vapor species are obtained. Unlike in PVT where Si and C vapor species are obtained from the condensation of SiC polycrystalline powder, Si and C vapor species are obtained from gaseous compounds containing silicon and carbon atoms in CVD. These Si and C vapor species are transported using a carrier gas (e.g. hydrogen) to a heated single-crystalline SiC substrate where they can form a relatively thick layer (up to 200 μm) via a surface-induced chemical reaction. The formation of the thick layer (also called epilayer) is pegged as epitaxial growth. When the epilayer matches the underlying substrate crystal structure, growth is *homoepitaxial*. The reverse case is called *heteroepitaxial*.

CVD growth occurs at temperatures typically above 1200˚C in either atmospheric or low pressure environment. In atmospheric pressure environment, CVD is referred to as APCVD, while it is referred to as LPCVD in low pressure. For years, SiC growth by CVD has been conducted under atmospheric pressure environment because of the availability of APCVD technology. Recently, however, CVD growth under low-pressure environment has become the industry standard because of the improvement in LPCVD technology, which has allowed for a more efficient control of the gas phase nucleation and impurity levels during growth. It should be noted that irrespective of the reactor configuration (i.e. horizontal or vertical), the deposition rate is affected by the distance from gas inlet, characteristic of the growth (mass transport or surface

reaction limited), and radial temperature gradient. A way to mitigate the effect of these factors is to tilt the substrate along the gas flow, increase the temperature along the substrate and use single wafer inside the growth reactor.

As mentioned previously, Si and C vapor species are obtained from gaseous compounds that contain silicon and carbon atoms. One characteristic those gaseous compounds must have is volatility. Variation of convection and diffusion during transport of gaseous species in the growth chamber can lead to silicon nucleation in the gas phase and result in harmful morphological defects. There exist several gaseous compounds used as Si and C precursors such as SiH_4, SiH_2Cl_2, $SiCl_4$, C_3H_8, CH_4, C_2H_4 and CCl_4. The effect of these precursors on the grown epilayer surface quality and growth rate has been investigated by other groups [25 - 27]. It follows from these investigations that methyltrichlorosilane (MTS) and halogenated silicon precursors (Si – X) help increase growth rate and improve epilayer surface compared to conventional silane (SiH4) precursor. These precursors act by preventing silicon nucleation in the gas phase as well as parasitic deposition. This suggests that for a particular precursor, the CVD growth process may need to be tailored to account for the differences in dissociation and nucleation kinetics of the precursor. Figures 1.7 illustrate the atomistic process occurring during CVD growth along with the temperature profile versus gas flow).

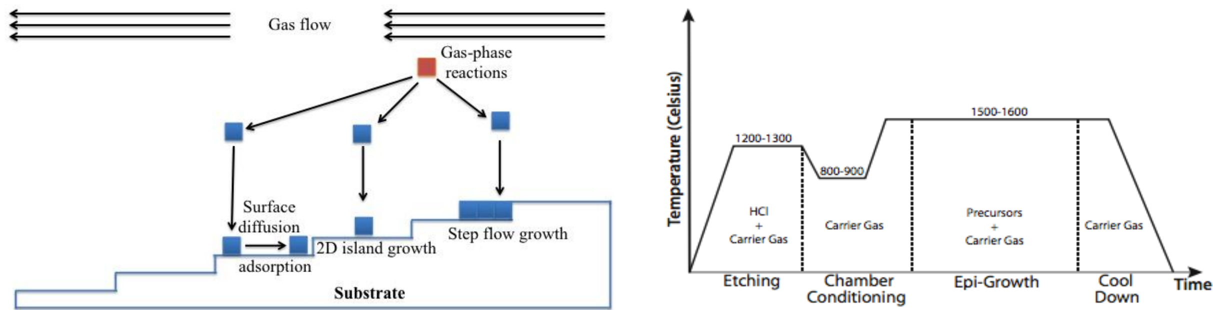

Figure 1.7. Atomic process and temperature profile versus gas flow for CVD homoepitaxial growth of SiC. Note the presence of steps on the substrate surface due to off-axis orientation of the substrate

Like the PVT technique, the nucleation, growth and formation of extended defects are associated with the temperature distribution inside the reactor. Small change in temperature gradient can cause thermal stress and result in the multiplication of basal plane dislocations (BPDs) by glide mechanism, which in turn can generate stacking faults (SFs). This can be avoided by suitable design of the growth reactor to mitigate the effect of radial thermal gradient.

The reader can refer to reference 28 for a list of different reactor configuration. The defects in the substrate have also been found to replicate into the epilayer [29, 30], prompting the need for a high quality seed (for PVT growth) and substrate (for CVD growth).

Additionally, polytype control, doping uniformity and concentration are highly critical to the development of silicon carbide technology. Improvement in both PVT and CVD technique has led to the development of growth along the (0001) on off-axis seed and substrate, and non-polar faces such as (1-100), (11-20) and (03-38) [31-33]. A novel growth technique, which purports to produce large high quality SiC single crystal with as low as 1 screw dislocation per square centimeter has recently been proposed by a group at NASA Glenn Research Center (GRC). This method, called Large Tapered Crystal (LTC) Growth, will be discussed in detail in chapter 4.

I.4 Growth of CZT

The growth methods for producing cadmium zinc telluride single crystals are either melt or vapor based [34-36]. Optimization of these methods has resulted in growth of single crystal CZT ingots up to 2-inch diameter. However, the poor thermo-physical properties of CZT at temperature near its melting point coupled with the nucleation and propagation of structural defects during the growth process constitute hurdles toward achieving more than 4-inch diameter CZT ingot at the industrial scale. In the subsequent sections, a brief discussion of the melt growth (Bridgman and traveling heater (THM)) and vapor growth (physical vapor transport (PVT)) methods is presented.

I.4.1 Melt growth

The melt growth of single crystals is influenced by the transport of crystallizing material from the bulk of the melt to the vicinity of the crystal surface, where melt molecules integrates into the crystal lattice. The transport of crystallizing material is ensured by convective heat, whereas the integration of melt molecules is influenced by the distribution coefficient κ.

$$\kappa = \frac{C_s}{C_m} \quad (11)$$

where C_s and C_m are respectively solid and melt concentration.

At $\kappa < 1$, impurity atoms from the surrounding of the crystal surface diffuse more readily to the melt. This coefficient is also temperature dependent because the diffusion of atomic species determines its magnitude.

Since the development of the Verneuil process in 1902, several melt growth techniques have been developed. Among those techniques are Tamman, Bridgman, Kyropoulos and Czochralski [34]. All these techniques are improved versions of the Verneuil process, and thus not fundamentally different. As mentioned in the previous section, the choice of a growth technique depends on the ease with which it can be carried out, the growth rate and yield, and the material properties. In the case of cadmium zinc telluride, the most widely used melt growth techniques are the Bridgman and Traveling heater methods. These methods are referred to as directional solidification because growth occurs along a particular direction.

Bridgman method: Conventionally, a seed crystal is placed at the opposite end of a polycrystalline powder inside a conically tapered ampoule with a sharp tip. The ampoule is evacuated, sealed and placed inside a furnace. Next, the polycrystalline powder is moved into a hot zone and heated above its melting point. The ampoule is then slowly moved from the hot zone to a colder zone, where one end of the resulting melt starts to solidify upon contacting with the seed crystal. Such approach allows control of the crystallization speed through the rate at which the crucible is moved, and should in principle result in high quality crystal since slow cooling is associated with a stable growth front.

However, in practice, the relative motion of the ampoule with respect to the furnace coupled with a non-uniform radiative heat transport that is associated with an unmodified temperature profile results in an unstable growth interface. The importance of the interface shape lies in its influence on the crystal quality. It has been proposed that an interface shape that is convex with respect to the crystal limit the propagation of defects that originate from stress at the ampoule wall to the bulk crystal, while a concave interface favors such propagation [37]. The factors influencing the interface shape have been studies, and the reader can consult references [38- 41] for further insight. It should be noted however that in general, the interface has a tendency toward a concave shape owing to a complex heat transfer process between the melt and the crystal coupled with a lower thermal conductivity of CZT crystal compared to the melt. A proposed solution to mitigate this effect is to use a multi-zone furnace where temperature programming to stabilize the heat transport and temperature variation across the melt. Such method is called Vertical Gradient Freeze (VGF) [42]. The readers can consult reference [42-44] for further insight into the VGF method.

Beside the instability in the melt interface, the use of an ampoule can have some adverse effects on the grown ingot. Contact with the ampoule wall confines the CZT melt expansion, and potentially favor stress built up during solidification of the melt. A direct consequence of this stress is the generation and multiplication of dislocations in the form of twin and subgrain boundaries. Better control over the thermal gradient and mass transport can mitigated the effect of ampoule wall contact. In the event of a lack of control over the temperature gradient, a large thermal gradient can result inside the grown ingot, and cause cracking. Another solution is to provide a protective layer between the CZT ingot and the inner walls of the ampoule. This is achieved by coating the ampoule wall with a thin layer of carbon [45]. The carbon atoms react with any O_2 and H_2O molecules and prevent adhesion of the CZT ingot to the ampoule wall.

There are several variants of the Bridgman technique categorized according to the magnitude of the pressure being used and the configuration of the growth ampoule. We thus distinguished on one hand low and high-pressure Bridgman technique, respectively LPB and HPB. On the other hand, we have horizontal and vertical Bridgman technique, i.e. HB and VB. Aside from the difference in design (HB vs. VB) and pressure (LPB vs. HPB), these variants consist of three temperature zones. The hot zone, i.e. last to freeze, has a temperature above the melting point of the powder. The cold zone, i.e. first to freeze, near the seed crystal has a temperature below the melting point of the powder. The middle zone, i.e. second to freeze, serves as an adiabatic buffer between the cold and hot zones. A conventional three-zone furnace for vertical Bridgman growth with its temperature profile is shown in Figure 1.8.

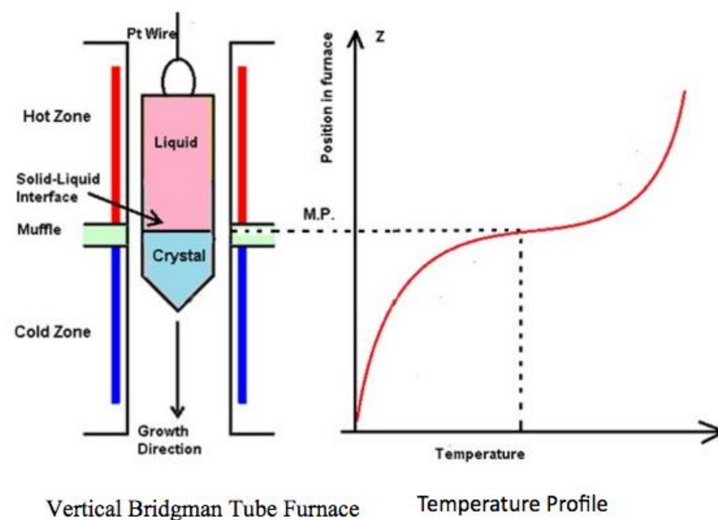

Figure 1.8. Conventional three-zone furnace for vertical Bridgman growth along with temperature profile [46]

Travelling heater method (THM): In a typical THM growth system for CZT, a Te-rich CZT melt is sandwiched between a seed and a polycrystalline CZT source material contained inside an ampoule. The Te-rich melt region is the hot zone where a heater is placed, whereas the seed and source material regions are colder zones. Translation of the heater towards the source material region results in its dissolution into the melt, which becomes supersaturated. Supersaturation of the Te-rich melt favors precipitation of CZT on the seed in the form of single crystal. Sustained bulk growth proceeds with continuous translation of the heater. An illustration of a THM technique is shown in Figure 1.9a.

This method offers a two-fold benefit. First, growth at temperatures far below the melting point of CZT (~300-350˚C) is made possible by the use of a Te-rich melt [47]. The low growth temperature implies a low thermal gradient. Since Te precipitates form because of the retrograde solid solubility of CZT during cooling down of the crystal ingot and that this solubility further decreases with temperature, it follows that the density of Te precipitates can be drastically reduced at lower temperature. This is observed in Figure 1.9b, where the solidus is 0.05% wide on the Te side in excess of stoichiometric value at 900˚C and 0.02% wide at 800˚C.

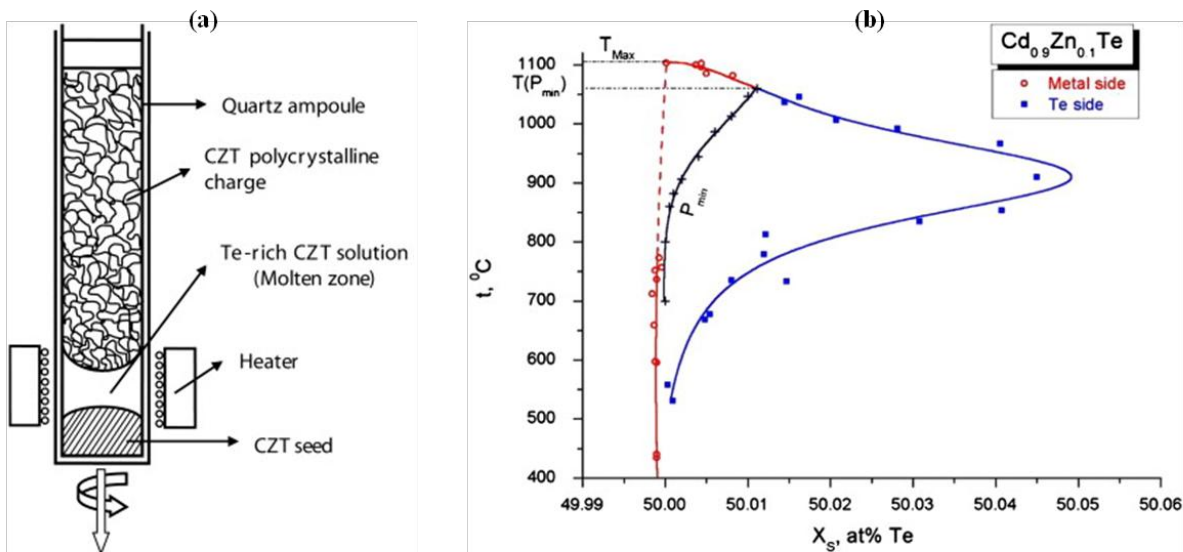

Figure 1.9. Schematic of the THM technique (a), and Temperature versus composition projection of Cd0.9Zn0.1Te1±δ solidus [47, 48]

While the density of Te precipitates can be significantly reduced by using THM, microscopic irregularities at the growth interface can lead to the capture of Te-rich melt at the interface and result in the formation of Te inclusions. The lower temperature prevents contamination from the ampoule walls and evaporation of compound species. The second benefit is that of self-

purification. The continuous passing of the Te-rich region through the source material effectively purifies it since the segregation coefficient of many of the impurities is higher in liquid Te than in liquid CZT. This is supported in the literature by work by Bell et al. [49], Triboulet and Marfaing [50], and K. Zanio [51]. Although THM yield higher crystal quality and compositional homogeneity compared to Bridgman grown CZT, its low growth rate of the order of few millimeters per day discouraged its broad integration on the industrial scale.

Since CZT is an alloy of CdTe and zinc telluride (ZnTe), a precise knowledge of the pseudo-binary phase diagram of the CdTe-ZnTe system is important. The phase diagram shows the location of the liquidus and solidus regions with respect to pressure, temperature and composition. This is illustrated in Figure 1.9, which shows a region of cohabitation separating the liquidus region from the solidus region. The melting points of the two pure binary components (CdTe and ZnTe) are determined from the end points of the curves. This phase diagram predicts that zinc (Zn) content is higher in the first-to-freeze region, where crystallization first occurs. Hence, the segregation of ZnTe in the CdTe-ZnTe pseudo-binary diagram can explain Zn segregation.

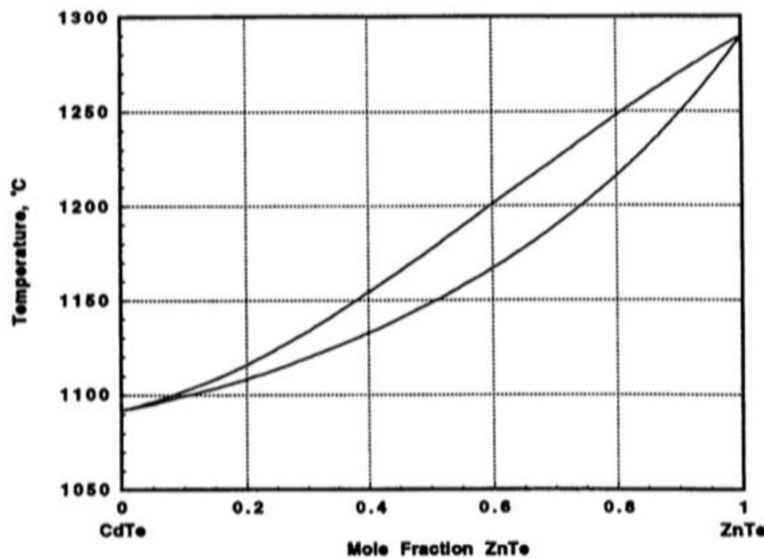

Figure 1.10. CdTe-ZnTe pseudo binary phase diagram [52]

In fine, Bridgman and travelling heater growth of CZT are processes driven by heat and mass transfer. The heat transfer affects the shape of the solid-melt interface, while mass transfer influences the formation of Te precipitates and/or inclusions. Improving the design of the growth system to control the interface shape has been achieved, though more progress are still needed [53, 54]. Mitigation of the tellurium inclusions and precipitates is imperative because these

defects are harmful to CZT-based detectors charge collection and transport properties [55, 56]. An approach to reach that end is proposed in chapter 7. This approach relies on the use of cadmium (Cd) overpressure to compensate for Cd evaporation and achieve stoichiometric melt, thereby preventing the formation of Te inclusions and precipitates.

I.4.2 Vapor growth

Because of the relatively high partial pressure of II-VI compound materials, growth of single crystals from the vapor phase is possible. Several variant of vapor growth of cadmium zinc telluride single crystals have been reported [57-59]. The followings are advantages of vapor growth over melt growth techniques:

- Lower processing temperature owing to high partial pressures of CZT compound hinders formation of Te secondary phase particles
- Lower processing temperature reduces thermal stress and contamination from crucible walls, and likely propensity to twinning
- Differential vapor pressures of the native elements and the impurities lead to purification of CZT source materials
- Possibility to achieve a morphological stable solid-vapor interface during growth

It follows from the above advantages that single crystals of high quality with low impurities concentrations and high homogeneous concentration distribution can be obtained by vapor growth. However, stumbling blocks in the path of this technique have prevented its widespread integration. These stumbling blocks are low growth rates/yield, low resistivity and poor reproducibility [60]. The low growth rate/yield and poor reproducibility depends on the precise control over stoichiometry of the source materials and vapor as well as the seeding. While vapor growth can be divided depending on the nature of the source (solid or vapor) or the transport mechanism (physical or chemical), herein, we briefly describe the variant that uses a solid source and in which the transport mechanism is physical. This variant is called **physical vapor transport** (PVT).

The crystal growth of several binary compounds such as SiC, HgI2 and CdTe has been successfully achieved using PVT [57, 36]. This method involves the sublimation of CZT source materials (preferentially CdTe and ZnTe binary) at about 1000°C followed by transport and condensation at the solid-vapor interface. Several configuration of the PVT method have been designed and implemented. These are the semi-open system [61, 62], stationary seeded growth in

a closed system [63], translational unseeded growth in a closed system [64], and growth under controlled partial pressure in a closed ampoule [65]. Although each of the PVT configurations yields ingots of differing quality, overall the ingots contain multiple grains with lamellar twins and a relative high density of dislocations.

I.5 Summary

Crystal growth is a process that starts with the formation of a nucleus, followed by its expansion into a macroscopic object consisting of a regular arrangement of atoms with a high degree of symmetry in three dimensions. It is driven by the chemical potential or supersaturation ($\Delta\mu$), which gives the conditions under which growth is irreversible. In principle, crystal growth is expected to occur under high supersaturation conditions. However, most experimental growth processes occur at lower supersaturation. The growth at low supersaturation has been ascribed to the presence of inhomogeneities on the surface of the growing crystal. Such inhomogeneities are screw dislocations, terraces, ledges, kinks and vacancies. They influence the growth mechanism, leading to either spiral growth or step growth. The spiral growth is mediated by screw dislocation, while the step growth is mediated by the terrace-ledge-kinks. Both spiral and step growth lead to 3D growth. When the growth surface does not exhibit any inhomogeneities, the surface is said to be smooth. In this case, 2D type nucleation is favored.

Several growth methods have been developed to achieve crystal growth. They are classified according to the type of phase transformation that occurs. There exist three main types: melt, vapor and solid growth. The choice of the growth method is influenced by factors such as material property, growth rate and yield, and ease of implementation. For material such as silicon carbide and cadmium zinc telluride, growth by vapor and melt are respectively privileged. Silicon carbide is mainly grown by vapor because it is difficult to obtain a melt at reasonable growth temperature and pressure. Though vapor growth of CZT can potentially produce high quality crystal, the low growth rate and cost benefit prevents it wide scale application, particularly in industry. Thus, CZT single crystals are mainly grown by melt using the Bridgman technique.

References

1. H. G. Van Bueren, "Imperfection in crystals", Amsterdam, North-Holland (1960)
2. W. Kossel, Nachr. Ges. Wiss. Goettingen Math. Phys. K1 11A, p 135, (1927)
3. F. C. Frank, Discuss. Faraday Soc. 5, p 48-54 (1949)
4. Werner Balhaus, Alessandro Pagella and Constantin Vogel, "A change of pace for the semiconductor industry", PricewaterhouseCooper (PWC) (2009)
5. A. A. Chernov, J. Cryst. Growth 264 (4), p 499-518 (2004)
6. J. P. Hirth and G. M. Pound, "Condensation and evaporation: Nucleation and growth kinetics", Progress in materials science, New York, Macmillan (1963)
7. John D. Weeks and George H. Gilmer, "Dynamics of Crystals Growth", Advances in Chemical Physics 40, p 157-228 (1979)
8. R. James Kirkpatrick, "Crystal Growth from the Melt: A Review", American Mineralogist 60, p 798-814 (1975)
9. Robert S. Feigelson, "Chapter 1: Crystal growth through the ages: A historical perspective", Handbook of crystal growth: Fundamentals (Thermodynamics and Kinetics) Vol 1, part A, 2nd edition, Ed Tatau Nishinaga, Elsevier (2014)
10. D. Kashchiev, "Nucleation:Basic theory with applications", Butterworth-Heinemann, Oxford (2000)
11. http://www.benbest.com/cryonics/lessons.html
12. J. W. Mullin, "Crystallization", 4th edn, Butterworth-Heinemann, Oxford (2001)
13. M. Volmer, Die Kinetik der Phasenbildung, Steinkopff, Dresden, 1939
14. I. N. Stranski, Z. Phys. Chem., 136, p 259 (1928)
15. Boyan Mutaftschiev, "The atomistic nature of crystal growth", Chapter 15, p 288, Springer-Verlag, Berlin Heidelberg (2001)
16. W. K. Burton, N. Cabrera and F. C. Frank, Phil. Trans. Roy. Soc. 243, p 299 (1951)
17. Pablo Cubillas and Michael W. Anderson, "Chapter 1, Synthesis mechanism: Crystal growth and nucleation", Zeolites and catalysis: Synthesis, Reactions and Applications, Eds Jiň Čejka, Avelino Corma, and Stacey Zones, Wiley-VCH Verlag GmbH & co, KGaA, Weinheim, p 1-55 (2010)
18. Guoqiang Li, Xiaolu Zhang, Hui Hua and Wanqi Jie, J. Electronic Materials 34 (9), 2005

19. R. Muller, U. Kunecke, D. Queren, S. A. Sakwe and P. Wellmann, Chem. Vapor Deposition 12 (8-9), p 557-561 (2006)
20. F. B. Romdhane, T. Björkman, A. V. Krasheninnikov, and F. Banhart, J. Phys. Chem. C, 118 (36), p 21001-21005, (2014)
21. C. M. Balkas, A. A. Maltsev, M. D. Roth and N. K. Yushin, Mat. Sci. Forum 338-342, page 79-82 (2000)
22. T. Kimoto and J. A. Cooper, Fundamentals of Silicon Carbide Technology: Growth, Characterization, Devices, and Applications, First Edition, Chapter 3, John Wiley & Sons, Singapore, (2014)
23. A. Itoh and H. Matsuma, Single crystal growth of SiC and electronic devices. Critical Reviews in Solid State and Materials Sciences 22 (2), p 111-197 (1997)
24. M. A. Fraga, M. Bosi and M. Negri, Chapter 1: Silicon Carbide in Microsystem Technology – Thin Film Versus Bulk Material, "Advance in Silicon Carbide Device and Processing", Edited by S. E. Saddow and F. La Via (2015)
25. T. S. Sudarshan, T. Rana, H. Song and M. V. S. Chandrashekhar, ECS J. Solid State Sci. Technol 2 (8), N3079-N3086 (2013)
26. T. Rana, M. V. S. Chandrashekhar and T. S. Sudarshan, Physica Status Solidi (a) 209 (12), p 2455-2462 (2012)
27. H. Pedersen, S. Leone, A. Henry, F. C. Beyer, V. Darakchieva and E. Janzen, J. Cryst. Growth 307 (2), p 334-340 (2007)
28. M. Skowronski and T. Kimoto, 2nd Edition Handbook of Crystal Growth: Thin Films and Epitaxy: Basic Techniques, and Materials, Processes, and Technology, edited by Tom F. Kuech, Chapter 28: Silicon Carbide Epitaxy, Elsevier B.V. (2015)
29. T. Ohno, H. Yamaguchi, S. Kuroda, K. Kojima, T. Suzuki and K. Arai, J. Cryst. Growth 260 (1-2), p 209-216 (2004)
30. H. Tsuchida, I. Kamata and M. Nagano, J. Cryst. Growth 306 (2), p 254-261 (2007)
31. N. Ohtani, M. Katsuno and T. Fujimoto, Jpn. J. Appl. Phys. 42, p L277-279 (2003)
32. J. Takahashi, M. Kanaya and Y. Fujiwara, J. Cryst. Growth 135 (1-2), p 61-70 (1994)
33. T. Furusho, H. Takagi, S. Ota, H. Shiomi and S. Nishino, Mat. Sci. Forum 457-460, p 107 (2004)

34. Hans J. Scheel, “Chapter 1: The development of crystal growth technology”, Crystal Growth Technology, Eds Hans J. Scheel and T. Fukuda, John Wiley & Sons, Ltd., p 3-14 (2003)
35. W. Palosz, K. Grasza, D. Gillies and G. Jerman, J. Cryst. Growth 169 (1), p 20-26 (1996)
36. T. E. Schlesinger, J. E. Toney, H. Yoon, E. Y. Lee, B. A. Brunett, L. Franks and R. B. James, Mater. Sci. Eng. R 32 (4-5), p 103-189 (2001)
37. W. A. Tiller, “Principles of Solidification”, In: Gilman JJ, editor. The Art and Science of Growing Crystals. John Wiley & Sons, Inc; p 276 (1963)
38. R. J. Naumann and S. L. Lehoczky, J. Cryst. Growth 61, p 707-710 (1983)
39. C. E. Chang and W. R. Wilcox, J. Cryst. Growth 21 (1), p 135-140 (1974)
40. S. Kuppurao, S. Brandon and J.J. Derby, J. Cryst. Growth 155, p 93 (1995)
41. S. Kuppurao and J. J. Derby, J. Cryst. Growth 172, p 350-360 (1997)
42. N. Zhang, A. Yeckel and J. J. Derby, J. Cryst. Growth 355 (1), p 113-121 (2012)
43. M. Azoulay, S. Rotter, G. Gafni, R. Tenne and M. Roth, J. Cryst. Growth 117 (1-4), p 276-280 (1992)
44. T. Asahi, O. Oda, Y. Taniguchi and A. Koyama, J. Cryst. Growth 161 (1-4), p 20-27 (1996)
45. M. J. Harrison, A. P. Graebner, W. J. McNeil and D. S. McGregor, J. Cryst. Growth 290, p 597-601 (2006)
46. Prof. F. Hossein Babaei, KNT University of Technology Electronic Department Crystal Growth Instructor, presented by M. H. Jalalpour and P. Talebnia (Fall 2014), http://slideplayer.com/slide/7668050/
47. U. N. Roy, A. Burger and R. B. James, J. Cryst. Growth 379, p 57-62 (2013)
48. J. H. Greenberg and V. N. Guskov, J. Cryst. Growth 289, p 552-558 (2006)
49. R. O. Bell and N. Hemmat, Phys. Stat. Solidi (a) 1 (3), p 375-387 (1970)
50. R. Triboulet and Y. Marfaing, J. Cryst. Growth 51 (1), p 89-96 (1981)
51. K. Zanio, J. Electron. Mater. 3 (2), p 327-351 (1974)
52. T. C. Yu and R. F. Brebrick, J. Phase Equilibria 13 (5), p 476-496 (1992)
53. L. Lun, A. Yeckel, J. J. Derby and P. Daoutidis, “Control of interface shape of cadmium zinc telluride grown via an electrodynamic gradient freeze furnace”, Proceedings of the 15th Mediterranean Conference on Control & Automation, July 27-29 (2007), Athens (Greece)
54. S. Sen and W. R. Wilcox, J. Cryst. Growth 28, p 26-40 (1975)
55. D. H. Kim, P. M. Adornato and R. A. Brown, J. Cryst. Growth 89, p 339 (1988)

56. A. E. Bolotnikov, G. S. Camarda, G. A. Carini, Y. Cui, L. Li and R. B. James, Nucl. Instr. Methods in Physics, Research section A: Accelerators, Spectrometers, Detectors and Associated Equipment 571 (3), p 687-698 (2007)
57. W. Palosz, M. A. George, E. E. Collins, K. -T. Chen, Y. Zhang, Z. Hu and A. Burger, J. Cryst. Growth 174 (1-4), p 733-739 (1997)
58. K. Yasuda, M. Minamide, K. Kawamoto and T. Maejima, J. Cryst. Growth 159 (1-4), p 121-125 (1996)
59. C. Paorici and G. Attolini, Prog. Cryst. Growth Charact. Mater. 48-49, p 2-41 (2004)
60. A. W. Brinkman and J. Carles, "The Growth of Crystals from the vpaour" Prog. Cryst. Growth Charact. Mater. 37 (4), p 169-209 (1998)
61. L. C. Greene, D. C. Reynolds, S. J. Czyzak and W. M. Baker, J. Appl. Phys. 29, p 1357 (1958)
62. W. W. Piper and S. J. Polich. J. Appl. Phys. 32, p 1278 (1961)
63. G. Cantwell, W. C. Harsch, H. L. Cotal, B. G. Markey, S. W. S. McKeever and J. E. Thomas, J. Appl. Phys. 71, p 2931-2936 (1992)
64. H. –Y. Cheng and E. Anderson, J. Cryst. Growth 96 (4), p 756-762 (1989)
65. J. R. Cutter, G. J. Russell and J. Woods, J. Cryst. Growth 32, p 179 (1976)

Chapter II: Introduction to Silicon Carbide

II.1 History

From the discovery of the existence of Si-C bond in 1824 by Jöns Jacob Berzelius [1] to its current applications in high power/high frequency devices, silicon carbide (SiC) crystal growth has gone through many stages. Those stages can be divided into three categories: discovery, lethargy and renaissance stage.

In the late 19th century, Henry Moissan discovered the presence of silicon carbide in meteorite in the Arizona desert [2]. Few years later, E. G. Acheson achieved the first synthesis of silicon carbide during experimental runs for diamond synthesis. Crystals grown by the Acheson method were polycrystalline in nature and had a high density of structural impurities [3]. Despite their polycrystalline nature, SiC grown in these days readily found application as abrasive materials and cutting tools because of their chemical stability and mechanical hardness. This early use of SiC promoted the development of a SiC industry geared toward mechanical application and concurrently further research to discover new properties of SiC.

Following the discovery of polytypism in early crystals and the investigation of its electronic properties, a gradual shift in application occurred. In 1907, the electroluminescence property of SiC was revealed with the making of the first light emitting diode (LED) [4]. This piqued interest in SiC as a new material for electronic applications. With this breakthrough in application, it became more pressing to efficiently control polytype transformation during crystal's growth. Several efforts were thus carried out, and in 1955, J. A. Lely developed a growth technique, which resulted in enhanced quality of the SiC grown crystals [5]. The Lely technique relied on the distillation of SiC through a vapor phase to produce platelets of high structural quality.

Although the Lely method yielded high quality platelets, growing large boules of high quality was still a challenge. First, the low growth rate made it difficult to produce large size boules, and obtain large enough substrates for electronic applications. Second, the lack of control over the nucleation process prevented prediction of the grown polytype. In the event large boules were obtained, they were polycrystalline and contained a relative high density of structural defects. Finally, the grown SiC crystals by the Lely method had non-uniform physical and electrical properties. These issues dampened the enthusiasm for silicon carbide research. As a result, SiC

was relegated to the realm of basic research, where it became the appanage of materials scientist and physicists.

With the enduring efforts of materials scientists and physicists, another breakthrough in the growth of silicon carbide occurred. In 1978, Tairov and Tsevtkov developed an improved version of the Lely's method, called *modified Lely's* or *Physical Vapor Transport (PVT)*. In this technique, a seed crystal was introduced into the growth chamber to improve control over the nucleation process. Growth proceeded by vapor transport of silicon (Si) and carbon (C) species from a source (e.g. $SiCl_4$ and C_3H_8 gas precursors) to the seed crystal. This resulted in better polytype control, increased growth rate and crystals of larger diameter (order of inches). This newly developed PVT technique brought back silicon carbide to the limelight as a viable alternative to silicon in the semiconductor industry, particularly for high power/frequency applications. A decade later, further progresses in growth were made with the implementation of a new step-controlled epitaxy technique. This new technique facilitated the growth of epitaxial layers at lower temperature on off-axis substrates, and made it easier for SiC based technology to take off [6].

In the late 1980s, SiC made its first appearance on the commercial market. A key contributor to this was Cree, a company created out of a laboratory at North Carolina State University in 1987. Today, silicon carbide single crystals of up to 6 inches in diameter are grown. The formation of structural impurities is better investigated and their formation mechanism elucidated. Growth schedules, which mitigate the propagation of certain structural defects or favor the conversion of others into less harmful types, have been designed [7]. Furthermore, the density of these structural defects is gradually and consistently decreasing, making SiC products more competitive with respect to other semiconducting materials in their class. For instance, the density of micropipe, a hollow core type of structural impurity has been reduced to close to zero, and that of threading screw dislocations (TSD) has decreased to the order of $10^2 cm^{-2}$ [8].

II.2 Crystal structure and material potential

II.2.1 Crystal structure

Silicon carbide (SiC) is a wide band-gap semiconductor that consists of group IV elements in the periodic table. Both silicon and carbon atoms are covalently bonded in equal stoichiometric ratio (1:1), and each atom of one kind is surrounded by four atoms of the other. Thus, the unit

cell of a silicon carbide single crystal can be seen as comprised of layers of corner sharing tetrahedra (Fig. 2.1) in which each silicon atom has four neighboring carbon atoms and vice versa. In such structure, the corner sharing tetrahedra can be stacked (i.e. arranged) in many different ways, giving rise to an extensive range of well-defined structures known as polytypes.

The stacking sequence of the corner sharing tetrahedra (i.e. Si-C bilayers) gives the signature structure of each polytype. In fact, successive Si-C bilayers may be arranged in two possible ways: translational and/or rotational along the close packed direction of the polytype. The rotation of a tetrahedron along its close-packed axis can be seen as twinning, where the rotated tetrahedron is its mirror image. This is illustrated in Figure 2.1. The projected stacking sequence along the [11-20] direction of four polytypes of SiC is also shown in Figure 2.2. It follows from the preceding that a key element in identifying silicon carbide polytypes is the height of the unit cell along the close-packed direction, which differs among polytypes.

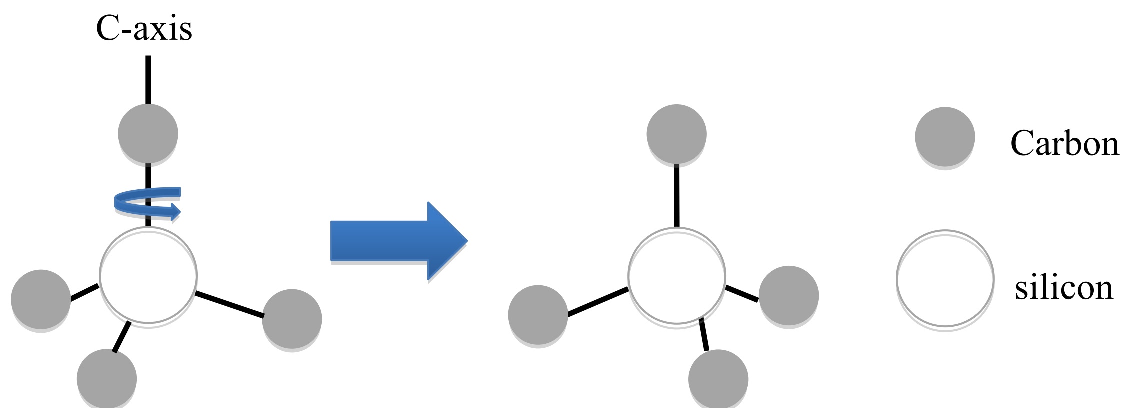

Figure 2.1. Tetrahedrons showing the building blocks of silicon carbide crystals. Note that the tetrahedron on the right is obtained by rotating the one on the left around its c-axis by 180°

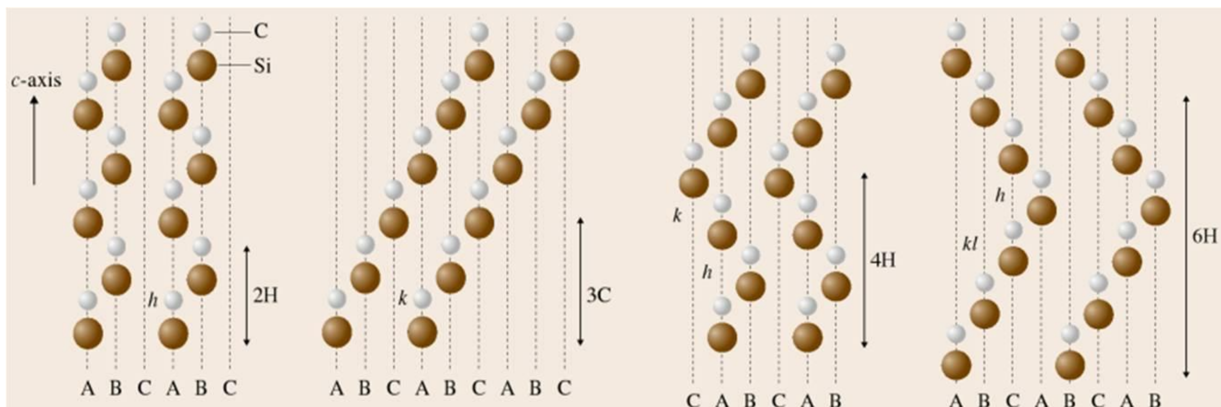

Figure 2.2. Stacking sequence of (a) 2H, (b) 3C, (c) 4H and (d) 6H-SiC polytypes, projected along [11-20] direction

To date, about 200 polytypes of SiC have been identified [9]. Zhdanov and Ramsdell notations are commonly used nomenclature to describe the different silicon carbide polytypes. The Ramsdell notation consists of a digit followed by a letter; where the digit accounts for the number of Si-C bilayers in the unit cell and the letter represent the crystal structure. For instance, a polytype having three Si-C bilayers and a cubic crystal structure will be described as 3C-SiC. In contrast, the stacking sequence of a polytype is described using two numbers in a bracket followed with a subscript $(n_1\ n_2)_{n3}$ when using the Zhdanov notation. n_1 is the sum of bilayers stacked in translation before rotation of the last bilayer in the first set of translation, while n_2 is the sum of bilayers stacked in translation following the first rotation, and n_3 corresponds to the number of repeat of n_1 and n_2 in the stacking. For the 6H-SiC polytype, the identification using Zhdanov notation would be (33).

II.2.2 Material potential

Silicon carbide is a wide-band compound semiconductor that possesses excellent thermal and mechanical properties. Its crystal lattice consists of corner sharing tetrahedra of silicon (Si) and carbon (C) atoms in which silicon and carbon atoms form strong covalent bonds with length of 1.89 Å and a 9.5 Mohs indice of hardness [3]. Because of its strong Si-C bond, which require a high temperature to be broken, SiC exhibit a high thermal strength. This thermal strength results in a high thermal stability and conductivity, resistance to irradiation and low thermal expansion. The combination of the aforementioned properties makes SiC suitable for high temperature and radiation prone environments such as nuclear power plants. Additionally, silicon carbide has shown promise in structural applications where it is used for its mechanical properties in abrasives, ceramics and cutting tool materials.

Besides its physical properties and ability to withstand high temperatures, silicon carbide occurs in several structural arrangements, i.e. stacking sequences that are identical in structure and composition, but have one of the dimensions of the unit cell that is different. The most common polytypes of SiC are 3C, 4H and 6H-SiC. Each one of these possesses a comparative advantage over the other in device applications. For instance, 3C-SiC polytype metal oxide semiconductor field effect transistors (MOSFETs) has a higher inversion channel mobility compared 4H-SiC (MOSFETs) [10] due to a lower density of interface states associated with the lower conduction band in 3C compared to 4H polytypes [11, 12]. A direct consequence of the lower density of interface states in 3C-SiC is a reduction in surface generation and recombination

of carriers that have been found to plague bipolar and metal oxide semiconductor (MOS) devices [13, 14]. Conversely, the wider bandgap energy 4H and 6H polytypes enables high breakdown voltage and makes them more suitable for high power and high frequency devices. It follows that the various atomic arrangements of silicon carbide, also called polytypes, do not have the same bandgap energy. Table 2.1 shows the room temperature bandgap energy of 3C, 4H and 6H-SiC.

Table 2.1. Room temperature bandgap of the most common grown silicon carbide polytypes

Polytype	3C-SiC	4H-SiC	6H-SiC
E_g (eV)	2.3[15]	3.2[15]	3.0[15]

These polytypes have a much wider bandgap than conventional semiconducting materials like Si (1.12ev) and GaAs (1.43ev) [16]. This is why SiC is identified as wide-bandgap (WBG) semiconducting material. As a wide band-gap material, silicon carbide has very robust electronic properties. Typical electronic applications of silicon carbide are found in light emitting diodes (LEDs), PiN diodes and power inverters [17] to name a few. Furthermore, SiC can be considered an insulator at room temperature because of its wide bandgap energy. Its valence band electrons are tightly bonded and require larger thermal energy to be excited to the conduction band. Therefore, intrinsic conduction at room temperature is prevented and the probability of leakage current is significantly reduced. In fact, leakage current is caused by intrinsic conduction when electrons that are excited from the valence band to the conduction band generate electron and hole pairs. So, reducing the probability of electron-hole pair generation decreases leakage current and allows for higher breakdown voltage, which is a requirement for power device applications.

Another advantage of a high breakdown voltage is a high thermal stability as intrinsic conduction becomes less sensitive to heat. Devices based on SiC can operate at temperature exceeding 600°C without the requirement for cooling that is necessary in the case of Si-based electronics [18]. A practical benefit of this high breakdown voltage can be illustrated by a comparison with silicon. For a silicon based power device, 100 times lower doping concentration in a 10 times thicker layer is required to match a SiC based power device [19]. This suggests that use of SiC in power device application has the potential of significantly reducing cost by reducing volume. Despite its lower carrier mobility compared to Si, SiC supersedes Si for high frequency switching device application owing to its higher saturated carrier drift velocity. These types of devices require a high carrier mobility and saturation drift velocity, which is desirable to avoid power loss during switching cycles.

Other than the excellent electronic properties owing to its being a wide band-gap material, the potential for the application of SiC in the jewelry industry has been harnessed; silicon carbide has been made into high purity and colorless gem [20]. Recently, silicon carbide has been considered as a substrate of choice for the growth of materials that are either very defectious when grown on native substrate or difficult to grow on native substrate. Examples of SiC polytypes used as foreign substrates are 3C, 4H, 6H and 15R-SiC. The 4H and 6H polytypes have been used in the growth of gallium nitride (GaN) and boron phosphide (BP) because of their hexagonal structure that has a comparable lattice match with the wurtzite structure of GaN [21, 22]. In comparison, the 3C and 15R-SiC polytypes is being considered as a substrate of choice in the growth of boron arsenide ($B_{12}As_2$).

In fine, silicon carbide is a very attractive semiconducting material for high end technological applications compared to current conventional materials such as Si and GaAs. The combination of its physical, chemical, thermo-electronic and mechanical properties makes it a suitable material for a variety of applications [23, 24]. Common applications in which SiC is used are high-voltage/high frequency devices [23-25], lighting, automobile and telecommunication.

Table 2.2. Comparison of the properties of common silicon carbide polytypes with other known conventional semiconductors [26]

Materials	T_w(K)	k (W/cm.K)	μe (cm^2/V.s)	μh (cm^2/V.s)	E_b (10^5V/cm)	V_s (10^7cm/s)
Si	410	1.31	1430	480	3	1
4H-SiC	1300	3.7 [27]	800	115	30	2
6H-SiC	1200	4.9 [27]	400	90	32	2
3C-SiC	1200	3.6 [9]	750[15]	40[15]	18	2.5
GaAs		0.55 [28]	6500[30]	320[30]	4	0.8[29]

T_w: working temperature; k: thermal conductivity; μ_e: electron mobility; μ_h: hole mobility, E_b: breakdown field; V_s: saturated carrier velocity. Note that electron mobility of 4H-SiC is isotropic, whereas that of 6H-SiC exhibit anisotropy along the direction parallel to the c-axis (it is 60 cm^2/V.s)

II.3 Challenges in the growth of silicon carbide

Recent advances in semiconductor technology have raised the interest in wide band-gap materials as viable alternative to silicon (Si) based technology. These materials possessed excellent properties that enable them to operate under harsh environments unlike their conventional counterpart. One such material is silicon carbide. A list of its properties, suggesting the variety of applications in which it can be used, is shown in Table 2.2. While it follows from Table 2.2 that SiC can be used in a variety of applications, effectively harnessing these properties

is hampered by challenges in the growth methods used to produce SiC, techniques of micromachining and material integration. The techniques of micromachining and material integration are beyond the scope of this thesis, and the reader can refer to reference [15, 31].

Silicon carbide does not naturally occur; and as such it has to be grown into thin film or wafer forms using specific growth techniques. These growth techniques are physical vapor transport (PVT), chemical vapor deposition (CVD) and top seeded solution growth (TSSG) to name a few. They can be divided into two categories: vapor based and solution based. Each category carries its own advantages and limitations, and knowing them is important as this allows for effective design of growth schedules and optimization of growth parameters that can in turn potentially yield high quality single crystal.

Despite the existence of about 200 polytypes, only 3C-SiC, 4H-SiC and 6H-SiC have found their niche in device applications. It should be noted, nonetheless, that these three polytypes do not enjoy the same degree of widespread use owing to a combination of factors such as their electronic properties, availability of high quality and large size crystals. For instance, 4H-SiC has a higher and isotropic carrier mobility, shallower dopant ionization energies and lower intrinsic carrier concentration compared to 6H-SiC [30]. Similarly, large and high quality single crystal wafers of 4H-SiC polytype are more readily available. Today, it is thus not uncommon to produce 4H and 6H-SiC micropipes (μPs) free wafers having a diameter of up to 6 inches [30, 32]. In contrast, 3C-SiC is limited in size and quality due to low growth yield and presence of high density of structural defects such as double positioning boundaries (DPBs) and anti-phase boundaries (APBs). In light of the aforementioned, 4H-SiC and 6H-SiC are the first and second most used polytype for high-power and high frequency device fabrication.

However, the current state of SiC based technology for all three polytypes suffers the same fundamental challenges as it pertains to their growth. These challenges involve polytype control, defects distribution/density, dopant control and doping uniformity in both substrate and epilayers. The consequence of these challenges is different from one type of application to the other. In power devices, use of low-resistivity substrates is desirable as it helps reduce power losses inherent to parasitic substrate and contact resistances [30]. On the other hand, use of semi-insulating substrates is preferable for microwave frequency devices as it helps reduce dielectric losses and parasitic failure. Thus, overcoming these challenges is vital for producing high efficiency devices.

In the subsequent sections, a brief overview of the challenges that plague silicon carbide technology as it relates to the growth of SiC large single crystal of high quality is addressed. These challenges revolve around the structural defects and growth techniques.

II.3.1 Point defects

These types of defects consist of vacancies, interstitials and substitutional atoms. Vacancies are defined as unoccupied atomic sites, whereas interstitials are impurity atoms occupying sites between host atoms. When an atom of the regular lattice occupies an interstitial site, it is said to be a self-interstitial. Other types of point defects are substitutional atoms. These occur when a foreign atom takes the site of a host atom in the crystal lattice. In the event these point defects originate from SiC elements, they are called intrinsic defects. In the contrary, they are called extrinsic defects. We should refer to silicon (carbon) vacancy and interstitial by V_{Si} (V_C), Si_i (C_i) respectively. Figure 2.3 is an illustration of these defects.

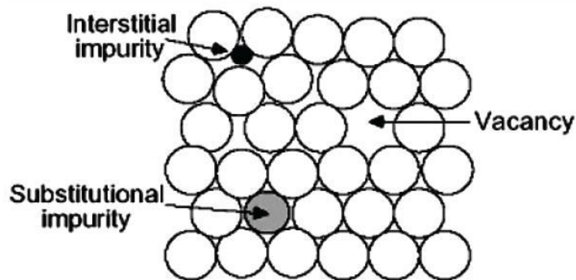

Figure 2.3. Illustration of different types of point defects

SiC is a binary compound whose different polytypes exhibit inequivalent lattice sites. It is therefore possible to encounter a combination of the aforementioned defects in their crystal lattice. These possible combinations can be classified as follows:

i. Frenkel pair, which occurs when an atom from a lattice site moves to an interstitial position; thereby creating a vacancy-interstitial pair.
ii. Divacancies, which occurs when two vacancies are close together (e.g. $V_{Si} – V_C$)

Additionally, the following pair of defects can occur, e.g. antisite - vacancy pair, vacancy – impurity pair. Note that an antisite forms when a Si atom replaces a C atom, and vice versa. Silicon and carbon antisite are respectively denoted Si_C and C_{Si}.

Point defects can also be created by the incorporation of foreign atoms into the silicon carbide crystal lattice. These point defects are called impurities, and the process of their incorporation is called doping. When doping is willful, it is called controlled doping. In the

contrary case, the process is called unintentional doping. Unintentional doping is the result of contaminant. Examples of impurities in silicon carbide are aluminum (Al) atom in Si site and nitrogen (N) atom in C site. The Al atom acts as an acceptor, and the nitrogen atom acts as a donor. It is well established that point defects are associated with localized energy states within the bandgap. Therefore, they can be further classified according to the energy level they create. Defects for which the energy level is either near the valence (E_v) or conduction band (E_c) are called shallow levels, whereas those that are associated with an energy level near the middle of the bandgap are called deep levels.

The study of point defects in silicon carbide is beyond the scope of this thesis, and will not be addressed further. However, the reader can consult references [33, 34].

II.3.2 Linear defects

Linear defects result from a misalignment of atoms or a collection of vacancies along a particular crystallographic direction. They are called so because of their one-dimensional structure, and are also referred to as dislocations. Dislocations are characterized by their line direction ***l*** and Burgers vector **b**. The Burgers vector represents the magnitude and direction of the shortest lattice translation. When the dislocation line is parallel to the Burgers vector, it is said to be a screw orientation. The structure of a screw dislocation can be thought of as that of a helical path that atomic planes in the crystal traces around a dislocation line. A more visual description would be that of a crystal cut half way along a particular plane and having one half of that plane slipping across the other by a lattice translation. On the other hand, when the line direction is perpendicular to the Burgers vector, the dislocation is said to be an edge dislocation. The edge dislocation can be seen as the insertion or removal of an extra half plane inside the crystal lattice. In a real crystal, most dislocations have mixed character, i.e. they have both screw and edge components. A schematic of a screw and an edge dislocation is shown in Figure 2.4.

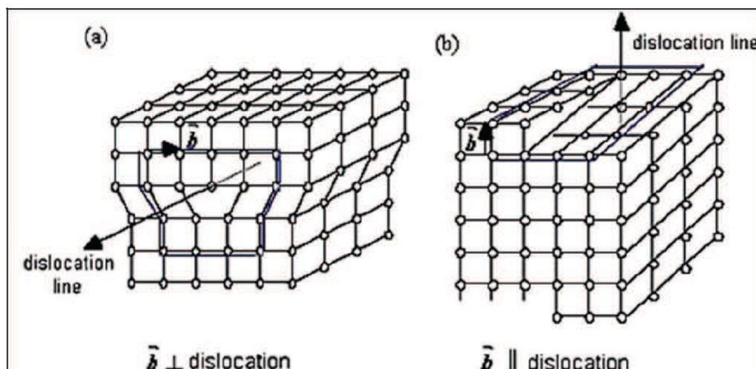

Figure 2.4. Schematic of edge (a), and screw (b) dislocations

In silicon carbide, linear defects can be classified in two categories: basal plane dislocations (BPDs) and threading dislocations (TDs). The BPDs are line defects that lie in the (0001) basal plane and have a Burgers vector of 1/3<11-20>. They can have a screw, edge or mixed character. Figure 3 shows an example of BPDs in both silicon carbide substrate and epilayer. The effects of BPDs on bipolar devices have been reported [35-37]. They were found to split into Shockley partials once they reached the active device layer of 4H and 6H-SiC devices, and cause forward voltage drop under forward bias. This splitting was associated with the formation of Shockley stacking faults (SFs) and described through a recombination-enhanced dislocation glide (REDG) mechanism [38, 39]. In REDG, Shockley partial dislocations have enough driving force to overcome their barrier to glide motion, and thus lead to stacking fault formation. An illustration of the splitting of a BPD into Shockley partials is shown in Figure 2.5.

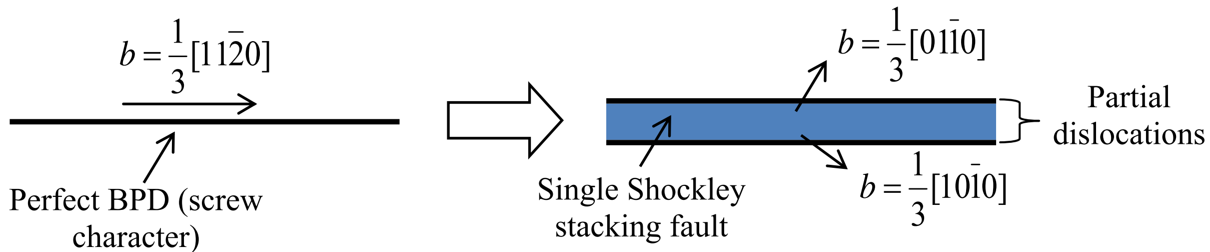

Figure 2.5. Schematic illustration of the splitting of a perfect BPD into Shockley partials

While basal plane dislocations are detrimental to silicon carbide devices, they effect can be mitigated. This can be done in one of two approaches. The first approach is more fundamental as it relates to growth conditions. This approach consists in developing growth schedules that produce uniform and lower thermal stress. Non-uniform temperature distribution induce localized high thermal stresses in the crystal, which in turn can lead to generation and multiplication of BPDs. Currently, the industry standard relies on growth on off-oriented seed typically 4° toward the [11-0] direction. If this standard has resulted in reduction in density of BPDs, its impact is not yet up to par with that of silicon growth technology.

The second approach, which builds on the first one, aims at converting BPDs to TEDs during epitaxial growth. The driving force for this conversion is the tendency of the BPD to minimize its elastic energy **W**. This elastic energy (equation 1) is proportional to the BPD line energy **E** and to the angle **α** between the BPD line direction and the growth normal. It is expressed in unit of energy per unit of grown epilayer [40].

$$W = \frac{E}{Cos\alpha} \qquad (1)$$

It follows from equation 1 that a suitable modification of the substrate surface morphology prior to epi-growth can enhance BPD to TED conversion. This can be achieved by using off-oriented substrate. Other methods have also been demonstrated to achieve enhanced BPD to TED conversion. These methods consist in causing shallow depressions to form at the location where BPDs intersect the substrate surface. They require the use of substrate preparation by molten potassium (KOH) or hydrogen (H_2) etching, of suitable C/Si ratio, growth rate, and the epi-growth face (i.e. C or Si face) [41-43]. High temperature annealing following epilayer growth has also been demonstrated to convert BPDs to TEDs [44]. X. Zhang and H. Tsuchida reported a 22% conversion rate of BPDs to TEDs following annealing of 4H-SiC epilayers at ~1800ºC [44].

Despite the effectiveness of the aforementioned methods, BPDs can easily glide under stress during epitaxial growth, particularly at high temperature, and cause the formation of interfacial dislocations (IDs) and half loop arrays (HLAs) [45-47]. Interfacial dislocations are BPDs that lie at the epilayer-substrate interface. Half loop arrays, on the other hand, can be seen as an array of short BPD segments that are pinned by two TEDs. A typical formation mechanism for these defects, summarized in a diagram shown in Figures 2.6, is as follow:

i. Glide of screw type BPD once epilayer reaches a critical thickness
ii. Conversion of mobile threading segment of the BPD, which adopted a more edge character, to TED during continued growth
iii. Pinning of the surface intersection of the mobile BPD segment by the sessile TED
iv. Escape of part of the mobile BPD segment through the epilayer surface leaving two further BPD surface intersections, which can convert to TEDs

These types of BPDs are harmful to SiC based technology. They have been associated with a drastic decrease in minority carrier lifetime in 4H-SiC epilayers [48, 49]. This is thus a challenge as most processing in silicon carbide occurs at high temperature because of the strong Si-C bonds.

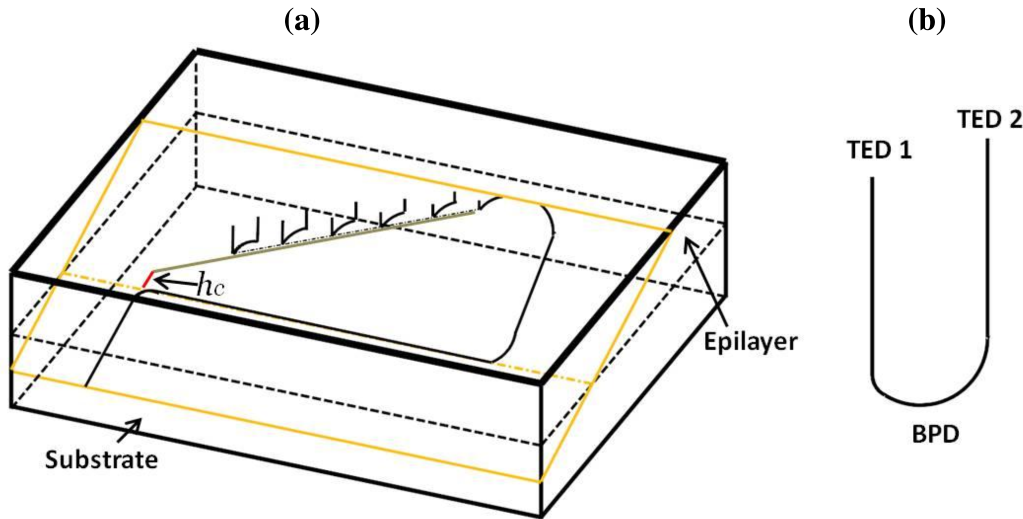

Figure 2.6. Diagram describing the formation mechanism of IDs and HLAs (a), and illustration of a single HLA (b).

The other types of linear defects in silicon carbide are threading dislocations, whose line direction is along the growth direction. They are comprised of threading edge dislocation (TED) and threading screw dislocation (TSD). The difference between a TED and TSD is their Burgers vector, 1/3<11-20> for a TED and <0001> for a TSD. A TSD has a closed core and can also have a Burgers vector that is inclined to the <0001> direction. This type of TSD is referred to as TMD, and has c- and a-axis component. TEDs can form by the conversion of BPDs from the substrate to the epilayer due to image force or prismatic plane tilt [50, 51]. In the case they form due to prismatic plane tilt, they align themselves to form low angle grain boundaries (LAGBs) as shown in Figure 2.7a. In synchrotron x-ray topography (SXRT) images, TEDs appear as very small white dots with a black contour as shown in Figure 2.7b. Figure 2.7b also shows contrast from TSDs and micropipes. The influence of TEDs on SiC device is not well understood [52, 53], although they are believed to be harmless.

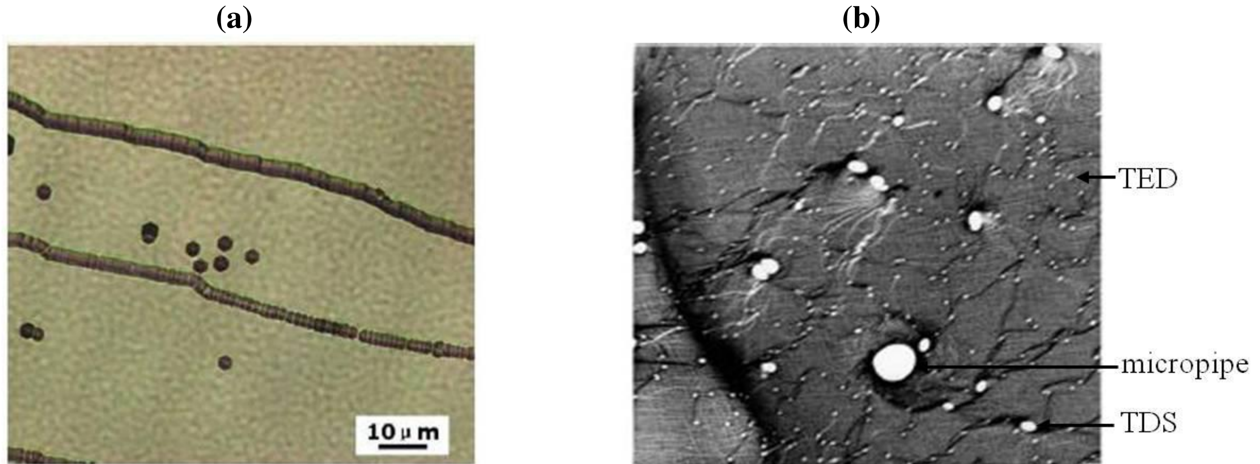

Figure 2.7. TEDs etch pits aligned along low angle grain boundaries (a), and transmission X-ray topograph showing defect contrast from TEDs, TSDs and micropipe (b)

By comparison, TSDs are more detrimental to the transport properties of SiC [52]. According to this study by S.I. Maximenko et al, the diffusion length of minority carrier is reduced in the TSDs owing to a stronger recombination activity compared to TEDs. They attribute this strong recombination activity to the presence of deep energy levels. The effect of TSDs on the electronic properties of SiC based devices has also been investigated [54-57]. The results from these studies [54-57] appear contradicting. On one end [54, 55], TSDs cause an increase in leakage current of p-n junction barrier schottky diodes. On another end, these defects seem not to correlate with any change in electrical properties [56, 57]. Further studies reported by T. Katsuno and coworkers [58] suggest that the morphology of the TSDs rather than the presence of the TSD is the main source of increased leakage current. According to Katsuno et al. TSDs observed in references [56, 57] do not have nanopits and are flat, unlike those observed in reference [54, 55]. It is important to note that TSDs form as a result of lattice closure failure, and can nucleate from the overgrowth of secondary phase particles (inclusion) on the growing surface by creating opposite sign pair of screw dislocations [59].

Furthermore, when the Burgers vector of a TSD exceeds an integral multiple of *c*, i.e. n*c* (where $n>2$), it is called a micropipe (μP). This type of dislocation has a hollow core and appears like small tubular void that runs in a direction parallel to the [0001]-axis on an optical micrograph. Micropipes have the same characteristic as TSDs. They also form as a result of a lattice closure failure between two or more SiC islands during growth and propagate along the growth direction. Dudley et al. reported that μP can nucleate at secondary phase particle such as

inclusion [60]. Several techniques, of which are wet etching in KOH and SXRT, exist to characterize μP. In SXRT, a μP exhibits a large white contrast surrounded by a black halo, whereas they appear as large hexagonal pit with no depth in Nomarski reflection micrograph. Their deleterious effect on high field SiC devices has been reported [30, 55]. However, their effect is mitigated in SiC device operating at an electric field that is kept in a small percentage of the theoretical breakdown field of SiC [61].

II.3.3 Planar defects

Typical planar defects that have been observed in silicon carbide are stacking faults (SFs) and grain boundaries (GBs). These defects have a two-dimensional structure; hence their name planar defects. A stacking fault is a small displacement in the regular atomic arrangement of the crystal lattice that results in a different stacking sequence. Stacking faults can be classified in two types depending on whether they are produced by vacancy or interstitial agglomeration. When a SF is the result of vacancy agglomeration, it is called intrinsic stacking fault (ISF). In the case the fault is produced by interstitial agglomeration, it is called extrinsic stacking fault (ESF). The vacancy agglomeration can be thought of as a removal of a plane of atoms. Conversely, the interstitial agglomeration can be seen as an insertion of a plane of atoms. Figures 2.8 are an illustration of intrinsic and extrinsic SFs.

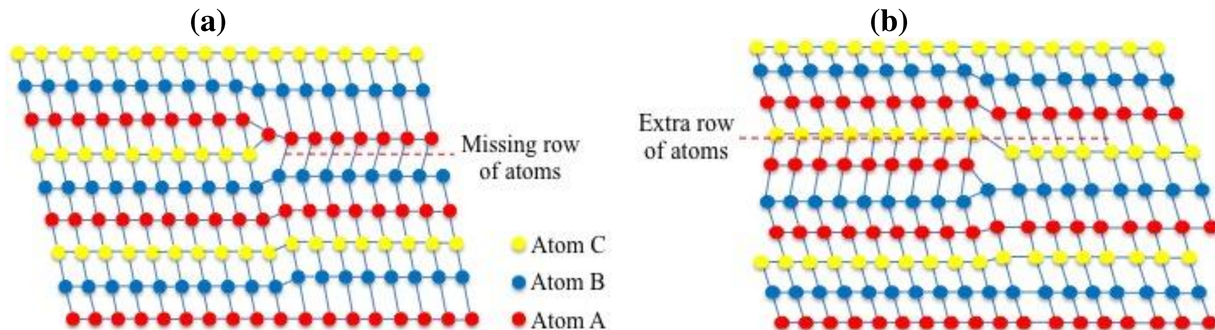

Figure 2.8. Intrinsic stacking fault (a), and Extrinsic stacking fault (b)

In addition, stacking faults can be classified according to the nature of the partial dislocations (PDs) that bound them. A stacking fault that is bounded by sessile partial dislocations is called a Franck Fault (FF). On the other hand, a stacking fault that is bounded by glissile partials is called a Shockley fault (SSF). A combination of these two types of faults can also be encountered. The origin of the formation of stacking faults in silicon carbide has been tied to plastic deformation that occurs in the crystal as a result of mechanical or thermal stress [62, 63]. Stacking faults can

also form in the SiC crystal during the growth process. It is important to note that the probability of formation of stacking fault in 2H-SiC polytype is low compared to the higher order polytypes. This is because there are not many available ways in which to switch the atomic layers in 2H polytypes. Here, the higher order polytypes refer to 3C, 4H, 6H and 15R-SiC polytypes, to name a few. In 2H-SiC polytype, the stacking sequence is of the type (ABABAB…). Formation of stacking fault in such a configuration can occur only by changing the B layer with a C layer to obtain a (ABABACBCB…) stacking sequence. For the case of a 3C-SiC polytype, having a stacking sequence of (ABCABC…), the formation of a stacking fault can occur by replacing the A, B or C layers with respectively a B or C, A or C, B or A layer, respectively.

In general, stacking faults in silicon carbide are observed to lie in the close packed plane, (111) plane for cubic polytype and (0001) for hexagonal polytypes. These stacking faults are referred to as basal plane stacking faults (BSFs). They result from the dissociation of a basal plane dislocation into partials. Stacking faults can also result from cross slip of partial dislocations that have a screw character from the prismatic plane to the basal plane [64]. Detail treatment of the formation mechanism of stacking faults in silicon carbide can be found in references 64-68. Regardless of their of their formation mechanisms, stacking faults are detrimental to SiC device performance.

This detrimental effect of stacking faults has been investigated for bipolar devices. According to Bergman and coworkers the forward voltage drop of 4H-SiC PiN diodes increased because of stacking fault expansion in the active layer of the device. They also revealed that these stacking faults acted as recombination centers; thereby reducing the lifetime of minority carriers [69]. The mechanism through which these stacking faults were generated has been described elsewhere as recombination enhanced dislocation glide (REDG). In this mechanism the electron-hole pair recombination at basal plane dislocations in the device active layer activates the SFs formation [70]. While stacking faults degrades the electrical and transport properties of SiC, they help enhance its tolerance to radiation [71]. This effect of the formation of SFs on radiation tolerance shows how these defects can be engineered for specific applications.

Unlike stacking faults, that are irregularities in the stacking sequence of a crystal, grain boundaries represent the interface between two regions of a crystal lattice. They are characterized by a high density of dislocations, which cause a misorientation of the interface (i.e. domain

wall). Depending on their degree of misorientation, GBs can be classified as low angle grain boundaries (LAGBs) and high angle grain boundaries (HAGB). The extent of the misorientation that determines whether a grain boundary is of the LAGB or HAGB types varies in the literature [72- 74]. However, it seems a common trend that the transition at which a LAGB turns into a HAGB lies between 10˚ and 20˚ [74]. Grain boundaries can also be classified based on the type of misorientation of the interface between misoriented grains. These types of misorientation of the interface are rotations of the boundary plane about the x, y or z axis.

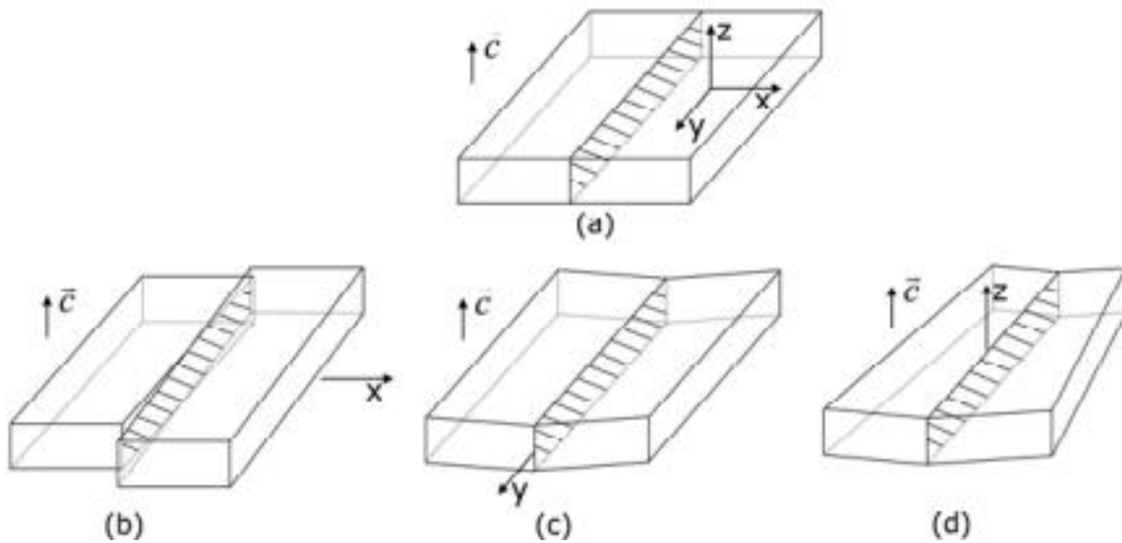

Figure 2.9. Diagram illustrating common domain misorientations in SiC. (a) misorientation free crystal, (b) twist boundary, (c) basal plane tilt boundary, and (d) prismatic plane tilt boundary

When this rotation is perpendicular to the normal of the boundary plane, a tilt boundary is formed. Two types of tilt boundaries exist: basal plane tilt boundary and prismatic plane tilt boundary. The illustration of these types of boundary is shown in Figure 2.9 below. The difference between a basal plane and a prismatic plane tilt boundary lies in the type of dislocations that cause their generation. On one hand, basal plane tilt boundaries form when basal plane dislocations pile up at the interface between misoriented grains, and their Burgers vectors lie in the c-plane, perpendicular to their line direction. On the other hand, prismatic plane tilt boundaries form as a result of prismatic plane tilt when threading edge dislocations (TEDs) nucleate and pile up along the c-axis with their Burgers vectors in the c-plane.

When the rotation is parallel to the normal of the boundary plane, a twist boundary is formed. The formation of twist boundaries has been associated with the alignment of micropipes/screw

dislocations into a straight line in the basal plane [75]. It should be observed that both twist and tilt boundaries result from dislocation pile up into straight lines. This is done so as to minimize the energy of the dislocations, and thereby the energy of the crystal. The influence of these boundaries on the transport and electronic properties of silicon carbide devices has been investigated [76, 77]. They have been associated with a decrease in electrical and thermal conductivity. A challenge grain boundaries pose to the development of silicon carbide technology is the formation of stacking faults. Two possible formation mechanisms of SFs at GBs. BPDs nucleated at GBs can glide under the influence of thermal stress and lead to the formation of SFs. Similarly, solute atoms incorporated as dopant during growth can diffuse to regions of tension or compression that exist in the grain boundary. This diffusion can alter the atomic configuration at the interface, resulting in the formation of SFs.

II.3.4 Volume defects

These are three-dimensional defects, which occupy a volume within the crystal lattice. Typical volume defects in silicon carbide are 3C-SiC inclusions, polytype, precipitate, voids and morphological defects.

Voids are small regions in a crystal where there are no atoms, i.e. they form as a result of the cluster of vacancy or trapped gases during solidification. They are found to propagate along the c-direction of hexagonal silicon carbide polytypes, with a size ranging from 5 to 30μm [78]. V. Jokubavicius et al. have proposed an origin for their formation. According to them, the excess of silicon causes carbon deficiency in the growing crystal and increases the probability of voids formation for high growth rate sublimation of 3C-SiC polytype. These defects have been found to reduce the electrical and optical properties to SiC. H. W. Shim and co-workers investigated the effect of void on the electrical properties of SiC epilayers. They found an improvement in the electrical properties of void free crystalline 3C-SiC thin film [79].

Like voids, ***precipitates*** can be thought of as cluster of impurities that form into small regions of different phases. ***Inclusions*** are foreign particles within the SiC crystal lattice. When the inclusion is of the same chemical composition, but a different stacking sequence than the crystal lattice, it is said to be a ***polytype***. An inclusion/polytype that forms during growth is called a primary inclusion; whereas one that forms after growth (as a result of post growth processing) is called a secondary inclusion. Regardless of whether an inclusion is primary or secondary, it can be the source for nucleation of screw dislocation pair and micropipe [60].

Morphological defects comprise growth pits, downfalls, triangular defects and inverted pyramids that form on the epilayer surface during growth. Several factors have been found to contribute to their formation. These are substrate surface defects resulting from cutting and polishing of the wafer, off-cut angle, growth conditions and defect in the substrate [80, 81]. The extent to which morphological defects impact the electronic and transport properties of SiC can be tied to their core structure. Konishi et al. reported that 3C-SiC type triangular defects was associated with an increase in leakage current at a reverse bias voltage as well as forward current at low bias voltage, whereas the (4, 2) type of triangular defects did not cause any degradation of device performance [82]. Similarly, Y. Wang et al. observed that morphological defects associated with other extended defects such as micropipes were more harmful than their counterparts, which were free of extended defects [83].

In the vicinity of point, planar and volume defects, the crystal lattice is distorted. The extent of the distortion depends on the strain/stress field of the particular defects. This distortion causes an increase in the total energy of the crystal. When the total energy of the crystal reaches a threshold, the crystal seeks to reduce it by generating defects called misfit dislocations. This process by which the energy of the crystal is reduced is called stress relaxation, and occurs to restore the crystal to its lowest energy configuration. For the case of epitaxial grown layers, Matthews and Blakeslee developed an elastic theory model based on thermodynamic that illustrates the process of stress relaxation [84] by describing the critical thickness at which misfit dislocations begin to form. Huanhuan Wang et al. used this model to measure the critical thickness for the formation of misfit dislocations in 4H-SiC epilayers [46]. Therefore, the investigation of the structure and impact of defects in silicon carbide is of paramount importance in today's SiC research.

II.3.5 Doping

Doping consists in the controlled addition of foreign atoms, referred to as dopants or impurities, to the semiconducting material in order to alter its intrinsic conductivity (i.e. n- or p-type), electrical conductivity and free carrier lifetime. It is an important step in the realization of electronic devices from semiconducting materials. Several techniques exist, which purport to favor uniform dopant incorporation. These techniques are ion implantation, thermal diffusion and In-Situ doping during crystal growth. A short description of each technique is herein

provided. The reader can consult references [85-88] for a detailed description of these techniques.

In ***Ion implantation***, doping is provided by bombarding a sample with high-energy ions. While the use of high-energy ions is efficient for localized doping, it can significantly damage the lattice of the targeted sample. In order to reverse/mitigate the damage on the lattice, post ion implantation annealing is often carried out [89]. This annealing has the benefit of favoring re-crystallization and activation of the implanted ions [90].

In ***doping by thermal diffusion***, a gas that contains the dopants flows over a SiC sample. This type of doping can also be achieved by placing the SiC sample near a solid dopant source and flowing an inert gas through the growth chamber. In either case, diffusion of dopants into the SiC sample is facilitated by the use of temperature above $1800^{\circ}C$.

In-situ doping occurs during crystal growth as the dopant source is incorporated to the growth system. This is typical in bulk growth of SiC by PVT as well as in epitaxial growth by CVD. During bulk growth by PVT, dopants are introduced in a gas phase. On the other hand, both liquid and gas containing dopants can be used during CVD growth. Although n-type doping is favorably realized during PVT growth, p-type doping remains a challenge due to the porosity of the graphite used in PVT system. To mitigate the challenges associated with p-type doping, a pipe was added to the conventional PVT system to improve doping [91]. This modification, called modified-PVT, combines the advantage of both conventional PVT and CVD. In principle, in-situ doping is preferred when large area doping is required.

Commonly used dopants for silicon carbide are aluminum, boron, nitrogen and vanadium. These common dopants are used to induce p-type conductivity (aluminum, boron), n-type conductivity (nitrogen) and semi-insulating conductivity (vanadium). In addition to altering the conductivity type, doping can favor polytype stability in SiC. T. Shiramomo et al. observed an improvement in 4H-SiC polytype stability during growth associated with nitrogen doping [92]. While polytype is desirable, doping can negatively affect the quality of the SiC single crystals. At high n-type doping ($>10^{-19}$ cm^{-3}), the SiC lattice hardens and can undergo structural changes, resulting in generation of stacking faults [93, 94]. For p-type doping, SiC ingots were shown to exhibit lower basal plane dislocation (BPDs) density [94]. M. Bickermann et al. attributed this low BPDs density to the position of the Fermi level of p-type doped SiC, which is below the mid-gap center [95].

Doping is crucial to the development of SiC-based electronics. As such, careful control of the doping process is necessary to ensure dopant uniformity. This is not easily achieved in practice because of challenges in controlling the flow of dopants. On one hand, the partial pressure of dopant species varies with time during growth, leading to axial and lateral doping non-uniformity. An example of the effect of dopant partial pressure on doping uniformity can be illustrated with aluminum p-type doping. Aluminum has a higher partial pressure compared to SiC gas species at typical PVT growth temperature. This results in an oversupply of aluminum vapor followed by depletion of dopant species and a variation in dopant concentration of more than two orders of magnitude [96]. On the other hand, growth surface effects such as faceting and interface roughness influence doping uniformity. While faceting can be used as a measure of crystalline quality, it can cause dopants redistribution.

In general, faceting occurs on crystal habit faces with low surface energy. These faces grow slowly and thus determined the final morphology of the crystal. In SiC, such low surface energy faces are {0001} basal planes. During PVT growth of SiC, the formation of {0001} facet and their terraces is favored by the dome-like interface shape of the growing crystal. This facet expands as growth proceeds and can be up to 20 mm [97]. Because of their low energy, dopant species are attracted to facet regions, where their density is highest. For CVD, facet formation can be described by considering the dependence of step density on the local growth front orientation with respect to the {0001) basal planes during step-flow assisted growth [98].

II.4 Motivation

Recently, growth of large (up to 6" diameter) and micropipe free silicon carbide single crystal boules have been achieved. Analysis of wafers cut from those boules has revealed a drastic reduction in the density of threading screw dislocations. An illustration of the current progress made in the growth of SiC in terms of wafer size and micropipe density is shown in Figures 2.10 and 2.11.

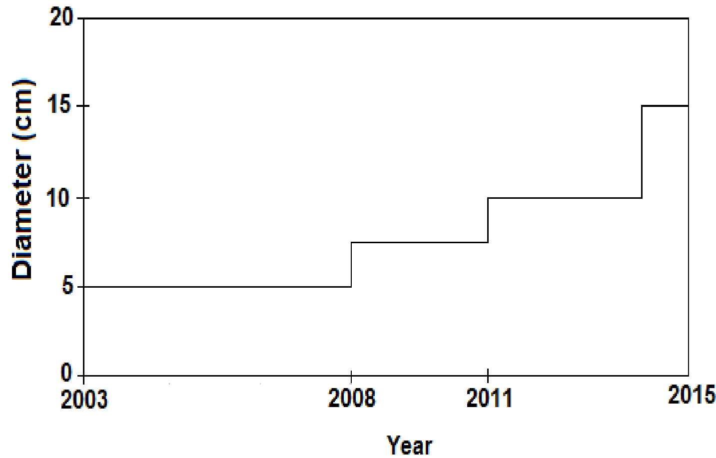

Figure 2.10. Evolution of diameter of commercially available SiC wafer [31]

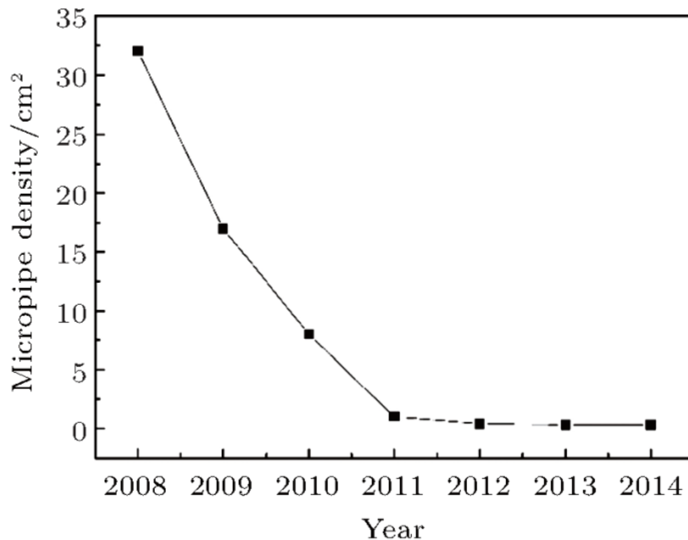

Figure 2.11. Evolution of micropipe density in SiC wafer [99]

While the production of large diameter boules has made the price of wafers more competitive, the improvement in wafer quality is not yet up to par with silicon wafers. In order to tap into silicon carbide very promising potential, and enjoy devices that can reliably operate at high temperature and under high frequency, a breakthrough must occur in the production of SiC single crystals. By production, we refer to the growth and processing of SiC boules. Several studies have been carried out to produce large SiC single crystal of high quality. These studies hinged on improving the current industry standard physical vapor transport (PVT) or developing a new growth method. The improvement of the PVT standard is done by optimizing growth parameters such as seed quality, Si/C ratio, supersaturation and precursor compositions to name a few. The development of new growth methods has been proposed to prevent the formation of micropipes, elementary dislocations (i.e. edge, screw and basal plane dislocations) and stacking

faults that occur during growth by the PVT technique. The Repeat-A-Face (RAF) developed by D. Nakamura and coworker has shown promise in the production of virtually dislocation free SiC single crystals [100]. These results have been confirmed by Y. Urakami and coworkers [101].

Despite the promising results of the new growth methods [100-103] in reducing dislocation density in the grown SiC boules, two obstacles makes them less appealing compared to the PVT standard. The complexity of these new growth methods confines them to the realm of laboratory research. The density of dislocations and the persistence of stacking faults is another obstacle. It is possible that as new growth and processing methods are experimented new types of defects will form, and that both the newly found and already known defects may be subject to new formation mechanism.

So, to validate a growth method, the presence of defects, their structure and distribution must be mapped. Moreover, the influence of those defects on the electronic, thermal and transport properties of SiC must also be investigated. These are done in the subsequent chapters. Chapter 4 discusses the development of a new growth method, large tapered crystal growth (LTC) for producing defect free SiC boules. Chapter 5 is a study of the effect of structural defects on minority carrier lifetime through a correlation with microwave photoconductance (μPCD) lifetime map.

References

1. J. J. Berzelius, Ann. Phys. Lpz. 1, p 169-230 (1824)
2. H. Moissan, C. R. Acad. Sci. Paris 140, p 405 (1905)
3. S. A. Kukushkin and A. V. Osipov, J. Physics D: Appl. Phys. 47 (31), p 1-41 (2014)
4. H. J. Round, Electrical World (New York) 49, p 309 (1907)
5. Jan A. Lely, Ber. Dt. Keram. Ges. 32, p 229-231 (1955)
6. H. Matsunami, Jpn. J. Appl. Phys. 43 (10), p 6835-6847 (2004)
7. R. Yakimova, M. Syväjärvi, T. Iakimov, H. Jacobsson, A. Kakanakova-Georgieva, P. Raback, E. Janzén, Appl. Surf. Sci. 184, p 27-36 (2001)
8. T. Kimoto and James A. Cooper, "Fundamentals of Silicon Carbide technology: Growth, Characterization, Devices, and Applications", Chapter 3: Bulk growth of silicon carbide, John Wiley & Sons, Singapore, p 39 (2014)
9. A. Fissel, Phys. Rep. 379 (3-4), p 149-255 (2003)
10. J. Wan, M. A. Capano, M. R. Melloch and J. A. Cooper Jr., IEEE Electron Device Lett. 23 (8), p 482-484 (2002)
11. M. Bakowski, A. Schöner, P. Ericsson, H. Strömberg, H. Nagasawa and M. Abe, J. Telecom. Info. Technology 2, p 49-56 (2007)
12. T. Ohshima, K. K. Lee, Y. Ishida, K. Kojima, Y. Tanaka, T. Takahashi, M. Yoshikawa, H. Okumura, K. Arai, T. Kamiya, Jpn. J. Appl. Phys. 42, p L625-627 (2003)
13. A. Agarwal, S. H. Ryu, C. Capell et al. In Silicon Carbide 2001– Materials, Processing and Devices, Ed. By S. E. Saddow, D. J. Larkin, N. S. Saks et al., MRS Symp. Proc. (Materials Research Society, Warrendale, PA, 2003), Vol. 742, p. K7.3.1
14. S. T. Sheppard, M. R. Melloch and J. A. Cooper, jr, IEEE Electron Device Lett. 17 (1), p 4 (1996) (Note that references 54, 58 and 62, i.e. 12, 13 and 14 are taken from Silicon Carbide: Recent major advances edited by J. W. Choyke, H. Matsunami and G. Pensl in Springer (2004)
15. M. B. J. Wijesundara and R. Azevedo, Chapter 2: SiC materials and processing technology, In Silicon Carbide Microsystems for Harsh Environments, MEMS Reference Shelf, Springer (2011).
16. R. J. Trew, Wide Bandgap Semiconductor Transistors for Microwave Power Amplifiers, IEEE Microwave Magazine 1 (1), p 46-54 (2000)

17. Mariana A. Fraga, Rodrigo S. Pessoa, Marcos Massi and Homero S. Maciel, “Chapter 13: Applications of SiC-based thin films in electronic and MEMS devices”, Physics and Technology of Silicon Carbide Devices, Ed. Yasuto Hijikata, p 313-336 (2012)
18. P.G. Neudeck, R. S. Okojie and L. Y. Chen, High-temperature electronics – A role for wide bandgap semiconductors, Proceedings of the IEEE 90 (6), p 1065-1076 (2002)
19. Y. S. Ravikumar and K. S. Gurumurthy, “Silicon carbide merged PiN Shottkey [MPS] diode power electronic control devices”, International Journal of Computer Science and Network Security 12 (1), p 88-93 (2012)
20. St. G. Müller, R. C. Glass, H. M Hobgood, V. F. Tsvetkov, M. Brady, D. Henshall, J. R. Jenny, D. Malta and C. H. Carter Jr., J. Cryst. Growth 211, p 325 (2000)
21. B. Padavala, C. D. Frye, Z. Ding, R. Chen, M. Dudley, B. Raghothamachar, N. Khan and J. H. Edgar, Solid State Science 47, p 55-60 (2015)
22. S. A. Kukushkin, A. V. Osipov, V. N. Bessolov, B. K. Medvedev, V. K. Nevolin and K. A. Tcarik, Rev. Adv. Mater. Sci. 17, p 1-32 (2008)
23. A. Grekov, Q. Zhang, H. Fatima, A. Agarwal and T. S. Sudarshan, Microelectron. Reliab. 48, p 1664 (2008)
24. H. Fujiwara, T. Kimoto, T. Tojo and G. Matsunami, Appl. Phys. Lett. 87, p 51912 (2005)
25. K. Semmelroth, N. Schulze and G. Pensl, J. Phys. Condens. Matter 16, p 1597 (2004)
26. H. Idrissi, M. Lancin, J. Douin, G. Regula, B. Pichaud, Mater. Sci. Forum 483-484, p 299-302 (2005)
27. Silicon carbide, http://en.wikipedia.org/wiki/Silicon_carbide
28. Gallium Arsenide, http://en.wikipedia.org/wiki/Gallium_arsenide
29. Tamás Hornos, “Theoretical study of defects in silicon carbide and at the silicon dioxide interface”, PhD Thesis (2008)
30. P. G. Neudeck, Chapter 5: Silicon Carbide Technology, The VLSI Handbook 2nd edition, edited by Wai-Kai Chen, CRC Press (2007)
31. M. Amorim Fraga, M. Bosi and M. Negri, Chapter 1: Silicon Carbide in Microsystem Technology – Thin Film Versus Bulk Material, Advanced Silicon Carbide Devices and Processing, edited by Stephen E. Saddow and Francesco La Via, ISBN: 978-953-51-2168-8
32. Cree MATCATALOG_SiC Data Sheets, 2013.

33. M. J. Zheng, D. Morgan and I. Szlufarska, Phys. Rev. B 88, p 054105 (2013)
34. J. Schneider and K. Maier, Point defects in silicon carbide, Phys. B: Cond. Matter 185 (1-4), p 199-206 (1993)
35. A. T. Blumenau, R. Jones, S. Öberg, P.R. Briddon and T.Frauenheim, Phys. B: Condensed Matter 340-432, p 160-164 (2003)
36. X. Zhang, M. Skowronski, K. X. Liu, R. E. Stahlbush, J. J. Sumakeris, M. J. Paisley and M. J. O'Loughlin, J. Appl. Phys. 102, p 093520 (2007)
37. A. Agarwal, H. Fatima, S. Haney and Sei-Hyung Ryu, IEEE Electron Device Letters 28 (7), p 587-589 (2007)
38. Y. Chen, M. Dudley, K. X. Liu and R. E. Stahlbush, Appl. Phys. Lett. 90, p 171930 (2007)
39. K. Maeda, K. Suzuki, M. Ichihara, Recombination Enhanced Dislocation Glide in Silicon Carbide Observed in-Situ by Transmission Electron Microscopy, Microscopy Microanalysis Microstructures 4 (2-3), p 211-220 (1993)
40. B. Kallinger, S. Polster, P. Berwian, J. Friedrich and A. N. Danilewsky, J. Appl. Phys. 114, p 183507.1-183507.8 (2013)
41. B. Kallinger, B. Thomas and J. Friedrich, Mater. Sci. Forum 600-603, p 143-146 (2009)
42. W. Chen and M. A. Capano, J. Appl. Phys. 98, p 114907 (2005)
43. K. Masumoto, S. Ito, H. Goto, H. Yamaguchi, K. Tamura, C. Kudou, J. Nishio, K. Kojima, T. Ohno and H. Okumura, Mater. Sci. Forum 778-780, p 99-102, 2014
44. X. Zhang and H. Tsuchida, J. Appl. Phys. 111, p 123512 (2012)
45. N. Zhang, Y. Chen, Y. Zhang, M. Dudley and R. E. Stahlbush, Appl. Phys. Lett. 94, p 122108 (2009)
46. H. Wang, F. Wu, M. Dudley, B. Raghothamachar, G. Chung, J. Zhang, B. Thomas, E. K. Sanchez, S. G. Mueller, D. Hansen and M. J. Loboda, Mater. Sci. Forum 778-780, p 328-331 (2014)
47. Z. Zhang, R. E. Stahlbush, P. Pirouz and T. S. Sudarshan, J. Electronic Mater. 36 (5), p 539-542 (2007)
48. N. A. Mahadik, R. E. Stahlbush, J. D. Caldwell, M. O'Loughlin and A. Burk, Mater. Sci. Forum 717-720, p 297-300 (2012)

49. Ouloide Y. Goue, Yu Yang, Jianqiu Guo, B. Raghothamachar, M. Dudley, J. L. Hosteller, R. L. Myers Ward, P. B. Klein and D. K. Gaskill, "Correlation of lifetime mapping of 4H-SiC epilayers with structural defects using synchrotron X-ray topography, International Conference on Silicon Carbide and Related Materials, Sicily, Italy (2015)
50. Hui Chen, B. Raghothamachar, W. Vetter, M. Dudley, Y. Wang and B. J. Skromme, "Effects of different defect types on the performance of devices fabricated on 4H-SiC homoepitaxial layer", MRS Proceedings 911, (2006)
51. M. Dudley, X. R. Huang and W. Huang, J. Phys. D: Appl. Phys. 32, p A139 (1999)
52. S. I. Maximenko, J. A. Freitas Jr, R. L. Myers-Ward, K. K. Lew, B. L. WanMil, C. R. Eddy Jr, D. K. Gaskill, P. G. Muzykov and T. S. Sudarshan, J. Appl. Phys. 108, p 013708 (2010)
53. J. J. Sumakeris, J. R. Jenny and A. R. Powell, "Bulk crystal growth, epitaxy and defect reduction in Silicon Carbide materials for microwave and power devices, MRS Bulletin 30 (4), p 280 (2005)
54. S. Izumi, I. Kamata, T. Tawara, H. Fujisawa and H. Tsuchida, Mater. Sci. Forum 457-460, p 1085-1088 (2004)
55. T. Katsuno, Y. Watanabe, H. Fujiwara, M. Konishi, T. Yamamoto and T. Endo, Jpn. J. Appl. Phys. 50, p 04DP04 (2011)
56. D. T. Morisette and J. A. Cooper Jr, Mater. Sci. Forum 389-393, p 1133-1136 (2002)
57. H. Saitoh, T. Kimoto and H. Matsunami, Mater. Sci. Forum 457-460, p 997-1000 (2004)
58. T. Katsuno, Y. Watanabe, H. Fujiwara, M. Konishi, H. Naruoka, H. Morimoto, T. Morino and T. Endo, Appl. Phys. Lett. 98, p 222111 (2011)
59. M. Dudley, N. Zhang, Y. Zhang, B. Raghothamachar and E. K. Sanchez, Mater. Sci. Forum 645-648, p 295-298 (2010)
60. M. Dudley, X. R. Huang, W. Huang, A. Powell, S. Wang, P. G. Neudeck and M. Skowronski, Appl. Phys. Lett. 75, p 784 (1999)
61. P. G. Neudeck, Mater. Sci. Forum 338-342, p1161-1166 (2000)
62. H. J. Chung, J. Q. Liu and M. Skowronski, Appl. Phys. Lett. 81, p 3759 (2002)
63. B. Groth, R. Haber and A. Mann, Int. J. Appl. Ceram. Technol. 12 (4), p 795-804 (2015)
64. F. Wu, H. Wang, S. Byrappa, B. Raghothamachar, M. Dudley, P. Wu, X. Xu and I. Zwieback, J. Electronic Mater. 42 (5), p 787-793 (2013)

65. J. W. Sun, T. Robert, A. Andreadou, A. Mantzari, V. Jokubavicius, R. Yakimova, J. Camassel, S. Juillaguet, E. K. Polychroniadis and M. Syväjärvi, J. Appl. Phys. 111, p 113527 (2012)
66. H. P. Iwata, U. Lindefelt, S. öberg and P.R. Briddon, Phys. B 340-342, p 165-170 (2003)
67. Won-Seon Seo and K. Koumoto, J. Am. Ceram. Soc. 83 (10), p 2584-2592 (2000)
68. P. Pirouz and J. W. Yang, Ultramicroscopy 51 (1-4), p 189-214 (1993)
69. P. Bergman, H. Lendenmann, P. Å. Nilsson, U. Lindefelt, P. Skytt, Mater. Sci. Forum 353-356, p 299-302 (2001)
70. A. Galeckas, J. Linnros and P. Pirouz, Appl. Phys. Lett. 81 (5), (2002)
71. Y. Zhang, M. Ishimaru, T. Varga, T. Oda, C. Hardiman, H. Xue, Y. Katoh, S. Shannon and W. J. Weber, Phys. Chem. Chem. Phys. 14, p 13429-13436 (2012)
72. D. G. Brandon, Acta Metall. 14, p 1479 (1966)
73. W. T. Read and W. Shockley, Phys. Rev. 78, p 275 (1950)
74. M. Winning and A. D. Rollett, Acta Mater. 53 (10), p 2901-2907 (2005)
75. P. Pirouz, Phil. Mag. A 78, p 727 (1998)
76. K. Watari, H. Nakano, K. Sato, K. Urabe, K. Ishizaki, S. Cao and K. Mori, J. Am. Ceram. Soc. 86 (10), p 1812-1814 (2003)
77. T. Terashige and K. Okano, IEEE trans. Electronic Devices 46 (3), p 555-556 (1999)
78. V. Jokubavicius, J. Palisaitis, R. Vasiliauskas, R. Yakimova and M. Syväjärvi, Mater. Sci. Forum 645-648, p 375-378 (2010)
79. H. W. Shim, K. C. Kim, Y. H. Seo, K. S. Nahm, E. K. Suh, H. J. Lee and Y. G. Hwang, Mater. Sci. Forum 264-268, p 195-198 (1998)
80. J. A. Powell, D. J. Larkin, L. Zhou and P. Pirouz, "Transactions third international high-temperature electronics conference 1, p II-3 – II-8 (1996)
81. H. Song, M.V.S. Chandrashekhar and T. Sudarshan, ECS J. Solid State Sci. Technol. 4 (3), p 71-76 (2015)
82. K. Konishi, S. Nakata, Y. Nakaki, Y. Nakao, A. Nagae, T. Tanaka, Y. Nakamura, Y. Toyoda, H. Sumitani and T. Oomori, Jpn. J. Appl. Phys. 52, p 04CP05 (2013)
83. Y. Wang, G. N. Ali, M. K. Mikhov, V. Vaidyanathan, B. J. Skromme, B. Raghothamachar and M. Dudley, J. Appl. Phys. 97, p 013540 (2005)
84. J. E. Matthews and A. E. Blakeslee, J. Cryst. Growth 27, p 118 (1974)

85. B. S. P. Mendis, Thermal diffusion of Dopants in Silicon Carbide, August 4, 2012
86. T. Kimoto, K. Kawahara, H. Niwa, N. Kaji and J. Suda, IEEE International Workshop on Juction Technology 1-6 (2014)
87. M. V. Rao, Chapter 5: Ion-Implantation in SiC, "in Optoelectronic Properties of Semiconductors and Superlattices, Silicon Carbide: Materials, Processing, and Devices" 20, Eds Z. C. Feng and J. H. Zhao (2004)
88. E. M. Handy, M. V. Rao, O. W. Holland, P. H. Chi, K. A. Jones, M. A. Derenge, R. D. Vispute and T. Venkatesan, J. Electron. Mater. 29 (11), p 1340-1345 (2000)
89. A. Heft, E. Wendler, J. Heindl, T. Bachmann, E. Glaser, H. P. Strunk and W. Wesch, Nucl. Instr. Metho. Phys. Res. B 113, p 239-243 (1996)
90. M. Lazar, C. Raynaud, D. Planson, J. –P. Chante, M. –L. Locatelli, L. Ottaviani and Ph. Godignon, J. Appl. Phys. 94, p 2992-2998 (2003)
91. P. Wellmann, G. Neubauer, L. Fahlbush, M. Salamon and N. Uhlmann, Cryst. Res. Technol. 50 (1), 2-9 (2015)
92. T. Shiramomo, B. Gao, F. Mercier, S. Nishizawa, S. Nakano, and K. Kakimoto, J. Cryst. Growth 385, 95 (2014)
93. P. Pirouz, M. Zhang, H. McD. Hobgood, M. Lancin, J. Douin and B. Pichaud, Phil. Mag. 86, 29-31 (2006)
94. K. Konias, R. Hock, M. Stockmeier, P. J. Wellmann, M. Miller, S. Ossege, and A. Magerl, Mater. Sci. Forum 556–557, 267 (2007).
95. M. Bickermann, R. Weingaertner, B. Epelbaum, Z. Herro, D. Hofmann, U. Kuenecke, T. Straubinger, P. Wellmann, and A. Winnacker, Mater. Sci. Forum 433– 436, 337 (2003).
96. P. Wellmann, G. Neubauer, L. Fahlbusch, Mich. Salamon, and N. Uhlmann , Cryst. Res. Technol. 50 (1), 2–9 (2015)
97. S. A. Sakwe, M. Stockmeier, P. Hens, R. Müller, D. Queren, U. Kunecke, K. Konias, R. Hock, A. Magerl, M. Pons, A. Winnacker and P. Wellmann, "Chapter 1: Bulk growth of SiC – review on advances of SiC vapor growth for improved doping and systematic study on dislocation evolution" in Silicon Carbide, Vol. 1: Growth, Defects, and Novel Applications, Eds P. Friedrichs, T. Kimoto, L. Ley, and G. Pensl, WILEY-VCH Verlag GmbH & Co. KGaA, Weinheim (2010)

98. I. D. Matukov, D. S. Kalinin, M. V. Bogdanov, S. Yu Karpov, D. Kh. Ofengeim, M. S. Ramm, J. S. Barash, E. N. Mokhov, A. D. Roenkov, Yu A. Vodakov, M. G. Ramm, H. Helava, Yu. N. Makarov, J. Cryst. Growth 266 (1-3), p 313-319
99. X. Hua-Yong, C. Xiu-Fang, P. Yan, X Ming-Sheng, S. Yan, H Xiao-Bo, X Xian-Gang, Chinese Physics B 24 (6), (2015)
100. D. Nakamura, I. Gunjishima, S. Yamaguchi, T. Ito, A. Okamoto, H. Kondo, Shoichi Onda & Kazumasa Takatori, Nature 430, p 1009-1012 (2004)
101. Y Urakami, I. Gunjishima, S. Yamaguchi, H. Kondo, F. Hirose, A. Adachi, S. Onda, Mater. Sci. Forum 717-720, p 9-12 (2012)
102. M. Katsuno, N. Ohtani, T. Fujimoto and H. Yashiro, Mater. Sci. Forum 457-460, p 83-86 (2004)
103. T. Furusho, R. Kobayashi, T. Nishiguchi, M. Sasaki, K. Hirai, T. Hayashi, H. Kinoshita and H. Shiomi, Mater. Sci. Forum 527-529, p 35-38 (2006)

Chapter III: Introduction to Cadmium Zinc Telluride

III.1 Overview

The interest in cadmium zinc telluride (CZT) stems from the need to develop room temperature detectors. The requirements for room temperature detector application are as follow [1]

- High atomic number because photoelectric absorption is proportional to atomic number. The higher the atomic number, the larger the absorption coefficient.
- Wide band-gap (>1.3eV) to reduce noise level
- Resistivity must be between 10^8 - $10^9 \Omega$cm
- Longer carrier lifetime compared to the transit time of carriers across active volume of detectors in order to mitigate trapping probability.

Numerous compound materials with characteristics that met the above requirements were investigated [2]. Two of these materials are mercury iodide (HgI_2) and cadmium telluride (CdTe). HgI_2 is unstable in air and toxic. Because of these limitations, HgI_2 based detectors must be encapsulated to prevent deterioration of the crystal surface. By comparison, CdTe is more stable and less toxic; and thus does not require any encapsulation. Despite the stability and negligible toxicity of CdTe, it exhibits a low energy resolution because of its poor collection of hole. Another drawback of CdTe is attributed to the change in counting rate with time, also known as polarization effect [3]. Microscopically, the polarization effect can be defined as the capture and release of charge carriers that affect the space-charge distribution as well as the electric field profile in the detectors.

In order to improve the properties of CdTe single crystals for detector application, doping was considered. In the wake of the 90's, development of a new growth method enabled the production of zinc (Zn) doped CdTe crystals [4]. This paved the way for the growth of CZT crystal with varying concentration of zinc.

III.2 Crystal structure and material potential

III.2.1 Crystal Structure

Cadmium Zinc Telluride crystallizes in zincblende structure with two interpenetrating face centered cubic (FCC) sub-lattices displaced with respect to each other by ¼ the length of the unit cell along the body diagonal. One sub-lattice comprises cadmium (Cd) atoms and the

substitutional zinc (Zn) atoms. The other sub-lattice comprises tellurium (Te) atoms. CZT crystal belongs to the II-VI compound material group. While its atoms form a bonding type intermediate between ionic and covalent, its atomic bonds are described as covalent to which a fraction is assigned to indicate its partial ionic character. The zincblende unit cell of CZT along with its (110) projection is shown in Figures 3.1. Note the AaBbCc stacking along the <111> direction, where capital letters indicate Cd or Zn atoms (i.e. group II), and small letters indicate Te atoms (i.e. group VI). This highlights that equivalent {111} planes are composed of groups II or VI atoms.

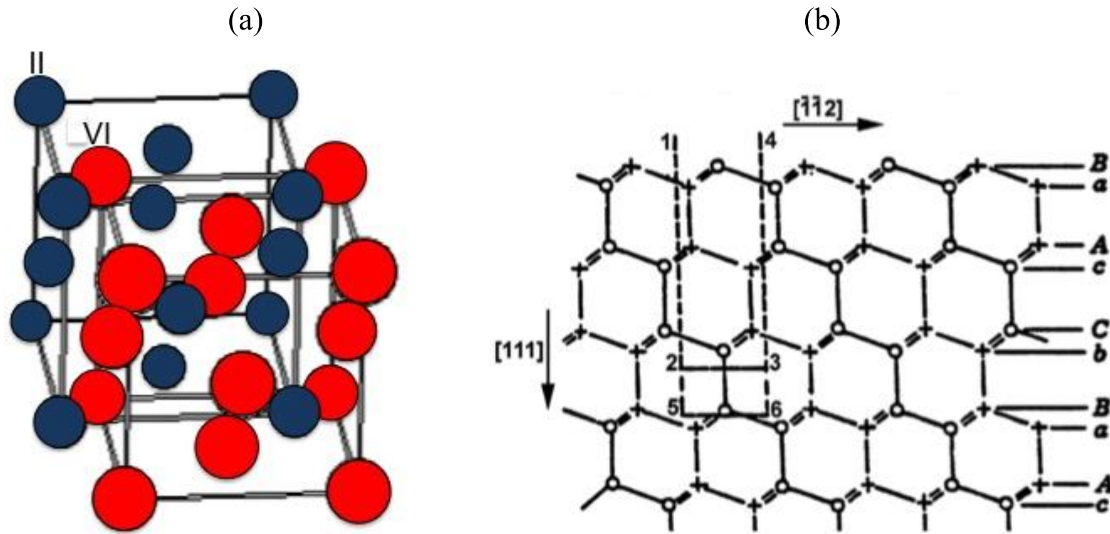

Figure 3.1. Unit cell structure of CZT (a), and atomic stacking sequence projected along [110] direction (b). Note that II indicate Cd or Zn atoms, while VI indicate Te atoms

There are two types of equivalent {111}. One consists of Cd and Zn atoms, and another consists of Te atoms. CZT crystal exhibits polarity along the <111> direction. This polar nature influences physical and chemical properties on opposed {111} and {-1-1-1} faces as well as <111> and <-1-1-1> directions. One consequence of this nature is the asymmetry of growth, which favors twin formation. Indeed, CZT like all zincblende structure does not have a center of symmetry.

The synthesis of CZT single crystal is achieved by substituting Zn atoms for Cd atoms in a CdTe matrix. These Zn atoms are obtained from the melt of zinc telluride (ZnTe). The control and monitoring of the Zn concentration (x) is essential to obtain the desired lattice parameter (a[x]). Vegards law provides the expression for the lattice parameter, from which the Zn concentration is derived [5].

$a[x] = a_1(1-x) + a_2(x)$ (1), where a_1 and a_2 are lattice constant for CdTe and ZnTe, respectively.

The numerical value of the lattice constant for CdTe and ZnTe are 6.481 and 6.104, respectively. The diffraction conditions inside a CZT crystal are pretty unique owing to it having a two-point basis FCC lattice: A_1 = (0,0,0) and A_2 =1/4(a,a,a). It follows from the expression of the structure factor (see equation 2) that there are no forbidden diffraction peaks for CZT.

$F(q) = \sum_1^2 f_i \, exp^{j(A_i.q)}$ (2), where f_1 and f_2 are the structure factor for Cd (equivalently Zn) and Te respectively.

III.2.2 Material potential

Cadmium zinc telluride is a II-VI compound semiconductor that is attracting growing interests in the development of hard X- and γ-rays detectors [4, 6]. This is in part due to its high atomic number (Z), close to 50. This high atomic number translates into a high stopping power, proportional to Z^5, for photons in the energy range below approximately 250 keV, where photoelectric effect dominates. As a result, much smaller detector volume can be used. One important aspect of radiation detectors is their ability to operate at room temperature without losing their functionality. This is important for practical purpose in cases of hand held detectors, where the use of cooling system is cumbersome.

CZT is a suitable material for room temperature detectors because of its wider band-gap compared to other solid-state radiation detectors. This band-gap is tunable with variation of the zinc content, and can oscillate between 1.4 and 2.2 eV [7]. It is important to note that the wider band-gap provides two advantages to CZT-based detectors. In one case, there is an exponential decrease in leakage current that is proportional to the band-gap. In the other case, the wide band-gap enables an increase in the resistivity of CZT-based detectors and allows them to operate at relatively higher temperatures.

In addition to its wide band-gap and high atomic number, CZT detectors exhibit promising energy resolution. The promise of an excellent energy resolution is associated with improvement in the growth of CZT single crystals. Since emerging as a room temperature detector in the early 1990's, the energy resolution CZT detectors has improved from ~3% at 662 keV [8] to below 1% at 662keV [9]. The improved energy resolution means improved imaging contrast. C. B. Hruska and M. K. O'Connor revealed that CZT detectors produced a distinctly better contrast of breast tumor compared to cesium iodide (CsI) photocathode [10]. Improvement in crystal quality

also allows harnessing the full charge collection potential of CZT. In fact, CZT crystals possess a very high charge collection potential compared to similar materials used for detector application. The excellence of the charge collection in CZT detectors also witnesses of their good charge transport properties. Table 3.1 shows the properties of common radiation detector materials [11].

Table 3.1. Physical properties of the principal compound semiconductors at T = 25 ˚C

Material	Si	Ge	GaAs	CdTe	$Cd_{0.9}Zn_{0.1}Te$	HgI_2	TlBr
Crystal structure	Cubic	Cubic	Cubic (ZB)	Cubic (ZB)	Cubic (ZB)	Tetragonal	Cubic (CsCl)
Growth method*	C	C	CVD	THM	HPB, THM	VAM	BM
Atomic number	14	32	31, 33	48, 52	48, 30, 52	80, 53	81, 35
Density (g/cm^3)	2.33	5.33	5.32	6.20	5.78	6.4	7.56
Band gap (eV)	1.12	0.67	1.43	1.44	1.57	2.13	2.68
Pair creation energy (eV)	3.62	2.96	4.2	4.43	4.6	4.2	6.5
Resistivity (Ω cm)	10^4	50	10^7	10^9	10^{10}	10^{13}	10^{12}
$\mu_e\tau_e$ (cm^2/V)	> 1	> 1	10^{-5}	10^{-3}	10^{-3} - 10^{-2}	10^{-4}	10^{-5}
$\mu_h\tau_h$ (cm^2/V)	~ 1	> 1	10^{-6}	10^{-4}	10^{-5}	10^{-5}	10^{-6}

* The more common growth methods: C = Czochralski, CVD = chemical vapor deposition, THM = traveler heater method, BM = Bridgman method, HPB = high-pressure Bridgman and VAM = vertical ampoule method

As a result of these excellent properties, the demand for CZT based room temperature detectors has soared. This is further encouraged by the implementation of new safety regulations for national security and nuclear proliferation as well as the development of new fields of applications. Common fields of applications in which room temperature radiation detection is in demand include nuclear medicine, nuclear physics, national security, astronomy and art science. The use of CZT detectors in nuclear medicine is associated with imaging techniques such as X-ray and γ ray tomography for cancer diagnosis and radiography [12, 13]. In the case of national security, CZT detectors are used to locate, monitor and identify radioactive materials for environmental protection and nuclear safety. In astronomy, CZT is used in advanced telescopes for imaging of astrophysical sources and phenomenon in the hard X-ray range (~20 – 100 keV). The national aeronautic and space agency (NASA) has developed CZT-based focal array space telescopes over the years. Two of the most renowned are the NuStar and high-energy focusing telescope (HEFT). An illustration of such telescopes is shown in Figure 3.2.

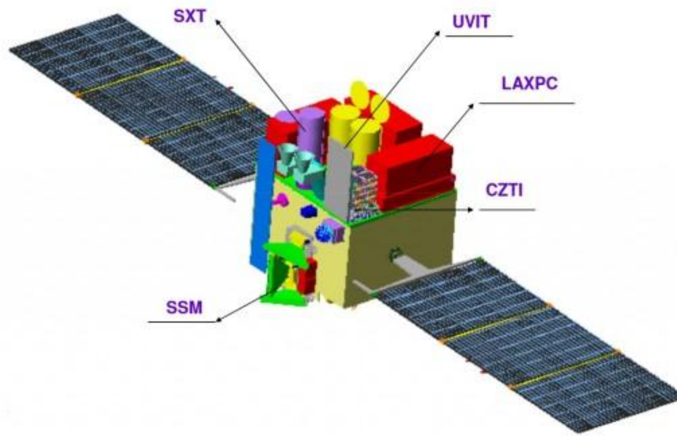

Figure 3.2. Typical CZT-based space telescope [14]

In addition, the non-destructive character of CZT detectors is used to examine art objects in museums and archeological sites [15]. In-situ fluorescence analysis on the "Portland" vase from Pompeii at the National Museum of Naples in Italy has been performed using a commercially available XR-100TCZT X-ray and γ-ray detector [16]. Aside from its use as detector of hard X-ray and γ-ray, CZT is increasingly used in photovoltaic applications and light emitting diodes (LEDs) [17-19].

While CZT crystals have a certain advantage over silicon (Si) and germanium (Ge) in the detection of hard X-ray and γ –ray radiations, the far higher density of structural defects in their crystal lattice constitutes their shortcoming. These structural defects are known to generate a large number of trapping sites, which prevent them from attaining their full charge transport potential. Another performance limiting factor to CZT detector is the chemical inhomogeneity of CZT crystal, which affects its chemical and mechanical properties. The combined effect of these shortcomings is the reduction of the practical size of CZT detectors, and a further addition to the challenge of realizing large area CZT detectors. In the next section, we discuss the current issues related to the growth of cadmium zinc telluride single crystals with an emphasis on the commonly encountered extended defects.

III.3 Challenges in the growth of cadmium zinc telluride

Cadmium zinc telluride has become the main substrate for epitaxial growth of mercury cadmium telluride (HgCdTe). Its use in X-ray and γ-ray detectors is well documented [6, 7]. To date, the largest single crystal CZT detectors are 2x2x1.5 cm3 in dimensions with an energy

resolution of about 0.5% at 662keV for single pixel event [9, 20]. While this achievement portends a good omen, the relatively high concentrations of extended defects in today's crystals hinder the realization of large volume detectors. Indeed, those extended defects degrade the performance of CZT detectors [21]. A description of the common types of extended defects encountered in CZT crystals is given below.

Dislocations are linear defects of two types: edge and screw dislocations. Their description as well as schematic has been provided in chapter 3. They are generated during growth at the ampoule wall as a result of thermo-mechanical stress. They can also result from the bending deformations of CZT crystals at high temperature [22]. They tend to form into a network [23] or align along a wall [24]. Their detrimental effects on nuclear detectors have been reported [22]. According to the authors of reference 21, dislocations create a large number of trapping centers in CZT detectors, which substantially reduce carrier lifetime. They further suggest that the inhomogeneous distribution of dislocations is also responsible for the observed non-symmetrical conductivity. The reported average density of these linear defects has been steadily decreasing from ~10^4-10^5 cm^{-2} [25, 26] to ~10^3 cm^{-2} [27].

Subgrain boundaries fall in the category of planar defects. Their formation mechanism has been attributed to stress caused by local compositional non-uniformities. W. Palosz and coworkers have reported two types of such defects [28]. One type, which they referred to as SB_1, was observed to form cell structures made of array of subgrain boundaries 50-200µm wide strewn with regions of very low dislocation density. The other type, referred to as SB_2, was observed to form long and straight lines and resulted from the polygonization of dislocations during growth or post growth cooling. The formation mechanism of SB_1 boundaries was attributed to the glide and climb of dislocations.

Twin boundaries are another class of planar defects. They form coherent grain boundaries with a high degree of symmetry that separate regions of a crystal sharing common lattice points. They occur either during growth as the material solidifies or plastic deformation, which caused by shearing between lattice planes. Growth twining occurs when two crystals, one of which is grown on the face of the other, share common lattice points. The formation of twin boundaries in CZT crystals is favored by the high iconicity of its atomic bonds. In Zinc blend compounds, first order twinning has the following structure [29]:

(i) Change in the atomic arrangement of {111} planes in the twinned region with respect to the matrix,

(ii) 180° rotation of the twinned region with respect to the matrix about a {111} plane normal,

(iii) 70°32’ or 250°32’ rotation of the twinned region with respect to the matrix about a <110> tilt axis. These twinning structures are called para and ortho twins, respectively. The ortho twins are the most observed of these two. They are low energy and are equivalent to a 180° rotation along {111} plane normal.

Twinning can be classified in terms of its order. We distinguish first, second or higher orders. The compositional surface of the first order twins, common to the twin and matrix region, are either coherent {111}-{111} or incoherent {511}-{111}, {411}-{110}, {211}-{211}, and {100}-{211}. Second or higher order twinning arises when further twining occurs within twinned regions. Predicting the new growth direction when a twin forms can be valuable. Such prediction has been proposed by Hulme and Mullin [30] using a matrix method. It should also be noted that twin boundaries form regions of sink to which Te precipitates and inclusions migrate.

Te precipitates are volume defects. Precipitates are smaller in size, and are quantified in nanometer (nm). They form during rapid cooling of non-stoichiometric CZT from high temperature because of the retrograde solid solubility effect inherent in the Bridgman growth process. In fact, Bridgman growth occurs under Te-rich conditions as a result of volatility of Cd owing to its high partial vapor pressure. They segregate along twin and grain boundaries, disperse or form a cellular structure in the crystal lattice. While precipitates can act as free electron traps, thereby degrading charge transport, their effect on the electrical properties of CZT detectors has been found negligible when they are dispersed in the crystal [30]. On contrary, they increase dark current and reduce charge collection properties when they form cellular network or align along grain and twin boundaries [31].

Te inclusions are another type of volume defects, which are distinctly larger than precipitates. Their size is quantified in unit of micrometer (μm). They form from the trapping of excess Te at the growth interface because of fluctuation in growth conditions such as temperature and pressure. Like Te precipitates, Te inclusions are found to decorate grain and twin boundaries, disperse or cluster inside the crystal lattice. They have also been reported to be detrimental to CZT detectors [32, 33].

Two approaches can be used to mitigate the impact of these types of defects on CZT detectors. On one hand, post growth annealing can be used. This approach can help reduce the size and density of these defects, and consequently improve the performance of the CZT detectors. This is explained by the fact that smaller volume defects amounts to larger volume of the detector accessible to the radiation (e.g. infrared) as these defects are opaque to radiation. The other approach aims at completely eradicating these defects by suitable control of Cd partial pressure during growth to maintain the stoichiometry of the melt. Ching Hua Su and S. L. Lehoczky have conducted empirical calculation to determine the necessary Cd pressure at which stoichiometric melt is maintained [34]. This latter approach has a two-fold advantage compared to the former. First, the dislocation fields resulting from the stress around these defects is eliminated. The suppression of these defects can also result in a more uniform crystal, leading to uniform charge transport properties for detectors.

III.4 Summary

Cadmium zinc telluride is the choice material for nuclear detector applications owing to its excellent properties. It can be applied to numerous areas such as defense and homeland security, cancer research and nuclear medicine, photovoltaic cells and space science. Despite progresses in the growth technology, realization of its full potential is limited by a high density of extended defects. The impact of these extended defects on CZT devices accentuates the urgency to eradicate them. The following digression serves to illustrate the interdependency between the quality of CZT crystals and the performance of CZT detectors:

i. Extended defects act as trapping center for free carriers. So, a non-uniform distribution of extended defects will cause a non-uniform charge trapping and results in a non-uniform charge transport property.
ii. An efficient collection of free carriers indicates excellent charge transport properties. This excellent charge transport is implied to be uniform, in which case it indicates uniform distribution and very low density of extended defects. We will assume here a baseline for very low density of extended defects to be below $10^2 cm^{-2}$.
iii. Excellent charge transport properties indicate excellent performance of room temperature CZT detectors. This in turn indicates the structural properties of the CZT crystal are very excellent.

It follows from this digression that improvement in the quality of CZT crystals will inevitably enhance the performance of room temperature CZT detectors in particular, and CZT devices in general. This is done in the next chapter, where we discuss the implication of using different cadmium overpressures to achieve stoichiometric melt growth and thus eradicate Te precipitates and inclusions.

References

1. Oluseyi S. Babalola, "Surface and bulk defects in cadmium zinc telluride and cadmium manganese telluride crystals", Vanderbilt University, PhD thesis (2009)
2. M. R. Squillante and K. S. Shah, "Other Materials: Status and Prospects", chapter 12, Semiconductors for Room temperature nuclear detector applications 43, Ed T. E. Schlesinger and R. B. James, Academic Press, p 456-491 (1995)
3. H. L. Malm and M. Martini, IEEE Trans. Nucl. Sci. 21, p 322-330 (1974)
4. Q. Li, M. Beilicke, K. Lee, A. Garson III, Q. Guo, J. Martin, Y. Yin, P. Dowkontt, G. De Geronimo, I. Jung and H. Krawczynski, Astropart. Phys. 34 (10), p 769-777 (2011)
5. L. Vegard, Z. Phys. 5, p 17 (1921)
6. L. A. Najam, N. Y. Jamil and R. M. Yousif, Indian J. Phys. 86 (4), p 267-272 (2012)
7. https://www2.warwick.ac.uk/fac/sci/physics/current/postgraduate/regs/mpags/ex5/intro/groupii-vi/
8. P. N. Luke, IEEE Trans. Nucl. Sci. 42, p 207-213 (1995)
9. F. Zhang, C. Herman, Z. He, G. De Geronimo, E. Vernon and J. Fried, IEEE Trans. Nucl. Sci. 59 (1), p 236-242 (2012)
10. C. B. Hruska and M. K. O'Connor, Phys. Med. 21 Suppl 1, p 72-75 (2006)
11. S. Del Sordo, L. Abbene, E. Caroli, Anna M. Mancini, A. Zappettini and P. Ubertini, Sensors 9, p 3491-3526 (2009)
12. Stephen J. Glick and Clay Didier, J. Appl. Phys. 114, p 144506 (2013)
13. Hyunki Kim, Lars R. Furenlid, Michael J. Crawford, Donald W. Wilson, H. Bradford Barber, Todd E. Peterson, William C. J. Hunter, Zhonglin Liu, James M. Woolfendend and Harrison H. Barrett, Med. Phys. 33, p 465 (2006)
14. http://spaceflight101.com/pslv-c30/astrosat/
15. F. -P. Hocquet, H. -P. Garnir, A. Marchal, M. Clar, C. Oger and D. Strivay, X-Ray Spectrom. 37, p 304-308 (2008)
16. http://amptek.com/art-archaeology-archaeometry-with-amptek-detectors/
17. J. R. Pugh, D. Mao, J. Zhang, M. J. Heben, A. J. Nelson and A. J. Frank, J. Appl. Phys. 74 (4), p 2619-2625 (1993)
18. B. E. McCandless, W. A. Buchanan and G. M. Hanket, IEEE 4th World Conference on Photovoltaic Energy Conversion, Waikoloa, Hawai, p 483-486 (2006)

19. J. E. Toney, B. A. Brunett, T. E. Schlesinger, J. M Scyovan, R. B. James, M. Goorsky, H. Yoon, E. Eissler and C. Johnson, Nucl. Instr. Meth. Phys. Res. A 380, p 132 (1996)
20. Y. Cui, A. Bolotnikov, G. Camarda, A. Hossain, G. Yang and R. B. James, 5th annual IEEE Long Island Systems, Applications and Technology Conference, Farmingdale, New York, (2009)
21. G. S. Camarda, K. W. Andreini, A. E. Bolotnikov, Y. Cui, A. Hossain, R. Gul, K. H. Kim, L. Marchini, L. Xu, G. Yang, J. E. Tkaczyk and R. B. James, Nucl. Instr. Meth. Phys. Res. A 652 (1), p 170-173 (2011)
22. G. Zha, W. Jie, T. Tan and L. Wang, Phys. Stat. Sol. (a) 204 (7), p 2196-2200 (2007)
23. A. Hossain, A. E. Bolotnikov, G. S. Camarda, Y. Cui, G. Yang and R. B. James, J. Cryst. Growth 310 (21), p 4493-4498 (2008)
24. A. Hossain, Y. Cui, A. E. Bolotnikov, G. S. Camarda, G. Yang, D. Kochanowska, M. Witkowska-Baran, A. Mycielski and R. B. James, J. Electronic Materials 38 (8), p 1593-1599 (2009)
25. A. Koyama, A. Hichiwa and R. Hirano, J. Electronic Materials 28 (6), p 683-687 (1999)
26. A. K. Garg, M. Srivastava, R. C. Narula, R. K. Bagai and V. Kumar, J. Cryst. Growth 260 (1-2), p 148-158 (2004)
27. A. Fauler, A. Zwerger, M. Dambacher and M. Fiederle, IEEE Nucl. Sci. Symp. Conf. Rec. R01-4, p 3585-3588 (2006)
28. W. Palosz, D. Gillies, K. Grasza, H. Chung, B. Raghothamchar and M. Dudley, J. Cryst. Growth 182, p 37-44 (1997)
29. A. E. Bolotnikov, S. Babalola, G. S. Camarda, Y. Cui, S. U. Egarievwe, R. Hawrami, A. Hossain, G. Yang and R. B. James, IEEE Trans. Nucl. Sci. 57 (2), p 910-919 (2010)
30. K. F. Hulme and J. B. Mullin, Solid State Electron 5, p 211 (1962)
31. C. Szeles and E. E. Eissler, MRS Symp Proc. 487, p 3-12 (1998)
32. A. E. Bolotnikov, N. Abdul-Jaber, S. Babalola, G. S. Camarda, Y. Cui, A. Hossain, E. Jackson, H. Jackson, J. James, K. T. Kohman, A. Luryi and R. B. James, R27-2, IEEE Nuclear Science Symposium Conference Record 3, Honolulu, Hawai, p 1788-1797 (2007)
33. Derek S. Bale, J. Appl. Phys. 108, p 024504 (2010)
34. Ching-Hua Su and S. L. Lehoczky, J. Cryst. Growth 319, p 4-7 (2011)

Chapter IV: Characterization Techniques

IV.1 Overview

This chapter articulates around two points. The first point provides the theoretical background of X-ray topography, which is the main technique used to investigate the defect structure and distribution of the compound materials studied in this thesis. In this part, we discuss key terms that govern the X- ray topography (XRT) technique. These terms are based on the fundamental theories of diffraction: dynamical and kinematical theories. Among these terms are dispersion surface, tie points, Bormann fan, pendollösung fringes, contrast and rocking curve width. In the second point, we present the different characterization techniques. The advantage of each technique is also discussed in light of their pertinence to complement the X-ray topography technique.

IV.2 Theory of X-ray topography

X-ray topography (XRT) is a non-destructive X-ray imaging technique that gives a 2D rendering of the 3D microstructure of a crystal. The recording of the X-ray topography image, called a topograph, can be done in several different geometries using either conventional or synchrotron X-ray sources. The possible geometries are transmission, back reflection, reflection and grazing. The fundamental difference between reflection and grazing geometries lies in the position of the detector or film placed to record the topograph.

In this study, a synchrotron X-ray source was used to generate the X-ray beam that impinged upon the given single crystal. This synchrotron X-ray source offers very high brightness and low divergence beam. Two types of X-ray beam were generated from the synchrotron source. One type, called monochromatic X-ray beam, was obtained by using a monochromator. In this case, the technique is referred to as synchrotron monochromatic beam X-ray topography (SMBXT). In the case no monochromator is used, the technique is referred to as synchrotron white beam X-ray topography (SWBXT). The use of either type of X-ray source has its own advantages. For instance, SMBXT is more sensitive to strain compared to SWBXT. Hence, X-ray topography studies of stress in a crystal can be better calculated using SMBXT. While XRT does not have a magnification tools like other imaging techniques such as TEM, SEM and optical microscopy, micrometer to centimeter size defects can be imaged with a resolution R_e ($< 1\mu m$). This is because XRT has a geometrical magnification as shown in equation 1. A diagram illustrating

how magnification can be improved in XRT is shown in Figure 4.1 for the case of a finite X-ray source.

$R_e = \frac{SD}{C}$ (1), where S is source dimension, D is specimen detector, and C is the source- specimen distance.

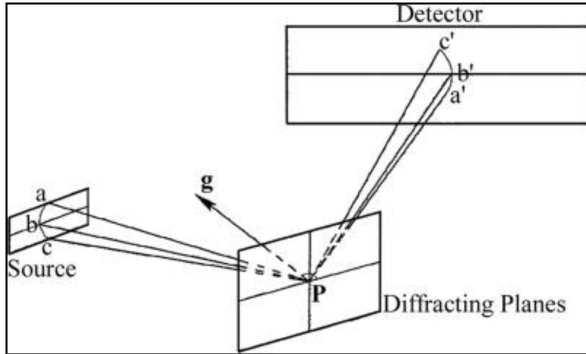

Figure 4.1. Schematic diagram showing the effect of finite source dimension on resolution. g is the active reciprocal lattice vector. The angle bPg, which is the semiapex angle of the Bragg cone of revolution, is 90- θB. θB is the Bragg angle [1].

It follows from Figure 4.1 that recording of the topograph at the detector or in our case at the X-ray film (see Figure 4.2) will occur only when diffraction conditions are met. These diffraction conditions are set by Bragg law as shown in equation 2. Bragg law gives the relation between the wavelength λ of the incident x-ray beam, its angle θ_B with the reflecting plane (hkl), and the interplanar spacing of the reflecting plane d_{hkl}. In the case of SMBXT, the crystal should be set at a specific Bragg angle in order for a given plane to diffract. Comparatively, SWBXT does not require the crystal to be set a specific Bragg angle. This is because diffracting planes can select from the broad spectrum being used the specific wavelength at which they diffract. A direct consequence of this wavelength selection is seen in the recording of several diffraction spots on an X-ray film. These diffraction spots, also called Laue spots, are distinct topographs that contain information about the spatial distribution of diffracted intensity inside the crystal as the beam passes through. Such distribution of the diffracted intensity, a function of the local scattering power and overall diffraction conditions inside the crystal, is attributable to the presence of structural irregularities, i.e. defects.

$$n\lambda = 2d_{hkl} \sin \theta_B \qquad (2)$$

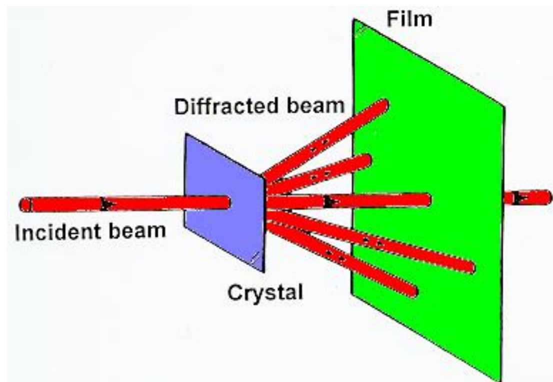

Figure 4.2. Schematic of XRT in transmission geometry

Defects within a crystal affect the X-ray diffracted intensity. The structure of those defects can be determined from the contrast they create as a result of their influence on the diffracted intensity. Since defects are identified based on the contrast they create, there exist conditions, i.e. crystallographic directions, under which they will not produce any contrast on an X-ray topograph. These conditions, for a dislocation type defects, are summed up in equation 3, which is referred to as invisibility criteria. On a typical topograph, regions of low scattering appear whiter, whereas regions of high scattering power appear darker relative to the surrounding matrix because of the presence of defects. These defects, more specifically dislocations, are characterized by their line direction and Burgers vector. The Burgers vector describes the shortest lattice displacement inside the crystal, and the line direction represents the dislocation propagation direction.

$g.b = 0$ and $g.(bxu) = 0$ (3), where g, b, and u are the diffraction vector, Burgers vector and displacement vector respectively.

Contrast formation

Contrast plays an important role in interpreting X-ray topograph. There are two types of contrast formation mechanism in XRT. These are *orientation* and *extinction contrasts*. These types of contrast can be influenced by the nature of the incident beam (monochromatic or white beam), the sample under study (e.g. absorbing power), and the interaction between the incident beam and the sample. The defect types and density as well as the choice of the experimental geometry also affect the contrast formation in XRT images. Here, the absorbing power refers to the ability of the crystal to absorb part of or the entire incident beam. This is expressed as μt, where μ is the linear absorption coefficient and t is the thickness of the crystal. Accordingly,

crystals can be classified into three groups based on their μt value:

- Low absorbing crystals (μt <2),
- Intermediately absorbing crystals (2<μt <10),
- High absorbing crystals (μt >10).

➢ **Orientation contrast**

Orientation contrast can be explained using Bragg law. In real crystal, some regions consist of atoms that are misoriented with respect to the crystal matrix. Such regions can form different grains, subgrains, domains, tilts or twins. Diffraction conditions in those regions are different from the crystal matrix. In this context, misoriented regions and crystal matrix do not satisfy the same Bragg equation. Illustration of orientation contrast is shown in Figure 4.3 for the case of monochromatic and white incident beam.

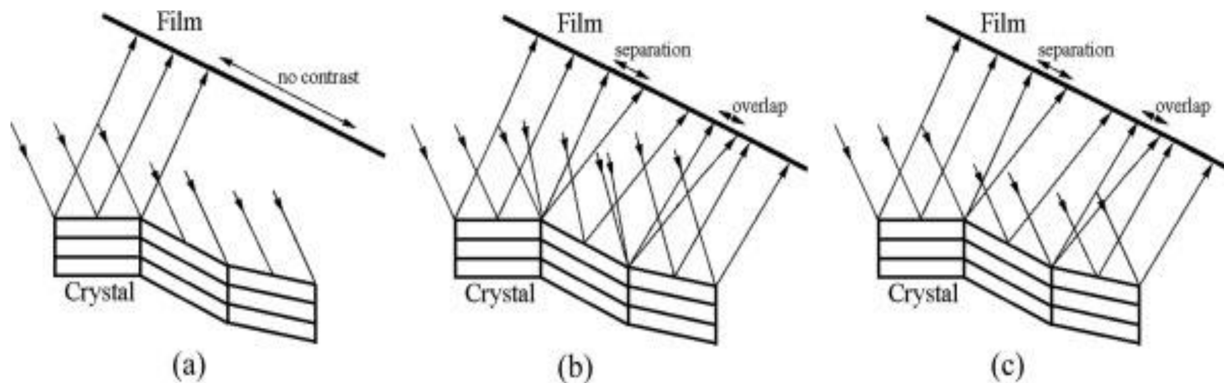

Figure 4.3. Orientation contrast arising from misoriented regions: (a) monochromatic radiation (beam divergence <misorientation); (b) monochromatic radiation (beam divergence > misorientation); and (c) white beam radiation [1]

Suppose an incident X-ray monochromatic beam upon a sample that consists of misoriented regions with respect to the crystal matrix. If the beam divergence is smaller than the misorientation, i.e. misorientation is outside the rocking curve width, these regions will not diffract. However, if the misorientation of these regions falls within the rocking curve width of the crystal, diffraction will occur. This will result in either separation or overlap (Figures 4.3a and b). Unlike monochromatic beam, a white beam or continuous radiation provides a broad spectrum of wavelengths, thereby allowing misoriented regions to select the wavelength at which Bragg diffraction is satisfied. This results in overlapping regions of enhanced intensity (Figure 4.3c).

- **Extinction contrast**

This type of contrast mechanism is explained based on the diffraction conditions near defective regions with respect to the perfect surrounding matrix. Defects in a crystal are known to distort the crystal lattice and cause the regions around them to behave differently from the perfect crystal in the presence of an X-ray beam. The local scattering power in those regions around the defects determines their diffracted intensity. Thus, extinction contrast arises as the difference in diffraction conditions from defective regions of the crystal with respect to the surrounding matrix. For a perfect crystal, the scattering power is proportional to the structure factor |F|; whereas for an imperfect crystal it is proportional to the square of the structure factor $|F^2|$. A thorough treatment of extinction contrast is given in the work of Tanner and Bowen [2], Cullity [3], and Zachariasen [4].

Kinematical theory has long been used to predict diffracted intensity and determine the structure of crystals. In this theory, the influence of matter on X-ray waves is neglected and it is assumed that X-ray scatters only once before it is detected. The kinematical theory considers a crystal to be made of small crystallites acting as independent scattering centers. The resulting total amplitude diffracted from such crystals is the sum of the amplitude scattered from each center, accounting for the phase difference between them. This is mathematically expressed in equation 4, where I is the total amplitude, I_0 is the amplitude from each center, k is the wave vector, and r_i is the center position.

$$I(k) = I_o \sum_i^n e^{-2\pi i(k.\mathrm{ri})} \quad (4)$$

Equation 4 suggests that the diffracted amplitude will increase with crystal size, which is in contradiction with the conservation of energy principle between incident and diffracted waves. This failure to meet the fundamental principle of energy conservation shows the limit of the kinematical theory. In fact, observation of scattered intensity in real crystals shows that this theory applies best to small (~1µm diameter) and highly distorted crystals, where dislocations act to divide the crystal into a mosaic structure of independently diffracting cells. The phenomenon of primary extinction (Figure 4.4) can be further used as an illustration.

When an incident X-ray traverses a crystal, it undergoes multiple diffractions from different atomic planes. The diffracted beams have a phase difference of π/2 with respect to the transmitted ones. Therefore, along each direction (transmitted and diffracted), wavefields are π out of phase. This results in decrease in intensity, which increases with the number of scatterings.

In short, primary extinction amounts to an increase in absorption from multiple scattering that results in overall reduction of intensity predicted by the kinematical theory. To account for the multiple interactions between the X-ray and the crystal, *dynamical theory* is used.

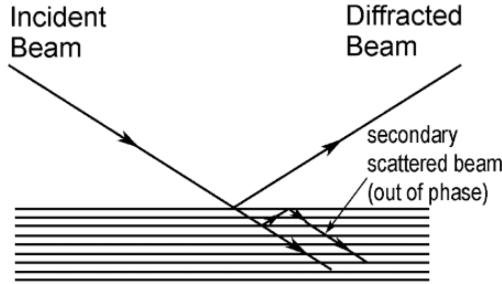

Figure 4.4. Schematic diagram demonstrating primary extinction [5]

Dynamical theory takes into account the multiple scattering that occurs as X-ray passes through a crystal, where diffracted wave fields are added to the reflected beam at the surface. In this case, the dynamic interaction between incident and diffracted beams dominates the diffraction process, and the scattering amplitudes are added before the total intensity is computed. This theory is generally seen in thick (>1μm) and nearly perfect crystal.

The main problem of the dynamical theory is to find solution to Maxwell equations inside a medium (e.g. crystal) with a periodic, anisotropic and complex dielectric susceptibility χ. These solutions must satisfy boundary conditions, i.e. match solutions which are plane waves outside the crystal given by the incident ($\mathbf{K_0}$) and diffracted ($\mathbf{K_h}$) X-ray beams. The set of solutions that conform to the periodicity of the crystal are called Bloch's functions. They are obtained by the superposition of plane waves, and can be written as a Fourier sum.

Below is a brief review of Max Von Laue proposed treatment of this problem. Laue established the relationship between diffracted beam inside the crystal and the incident beam wavevector with the reciprocal lattice vector $\mathbf{R_h}$. This is given in an equation called Laue equation.

$$\boldsymbol{K_h} = \boldsymbol{K_o} + \boldsymbol{R_h} \qquad (5)$$

The fundamental Maxwell equations are given below along with an expression of χ as a Fourier sum over the reciprocal lattice.

$$\nabla \times \mathbf{H} = -\frac{1}{c}\left(\frac{\partial D}{\partial t} + 4\pi J_t\right), \nabla \times \mathbf{E} = -\frac{1}{c}\frac{\partial B}{\partial t}, \chi(r) = \sum \chi_h e^{-2\pi i (R_h r)} \qquad (6)$$

H, **D**, **E, B** and $\mathbf{R_h}$ are magnetic field, electric displacement, electric field, magnetic induction, and reciprocal lattice vector, respectively. "c" is the speed of light in vacuum, χ_h is susceptibility constant that is related to the structure factor as given by equation 7.

$$\chi_h = \frac{r_e}{\pi V_c}\lambda^2 F_h \quad (7)$$

Here, r_e is the electron radius, λ is X-ray wavelength, F_h is the structure factor and V_c is unit cell volume. Since a crystal is neutral, J_t is neglected from the equation of the curl of the magnetic field. Thus the curl of the magnetic field becomes:

$$\nabla \times \mathbf{H} = -\frac{1}{c}\frac{\partial \mathbf{D}}{\partial t} \quad (8)$$

In solving for the solutions of Maxwell equations, the periodicity of the crystal is important factor to consider. A wave that travels through a crystal will experience this periodicity. Thus, the electric displacement in (8) can be express as a Fourier sum.

$$D = \Sigma D_n e^{-2\pi i(\mathrm{v}t - \mathbf{K_h}.\mathbf{r})} \quad (9)$$

We will forgo any mathematical formalism, and provide the fundamental equations of the dynamical theory derived from the expression of χ in (6) and D in (9). These equations describe the wavefield inside a crystal for a given set of plane waves. Only reciprocal lattice points that are very close to the surface of the Ewald sphere give a diffracted wave of appreciable amplitude. In fact, very rarely does more than one lattice point provide any appreciable diffraction. Thus, only two waves, one associated with the incident wave and another associated with the diffracted wave from a reciprocal lattice vector **h**, are considered. The solutions of Maxwell equations inside a crystal are then expressed in terms of the amplitudes of electric displacement of incident wave $\mathbf{D_0}$ and diffracted wave $\mathbf{D_h}$.

$$[k^2(1+\chi_o) - \mathbf{K_o}.\mathbf{K_o}]D_o + k^2 C\chi_h \mathbf{D_h} = 0 \quad (10.a)$$

$$[k^2 C\chi_h \boldsymbol{D_o} + [k^2(1+\chi_o) - \mathbf{K_h}\mathbf{K_h}]\mathbf{D_o} = 0 \quad (10.b)$$

where C is the polarization factor.

For σ polarization, which is normal to the plane containing $\mathbf{K_0}$ and $\mathbf{K_h}$, C is unity and the displacement vector $\mathbf{D_0}$ and $\mathbf{D_h}$ are parallel. In the case of a π polarization, which is parallel to the plane containing $\mathbf{K_0}$ and $\mathbf{K_h}$, C is equal to $\cos 2\theta_B$, but the displacement vectors $\mathbf{D_0}$ and $\mathbf{D_h}$ are not parallel to one another. Setting equations 10 in matrix form and solving for the nontrivial solutions gives the permitted wave vectors. While the dynamical theory approximates the kinematical theory in the limit of small (<1μm) and imperfect crystals, deviation parameters α_0 and α_h are included to account for the case of large and perfect crystals, foreign to the kinematic assumption.

$$\alpha_o = \frac{1}{2k}[\mathbf{K_0}.\mathbf{K_0} - k^2(1+\chi_0)] \quad (11.a)$$

$$\alpha_h = \frac{1}{2k}[\mathbf{K_h}.\mathbf{K_h} - k^2(1+\chi_0)] \quad (11.b)$$

Taking the product of 11.a and 11.b, we arrive at the following solution:

$$\alpha_o\alpha_h = \frac{1}{4}k^2C^2\chi_h\chi_{\bar{h}} \quad (12)$$

The electric field displacement gives the amplitude of the wave as it propagates in the crystal. The relative amplitude of the diffracted $\mathbf{D_h}$ and incident $\mathbf{D_0}$ components is called amplitude ratio. It is given in equation 13.

$$R = \frac{D_h}{D_0} = \frac{2\alpha_0}{Ck\chi_{\bar{h}}} = \frac{Ck\chi_h}{2\alpha_h} = \left(\frac{\alpha_0\chi_h}{\alpha_h\chi_{\bar{h}}}\right)^{1/2} \quad (13)$$

Equations 12 and 13 are the fundamental equations that are used to predict the wavefields and their intensity inside and outside the crystal. The solutions to Maxwell equations usher in an important concept that furthers the understanding into wave interaction with crystalline matter. This concept is called dispersion surface.

Dispersion surface given by equation 12 describes the plane containing $\mathbf{K_0}$ and $\mathbf{K_h}$. The simplicity of this definition does not give justice to its importance to the theory of X-ray diffraction. Thus, a geometric formalism is used to explain the concept of dispersion surface. Consider a pair of spheres of radius given by the wavevector K centered at the origin O and the reciprocal lattice point H. These spheres intersect at a point L, which correspond to the center of the Ewald sphere. The center of the Ewald sphere is the so-called Laue point. This illustration corresponds to the kinematical theory (KT). As discussed earlier in the context of primary extinction, KT violates the conservation of energy principle. Thus, a new construct for the dispersion surface, which accounts for the mean refractive index, is proposed using dynamical theory (DT).

Suppose again a pair of spheres under the same conditions as above, but with a radius given by $K(1+\chi/2)$. The point of intersection of these spheres is called Lorentz point. This construct takes into account the refractive index $(1+\chi/2)$ in the crystal. It is important to note that the refractive index varies with lattice periodicity. In this case, the reciprocal lattice point lie near the Ewald sphere, ensuring that the diffracted amplitude do not become infinite.

Illustration of the dispersion surface for these two cases is shown in Figure 4.5a. As the radius of the spheres described in the above cases differ by about 10^{-6}, a section through the

intersection around the Laue point is drawn and shown at a very high magnification (~10^6), Figure 4.5b. This allows a plane view of the spheres as tangent lines that represent two branches (upper branch denoted 1 and lower branch denoted 2) of a hyperboloid of revolution with OH as its axis. It should be noted that the arc of circle O'O" and H'H" in Figure 4.5b can be approximated as surfaces. Furthermore, point A denotes the *tie point* at which diffraction occurs.

The σ and π polarization states have each two branches that correspond to a dispersion surface. The hyperboloid describes the equation of a dispersion surface, and is the loci of wavefield having the Lorentz point as it center for the DT case, and the Laue point as its center for the KT case. When the deviation parameters α_0 and α_h are equal, the semi-diameter of the hyperbola is given by:

$$D_h = \frac{1}{4} kC(\chi_h \chi_{\bar{h}})^{1/2} \sec\theta \qquad (14)$$

As seen in Figure 4.5b, α_0 and α_h are perpendicular distance from point A to the two intersecting spheres of radius K(1+ χ/2). The importance of the tie point A does not only lie in its relation to the dispersion surface, it also helps to determine the position and amplitude of the wavevector. As waves propagate inside a crystal, it experiences lattice periodicity. The direction of energy flow can thus be described. This is done using the Poynting vector **P** normal to the dispersion surface at the tie point.

$$\mathbf{P} = \mathbf{E} \times \mathbf{H} \qquad (15)$$

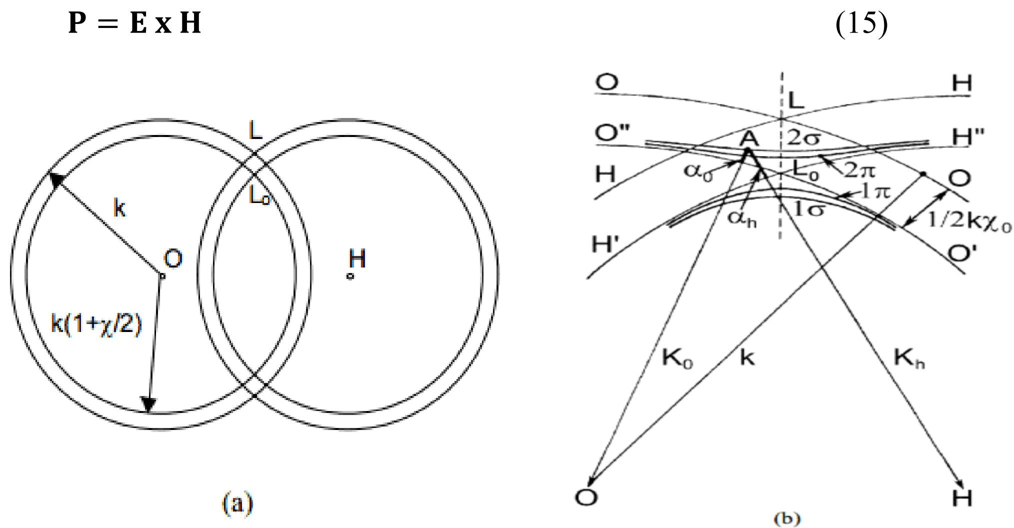

Figure 4.5. Construction of the dispersion surface: (a) Spheres of radius k and k(1+χ/2) about origin O and the reciprocal lattice point H in reciprocal space showing the positions of Laue point L and Lorentz point L0; (b) Dispersion surface for σ and π polarization states [5].

The determination of the amplitude of the wavevectors requires consideration of boundary conditions because wavevectors continuity must be met across the surface. For a plane wave incident upon a crystal, the displacement is given by D_1, while a Bloch wave inside a crystal has a displacement given by D_2, and the continuity condition are given in equations 16.

$$D_1 = D_o e^{-2\pi i(\mathbf{K_o}.\mathbf{r})} \quad (16.a)$$

$$D_2 = \sum D_h \, e^{-2\pi i(\mathbf{K_h}.\mathbf{r})} \quad (16.b)$$

$$e^{-2\pi i(\mathbf{K_o}.\boldsymbol{\tau})} = e^{-2\pi i(\mathbf{K_h}.\boldsymbol{\tau})} \quad (16.c)$$

where $\boldsymbol{\tau}$ is a unit vector in the surface.

The above equations provide the relationship between the wavevectors inside and outside the crystal. They differ by a vector normal to the crystal surface, and can be obtained for each branch (i = 1, 2) of the dispersion surface using equation 17.

$$\boldsymbol{K_0} - \boldsymbol{k_o} = \boldsymbol{\delta n} \quad (17)$$

Where $\mathbf{n}$ is a unit vector normal to the surface.

A construct of this relationship can be obtained by drawing a line normal from the tip of the incident wavevector k_0 intersecting the dispersion surface at the excited tie points. In the Laue case (Figure 4.6a), two tie points (A and B), one on each branch, are excited. From each point, we draw wavevectors toward the O and H, previously described as center of pair of spheres. Since each polarization has two branches, we can generate four wavevector per polarization and eight in all. The direction of energy flow is along the Poynting vector, and despite the splitting of the waves at the exit surface, boundary conditions remain identical for waves leaving and entering the crystal.

In the Bragg reflection case (Figure 4.6b), two scenarios are possible. There can be two tie points on the same dispersion surface or none at all. When the tie points are on the same surface, they have different Poynting vectors, and the energy flow from one point is into the crystal while for the other point, the energy flows outwards. However, only when energy flows into the crystal is a wavevector generated. Conversely, when energy flows outwards, no wavevector is generated. In the case where no tie point is excited, no wavevector is generated, and the crystal does not absorb X-ray. The crystal is said to totally reflect.

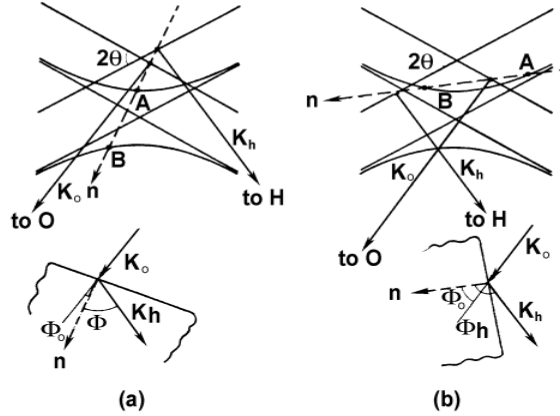

Figure 4.6. Dispersion surface construction showing the tie points excited by an incident wave in (a) the Laue geometry: One tie point on each branch (A on branch 1 and B on 2); (b) The Bragg geometry: Two tie points (A and B) on the same branch [5]

Sometimes, a crystal may be unusually transparent to X-ray. This is known as anomalous transmission or *Bormann effect*.

Bormann effect describes the anomalous increase in the intensity of X-rays transmitted through a crystal set at Bragg condition. This increase in intensity is equivalent to a decrease in absorbing power of the crystal discussed earlier. The effect was discovered by Bormann in calcite [6, 7], and can be mathematically described by considering the intensity of standing waves inside a crystal. Consider a crystal in which travelling waves are not plane waves. These travelling waves are Bloch waves due to lattice periodicity. Bloch waves generates standing waves that are normal to the Bragg planes, and have amplitudes that are modulated with the periodicity corresponding to the Bragg planes as shown in equation 18.

$$\mathrm{I} = \mathrm{D}^2 = \mathrm{D}_0^2[1 + \mathrm{R}^2 + 2\mathrm{RC}\cos(2\pi\mathbf{h}.\mathbf{r})] \qquad (18)$$

The intensity modulation factor is cos(2π**h.r**), with maxima at **h.r** = n and minima at **h.r** = (2n +1)/2) occurring either at or halfway between the atomic planes. n is an integer and h is the diffraction vector. Maximum modulation occurs when R and C equal unity for σ polarization of centrosymmetric crystals ($\chi_h = \chi_{\bar{h}}$) set at the exact Bragg condition. The sign of R determines whether maxima or minima occur at the atomic planes. When R is positive, intensity maxima occur, while minima occur for negative R. We note that the sign of R is opposite for wavefields with tie points on opposite branches of the dispersion surface.

Absorption effect occurs mainly by photoelectric process at crystallographic wavelengths. Since the electron density is the greatest at atomic planes, the Bloch wave with intensity maxima

at the atomic planes will undergo the greater photoelectric absorption compared to a wave with intensity minima between atomic planes. We can consider the case where branch 2 wavefield of the dispersion surface absorbs more strongly than branch 1 (see Figure 4.7). This effect is a property of perfectly periodic crystal, and is very sensitive to imperfections. It can thus be used to gauge of the degree of perfection of a lattice.

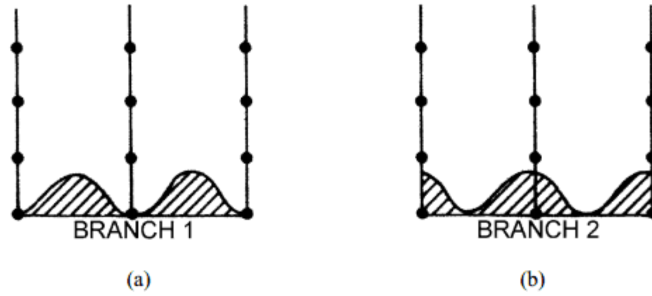

Figure 4.7. Standing wavefields of (a) branch 1 and (b) branch 2, with a period corresponding to the spacing between the Bragg planes produced at the exact Bragg condition [5].

Pendollösung effect describes the interference effect that occurs between two Bloch waves that are generated when an incident plane wave excites two tie points on the dispersion surface. Because the interference is alternatively constructive or destructive, beats are produced; hence the name pendollösung. The depth of the layer at which complete alternation occurs is called the extinction distance (ξ_g). This distance is the reciprocal of the dispersion surface diameter d_h, and measures the X-ray penetration depth when Bragg condition is satisfied.

$$\xi_g = d_h^{-1} = \frac{cos\theta_B}{Ck(\chi_h \chi_{\bar{h}})^{1/2}} = \frac{\pi V cos\theta_B}{r_e \lambda C(F_h F_{\bar{h}})^{1/2}} \quad (19)$$

where F_h and $F_{\bar{h}}$ are the structure factors of (hkl) and $(\overline{hkl})$, respectively.

In the case Bragg condition is not satisfied, the extinction accounts for the deviation parameter η that expresses how far the Bragg position ($\Delta\theta$) is to the tie points.

$$\xi_g' = \frac{\xi_g}{(1+\eta^2)^{1/2}}, \qquad \eta = \frac{Sin2\theta_B}{C(\chi_h \chi_{\bar{h}})^{1/2}} \Delta\theta \quad (20)$$

When η approaches infinity, ξ_g' is equal to ξ_g, no interference occurs. The pendollösung effect can be summarized as a process whereby energy is alternatively traded between direct and diffracted beams inside the crystal. It is an optical phenomenon that can also be used to determine the quality of a crystal.

In the above treatment, a plane wave was assumed. This is not the case in practice where significant angular divergence in x-ray sources causes the entire dispersion surface to be excited simultaneously. As a consequence, energy flows in a range of direction that can be described by the *Bormann fan* (Figure 4.8).

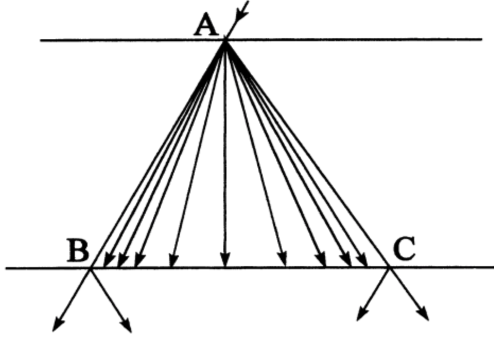

Figure 4.8. Bormann fan bounded by the incident (AB) and diffracted (AC) beams showing the distribution of energy for an incident spherical wave that excites all tie points along the dispersion surface [5].

Rocking curve width describes the angular range through which Bragg condition is satisfied. On a plot of angular rotation (θ) versus diffracted intensity, it represents the point at which half of the maximum Bragg intensity occurs. This point is also called full width at half maximum (FWHM). The equations describing the FWHM are given below for the Brag and Laue case, respectively.

$$\omega = \frac{2C(\chi_h\chi_{\bar{h}})^{1/2}}{Sin2\theta_B}\sqrt{\frac{|\gamma_h|}{\gamma_0}}, \text{ for asymmetric Bragg reflection} \qquad (21.a)$$

Setting $\gamma_0 = \gamma_h$, we obtain the case of symmetric Bragg reflection.

$$\Omega = \frac{2C(\chi_h\chi_{\bar{h}})^{1/2}}{Sin2\theta_B} \quad , \qquad (21.b)$$

$$\Delta\theta = \frac{2C|\chi_h|}{Sin2\theta}\sqrt{\frac{|\gamma_h|}{\gamma_0}}, \text{ for Laue case} \qquad (22)$$

As pointed out before, there are two mechanism of contrast formation: orientation and extinction contrast. We will not recall these two types of contrast. On contrary, we will discuss the three types of images of crystal defect observed in X-ray topograph. These types of images (direct, dynamical, and intermediate) have been determined by Authier [7]. They are schematically shown in Figure 4.9a. Their contrast arises in region of high strain gradient where the defect behaves like the crystal surface. Distinction of each type of image requires insight into their mechanism of formation.

A real crystal can be divided into three regions: a perfect region above the defect, a perfect region below the defect, and a region around the defect. Due to lattice strain caused by the defect, region around the defect will be misoriented with respect to the other two regions. This strain may be small or large. In the event of small strain, the tie points migrate along the dispersion surface and the wavefields do not decouple. The wavevectors then propagate along the lattice plane curvature, leading to a curved trajectory. As a result, a contrast arises from the variation in intensity between the forward and diffracted beams (Figure 4.9b). When the defects cause large strain, the tie point on one branch (say branch 1) jumps to the other branch (say branch 2). This is known as interbranch scattering or tie-point jumping. Interbranch scattering leads to decoupling of the wavefield into its plane wave components upon passing the highly distorted region, creating new Bloch wavefields in the region below, where distortion is small.

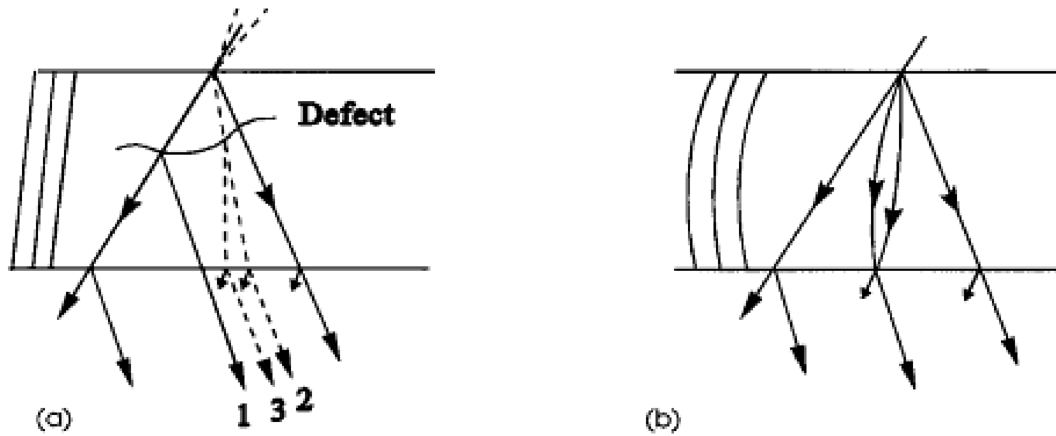

Figure 4.9. (a) Formation of the three types of image under high strain gradients: 1- Direct image; 2- Dynamical image; 3- Intermediary image; (b) contrast formation under low strain gradients [5].

Direct image contrast appears dark against the background on X-ray topograph. It arises from diffracted X-rays, which are outside the diffraction range of the perfect crystal. This occurs when the misorientation of the region around the defect is greater than the perfect crystal reflection range and smaller than the beam divergence. It is important to note that the effective misorientation $\delta\theta$ around a defect is the result of the tilt in the plane of incidence $\delta\varphi$ and the change in Bragg angle caused by dilation δd (see equation 22)

$$\delta\theta = -\tan\theta_B \frac{\delta d}{d} \pm \delta\varphi \quad (22)$$

It follows that the X-ray diffracted from the region around the defect suffers no primary extinction, leading to an enhanced intensity compared to the rest of the crystal. This kind of contrast is called dynamical or kinematical image, and dominates under low absorption regime ($1<\mu t<2$). Huang et al. [8] have revealed that orientation contrast significantly contributes to direct dislocation image under low absorption in their work on contrast formation mechanism in large Burgers vector superscrew dislocation in SiC. This was further supported by Dudley et al. [9] whose orientation contrast model indicates that in the low absorption regime, the contribution of orientation contrast in direct dislocation image arises from either the overlap or separation of the inhomogeneously diffracted x-rays with continuously varying directions.

Dynamical image contrast is formed from the change in intensity in the Bloch wavefields that traverse the perfect crystal. Insight into this type of contrast can be obtained by considering the Bormann fan. Suppose two wavefields propagate along a given direction within the Bormann fan spanning a line defect. When the wavefields passes across the region around the defect, they separate into their plane wave components, and create new wavefields upon re-entering the perfect crystal region. This results in a loss of intensity in the propagation direction beyond the defect, casting a shadow called dynamical image [10]. Such images of defects appear as white shadow on X-ray topographs, and are observed under high absorption ($\mu t>10$). The new wavefields described above propagates along a path that is deviated from their parent wavefields, and can lead to contrast formation.

Intermediate image contrast is the result of the interference between the newly created Bloch wavefields described in the dynamical image contrast and their parent wavefields. Like the dynamical image, this contrast can be described on the basis of the Bormann fan. Suppose two wavefields encounters a strongly deformed region around the defect (e.g. core of a dislocation). Upon re-entering the perfect region below the defect, these wavefields separate into their transmitted and diffracted component. This leads to interbranch scattering and newer Bloch wavefields are created. The interference between these newer wavefields and the original ones results in the formation of fringes seen under intermediate absorption conditions ($2<\mu t<4$); whence the name intermediate image. A topograph showing these three types of dislocation images is shown in Figure 4.10, where the poor spatial resolution of dynamical and intermediate images can be seen.

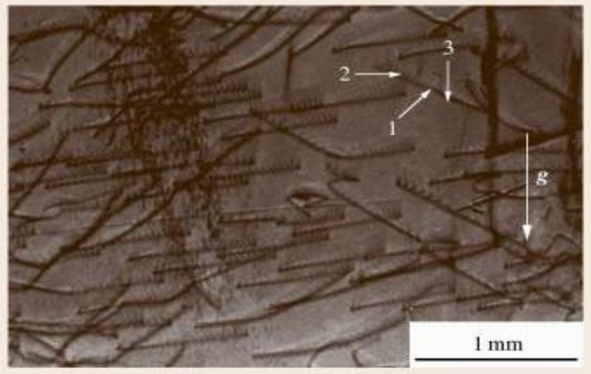

Figure 4.10. SWBT transmission topograph (g = 10-10, λ = 0.75Å) recorded from an AlN single crystal under intermediate absorption conditions (μt = 8) showing the direct (1), dynamical (2), and intermediary (3) images of a dislocation [6]

IV.3 Experimental Techniques

The following techniques were used to characterize the compound materials in this thesis:

- Synchrotron X-ray topography geometries (Transmission, reflection, back reflection and grazing)
- Raman spectroscopy
- Transmission electron microscopy (TEM)
- Transmission infra-red microscopy
- Light microscopy

IV.3.1 Synchrotron X-ray topography geometries

Transmission geometry corresponds to the case where the entrance side of the incident beam is opposite the exit side of the diffracted beam. This geometry is shown in Figure 4.11.a. Because the X-ray beam traverses the entire crystal thickness, information about the bulk microstructure can be obtained. Typical defects observed using this geometry for a silicon carbide single crystal are basal plane dislocations (BPDs).

Reflection geometry describes the geometry in which the entrance face of the incident beam corresponds to the exit face of the diffracted beam as shown in Figures 2.11b and c. Such geometry is preferentially used to survey the microstructure of crystals that are either very thick or highly absorbing to permit the use of transmission geometry. It is also suitable to characterize crystals that have a large defect density as well as epitaxial layers. An important advantage that this geometry offers is control over the penetration depth of the incident X-ray beam. This penetration depth is determined by the kinematical theory for the case of imperfect crystals or by the dynamical theory for the case of structurally perfect crystals. The equations of penetration

depth as defined by the kinematical (t_k) and dynamical (Z_e) theories are provided below [11, 12].

$$t_k = \frac{\ln\left(^{I_0}/_{I}\right)}{\mu\left(\frac{1}{\sin\emptyset_0}+\frac{1}{\sin\emptyset_h}\right)}, \quad Z_e = \frac{\varepsilon_g}{2\pi\sqrt{1-\eta^2}} \tag{23}$$

Back reflection geometry is a variant of reflection geometry. It corresponds to the case where the incident beam penetrates the crystal at large Bragg angle closely parallel to the normal of the crystal surface, while the diffracted beam exits the same face at a large angle. This is a Bragg case of symmetric reflection. With this geometry, defects that threads along the crystal surface can be resolved, and the magnitude of their Burgers vector determined. The orientation of a crystal can also be determined using this geometry. An illustration of this geometry is shown in Figure 4.11b.

Grazing geometry is a Bragg case of asymmetric reflection where the incident beam enters the crystal surface at a shallow angle, usually within 5˚, and exit at angle nearly parallel to the crystal surface. Because of the surface sensitivity of this technique, defects at different depth below the crystal surface can be imaged by controlling the penetration depth of the x-ray source. Common defects observed in silicon carbide single crystals using grazing incidence geometry are threading dislocations (TSDs and TEDs), and micropipes (MPs). A schematic illustrating the grazing incidence geometry is shown in Figure 4.11c.

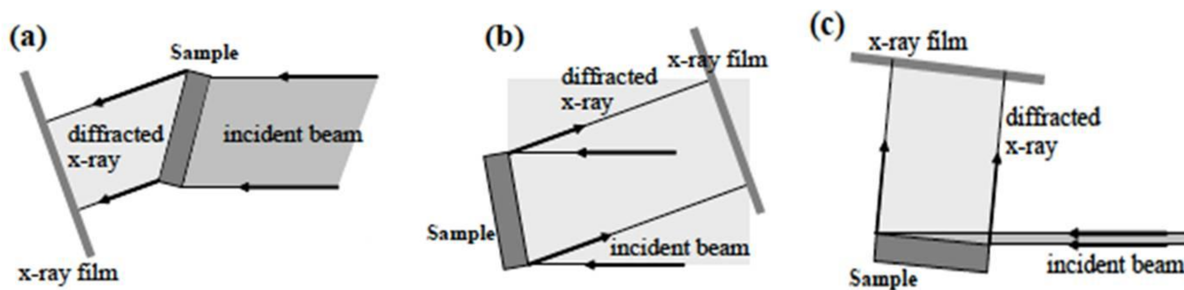

Figure 4.11. Transmission geometry (a), back reflection geometry (b), and Grazing geometry (c)

IV.3.2 Raman spectroscopy

When a laser light impinges upon a crystal, it is scattered. The phenomenon in which the scattered light has a different wavelength compared to the wavelength of the incident laser light is called *Raman scattering*. It is a non-destructive technique that consists essentially of two parts:

- an illuminator: this is the laser source

- a detector and software: where Raman signals are collected and mathematically outputted on spectra as an intensity versus frequency shift between the incident and the scattered light.

The basic equation governing Raman scattering is given:

$h\upsilon + E_i = h\upsilon' + E_f$ (2), where h is Planck's constant, ν is the frequency of the incident photon, ν' is the frequency of the scattered phonon, E_i is the initial energy state of the molecule and E_f is the final energy state of the molecule.

This technique appeals to us because it is non-destructive, sensitive to both chemical and physical properties of materials. Its unique selection rules are well suited for the identification of materials. Further, by measuring the shift of peak from their ideal position, the stress and strain in crystals can be evaluated. The effectiveness of Raman in identifying polytypes, detecting crystal disorder and other defects in SiC is well documented [13 - 17]. Raman spectroscopy in these studies was carried out in the Laboratory for Surface Analysis and Corrosion Science at Stony Brook University using a Nicolet Almega XR dispersive Raman spectrometer. This spectrometer offers high spatial resolution (~ 1μm), great sensitivity to Raman emission, and uses lasers in the range (400-787 nm).

IV.3.3 Transmission electron microscopy

Transmission electron microscopy (TEM) is a destructive imaging technique that can produce atomic-scale images of a specimen. The specimen can be a crystal, a composite or a polymer. The formation of the image is obtained from the interaction of an electron beam with the specimen. In order to acquire a good quality image, the specimen must be electron transparent, i.e. thinned downed to about 100-150 nm. This is achieved through an involving process referred to as sample preparation. Common sample preparation techniques are focus ion beam (FIB), ion milling, mechanical polishing and dimpling.

Despite the rigorous requirement for specimen preparation, TEM has compelling arguments that make its usage a necessity for our studies. It uses a high-energy beam source (~ 100 -400 keV) [18], operates under vacuum, has a high depth of field and resolution [19, 20]. It also offers dark and bright field imaging modes. These excellent features of TEM enable reliable probing of crystal microstructure.

In this thesis, high-resolution transmission electron microscopy (HRTEM) was used to investigate the stacking fault and polytypes structure in axial and transverse 4H/6H-SiC a/m pseudo fiber laterally grown in HWCVD using JEOL 2100F at the Center for Functional Nanomaterial (CFN) at Brookhaven National Laboratory (BNL). HRTEM is based on phase contrast imaging, and unlike bright and dark field imaging mode requires the selection of more than one beam to produce higher resolution. The JEOL 2100F is a field emission TEM that produces a highly stable and bright electron probe that is superior to that of conventional thermionic electron gun. It allows a resolution pole-piece of 0.19 nm. Additionally, the wide range of operating voltage (80– 200kV) is an added advantage that enables fine-tuning of the resolution to specific end as well as selection of accelerating voltage to avoid irradiation-induced damages in TEM specimen. Bright field images of TEM specimen taken from these samples were also recorded. Figure 4.12 shows a conventional JEOL 2100F.

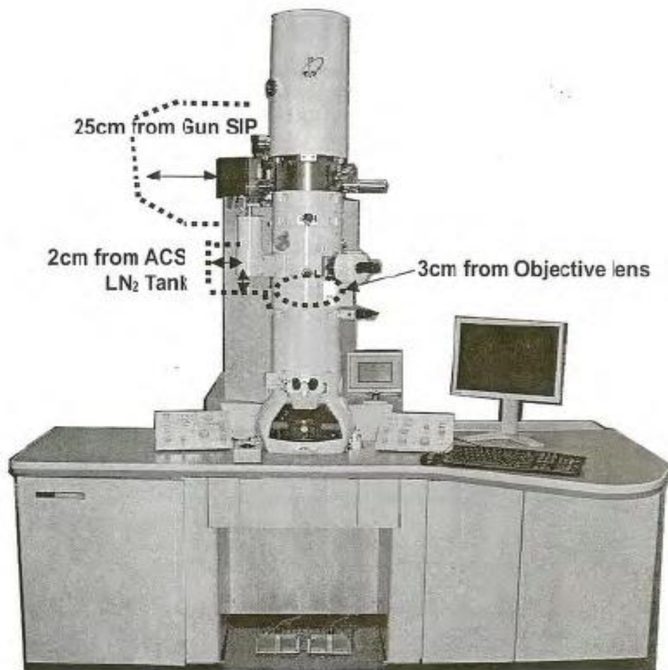

Figure 4.12. Conventional JEOL 2100F

IV.3.4 Transmission infrared microscopy

This is a versatile nondestructive technique that enables imaging of the microstructure of a material that is infrared transparent. Where defects are present, the material is opaque. This opacity to infrared radiation in the presence of defects makes transmission infrared microscopy (TIM) suitable for the investigation of the surface and bulk microstructure of infrared transparent

materials. One material, which exhibits transparency to infrared radiation, is cadmium zinc telluride.

Cadmium zinc telluride is attracting increasing interest in the development of X-ray and gamma ray detectors. However, the relatively high density of structural defects in CZT single crystals prevents the realization of the full potential of these detectors. Such defects, which form because of CZT's incongruent melting, are tellurium inclusions and precipitates. These Te defects are opaque to infrared radiation. It is well known that Te defects decorate grain and twin boundaries. Therefore, grain and twin boundaries are opaque to infrared radiation. Besides Te inclusions and precipitates, grain and twin boundaries, cracks are also opaque to infrared radiation.

Transmission infrared microscopy essentially relies on the absorption of infrared radiation as it traverses a material. It provides a high spatial resolution of a few micrometers and allows imaging of samples as small as 7 μm. While Te inclusions can be observed in SXRT images, Te precipitates cannot because their size falls below the resolution limit of SXRT. In this thesis, TIM is used to investigate the presence of tellurium inclusions and precipitates in cadmium zinc telluride single crystals grown by directional solidification Bridgman method at various cadmium overpressure. An illustration of a transmission infrared microscope is shown in Figure 4.13. This figure does not show the computer/software component that allows the recording of the image.

Figure 4.13. Transmission infrared microscope

IV.3.5 Light microscopy

Light microscopy is an imaging technique that uses a visible light source to characterize single crystal materials. It has a lower resolution compared to TEM. While its resolution is comparable to SXRT, it does not enable imaging of structural defects on the same scale. Despite this limitation, light microscopy offers several advantages. First, it is a non-destructive technique and does not require very complex sample preparation unlike TEM. Like in SXRT, large size samples can be imaged with the aid of a translational stage. It distinctly resolves scratches and mechanical polishing damages, which degrade quality of SWBXT images and TEM specimen. The nature of certain features that exhibit precipitate-like contrast on SXRT images can also be ascertained under light microscopy.

Likewise, single crystals can be imaged in two geometries: reflection and transmission. The transmission geometry is suitable to light transparent sample. Relatively thick samples that are transparent can also be imaged in transmission geometry. Comparatively, the reflection geometry is suitable for light opaque sample, where the visible light cannot be transmitted through the sample to the viewing aperture. Beside these two geometries, samples can be imaged in bright and dark field, Nomarski and polarization modes. Each one of these modes allows a different contrast of the image. On one hand, *bright field imaging mode* offers a contrast that arises from the absorption of light in the sample. In *dark field mode*, the contrast arises from the scattering of light by the sample. In Nomarski mode, is a phase contrast mode in which the interference between different optical path lengths through the sample produce the contrast. The *polarization mode* enables a contrast that comes from the rotation of light by a polarizer through the sample.

In our studies, we use a Nikon Eclipse E600W Pol optical microscopy at the Laboratory for X-ray Synchrotron Topography to complement SXRT results. Most images were recorded in Nomarski mode in both transmission and reflection geometries. Bright field and dark field image modes were also used.

References

1. B. Raghothamachar, G. Dhanaraj, J. Bai and M. Dudley, Microsc. Res. Tech. 69, p 343-358 (2006)
2. D. K. Bowen and B. K. Tanner, "High Resolution X-ray Diffractometry and Topography" Taylor and Francis, London. 1998.
3. B. D. Cullity, "Element of X-ray Diffraction", Addison-Wesley publishing Company, Inc, Reading, Massachusetts (1956)
4. W. H. Zacharissen, "Theory of X-ray Diffraction in Crystals", Wiley, New York. 1945.
5. B. Ragothamachar, "Synchrotron White Beam X-ray Characterization of Growth Defects in Bulk Compound Semiconductors", Stony Brook University, PhD Thesis (2001)
6. B. Raghothamachar, M. Dudley and G. Dhanaraj, "Chapter 42: X-ray topography techniques for defect characterization of crystals", Eds G. Dhanaraj, K. Byrappa, V. Prasad, and M. Dudley, Springer Handbook of Crystal Growth, p 1425 (2010).
7. Andre Authier, "Dynamical Theory of X-ray diffraction", Oxford University Press, New York (2001)
8. X. R. Huang, M. Dudley, W. M. Vetter, W. Huang, W. Si and C. H. Carter Jr., J. Appl. Crystallogr. 32 (3), p 516-524 (1999)
9. M. Dudley, X. R. Huang and W. Huang, J. Phys. D: Appl. Phys. 32, p A139-A144 (1999)
10. Andre Authier, "Diffraction and imaging techniques in materials science", ed. S Amelincks, R. Gevers and J. Van Landuyt, Amsterdam: North-Holland, 1978
11. M. Dudley, J. Wu and G. D Yao, Nucl. Instr. Meth. Phys. Res. B **40-1**: p. 388-392 (1989)
12. B. K. Tanner, "X-ray diffraction topography", 1st ed. International series in the science of the solid state v 10. 1976, New York: Pergamon Press. xiii, p. 174.
13. T. Tomita, S. Saito, M. Baba, M. Hundhausen, T. Suemoto and S. Nakashima, Phys. Rev. B 62 (19), p 12896-12901 (2000)
14. S. Rohmfeld, M. Hundhausen, L. Ley, Phys. Rev. B 58, p 9858-9862 (1998)
15. S. Nakashima, Y. Nakatake, Appl. Phys. Letters 77, p 3612-3614 (2000)
16. S. Nakashima, H. Harima, T. Tomita, T. Suemoto, Phys. Rev. B 62, p 16605-16611 (2000)
17. E. Martin, J. Jimenez and M. Chafai, Solid State Electron. 42, p 2309-2314 (1998)

18. Elizabeth M. Slayter and Henry S. Slayter, "Chapter 14: The conventional transmission electron microscope", Light and Electron Microscope, Cambridge University Press, United Kingdom (1992)
19. David B. Williams and Barry C. Carter, "Transmission electron microscopy: A textbook for material science", 2nd edition, Springer, (2009)
20. J. Leininger, G. D. U'Ren, C. D. Moore, R. Shandhu, M. S. Goorsky, J. Phys. D: Appl. Phys. 32, p A8-A11 (1998)

Part II: Experimental Results

Chapter V: Development of Large Tapered Crystal Growth Technique

V.1 Overview

The performance of commercially available silicon carbide (SiC) power devices is limited due to inherently high density of screw dislocations (SD), which are necessary for maintaining polytype during boule growth and commercially viable growth rates. Attempts at growing single crystals with low density of screw dislocations, such as the PVT repeated a-face (RAF) growth process, have been reported [1, 2]. They are involving and the crystals grown contained a relatively high dislocation density and SFs [1]. The NASA Glenn Research Center (GRC) has recently proposed a new bulk growth process based on axial fiber growth (parallel to the c-axis) followed by lateral expansion (perpendicular to the c-axis) for producing multi-faceted a/ m-plane SiC boules that can potentially produce wafers with as few as one SD per wafer [3]. The implementation of this novel growth technique is a two-staged process. First, the growth of long, high quality single crystal SiC seed fiber must be achieved in a direction parallel to the c-axis of hexagonal polytypes, followed by the lateral homoepitaxial growth expansion of the seed fiber without introducing a significant number of additional defects. This chapter can be divided into two parts: growth of long seed fiber by solvent-laser heated floating zone (solvent-LHFZ) and lateral homoepitaxial expansion by horizontal hot wall chemical vapor deposition (HWCVD). In the first part, detail insight about the growth of the seed fiber is presented along with results of the characterization of the grown fiber. In the second part, results of the growth by lateral expansion in HWCVD are presented. Further, results of characterization of the boules grown by lateral expansion are discussed in light of its feasibility.

V.2 Motivation

Despite silicon carbide's (SiC) promise over silicon for the design of next-generation semiconductor and opto-electronic devices, broad adoption of this potentially performant compound material is limited by the substrate cost compounded with the presence of a relative high density of harmful structural defects such as micropipes (μPs), threading screw dislocations (TSDs), basal plane dislocations (BPDs), etc. For instance, micropipes were associated with failure microplasma, which cause premature electrical failure in SiC devices larger than 1 x 1mm^2 [4]. In a similar manner, albeit not with the same magnitude as micropipes, threading screw dislocations were found to reduce the reverse-bias current-voltage characteristic of 4H-SiC

p+n diodes by 5% to 35% [5]. Furthermore, basal plane dislocations have been proved harmful in SiC pin diode; where under the mechanism of recombination enhanced-dislocation glide (REDG) resulting from an electron-hole recombination, they expand into triangular stacking faults in the device active layer and cause a drop in the forward voltage [6]. While the presence of these types of defects in SiC forecast a grim outlook on the short-term realization of SiC semiconductor and opto-electronic devices, their eradication or mitigation is compromised by the technique currently in force to grow bulk silicon carbide.

Because SiC sublimes before melting, growth of SiC is achieved using vapor-based techniques. The current industrial standard for growing bulk SiC is the *physical vapor transport* (PVT) in which silicon (Si) and carbon (C) source materials are evaporated onto a seed crystal under a high vertical thermal gradient (>2000 ˚C) to produce a SiC single crystal boule. The issue with this technique is two-fold. First, its reliance on elementary screw dislocations in the seed crystal ($>10^2$ cm^{-2}) to provide surface steps for polytype control and achieving commercially viable growth rate along [0001] direction makes it fundamentally flawed. For instance, elementary screw dislocations, which have a Burgers vector of 1c, are constrained to propagate along the [0001] growth direction. This results in grown boule having at least the same density of elementary screw dislocations as the seed. E. K. Sanchez and coworkers observed an increase in the density of these elementary screw dislocations from 20 cm^{-2} to 4 x 10^3 cm^{-2} for growth rate increasing from 0.02 to 1.5 mm/h [7].

The second issue is related to the high thermal gradient, which generates a high thermal stress in both radial and axial direction during growth. Since thermal gradient is designed to promote mass transport from the source material to the seed crystal, it follows that the temperature of the growing surface is higher than the seed crystal. Furthermore, the temperature at the boule periphery is higher than in the center because of radiation from the crucible wall. As a result of these axial and radial temperature gradients, the growing boule undergoes inhomogeneous thermal expansion, which cause bending of the basal planes and favors dislocation nucleation. These nucleated dislocations, referred to as grow-in dislocations, form during growth and occur when the thermal stress produces a resolved shear stress that exceeds a critical value σ_{rss}; the value of which is given by equation 1 [8].

$$\sigma_{rss} = (\sigma_{rr} + \sigma_{rz}) \cos\phi - \sigma_{\phi\phi} \sin\phi \qquad (1)$$

In addition to the critical resolved stress, which induces nucleation of basal plane dislocations, a critical normal stress σ_{ns} must be considered. This normal stress has been associated with the nucleation of prismatic dislocations (Fig. 5.1). While both stresses are known to vary with temperature, the shear stress associated with the nucleation of basal plane dislocations is the smaller. A graph showing the variation of critical resolved shear stress with temperature for the 6H-SiC polytype is shown in Figure 5.2. It follows from this graph that the generation of BPDs always occurs during PVT growth of SiC. These BPDs can coalesce to form slip bands during post-growth cooling [9] or dislocation walls along the <1-100> directions near the periphery as seen on SiC wafer [9,10].

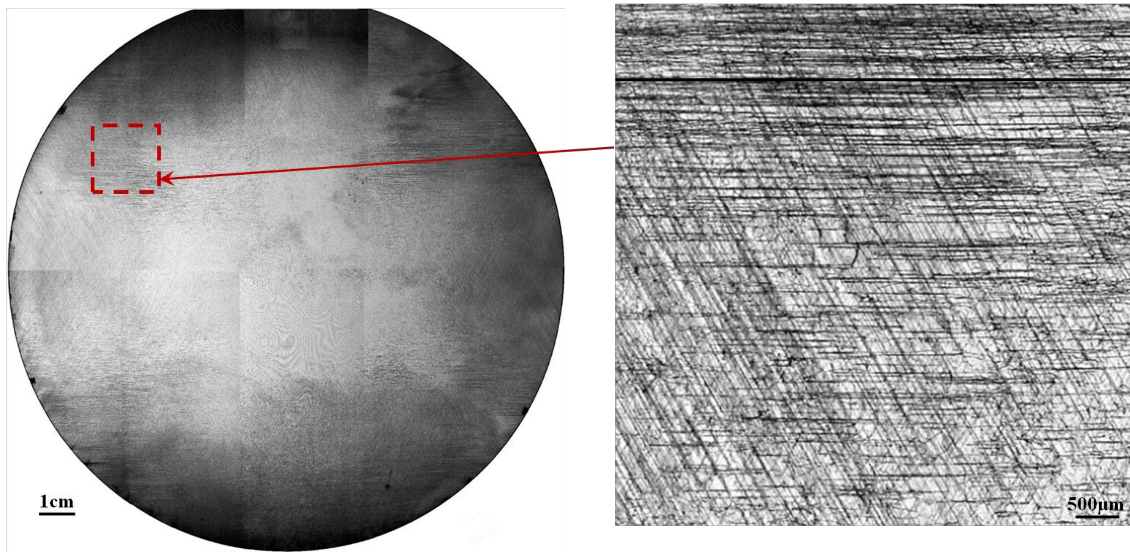

Figure 5.1. Synchrotron white beam X-ray transmission topograph of 4H-SiC substrate showing prismatic dislocations

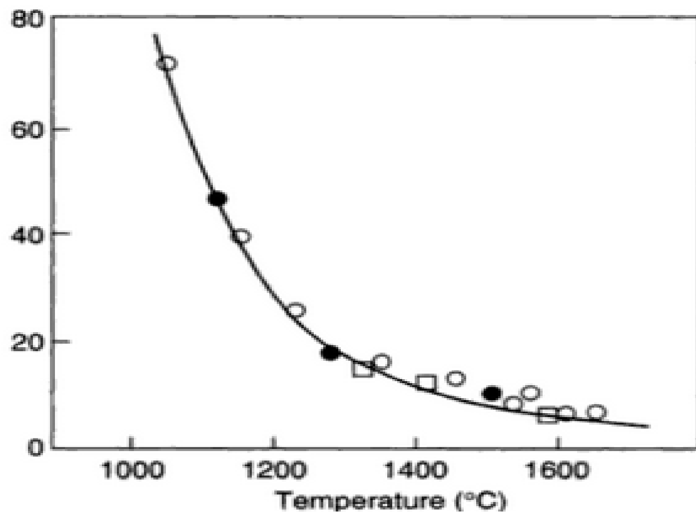

Figure 5.2. Temperature dependence of critical resolved shear stress for 6H-SiC [8]

Despite progresses made to improve the PVT method by lowering the growth temperature, controlling the temperature gradient and using off-oriented seed crystals, achieving a reduction in the density of structural defects and thus producing boules with a quality up-to par with silicon is hypothetically farfetched. Furthermore, the Repeat-A-Face (RAF) method proposed by D. Nakamura et al. although resulting in higher crystal quality is involving and results in the generation of undesirable defects such as stacking faults [1, 11]. In light of these fundamental issues associated with the PVT method, the known impact of structural defects [4-6] as well as the short-coming of currently proposed methods [1, 2, 11, 12] to grow high quality and cost effective SiC single crystal boules, an alternative growth method is much needed. In this study, the development of a novel growth technique, called Large Tapered Crystal (LTC) growth is proposed. This technique, developed by a research group at NASA Glenn Research Center (GRC), can potentially produce large, low-defect-density single crystal SiC boules [3]. In addition to the growth of SiC, this new technique can be employed to grow wide bandgap semiconductor materials such as aluminum nitride (AlN) and gallium nitride (GaN).

In order for this bulk SiC growth method, called Large Tapered Crystal (LTC) growth, to become a reality, growth of both long single crystal SiC fibers and lateral growth of the fiber by CVD must be achieved. To that end, two parallel tracks are developed. The first track involves the growth of a long single crystal SiC fiber in a direction parallel to the c-axis of hexagonal polytypes. The second track relies on chemical vapor deposition to laterally expand the SiC fiber. The aim of this study is to investigate the feasibility of LTC for growing large size and high quality single crystal SiC; determine how growth temperature, source material composition, and growth process affect growth rate and mode (crystallinity) and generation/propagation of structural defects (polytype, stacking faults, etc.). Successful implementation of each of these tracks will help consolidate the LTC growth into a single integrated technique, and spur its broad scale integration at the industry level.

V.3 Brief description of LTC technique

Conceptually, the LTC technique is based on the growth of an axial fiber (parallel to the c-axis) by solvent-laser heated floating zone (Solvent-LHFZ) followed by lateral expansion (perpendicular to the c-axis) by hot wall chemical vapor deposition (HWCVD). The growth parallel to the c-axis is carried out on a small area seed fiber (~1mm) that contains a single screw dislocation. The lateral expansion is carried out on a-faces (i.e. perpendicular to the c-axis) to

form large-diameter crystal that can be cut into SiC wafers of far superior quality (>100-fold dislocation reduction) than conventional SiC wafer growth approach. Note that the 100-fold dislocation reduction is a direct consequence of growth along a-direction; where dislocation dynamic is not the same as for the case of growth along the c-axis. For instance, screw dislocations with a *1c* Burgers vector propagate only along the c-axis as opposed to any direction perpendicular to the c-axis.

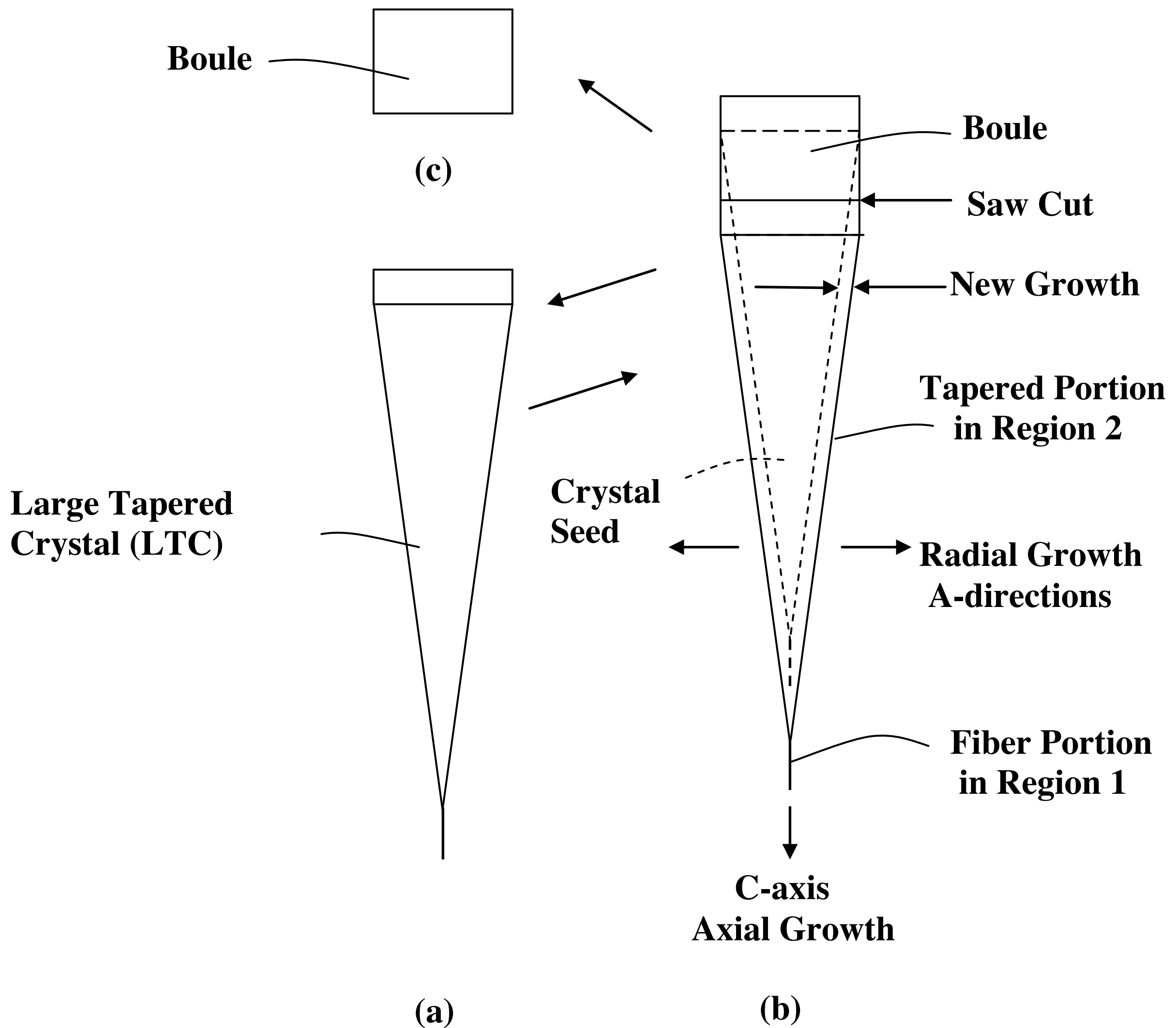

Figure 5.3. Schematic description of Large Tapered Crystal Growth (LTC) Process

The experimental set up of the LTC process consists of two growth regions (regions 1 and 2) as illustrated in Figure 5.3a. A portion of the tapered seed fiber, with its central axis parallel to the c-axis, lies in region 1 (Figure 5.3b), while the other larger portion lies in region 2. Longitudinal growth along the c-axis takes place in region 1 on the smaller diameter tip with no

variation in diameter. Radial enlargement, i.e. lateral expansion along a-directions, occurs in region 2 and can reach dimensions greater than 100 mm for instance. As growth proceeds, the crystal is physically moved upward so that the small-diameter tip is maintained at the same position inside region 1. Since screw dislocations are not required for growth perpendicular to the c-axis, the resulting crystal will ideally contain a single screw dislocation along its central axis. In consequence, the vast majority of the crystal boule, except for the small volume of the central seed fiber, will be defect-free. Furthermore, the small seed fiber will provide the polytype sequence for the radially growing crystal in region 2. It should be noted that the longitudinal growth rate parallel to the c-axis is much greater (~1 mm/hour) than the radial growth rate because of the large area of the tapered side of the LTC seed fiber.

At the end of each growth cycle, the boule (Fig. 5.3c) will be cut (saw cut in Fig. 5.3b) from the whole crystal, and the remainder of the LTC crystal will be used as a seed crystal in a subsequent growth cycle. Note that in a subsequent growth cycle, the large end (the boule end) of the LTC will immediately begin growing in the c-axis direction at the same growth rate as the rapid growth of the LTC fiber end. Ideally, a completed boule will contain only a single screw dislocation along the central axis of the boule. Additional advantages of the LTC process are that boules can be grown at high growth rates and the process can easily be scaled up to larger diameter boules, resulting in increased wafer size and reduced wafer cost. Also, the process should be capable of boules of greater length than is possible with current SiC growth techniques.

V.4 Solvent-Laser heated floating zone (Solvent-LHFZ)

Solvent-laser heated floating zone (Solvent-LHFZ) method embodies two well established growth techniques: Laser Heated Floating Zone (proven for oxide-based crystals) [13] and Traveling Solvent Method (demonstrated for SiC) [14]. In the laser heated floating zone (LFHZ), a laser heats a feed rod (source material) placed below a seed crystal. Once a melt is obtained, the seed crystal is brought in contact with the melt, and then slowly pulled upward as growth proceeds, keeping the growth front at constant position in the heated zone. Next, the feed rod is moved upward as the growing crystal consumes it to sustain further crystal growth. Figure 5.4 shows an illustration of the LHFZ method. In order to ensure a congruent melt of SiC and facilitate fiber growth, a solvent that can dissolve both silicon (Si) and carbon (C) species and transport them to the growing surface without significant solvent incorporation into the crystal is

used; hence the name solvent-laser heated floating zone. The melting and wetting processes are critical to the success of the experiments; if the feed rod fails to melt into a stable liquid, or wet the seed crystal, then no crystal growth can occur.

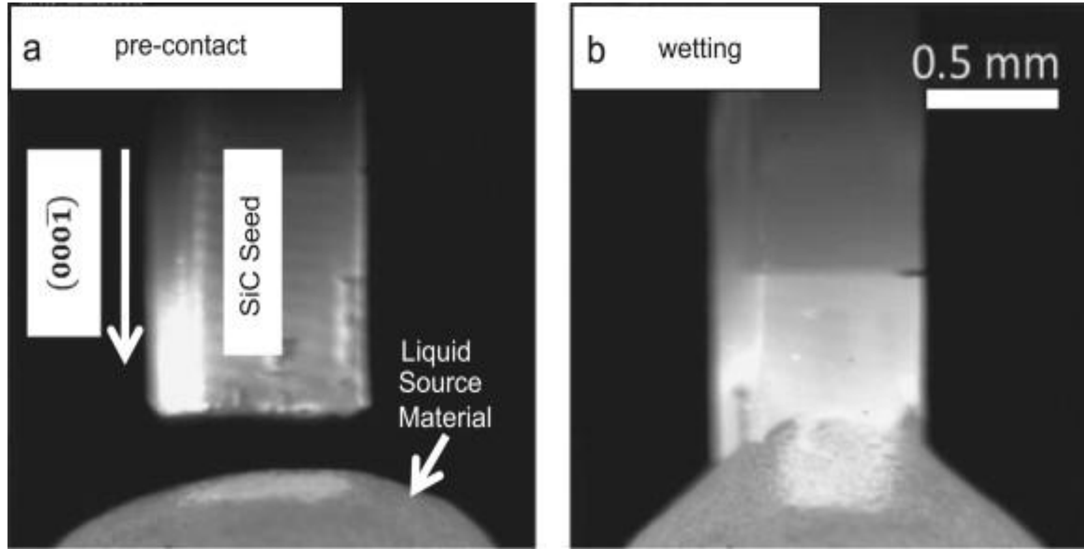

Figure 5.4. Long range optical images of melted source material seed crystal: (a) before wetting and (b) after wetting [15].

V.4.1 Experiment

The growth of long single crystal SiC fibers was carried out in a custom vacuum system (Figure 5.5) at 15 slm flow of argon at 115 Torr and using a carbon dioxide (CO_2) laser (10.6 μm) as heat source. A 0.5 x 0.5 x 15 mm^3 SiC seed crystal (long axis parallel to <0001>) diced from commercially purchased a-face or an m-face 4H-SiC wafer was mounted at the center of the growth chamber. The growth surface varied from roughly on axis to about 10° from (000-1). The seed crystal was mounted so that its carbon (000-1) face was placed directly above a vertically positioned 2mm diameter feed rod (source material for crystal growth). The feed rod was formed by pressing powder of iron (Fe), C/graphite and Si by cold isostatic press followed with sintering into hydrogen (H_2) environment at 1150 °C to increase density of the rod and give it structural strength. No visible sign of melting or dissociation was observed following sintering. Table 5.1 shows density of feed rod after sintering as per Archimedes' principal.

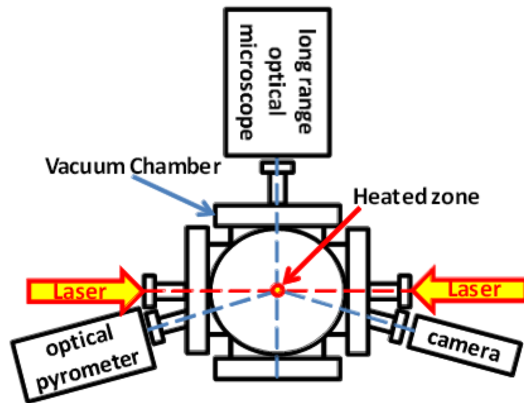

Figure 5.5. Top-down view of solvent-LHFZ system schematic [16]

Fe/Si (atomic ratio)	C (%)	Density (g/cm^3)	
		Un-sintered	Sintered
High-Si (Fe/Si ~ 0.35)	8	3.10	4.33
	16	2.48	3.93
High-Fe (Fe/Si~ 1.9)	8	4.78	6.23

Table 5.1. Un-sintered and sintered feed rod densities as determined by Archimedes' principal

In order to ensure uniform heating on each side of the feed rod, the laser source was split into two beams and passed through ports 180 °C apart. The two beams were focused into oval shape with an aspect ratio between long and short axis of 2:1, where the short axis is vertical and made parallel to the feed rod. The beams created a heated zone of about 2mm x 4mm in the center of the growth chamber. The temperature was measured using a single color optical pyrometer with spot size of 2mm at the heat zone. Due to the small size of the seed crystal (comparable to the spot size of the optical pyrometer) with the changing emissivity of SiC and averaging nature of the pyrometer, accurate recording of the absolute growth temperature could not be obtained. Thus, to obtain the growth temperature (T_g), we subtracted the temperature at which the feed rod melts (T_m) from the observed temperature (T_o). During growth run, the feed rod and seed crystal were not rotated.

Because of the wealth of work documenting its ability to dissolve C and Si, Fe was used as solvent [17, 18]. The composition of the source material was obtained from Fe-Si-C phase diagram [18]. Effect of Fe content on growth was investigated for Fe/Si ~1.9 and Fe/Si~0.35 at C=8%. Additionally, a third composition (C=16% for Fe/Si~0.35) was investigated to study the

effect of carbon concentration. Details regarding seed crystal, feed rod, and post experimental crystal processing can be found elsewhere [15, 16, 19]. Prior to characterization of grown SiC fiber, a 4 hours HF: HNO_3: HCl (1:1:2) bath was used to remove excess growth material that did not incorporate into the crystal.

Characterization of the grown crystals and their growth fronts were carried out by depth profile, cross sectional analysis and X-ray techniques. Secondary ion mass spectroscopy (SIMS) was performed on the C-face (000-1) face of several samples with an analysis area of ~ 175 µm x 175 µm in order to create depth profiles of the metal solvents incorporated into the grown crystals. Focused ion beam (FIB) milling and mechanical polishing were used to make cross sections of the crystals, which were then examined by scanning electron microscopy (SEM) and energy dispersive spectroscopy (EDS), and orientation and structural characterization studies were carried out by X-ray transmission Laue diffraction and white beam X-ray topography at the Stony Brook Synchrotron Topography Station, Beamline X19C at the National Synchrotron Light Source, Brookhaven National Laboratory.

V.4.2 Results and discussions

For the SiC fiber grown with Fe/Si~ 1.9 and 8% carbon concentration, no crystal growth occurred due either to lack of stable melt or dissolution of the seed crystal upon contact of the melt. For the SiC fiber grown with Fe/Si ~ 0.35, a stable melt was formed at 1170°C and 1195°C respectively for 8% and 16% carbon concentration. Two observations were made of the effect of temperature and carbon concentration on growth rate. On one hand, growth rate was observed to increase with temperature, while it increases with increased carbon concentration at a given temperature. These results indicate the critical role of temperature and the amount of carbon on growth in a manner similar to the case of liquid phase growth of SiC where carbon is supplied by a graphite crucible. For both low and high carbon concentration, a stable melt was formed at T_m+190°C. At Tm+325°C, only feed rod with low carbon concentration produces a stable melt and sufficiently wet the SiC seed crystal to favor the experiment. However, for high carbon concentration, feed rod behaves uncontrollably with simultaneous etching and crystal growth. The growth rate for different temperature and source material composition are summarized in Table 5.2.

			Growth rate (µm /hr)		
Fe/Si (atomic ratio)	C(%)	T_m (°C)	T_m + 90°C	T_m + 190°C	T_m + 325°C
High-Si (Fe/Si ~ 0.35)	8	1170	~4	~40	~135
	16	1195	~50	~120	NA
High-Fe (Fe/Si~1.9)	8	NA	No Growth		

Table 5.2. Summary of growth rate for different temperature and source material composition

❖ **Synchrotron white beam transmission topography (SWBXRT)**

X-ray transmission Laue diffraction pattern (Figure 5.6 (a)) recorded using synchrotron white beam on selected grown crystals matches exactly with (1-100)-oriented 4H-SiC X-ray transmission Laue diffraction pattern (Figure 5.6(b)) simulated using the LauePt software [20]. The grown crystal was single crystal, retaining both the orientation and polytype of the seed crystal. SWBXRT (Figure 5.6(c)) from the grown crystals revealed a highly distorted SiC fiber due to significant inhomogeneous strain.

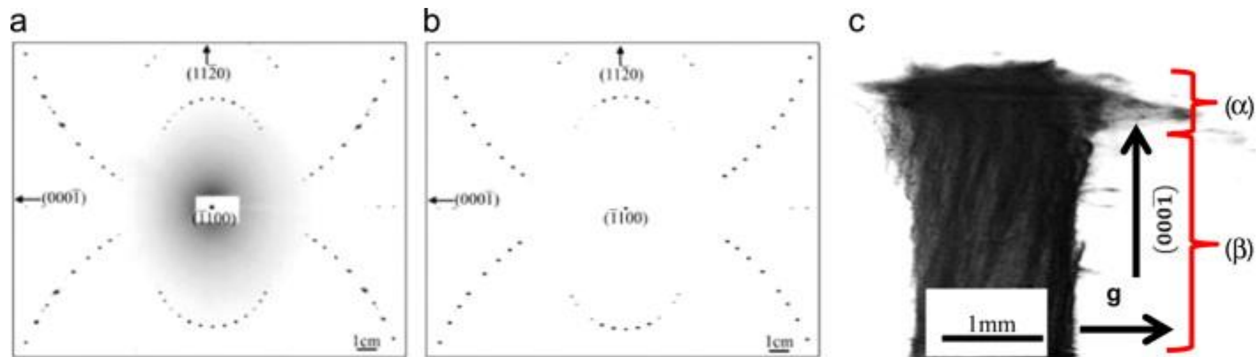

Figure 5.6. X-ray transmission Laue diffraction pattern (a) recorded form the LHFZ portion of fiber sample (b) simulated Laue diffraction pattern and (c) SWBXT transmission topography

❖ **Scanning electron microscopy (SEM)**

SEM characterization of the grown crystals reveals two different morphologies of the growth front, a platelet-like morphology (observed on ~75% growth fronts examined) and a step flow like growth front (observed on about 25% of the grown surfaces examined). It is important to note that the occurrence of either type of growth front did not correspond to a specific growth condition, and in a couple of cases both morphologies were produced in different regions of the same single crystal surface. The platelet-like growth fronts exhibited hexagonal features, with

cantilevered overgrowth creating pocket/sinks formation. These platelets are indeed competing individual growth fronts whose pockets can potentially trap solvent, and contribute to the formation of defects as the SiC growth closes on the solvent-rich pockets (Figure 5.7c). Foreign material trapped in a SiC crystal has been previously shown as a defect creation mechanism, specifically micropipes in SiC crystals grown by physical vapor transport [15]. Since micropipes are super screw dislocations (Burgers vector>1), these inclusions could also create elementary screw dislocations capable of promoting *c*-axis growth. Therefore, the total growth sequence is a highly disorganized mixture of *c*-axis, lateral growth and defect formation, which may be limiting the overall growth rate of the crystal. Further, SEM-FIB cross-section of the growth fronts reveals many voids (Figure 5.7 (a)) and Fe rich pockets (confirmed with EDS, Figure 5.7(b)) sealed in the grown crystal layer to which the origin of the inhomogeneous strain observed in the SWBXT topograph could be attributed.

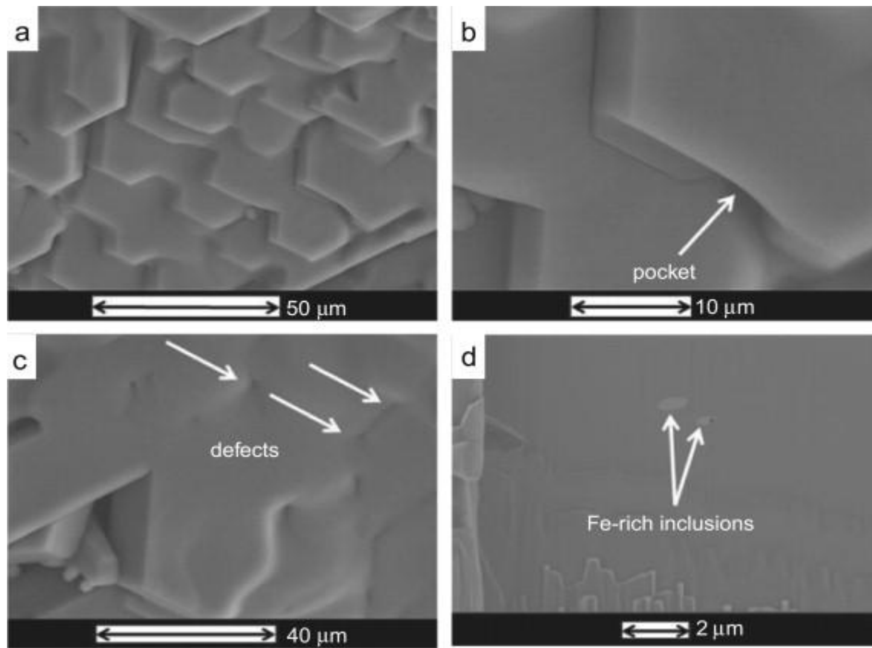

Figure 5.7. SEM images of a growth front of a solvent-LHFZ grown crystal (a) The hexagonal platelet growth fronts, (b) webbing between growth fronts, (c) defect creating pockets are completely webbed over and (d) a cross sectional area (created by FIB) showing Fe-rich inclusion

			Fe Concentration (atom/cm^3)	
Fe/Si (atomic ratio)	C(%)	T_m (°C)	T_m + 90°C	T_m + 190°C
High-Si (Fe/Si ~ 0.35)	8	1170	~10^{17}	~10^{17}
	16	1195	~10^{18}	~10^{18}
High-Fe (Fe/Si~1.9)	8	N/A	No Growth	

Table 5.3. Summary of results Tm = temperature at which feed rod forms a melt, at % = atomic. Temperatures are not corrected for emissivity. Approximate Fe concentrations in the SiC crystal layers are listed

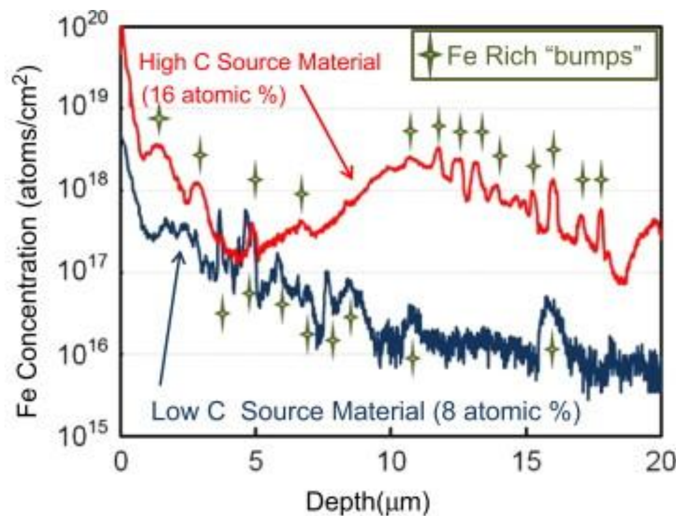

Figure 5.8. SIMS depth profile analysis of 4H-SiC layer grown using high C (at 16%) and low C (at 8%) source material grown at T_m+190°C for a 175 μm x 175 μm area taken in middle of C face

❖ **Secondary ion mass spectroscopy (SIMS)**

SIMS depth profile analysis carried out on a ~175 μm×175 μm area in the middle of the C face (000-1) of selected grown crystals (Figure 5.8) shows that the concentration of Fe in the grown crystals varies in three significant ways. First, "bumps" were observed in the SIMS profile as indicated by the arrows in Figure 5.8. These bumps are believed to arise from the Fe rich inclusions seen by FIB cross sectional analysis (Figure 5.7d). With an analysis area much larger than the inclusions, the "bump" width and magnitude is an average over the entire SIMS analysis area. This explains why the "bumps" visible by SIMS are also visible by SEM/energy dispersive spectrometry. The second variation indicates that for both high and low C concentration source materials the Fe concentration decreases more than an order of magnitude from the surface. It is possible that as growth proceeds, a change in melt composition occurs; thereby decreasing the Fe concentration. Parallely, for crystals grown with low C concentration source material, the Fe

concentration drops by two orders of magnitude in the first 0.25 μm. The reason for this large change is unknown, though it could be speculated it originates from artifact of the SIMS characterization process. The third variation, indicated in Table 5.3, reveals that Fe concentration increased by an order of magnitude in crystals grown with source material containing a higher C concentration compared to less C at either growth temperature. This result suggests that Fe incorporation into grown crystals exhibits the same correlation to C concentration in the source material independent of growth rate. Therefore C concentration in the source material seems to control the solubility of Fe solvent into the matrix of the grown crystal. Because of the complex nature of the growth front, the sensitivity of Fe concentration to growth temperature is difficult to determine. Additional work is required to understand these phenomena.

V.4.3 Summary

SiC single crystal fibers were grown by Solvent-LHFZ at growth rates of 4-135 μm/h. The factors influencing growth rate, Fe incorporation into the grown crystal, and the effects of C concentration in the initial feed rod on the growth process have been studied. A dependence of growth rate on carbon concentration in the initial feed rod and temperature was observed. The grown single crystal fibers were dominated by a significant amount of inhomogeneous strain due to competing growth fronts. Further, the optimum process window was determined to be between T_m and T_m+300°C at a carbon concentration of 8% and a high Si ratio (Fe/Si ~ 0.35).

V.5 Lateral Expansion by hot wall chemical vapor deposition (HWCVD)

In order to implement the LTC growth technique, the lateral homoepitaxial growth expansion of a SiC fiber without introducing a significant number of additional defects is critical. To that end, lateral expansion of small mixed polytypes 4H/6H-SiC and 6H-SiC slivers was realized by hot wall chemical vapor deposition (HWCVD). Small slivers cut from a-oriented (11-20) and m-oriented (1-100) SiC boule slices containing regions of 4H and 6H-SiC or just single polytype 6H-SiC were exposed to HWCVD conditions using standard silane/propane chemistry for a period of up to five (fiber 1) and eight hours (fiber 2). The slivers exhibited approximately 1500 μm (1.5 mm) of total lateral expansion. Initial analysis by synchrotron white beam x-ray topography (SWBXT) confirms that the lateral growth was homoepitaxial, matching the polytype of the respective underlying region of the seed sliver. Further, characterizations of axial and transverse cut from the as-grown crystal samples were carried out using a combination of

SWBXT, transmission electron microscopy (TEM) and micro-Raman spectroscopy to map defect types and distribution.

V.5.1 Experiment

Slivers (0.8 mm x 0.5 mm x 15 mm), diced from polished m-oriented (1-100) SiC boule slices obtained from a commercial source, were used as source of single crystal SiC fibers. The crystal orientation of the slivers, herein referred to as fiber, is shown in Figure 5.9. One m-oriented SiC boule slice contained a thick region of 6H-SiC and small 4H-SiC region; the other boule slice was single crystal 6H-SiC. Both contained numerous micropipes. Two growth schedules were carried out: five (fiber 1) and eight (fiber 2) hour long growth runs. Fiber 1 corresponded to a growth using the mixed polytype 4H/6H-SiC m-oriented SiC boule slice, while fiber 2 was from 6H-SiC polytype. The dicing resulted in a fiber with two polished m-plane faces and two saw cut a- plane faces.

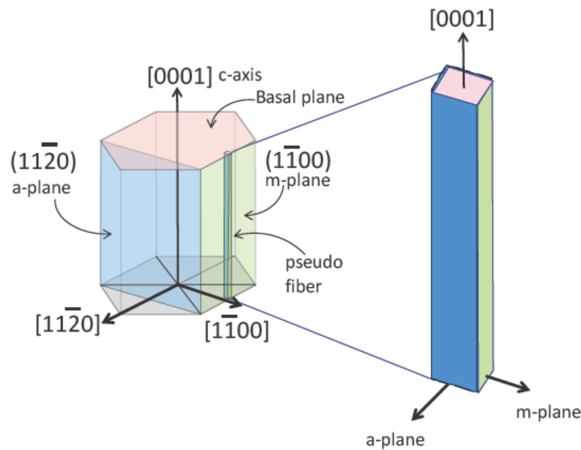

Figure 5.9. Schematic diagram showing the SiC unit cell with associated crystallographic planes and the orientation of the seed slivers (pseudo fibers) as cut from m-plane polished boule slices

Prior to growth, fibers were immersed in a 1:1 solution of H_2SO_4 and H_2O_2 for 15 minutes, blown dry with N_2, then immediately transferred to an argon filled glove box. All growth experiments proceeded within four hours of cleaning. Growth runs were accomplished in a custom designed, inductively heated, horizontal flow hot wall reactor. The tantalum carbide coated tubular susceptor has a 40mm inside diameter and a length of 140mm. A carbon foam insulation package was used to reduce heat loss and improve temperature uniformity. The fibers were supported in the reactor by an uncoated graphite carrier, which also facilitated in the loading and unloading of the fibers (Figure 5.10). Approximately, two millimeters of the fibers' overall length were used for mounting and do not participate in growth. With the exception of the mounted portion of the fiber, the rest of the fiber is uniformly exposed to growth conditions.

The carrier gas was hydrogen (H_2) with propane (C_3H_8) and silane (SiH_4), respectively as standard carbon and silicon precursors used for growth. HCl was added to the gas stream to improve pregrowth etching performance and reduce gas phase nucleation during growth. A twelve minute *in-situ* pregrowth etch was performed on the fibers before transitioning directly to growth. Aggressive etching conditions were employed to remove crystalline damage caused by the saw cutting operation. Growth parameters for both fibers are given in Table 5.4.

The morphology and crystalline quality of the as-grown crystals were investigated using scanning electron microscopy (SEM) and SWBXT. Then, the grown crystals were sectioned into axial [m-(1-100) and a-(11-20) plane] and transverse [c-(0001)] plane slices, and mechanically polished with diamond abrasive films. Overall defect microstructures of the axial and transverse slices were investigated using a combination of SWBXT, TEM and micro-Raman spectroscopy (μRS). First, SWBXT imaging in transmission geometry was carried out at the Stony Brook topography station, Beamline X19C, at the National Synchrotron Light Source (NSLS) at Brookhaven Nation Laboratory (BNL). The images were recorded on Agfa Structurix D3-SC films. Second, μRS was measured for a region across the seed crystal on selected samples. Results from SWBXT and μRS enabled identification of region of interest, from where TEM specimens were taken. The stacking sequence of these TEM specimens was investigated by way of high-resolution transmission electron microscopy (HRTEM) on a JEOL 2100F at the Center for Functional Nanomaterials (CFN at BNL with an accelerating voltage of 200keV. The TEM specimens were cut at the interface across the seed and the grown crystal using focus ion beam (FIB) along the [11-20] direction for both axial and transverse samples.

Growth	In-Situ HCL etch (min)	Etch Pressure (mbar)	Growth (min)	Growth Pressure (mbar)	Hydrogen (sccm)	Silane[1] (sccm)	Propane[1] (sccm)	HCL[1] (sccm)	Estimated Temperature[2] (°C)
Fiber 1	12	40	300	325	4260	0/4	1.5/1.5	15/20	1600
Fiber 2	12	40	480	325	4260	0/8	1.5/2.25	15/40	1590

1. First number is for etching conditions, second number for growth conditions
2. No direct observation of temperature by pyrometry was possible. An inferred temperature was calculated based upon the melting points of Si and Pd.

Table 5.4. Growth parameters for two separate growth runs. Fiber 1 was five hours in length. Fiber 2 was eight hours in length. Note that the intentional Si/C is 2.7 and 3.5 respectively. There is a substantial and unknown quantity of carbon contribution coming from the uncoated graphite sample carrier and carbon foam insulation

V.5.2 Results and discussions

V.5.2.1 Lateral growth expansion of 4H/6H-SiC m-plane pseudo fiber crystals

Since the fibers in both growth schedules were mounted approximately vertically in the growth chamber, all surfaces (excluding the 2mm portion used for mounting) were exposed to the growth conditions (Figure 5.10). The as-grown crystals from fibers 1 and 2 exhibited hexagonal crystal symmetry (Figure 5.11(a-b)) with the greatest lateral expansion in the <1-100> directions. Growth advanced on the a-plane side of the fiber, led by nucleation of the m and a-planes. A trough due to slow growth in the middle compared to the corner was observed along the a-plane side of the as-grown crystals. Like on the a-plane side, a very small depression was observed on the m-plane face. It is important to note that the growth rate behavior was different between both growth schedules.

For fiber 1, the overall growth rate is ~80 μm/hr in the<11-20> directions, and 60 μm/hr in the <1-100> directions. This is expected because the surface energy of the (11-20) is lower than that of (1-100). The fiber has increased in width by ~440 μm along the <11-20> direction. Unlike fiber 1, the overall growth rate in fiber 2 is ~180 μm/hr in the <1-100> directions, and 30 μm/hr in the <11-20> directions. The total lateral expansion was greatest along the <1-100> direction at about 1500 μm (1.5 mm) for fiber 2. This deviation from the well understood <11-20> direction of fast growth in hexagonal crystal structure finds its origin in the evolving crystal shape of fiber 2 type crystals (grown under conditions of high supersaturation). In fact, analysis of the shape of fiber 2 as-grown crystals indicates a highest nucleation probability at the edges/corners formed by intersecting m-planes (Figure 5.11b). The oddity of this observation has been reported by researchers at NASA GRC on growth behavior obtained on hexagonal shaped mesas whose sidewalls share the same crystallographic orientation as the sides of the fibers [21]. Additionally, 3C-SiC crystallites were observed on both fibers near the tip along with a large number of steps, particularly on the five hour growth fiber (fiber 1). This could be due to the imperfect nature of the starting sliver and carbon particulates from the uncoated graphite carrier. Takahashi et al. observed similar results for growth on (1-100) and (11-20) surface, and proposed a model for such behavior [10, 22, 23].

Figure 5.10. Post growth results for the eight hour growth showing three m-plane fibers mounted on top of an uncoated graphite carrier. Two other control fibers protrude from the front of the carrier. Yellow 3C-SiC decorates the surface of the as-grown crystals

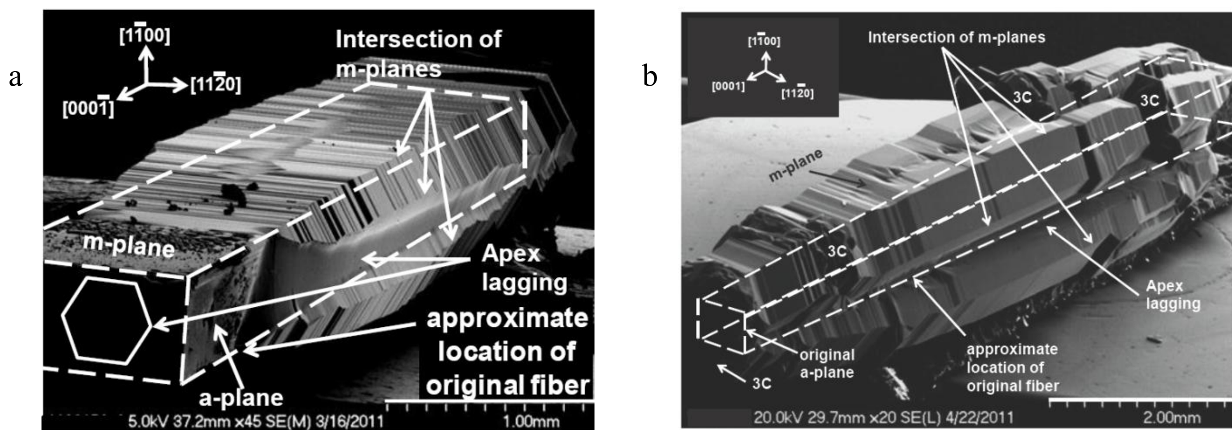

Figure 5.11. SEM of 4H/6H-SiC m-plane (fiber 1) after five hours of growth showing the hexagonal unit cell orientation on the end of the fiber (a), and 6H-SiC m-plane (fiber 2) after eight hours of growth showing some regions of 3C-SiC nucleated near either end of the fiber (b). Note the growth at the intersection of the m-planes dominates. The portion of fiber visible in the lower left of the SEM was used for mounting and exhibits almost no growth

Results from synchrotron white beam x-ray topography (SWBXT) confirm that in both fibers 1 and 2, the growth is homoepitaxial, matching the polytype of the respective underlying region of the fiber. Further, the facets are of high crystalline quality and are mostly free of strain (Figure 5.12).

Figure 5.12. SWBXT topograph of fiber 2 showing developing facets

V.5.2.2 Structural defect behavior in laterally grown 6H-SiC a/m-plane seed crystals by Hot wall CVD

- **Synchrotron white beam x-ray topography**

In order to study the behavior of structural defects, axial and transverse slices were cut from selected as-grown crystals. Preliminary SWBXT results from two axial-cut slices (samples 1 and 2) are shown in Figure 5.13. Other than the polishing marks and surface artifacts, the samples are characterized by linear defects propagating from the seed in the middle and running parallel to the basal planes. These are likely basal plane dislocations, but stacking faults (SFs) can also be expected to be present, which has been reported [24]. Examination of one of the transverse c-plane slices revealed a central seed region (Figure 5.14) characterized by high defect densities from which bundles of dislocations emanate along the m-axis directions. These dislocations appear to be mostly replicated from the seed although nucleation of new dislocations at the seed-epilayer interface cannot be ascertained due to the high dislocation densities involved. Any stacking disorders present in the seed will also likely be replicated into the epilayer, albeit at a possibly lower density. Analysis of these dislocation bundles by g.b = 0 and g.b X l = 0 criteria (where **g** is the reflection vector and **b** is the Burgers vector) reveals these are edge-type 1/3<11-20> dislocations.

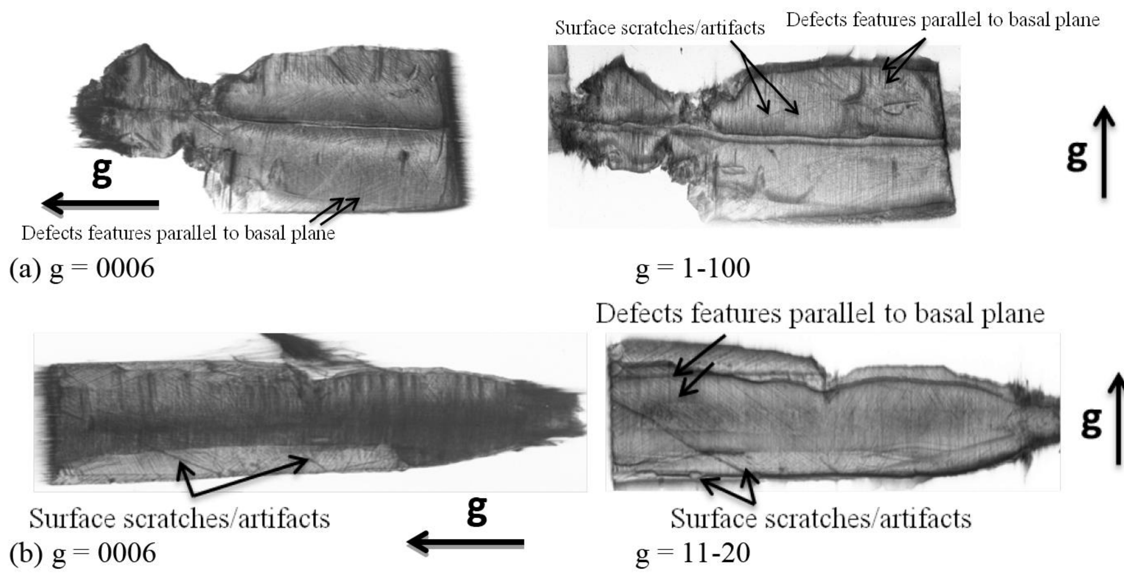

Figure 5.13. SWBXT transmission topograph of (a) a-plane cut (sample 1) and (b) m-plane axial cut (sample 2) from as-grown crystals

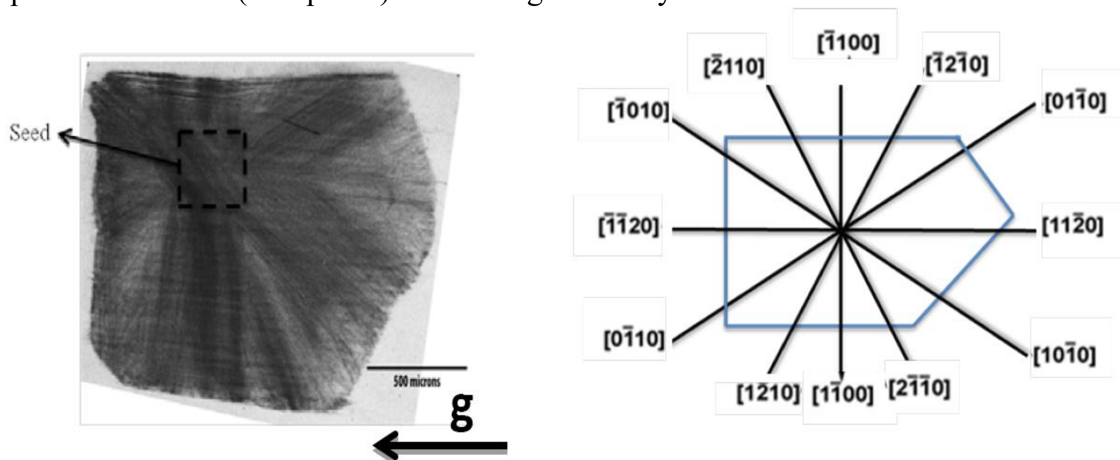

Figure 5.14. SWBXT transmission topograph of a transverse (0001) slice along with sketch showing crystallographic directions. Note the bundles of dislocations running along the <1-100> directions

Since the dislocation bands (in the transverse slice, referred to as sample 3) emanate from the seed region of the crystal, Raman map of a region encompassing the seed crystal and epilayer was recorded (Figure 5.14). Additionally, Raman spectra for selected regions as indicated on the schematic of sample 3 were recorded (Figure 5.15). The Raman studies were conducted to evaluate the quality (i.e. presence of stacking disorder or polytype) of the seed as well as the epilayer.

❖ **Micro-Raman spectroscopy (µRS)**

Raman intensity profile and frequency shift of SiC polytypes have well been documented [25-27]. Furthermore, studies have been carried out, which harness the nondestructive character of Raman scattering to study polytypism and stacking disorder in SiC [25, 26]. Analysis of the relative intensity for the folded transverse acoustic (FTA) and folded transverse optic (FTO) phonon modes on the Raman spectra recorded from region 2 to 6 in Figure 5.15 indicates the presence of foreign polytypes in the 6H-SiC matrix. These polytypes are 3C, 4H and 15R-SiC as evidenced by Raman peaks at 800 cm^{-1}, 205 cm^{-1} and 571 cm^{-1}. For the Raman spectra recorded inside the seed at region 1 in Figure 5.16, the non-uniform peak broadening in the lower frequency shift region is indicative of a high stacking disorder. The origin of this stacking disorder is the result of the inhomogeneity of the seed and could be due to the presence of short-range order of different SiC polytypes.

Stacking disorder in the seed is further confirmed by Raman mapping shown in Figure 5.15. Raman mapping is an effective imaging technique to survey changes in the microstructure of silicon carbide such as polytype and stress/strain distribution. The Raman map is obtain from the recording of individual spectrum in a raster scan over a desired area, followed by the combining of these spectra into color coded images that are based on the material composition, crystallinity, phase and stress/strain. In our studies, the Raman map was obtained from the integration of the peak intensity ratio of the FTO (0) mode at 797 cm^{-1} associated with the presence of 3C-SiC polytype. The different colors observed in this figure indicate a variation in the intensity of this peak from one micro-region to another. In the seed, the intensity of the FTO (0) is non-uniform and stronger. This non-uniformity of the intensity in the seed is most likely due to stacking disorder. While outside of the seed region, the intensity is lower and uniform. It should be noted that variation in the intensity of a peak indicates a change in the concentration of the element or phase corresponding to the say peak. Hence, low intensity amounts to low concentration, and the concentration of 3C polytype in the epilayer is lowest. This is in agreement with spectra recorded in regions 2 to 6 (Figure 5.15). Presence of other polytypes can be revealed from the map by investigating the spectrum associated with a given color or at a given position within a given color.

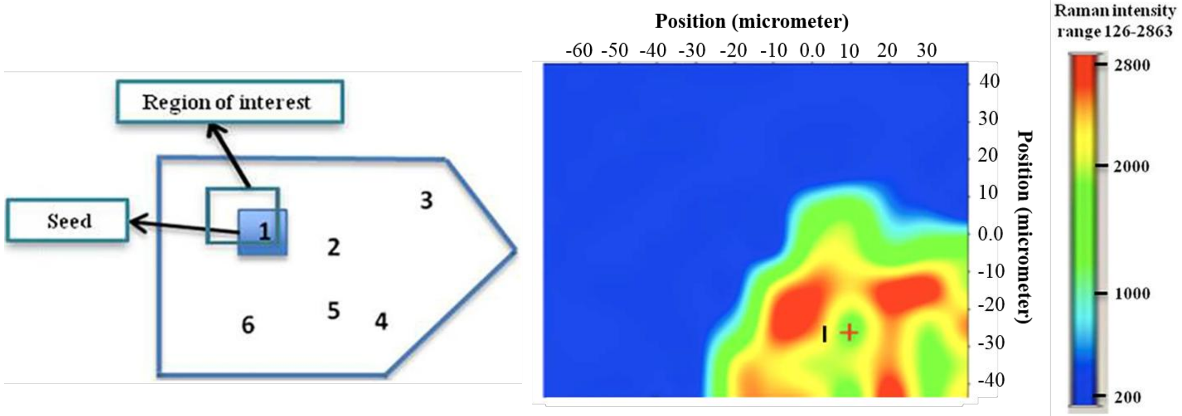

Figure 5.15. Schematic of transverse slice showing region of interest, seed and regions 1 through 6 (left), Raman map of region of interest along with color scale (right)

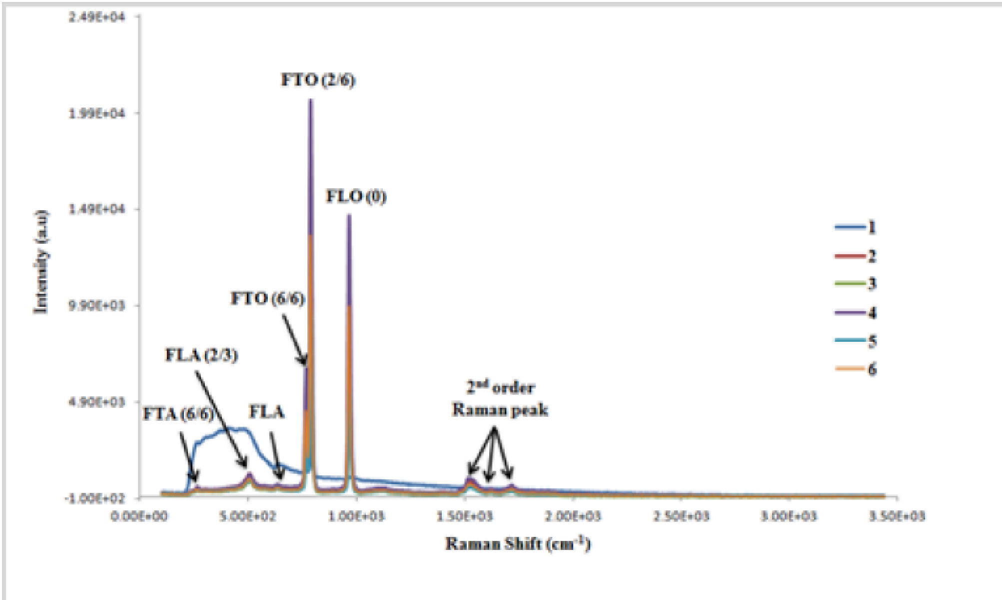

Figure 5.16. Raman spectra for regions marked 1 through 6 as shown in schematic of transverse slice above

Another transverse slice taken from an m-plane boule (called sample 4) was mapped using Raman scattering. Figure 5.17 shows optical micrographs of sample 4 and mapped region, respectively. Preliminary results indicate the presence of 3C, 4H and 15R-SiC polytypes in the mainly 6H-SiC matrix. This is evidenced by presence of Raman bands at 800cm^{-1}, 205cm^{-1} and 571cm^{-1} corresponding to 3C, 4H and 15R-SiC respectively, and on spectra recorded at different location of the sample (Figures 5.18). It is important to note that the observed Raman frequencies in our experiment are slightly larger than frequencies published for these polytypes [28],

indicating the contribution of strain. It has been reported that strain in a material can cause the Raman frequency of a vibration mode to shift either to the left or the right depending on the nature of the strain, i.e. compressive or tensile. The origin of the strain can be attributed to doping as reported by Xiang Biao Li et al. [29]. They indicated a shift toward higher frequency on the Raman spectra of 6H-SiC subjected to increasing doping concentration of aluminum (Al) and nitrogen (N_2). Similarly, the wavelength of the laser power source has been reported to affect the position and shape of Raman bands [30, 31]. The Raman map (Figure 5.18) shows red and turquoise spots in the seed that are also scattered in the matrix. These spots are foreign phases that indicate the inhomogeneity of the sample.

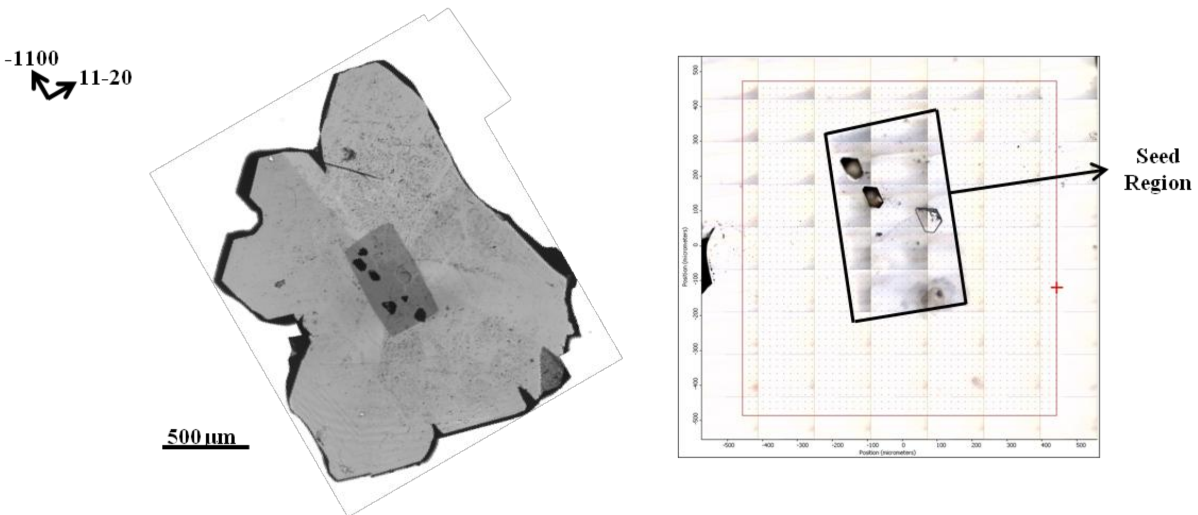

Figure 5.17. Optical micrograph of sample 4 (left), and Raman mapped region (right)

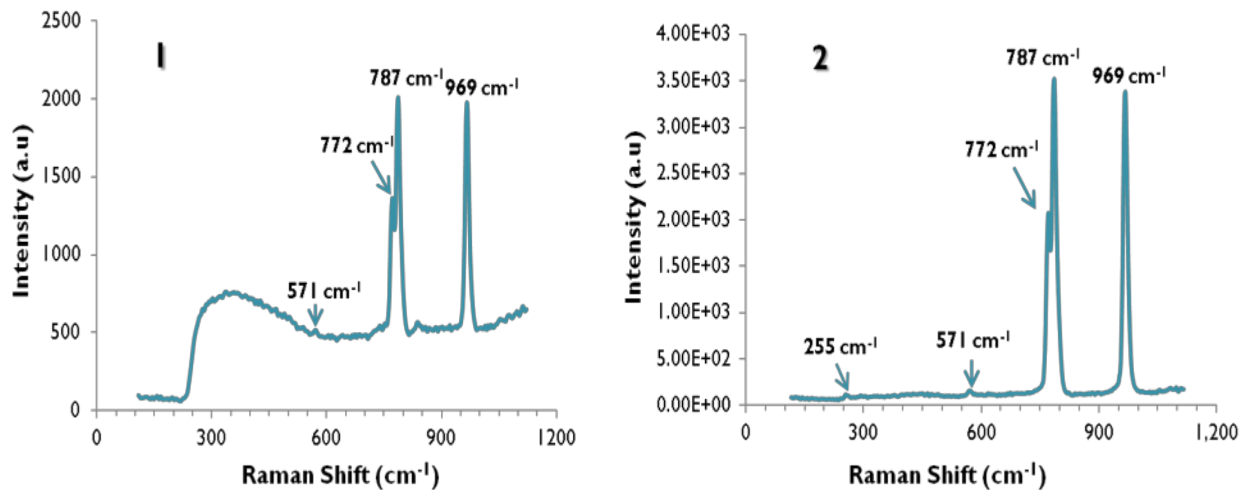

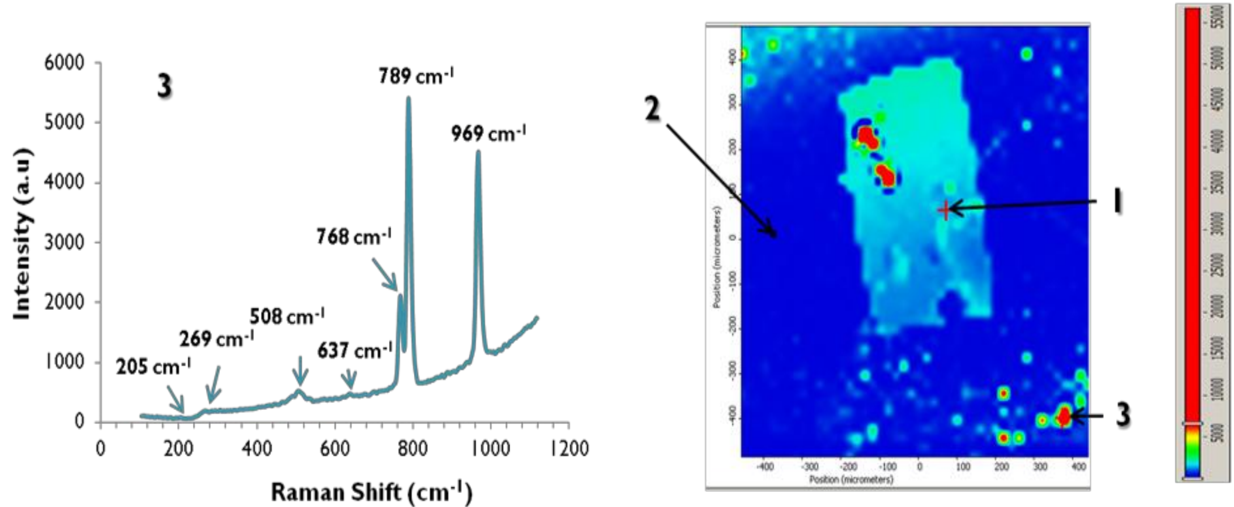

Figure 5.18. Raman map of selected region on sample 4 and spectra at x=84.4µm (1), x=-375.1 µm (2) and x=372.1 µm (3)

To complement the SWBXT and Raman results, TEM specimens were prepared by focused ion beam (FIB) parallel to the [11-20] direction for both axial and transverse samples.

❖ **High-resolution Transmission electron microscopy (HRTEM)**

Figure 5.19 is a high-resolution TEM image of a specimen taken from sample 2. Presence of large area 3C inclusions disrupted by stacking faults (SFs) and 8H-SiC polytypes were observed. The stacking faults are seen as resulting from the glide of SiC bilayers in the basal plane in a direction opposite that of the 3C normal gliding sequence. It is observed that these SFs are the premises to polytype phase transformation during growth, and could be replicated from the seed or formed during growth.

Another axial slice taken from an m-plane boule (sample 5) was investigated using TEM. Analysis of several bright field micrographs taken with g vector (0006) from the sample reveals the presence of dislocations, SFs and an inclusion-like feature (Figures 5.19). In the middle image (Figure 5.20), two types of stacking faults were observed; one that forms inside the epilayer (SF_1) and another that extends across the seed interface (SF_2). It is suspected that the dislocations seen on the left micrograph were introduced during sample preparation by focus ion beam. The extent of FIB induced damage of copper has been studied and associated with the kinetic energy of the ion beam and incidence angle [32]. Jeanne Ayache et al. in their book Sample preparation handbook for transmission electron microscopy [33] reported that FIB can generate dislocations during sample preparation. Further, M. Andrzejczuk et al. confirmed the

formation of FIB induced parallel dislocations with edge character near the surface of austenite thin foils [34].

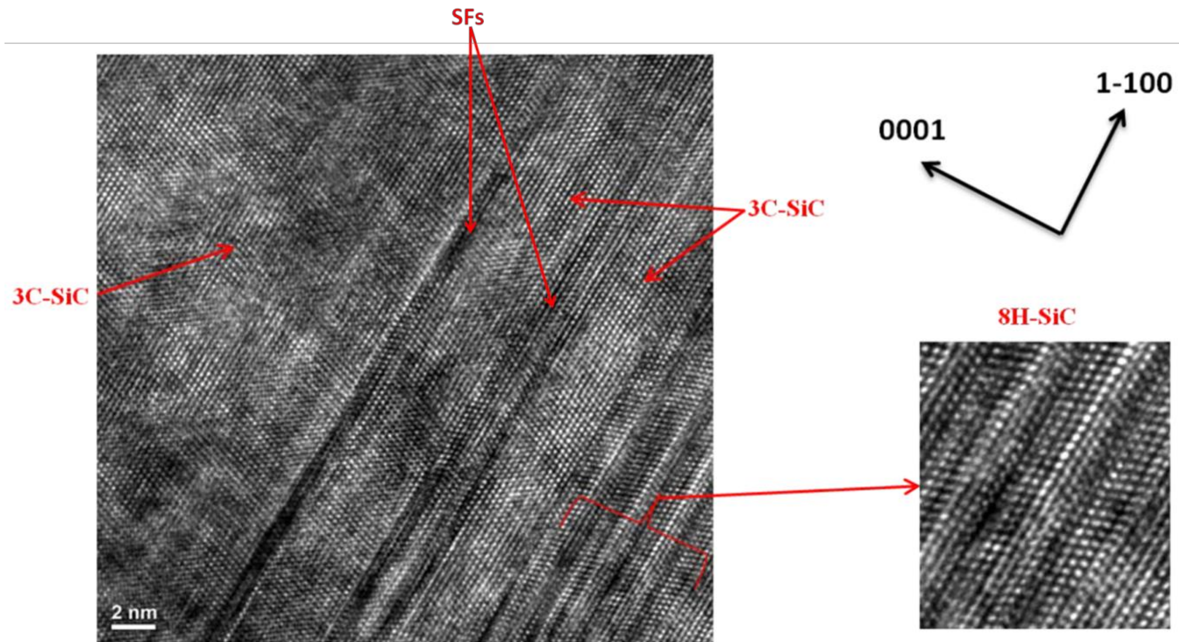

Figure 5.19. HRTEM image of 6H-SiC axial slice (sample 2) showing 3C and 8H-SiC polytype

Based on the bright field images, high resolution TEM of SF_1 (oval circle in figure 5.20) and SF_2 were recorded to determine their stacking sequence. Figure 5.21 shows the stacking sequence of SF_2. The formation mechanism of stacking faults (both SF_1, SF_2 and those not shown here) is discussed. The HRTEM shows lattice plane distortion and high disordering in the stacking sequences of the 6H-SiC matrix. The origin of the lattice distortions could be attributed to two causes. First, the different attachment mechanism of atoms on each facet within the same interface as growth proceeds on many facets during lateral homo-epitaxial expansion can result in the misalignment of stacking sequences leading to lattice distortion [35, 36]. Tsuchida et al proposed that misalignment of stacking sequences arises when step spirals associated with threading screw dislocations (TSDs) meet vicinal steps during homoepitaxial growth [37]. Given that TSDs have a burgers vector and propagate along the c-axis of SiC hexagonal polytypes, and that lateral expansion proceeded in directions perpendicular to this c-axis, the model proposed by Tsuchida cannot be used to explain the observed lattice distortions.

The other cause for the lattice distortion could be attributed to the propagation of isolated partial dislocations (PDs) during growth of the 6H matrix as observed in Figure 5.21. Those PDs

modify the stacking sequence of the 6H matrix, and result in the formation of high density of stacking faults (SFs). These stacking faults appeared as SiC nanobands of different polytypes and varying thickness. Furthermore, we observed a shift in the stacking sequence from left to right, and lattice distortion along the c-axis. These observations are in agreement with results reported by Tsuchida et al. in their paper "Formation of extended defects in 4H-SiC epitaxial growth and development of a fast growth technique", where they discussed the formation of prismatic stacking faults (PSFs) as a series of two-bilayer height distortions at intervals of two bilayers [38]. Hence, the observed lattice distortions and stacking faults most likely lead to polytype transformation. So, does growth along direction perpendicular to the c-plane axis favor stacking fault formation and polytype transformation?

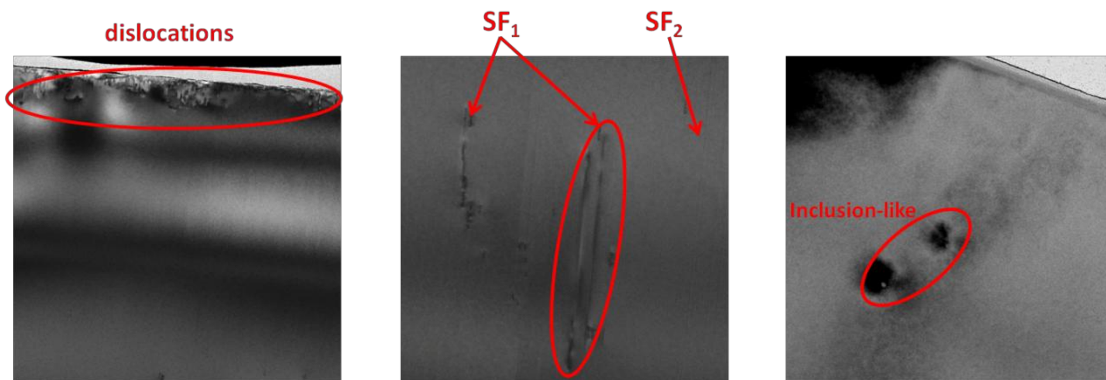

Figures 5.20. Bright field images showing dislocation loops (left), SFs (middle), and inclusion-like feature (right)

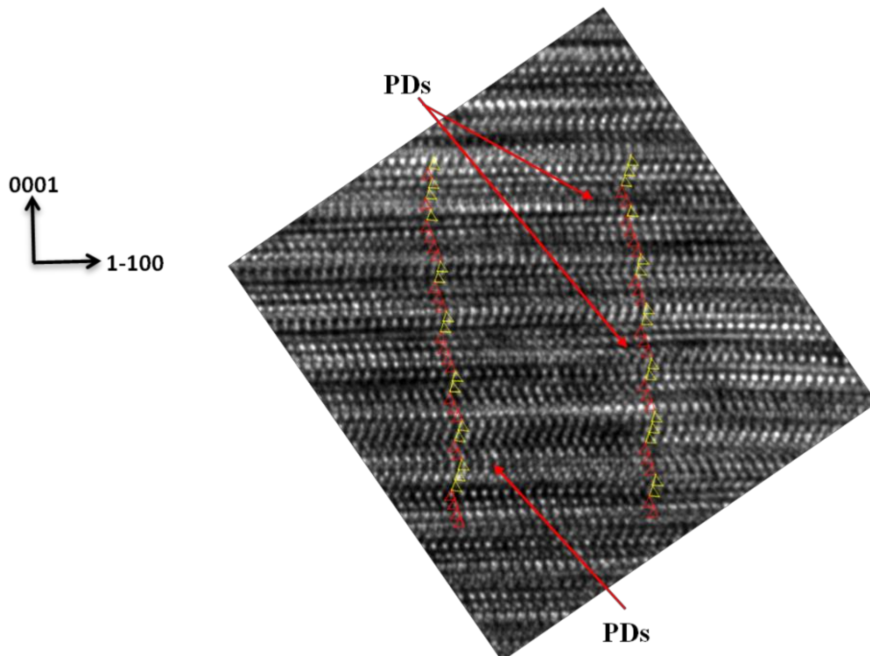

Figure 5.21. Stacking sequence in SF_2 showing the presence of partials dislocations (PDs), lattice distortion and shift in sequence form left to right

Partial dislocations are known to generate SFs, and have been observed in the HRTEM images. Other groups have carried out growth on (1-100) and (11-20) seed and direction [20, 21, 39]. It has been reported that growth along these directions are prone to stacking fault formation. The reason to this has been proposed by Takahashi et al. They have suggested that when disregistry at the boundaries between (1-102) and (1-10-2) subsurfaces of (1-100) surface is relaxed, SFs are generated. The generation of stacking faults, which relaxes the disregistry at the boundaries, also relieves the large localized strain at the boundaries most likely in the form of partial dislocations. The model proposed by Takahashi et al. appears to be in agreement with our results [23]. Figure 5.22 shows the stacking sequence on a (1-100) surface. It is important to note that the SiC nanobands observed in the HRTEM images correspond to macro- steps observed on the surface of the as-grown laterally expanded boules, in agreement with observations made by Takahashi for growth of 4H and 6H-SiC on (1-100) seed. Additionally, the aperiodicity in the stacking sequence suggests a transformation mechanism, which combines both Frank and Shockley mechanism.

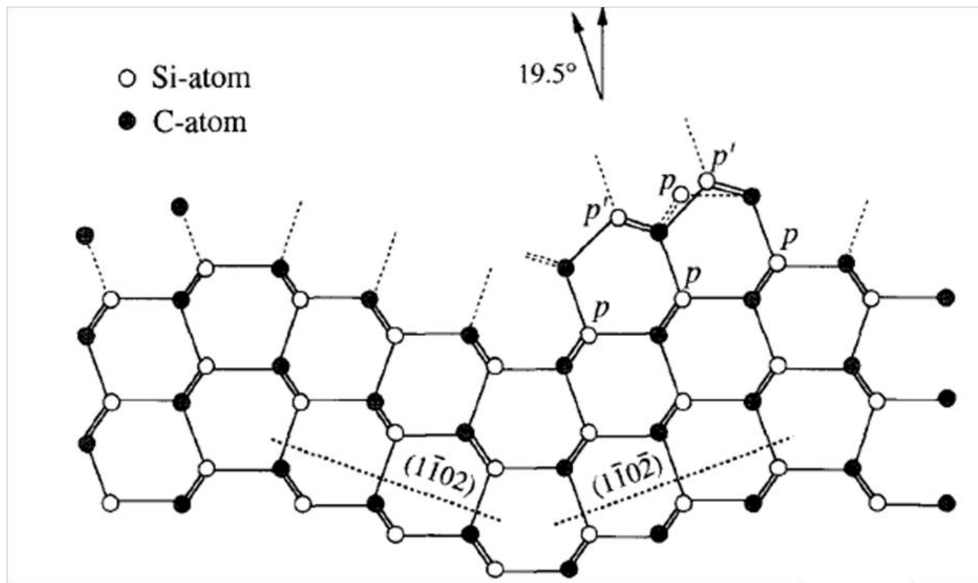

Figure 5.22. Atomistic surface model for 6H-SiC (1-100) surface [23]

V.5.2.3 Summary

HWCVD homoepitaxial lateral expansion of 6H-SiC a/m-plane oriented pseudo fibers has been demonstrated. SEM revealed the hexagonal tapered morphology of the grown boules,

indicating the presence of steps on the as-grown surface. SWBXRT confirmed growth was homoepitaxial. Analysis of axial and transverse slice showed bands of edge type dislocations that propagated from the seed crystal, with significant strain at the seed/epilayer interface. μRS and HRTEM revealed the existence of several SiC polytypes in the 6H-SiC matrix and the nature of their stacking sequences.

V.6 Conclusion

Solvent-LHFZ growth of long SiC seed crystal and enlargement of SiC pseudo fiber by lateral expansion in HWCVD have been successfully implemented. This demonstrates the feasibility of growth of silicon carbide single crystals by large tapered crystal (LTC) technique. One limitation toward wide scale implementation of the LTC technique is the growth of a long seed crystal containing a single screw dislocation. For our experiments, seed crystals with an area defect density much greater than 10,000 per cm^2, which amounts to more than 23 initial screw dislocation per growth front, were used. This resulted in the creation of many small competing growth fronts, and led to the instability of the growth front over the face of the seed crystal and poor quality single crystal fiber with significant inhomogeneous strain.

In the first implementation step of the LTC technique (Solvent-LHFZ), variation in carbon concentration and growth temperature was shown to be directly proportional to the growth rate. Growth rates of 4–135 μm/h were achieved. While a low carbon concentration (8 at. %) feed rod was observed to be C limited, we could not determine whether the high carbon content feed was also C limited due to lack of sufficient data. The growth of a long single crystal fiber suitable as a seed crystal for implementation of the lateral expansion step of the LTC process requires the formation and control of a much more uniform growth front. The optimum process window was determined to be between T_m and T_m+300C for a carbon concentration of 8% at a high silicon ratio (Fe/Si ~0.35). These values were determined based upon the ability to form a stable melt.

In the implementation of the second step of the LTC technique (homoepitaxial lateral expansion in HWCVD), 6H-SiC homoepitaxial boules were obtained from a/m-plane oriented fibers subjected to uniform growth conditions. SWBXT revealed the existence of strain at the seed/epilayer interface, and the presence of bands of edge dislocations extending from the seed in a/m axis lateral direction. These bands of dislocations, confirmed by μRS and HRTEM to be regions of different polytypes, were found to originate from macrosteps observed on the as-grown surface in agreement with previous results reported by Takahashi et al. Growth along the

a/m plane directions have been reported to be prone to stacking fault generation. The model proposed by Takahashi et al., described above, most likely explain the formation of stacking fault/polytypes observed in our experiment.

Since the seed fiber used for lateral expansion was of poor quality, containing high density of micropipes and voids, using a high quality single crystal seed and optimizing the growth conditions can help mitigate the generation of stacking faults. One current usefulness of these results is that SiC nanobands (or nanorods) can be produced, leading to potential application in heterojunction devices. In the end, more work need be done to see the limit of the LTC technique, optimize it, and make it more viable.

References

1. D. Nakamura, I. Gunjishima, S. Yamaguchi, T. Ito, A. Okamoto, H. Kondo, S. Onda and K. Takatori, Nature 430, p 1009 (2004)
2. N. Ohtani, M. Katsuno and T. Fujimoto, Jpn. J. Appl. Phys. 42, p L277-279 (2003)
3. US Patent 7,449,065
4. P. G. Neudeck and J. A. Powell, IEEE Elec. Device Letters 15 (2), p 63-65 (1994)
5. P. G. Neudeck, W. Huang and M. Dudley, Solid State electron 42 (12), p 2157-2164 (1998)
6. J. D. Weeks, J. C. Tully and L. C. Kimerling, Phys. Rev. B. 12 , p 3286 (1975)
7. E.K. Sanchez, J. Q. Liu, M. De Graef, M. Skowronski, W. M. Vetter and M. Dudley, J. Appl. Phys. 91, p 1143-1148 (2002)
8. S. Fujita, K. Maeda and S. Hyodo, Phil. Mag. A 55 (2), p 203-215 (1987)
9. S. Ha, N. T. Nuhfer, G. S. Rohrer, M. De Graef and M. Skowronski, J. Cryst. Growth 220, page 308-315 (2000)
10. J. Takahashi, N. Ohtani and M. Kanaya, J. Cryst. Growth 167, p 596-606 (1996)
11. M. Katsuno, N. Ohtani, T. Fujimoto, H. Yashiro, J. Electronic Materials 34 (1), p 91-95 (2005)
12. Y. Urakami, I. Gunjishima, S. Yamaguchi, H. Kondo, F. Hirose, A. Adachi and S. Onda, Mater. Sci. Forum 717-720, p 9 (2012)
13. C. A. Burrus and J. Stone, Appl. Phys. Lett. 20 (26), p 318-320 (1975)
14. L. B. Griffiths and A. I. Mlavsky, Electrochem. Soc. 111, p 805 (1964)
15. Andrew A. Woodworth, Philip G. Neudeck, A. Sayir, F. Solá, M. Dudley, B. Raghothamachar, J. Cryst. Growth 392, p 34-40 (2014)
16. Andrew A. Woodworth, Philip G. Neudeck and Ali Sayir, “A new method to grow SiC: Solvent-laser heated floating zone”, 6th International Symposium on Advanced Science and Technology of Silicon Materials (JSPS Si Symposium), Kona, Hawaii, (2012)
17. S. Kawanishi, T. Yoshikawa, K. Morita, N. Okada, K. Kusunoki and K. Kamei, J. Cryst. Growth 381, p 121-126 (2013)
18. T. Yoshikawa, S. Kawanishi and T. Tanaka, International Conference on Advanced Structure and Functional Material Design (2008), J. Phys.: Conf. Series 165, p 012022 (2009)

19. Andrew A. Woodworth, A. Sayir, Philip. G. Neudeck, B. Raghothamachar and M. Dudley, MRS Proceedings 1433, (2012)
20. X. R. Huang, J. Appl. Crystallogr. 43 (4), p 926-928 (2010)
21. Philip G. Neudeck and Adrian J. Powell, Silicon Carbide: Recent Major Advances, Edited by W. J. Choyke, H. Matsunami and G. Pensl, Eds. Heidelberg, Germany: Springer-Verlag, p 179-205 (2003)
22. J. Takahashi, N. Othani and M. Kanaya, Inst. Phys. Conf. Ser. 142, p 443 (1996)
23. J. Takahashi, N. Ohtani, M. Katsuno and S. Shinoyama, J. Cryst. Growth 181, p 229 (1997)
24. T. Mitani, S. Nakashima, H. Okumura and H. Nagasawa, Mater. Sci. Forum 527-529, p 343 (2005)
25. M. Hundhausen, R. Püsche, J. Röhrl and L. Ley, Phys. Stat. Sol. (b) 245 (7), p 1356-1368 (2008)
26. S. Nakashima and K. Tahara, Phys. Rev. B 40, p 6339 (1989)
27. S. Nakashima and M. Hangyo, Sol. State Com. 80 (1), p 21-24 (1991)
28. Thomas Werninghaus, "Micro-Raman Spectroscopy Investigation of Hard Coatings", Universität Chemnitz-Zwickau, PhD Thesis (1997)
29. Xiang-Biao Li, Zhi-Zhan Chen, Er-Wei Shi, Physica B: Condensed Matter 405 (10), p 2423-2426 (2010)
30. Ru Han and Xiaoya Fan, Mod. Phys. Lett. B 27, p 1350035 (2013)
31. Yanling Ward, Robert J. Young and Robert A. Shatwell, J. Appl. Phys. 102, p 023512 (2007)
32. D. Kiener, C. Motz, M. Rester, M. Jenko and G. Dehm, Mater. Sci. Eng. A 459 (1-2), p 262-272 (2007)
33. J. Ayache, L. Beaunier, J. Boumendil, G. Ehret and D. Laub, "Sample Preparation Handbook for Transmission Electron Microscopy, Chap 6, Springer, Berlin, p 148 (2010)
34. M. Andrzecuk, T. Płociński, W. Zieliński, K. J. Kurzydłowski, J. Microscopy 237 (3), p 439-442 (2010)
35. E. N. Mokhov, M. G. Ramm, M. S. Ramm, A. D. Roenkov, Yu. A. Vodakov, S. Yu Karpov, Yu A. Makarov, H. Helava, Mat. Sci. Forum 433-436, p 29 (2003)
36. N. Sugiyama, A. Okamoto and T. Tani, Inst. Phys. Conf. Ser. 142, p 489 (1996)

37. H. Tsuchida, I. Kamata and M. Nagano, J. Cryst. Growth 310 (4), p 757-765 (2008)
38. H. Tsuchida, M. Ito, I. Kamata and M. Nagano, Phys. Stat. Sol. (b) 246 (7), p 1553-1568 (2009)
39. H. J. Rost, M. Schmidbauer, D. Siche and R. Fornari, J. Cryst. Growth 290, p 137-143 (2006)

Chapter VI: Correlation of Lifetime Mapping of 4H-SiC Epilayers with Structural Defects Using Synchrotron X-ray Topography

VI.1 Overview

Progress in SiC technology has been stalled by the presence of structural defects in both the substrate and epilayer. For instance, threading screw dislocations (TSDs) and basal plane dislocations (BPDs) have been found to be electrically active defects that degrade the performance of SiC based PiN diodes and MOSFETs devices [1, 2]. Additionally, a decrease in the minority carrier diffusion length has been observed in the vicinity of dislocations and micropipes [3]. This decrease in carrier diffusion length can in turn result in a reduction of their lifetime. Other structural defects such as stacking faults and grain boundaries can be expected to affect electrical properties of SiC devices. In this chapter, we investigate the defect structure of two 4H-SiC epilayers (a quarter wafer and a half wafer) grown by chemical vapor deposition (CVD) and discuss their formation mechanism. Next, we correlate these defects with lifetime photoconductive decay mapping, and discuss how the structural defects influence the carrier lifetime.

VI.2 Motivation

Minority carrier lifetime is an important measure of a semiconductor material's purity, and controls the performance of high voltage/ high power and frequency devices. It can be defined as a physical process that describes the recombination process between an electron and a hole in a semiconductor material. It is thus not an intrinsic semiconductor property, but a relationship involving charge carriers and semiconductor properties. While a uniform lifetime is desirable, its desired value is application specific. In high power device applications, a longer carrier lifetime is necessary to mitigate power loss under forward bias. As for high frequency applications, a shorter lifetime is more suitable to reduce power loss during switching cycles.

Despite recent studies linking certain peculiar defects present in silicon carbide to variation in carrier lifetime [4-8], little is known about these lifetime limiting defects and their recombination properties because of variability in measurement. For instance, $Z_{1/2}$ defects have been perceived as lifetime killer defects in n-type epilayers at very high concentration (> $5x10^{12}cm^{3}$), whereas at low $Z_{1/2}$ concentration, other factors seem to limit carrier lifetime [5]. These factors could be attributed to growth conditions, epilayer thickness and structural defects.

Recent studies by L. Lija and coworkers have shed light on the role of growth temperature on carrier lifetime [6]. They reveal that at higher growth temperature, $Z_{1/2}$ concentration increases and carrier lifetime is reduced. Similarly, the effect of structural defects, known to act as recombination center, has been investigated [5, 7].

The propensity of structural defects to form, and thereby their density, is growth condition sensitive. In order to achieve SiC-based devices, growth of high quality and uniform epitaxial layer is desirable. The layer must replicate the polytype of the underlying substrate to avoid the formation of deleterious defects that could result from lattice mismatch. This type of growth is referred to as homoepitaxial, and is carried out by chemical vapor deposition (CVD). Essentially, homoepitaxial growth is a step-controlled process that is achieved on (0001) off-cut substrate [9, 10]. The vicinal substrate provides steps, which contain the polytype sequence of the underlying substrate and favor its replication during epitaxial growth. When the distance (i.e. terrace) between adjacent steps is sufficiently long, poor control of growth conditions and incoming adatoms from silicon and carbon sources do not have sufficient speed to reach a step and be incorporated into the growing crystal, 2D nucleation occurs. The 2D nucleation results in the formation of 3C polytype inclusion [9, 10]. An illustration of step-flow growth is shown in Figure 6.1.

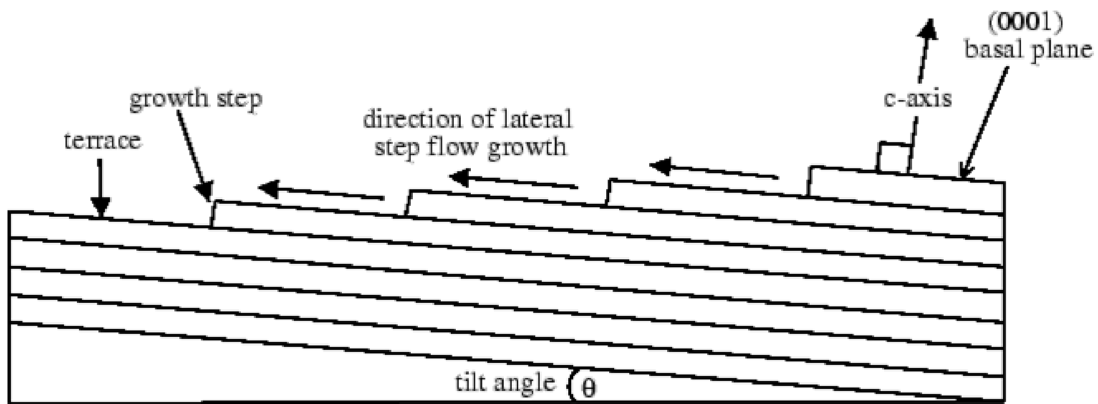

Figure 6.1. Illustration of step flow growth during CVD growth [11]

To remedy the formation of 3C inclusions, off-cut angle of the substrate can be suitably chosen. Current of off-cut angle for commercial 4H- and 6H-SiC substrates are 4 and 8 degree [12]. Poor control of growth conditions can also result in the formation of morphological defects that can be detrimental to SiC device processing and performance [9]. T. S. Sudarshan et al. have reported the formation of morphological defects associated with silicon gas phase decomposition during epitaxial growth [13, 14]. Similarly, J. A. Powell and D. J. Larkin have shown that a pre-

growth wafer polishing and growth initiation significantly prevent the formation of epitaxial growth-related defects [8]. Another challenge encountered during SiC CVD growth is the relative ease of stacking fault formation at high doping concentrations [15, 16]. It is important to highlight that high doping is necessary to achieve conductivity up to par with metals.

We could safely speculate that as growth process evolves and material quality improves, new type of defects may be generated that change overall relative defect density and become more overbearing on the recombination properties of the material. Thus, it becomes opportune to investigate the formation mechanism of these structural defects in SiC epilayers (e.g. 4H and 6H-SiC) and discuss their recombination properties in light of their growth conditions with a focus on minority carrier lifetime.

Several techniques exist to investigate extended defects in silicon carbide single crystals. These techniques can be classified in two categories based on their destructive/non-destructive nature. An ideal characterization technique would offer high spatial resolution and sensitivity to defects coupled with a non-destructive character. The technique would also allow for survey of entire sample and provide a topological map. Synchrotron X-ray topography (SXRT) is an appropriate candidate that fulfills these requirements. Two types of SXRT sources exist, of which are white and monochromatic beam. The white beam source allows for an enhanced tolerance of lattice distortion, whereby for a single crystal exhibiting a uniform range of lattice orientation or a mosaic structure (due to subgrains, or twinned regions) a single exposure image can be obtained. In contrast, the monochromatic source does not allow for an enhanced tolerance of lattice distortion as the acceptance angle for diffraction is restricted by the convolution of characteristic line width with the beam divergence in a manner similar to conventional X-ray topography. In this case, only regions of a single crystal that exhibit misorientation smaller than the acceptance angle for diffraction will diffract at a given time and produce contours that delineate regions satisfying Bragg conditions from those that do not. Consequently, dynamic studies of structural defects in large single crystal using monochromatic source can be tedious. It is nonetheless important to mention that a monochromatic source is more sensitive to strain and allows for a higher resolution topographs compared to white beam. So there lies the trade off and complementarity.

Similarly to extended defects, carrier lifetime in semiconductor in general, and particularly in silicon carbide, has been measured using various techniques [4, 17, 18]. The variability in

measurements from these techniques has raised the need for reliable carrier lifetime measurements. For instance, the photoconductance decay methods used to measure lifetimes fails at low injection level as it is sensitive to artifacts such as minority carrier trapping [19]. This raises the need to mitigate this variability in measurement through improvements in instrument design and capability. Luis Vasquez in his master thesis has attempted to tackle this issue of variability in measurement with relative success [20]. Currently, contactless photoconductive decay (PCD) techniques have emerged as reliable methods to measure carrier lifetime because they enable measurement of carrier lifetime at any stages of device processing, from bare wafers to contacted devices. This makes contactless PCD techniques very useful tool to screen, select bare wafers for device fabrication, and assess the impact of processing conditions on device quality. In this study, however, two different methods were used to measure minority carrier lifetimes. These methods are photoluminescence (PL) decay, and microwave photoconductance (μPCD).

Understanding the dynamic of the formation of extended defects and their concentrations in SiC epilayers from growth conditions, coupled with the influence of those defects on carrier lifetime will help forecast the recombination characteristic of SiC power devices; and consequently their performance. The broader aim of this chapter is to identify and subsequently classify extended defects in epitaxial layers grown by chemical vapor deposition (CVD) with respect to their lifetime limiting power. The implication of these results on the selection and processing of silicon carbide substrates for epilayer growth is further discussed in light of the lifetime maps.

VI.3 Experiment

Two homoepitaxial wafers (samples 1 and 2) grown by chemical vapor deposition (CVD) on 4˚ off axis 4H-SiC substrates were used in this study. Sample 1 was a quarter wafer and sample 2 was a half wafer. Each epiwafer had a thickness of about 25μm and were unintentionally n-type doped with a concentration of $\sim 4x10^{14}cm^{-3}$. Sample 1 contained two facets; one near the center (facet a) and one off center (facet b). Both facets had nearly the same doping concentration as measured using reflectance spectroscopy. The measured doping concentration for facets a and b were $8.8\ x10^{18}$ and $6.8\ x10^{18}\ cm^{-3}$, respectively. Measurement of carrier lifetime was performed at room temperature using a 355 nm frequency-doubled, cavity-dumped Ti: sapphire laser as the source for free carriers. The laser generated 150 femtosec pulses at 100 kHz, with average pulse

energy of about 5nJ. The emitted light was analyzed by a ¼-m double spectrometer and detected by a cooled GaAs photomultiplier and time-correlated single photon counting. Measurements were carried out under low-injection conditions ($n = 4x10^{14}$ cm^{-3}). The carrier lifetimes were extrapolated from the exponential decay of the room temperature band-edge photoluminescence peak at 391 nm. Then, a lifetime map for each epiwafer was obtained by microwave photoconductance decay (µPCD). Finally, the carrier lifetime maps were compared with synchrotron white beam and monochromatic beam x-ray topography (SWBXT and SMBXT) defect distribution maps. Additional differential interference contrast (DIC) microscopy images were used to map the surface for morphological defects.

VI.4 Results and discussion

VI.4.1 Lifetime measurements

In silicon carbide single crystal epilayers, extended defects such as TEDs, TSDs, BPDs, low angle grain boundaries (LAGBs) and micropipes are observed to replicate from the substrate into the epitaxial layer, whereas carrot defects, in-grown stacking faults (IGSFs) and other morphological defects are not [21-23]. These types of defects become harmful to SiC power devices once they reach the device active layer [2]. Similarly, these defects can act as recombination centers, and decrease the effective diffusion length of minority carriers. For instance, studies by M. T. Azar and coworkers have shown that minority carrier diffusion length is reduced in the vicinity of dislocations and micropipes [3].

The variation in carrier lifetime across samples 1 and 2 was measured using photoluminescence decay (PL decay) and microwave photoconductance decay (µPCD). Figures 6.2 show the microwave photoconductance decay mapping for samples1 and 2. In these figures, the carrier lifetime across the epiwafers is seen to decrease toward the periphery. In sample 1 (Fig. 6.2a), we observe a region of very low carrier lifetimes indicated by a rectangle. This region corresponds to facet a with a doping concentration of $8.8\ x10^{18}\ cm^{-3}$. Like facet a, which displays the lowest carrier lifetime, facet b indicated by an oval circle also shows lower lifetimes albeit at higher values than facet a. It is important to note that both facets have about the same doping concentration, $6.8\ x10^{18} cm^{-3}$ for facet b. Thus, the difference in lifetime between these two facets cannot be attributed to their doping concentration. One might suggest, however, that the observed lower lifetimes in these facets with respect to the rest of the sample is likely due to

the doping concentration difference between these facets and the rest of the sample. It is possible that the high doping in the facets results in an increase in recombination centers; hence a reduction of the carrier lifetimes. This could be explained using the Shockley-Reed-Hall (SRH) recombination statistics [24], where carrier lifetime is inversely proportional to concentration of recombination centers.

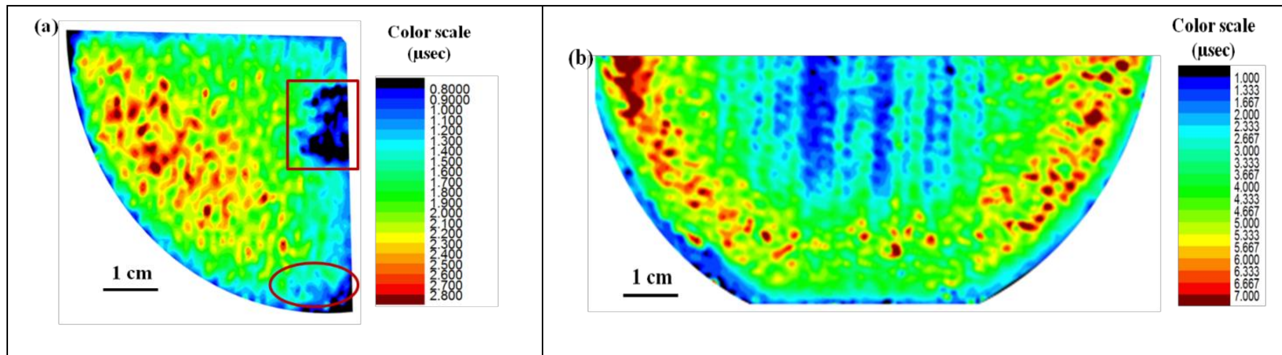

Figure 6.2. Microwave photoconductance decay maps of sample 1 (a) and sample 2 (b)

In contrast to sample 1, sample 2 did not have any facet. Microwave photoconductance map of sample 2 revealed the existence of vertical bands of various thicknesses running parallel to the [1-100] crystallographic direction. These bands were observed to be associated with very low carrier lifetimes. It is worth underlining that sample 2 shows a higher lifetime by a factor of 2 compared to sample 1. This variation in lifetime could be attributed to a difference in growth conditions and substrate/epilayer quality in agreement with results previously reported by L. Lija and coworkers [6], and Jawad and coworkers [25]. In fact, samples 1 and 2 were subject to different growth conditions and resulted in surface morphology. Sample 1 with an overall thickness of 379μm has a surface morphology dominated by parasitic particulates and pits (Fig. 6.3a). On the other hand, sample 2 has an overall thickness of 430μm, and is dominated by triangular defects (Fig. 6.3b). Thicker epilayers have been found to yield longer lifetime most likely because of the reduced influence of the carrier diffusion into the lower quality substrate [7, 26].

μPCD measurements are known to induce high injection level at the front surface of the sample, and are therefore more sensitive to surface recombination effects. In order to uniformly probe the sample and account for more bulk effect, lifetime measurements by photoluminescence decay (PLD) at room temperature were performed for each sample. These measurements were

carried out to complement the μPCD results. Figure 6.4 shows the photoluminescence decay time curve variation along the facets for sample 1 and the corresponding sample schematic. We observe an aperiodic variation in carrier lifetimes, with the lowest values obtained in the range of ~15 to 22μm. This range corresponds to the region encompassed by facet a. While this observation agrees with the general trend of the μPCD results, the measured lifetime values are a factor of 1/3 smaller than the values obtained using μPCD.

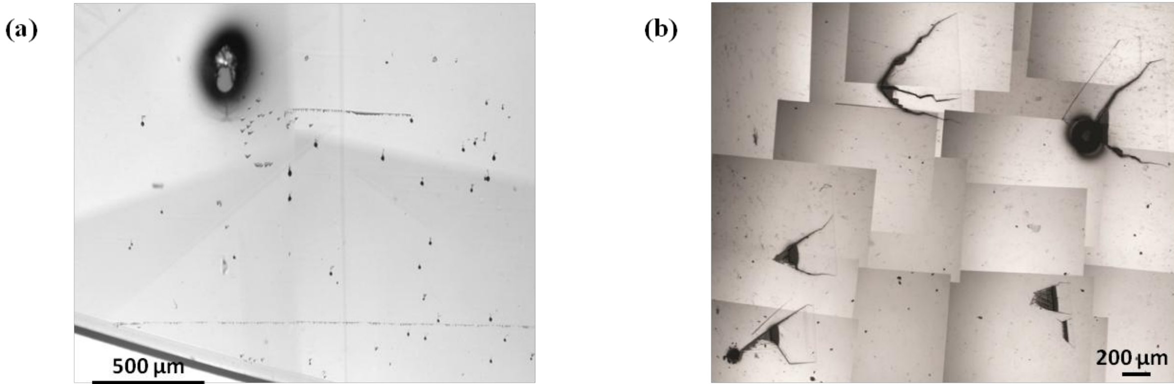

Figure 6.3. Typical surface morphology of sample 1 (a) and sample 2 (b). Note that (a) and (b) are representative area of samples 1 and 2, respectively.

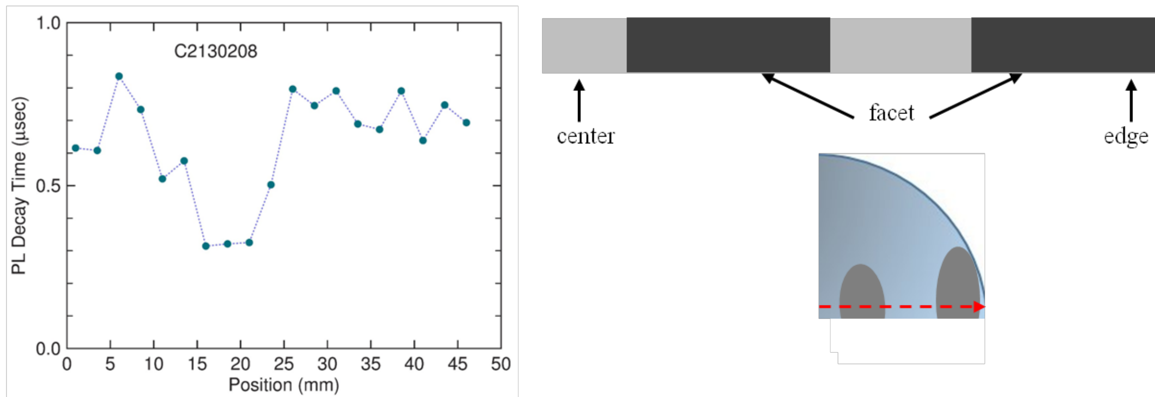

Figure 6.4. Photoluminescence decay time curve of sample 1 along with sample schematics

Photoluminescence decay time measurements for sample 2 are shown in Figure 6.5. Along the x-direction, the carrier lifetimes have a parabola-like behavior in the range [-45 to 45μm], with the shortest lifetime observed around the central region. Outside of this range, the lifetimes are seen to decrease toward the edge. Along the y-direction, the lifetimes are observed to increase away from the edges in the range [-50 to 40μm], and then decrease toward the middle of the sample. This is in agreement with the μPCD mapping, which revealed a lower lifetime in the

middle of the sample and near the edges. It is interesting to observe that the difference in lifetimes between the μPCD and the PLD measurements is about a factor of 2. This difference in lifetimes can be attributed to the surface recombination effect, which is dominant in the μPCD measurement. In fact, the surface recombination sensitivity of the μPCD technique allows generated carriers to diffuse more readily into the surface region before bulk recombination occurs. In addition to the possible surface recombination effect, the difference in the carrier injection density between the two measurements is also a likely cause for the variation in the lifetime values.

Despite the difference in measured lifetime values between the PLD and μPCD techniques, both techniques show a common trend in the lifetime distribution across each epiwafer. For instance, in sample 1 the lifetimes are higher in the central regions compared to the periphery; whereas the lifetimes in sample 2 are higher in regions between the middle of the wafer and the periphery. This could be related to the better crystalline quality in these regions of the epiwafers. This better crystalline quality is traduced by low density of dislocations and other structural as well as morphological defects. It has already been demonstrated that carrier diffusion length is reduced in the vicinity of dislocations and micropipes [3]. This reduction in carrier diffusion length translates into a reduction in carrier lifetimes.

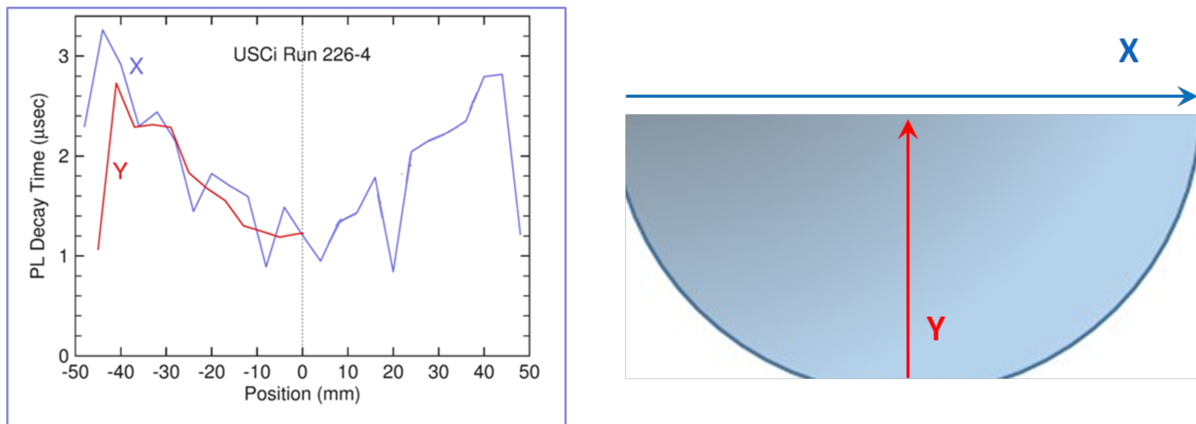

Figure 6.5. Photoluminescence decay time curve of sample 2 along with sample schematics

VI.4.2 Synchrotron X-ray Topography

In the vicinity of a dislocation, the long-range strain field surrounding the dislocation produces a dipole potential that can influence the spatial distribution of carrier recombination centers by attracting the photogenerated excess carriers (electrons and holes) to the non-radiative

core region [27]. Stated otherwise, dislocations create a distribution of energy levels inside the band-gap of the material. The effective influence of these energy levels on carrier lifetimes depends on their position within the band-gap, i.e. whether they lie within a window determined by the position of the Fermi level [28]. Several studies have been carried out to assess the influence of dislocations (i.e. extended and morphological defects) on lifetime for different semiconductor materials. McKelvey [29], Wertheim and Pearson [30] investigated the influence of dislocations on the recombination lifetime in germanium (Ge) samples and revealed an inverse relationship between lifetime τ_r and dislocation density ρ_d for $\rho_d \geq 10^4 cm^{-2}$.Similarly, M. J. Marinella and coworkers reported that at density higher that $10^6 cm^{-2}$, dislocations limit carrier recombination lifetime in 4H-SiC [31]. Jawad Hussein and coworkers studied the influence of extended defects on carrier lifetime in SiC [7].

In light of the potential influence of extended and morphological defects on lifetime, investigation of their formation mechanism as it pertains to the growth conditions of the single crystal and assessment their influence of minority carrier lifetime becomes necessary. To this end, synchrotron x-ray topography (SXRT) characterization was carried out in both transmission white beam (SWBXT) and monochromatic grazing (SMBXT) geometry to probe the structural integrity of the two samples and compare the defect distribution map with the μPCD map. Figure 6 reveals the underlying microstructure of facets a and b, as well as the overall defect structure of sample 1. In facet a (Fig. 6.6), we observe low angle grain boundaries (LAGBs) oriented along the <1-100> directions and forming domain walls with Burgers vector 1/3<11-20>. These LAGBs, at the center of which lies a cross feature, are overlapped by multi-layer stacking faults (SF). The cross feature has segments along <11-20> directions and an inclusion-like defect, which is a pit associated with a micropipe, at its core. The formation of stacking faults due to glide of glissile partials cross-slipping from the prismatic plane has been previously reported by Fangzhen Wu et al. for a 4H-SiC substrate grown by PVT [32]. In their studies, Wu et al. revealed that a micro-pipe was associated with the formation of a 6-pointed star stacking fault and proposed a formation mechanism for the fault (Fig. 6.7). Details about this mechanism can be seen in reference 32. While the observations by Wu et al appear to agree with our results, the formation of SF should not be attributed to the same mechanism. First, observation of facet a by Nomarski optical microscopy in both reflection and transmission geometry reveal that the cross feature is most likely lying inside the substrate; though it can also intersect the substrate-epilayer

interface. The Nomarski images of the cross feature inside facet a for both silicon and carbon faces are shown in Figure 6.8. Secondly, if the cross feature was due to prismatic slip, each of its segment would appear as an array of threading edge dislocations (TEDs) along the <11-20> directions on a grazing x-ray topography image. Analysis of a synchrotron monochromatic beam grazing topograph (SMBXT), shown later, suggests it is not the case. So, it could be safe to assume that since the cross feature is not due to prismatic slip, it is the result of some artifacts on the substrate surface. So, what is the exact origin of the stacking faults SF inside facet a?

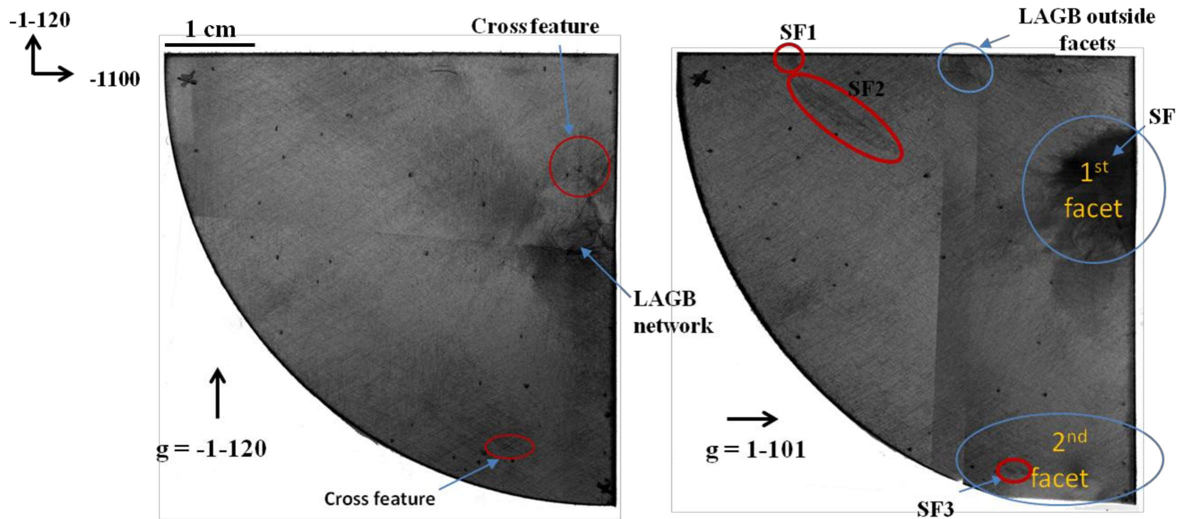

Figure 6.6. SWBXT transmission topographs for (-1-120) and (1-101) diffracting plane. Note that the scale is the same for both reflections

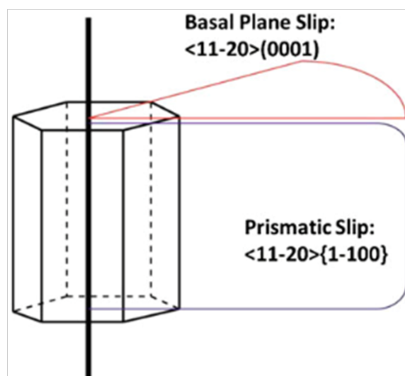

Schematic of dislocations nucleating from a micropipe in both basal and prismatic slip systems

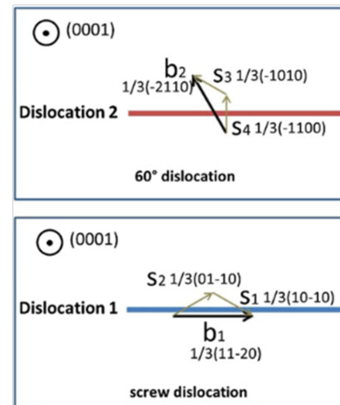

Burgers vector and partials of a 60° dislocation and a screw dislocation on the basal plane

Figure 6.7. Formation mechanism of stacking fault associated with micropipe as suggested by Wu et al. [32]

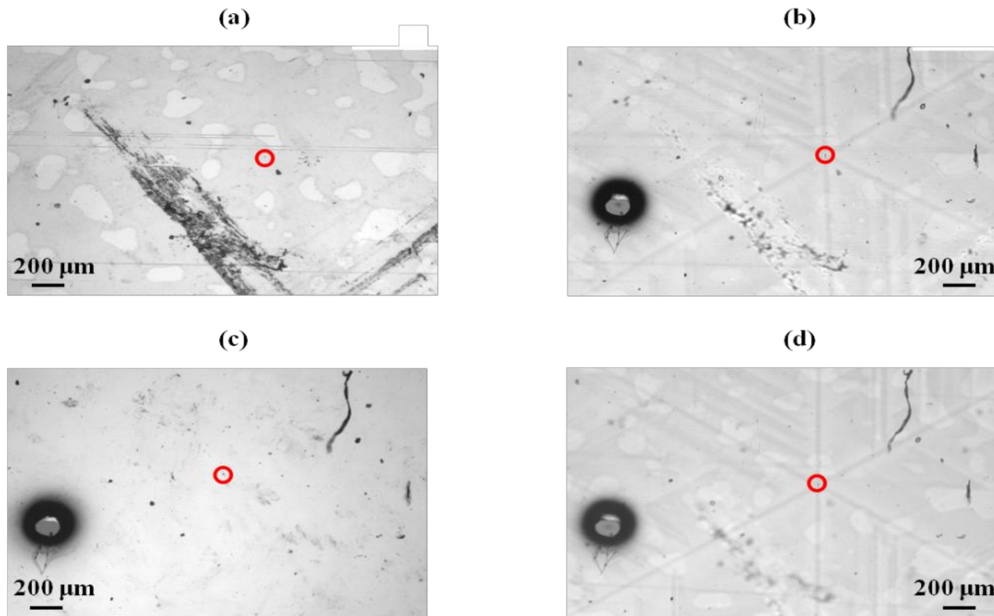

Figure 6.8. Nomarski micrograph of cross feature in facet a in (a) reflection on carbon face, (b) transmission on carbon face, (c) reflection on silicon face and (d) transmission on silicon face. Note the pit associated with micropipe at the center of the cross in red circle

In order to further investigate the origin of stacking faults SF, high-resolution grazing topograph was recorded using synchrotron monochromatic beam, i.e. SMBXT. The SMBXT topography image, juxtaposed with SWBXT transmission images of the same area, is shown in Figure 6.9 for facet a. From the (1-101) diffracting plane topography image, we notice that while the LAGBs act as a barrier to the expansion of stacking faults SF along the downstep direction, other stacking faults seem to propagate from it. This suggests that in addition to the LAGBs providing a source for the nucleation of the stacking faults SF, another source for the formation of SF exists, which lies on the substrate surface. This is further supported by the observation of isolated triangular stacking faults in facet a (Fig. 6.9). The epilayer thickness was derived from the product of the height of one of the triangular stacking faults to the tangent of the substrate off-cut angle. So, what is the nature of this second source that generated stacking faults SF?

Close look at the (1-101) topography image shows that SF occupies an area that encompasses the cross feature and extend to the LAGBs. As mentioned before, the cross feature is an artifact on the substrate surface, which may be due to substrate preparation prior to epitaxial growth. During substrate preparation, scratches or other artifacts such as depressions, step bunching and micro-steps to name a few, can form on the substrate surface. These substrate preparation damages can lead to the formation of morphological and extended defects such as stacking faults

in the epilayer. Mention articles that report on the formation of stacking fault in epilayer from defects on surface of substrate. As such, it is very likely that the cross feature is the second source for the nucleation of stacking faults SF. It is important to note that these stacking faults SF inside facet a could be double Shockley stacking faults (DSSFs). An electronic mechanism proposed by Kuhr [15] and observed by Pirouz [16] explains the spontaneous nucleation and propagation of DSSFs under no shear stress. This mechanism proposes that when the dopant concentration in the facet region exceeds threshold doping levels for onset of DSSF generation during epigrowth, the local Fermi energy in the facet region is raised above the DSSF energy level thereby driving the spontaneous nucleation of DSSFs once the activation barrier for dislocation glide is overcome. Although facet b has nearly the same doping concentration as facet a, it contains a low density of stacking faults referred to as SF_3 (Fig. 6.6). This low density of stacking faults in facet b is due to the low density of available nucleation source compared to facet a. Contrast analysis of the three reflection vectors (11-20), (1-100) and (1-101) reveals the structure of SF_1 and SF_2. SF_1 is a Shockley fault as it does not show contrast only in (11-20) reflection, and SF_2 is a combination of both Franck and Shockley since one of its portions is missing in both (11-20) and (1-100) reflections and the other only in (11-20). Topographs that served for contrast analysis of SF_1 and SF_2 are shown in Figure 6.10.

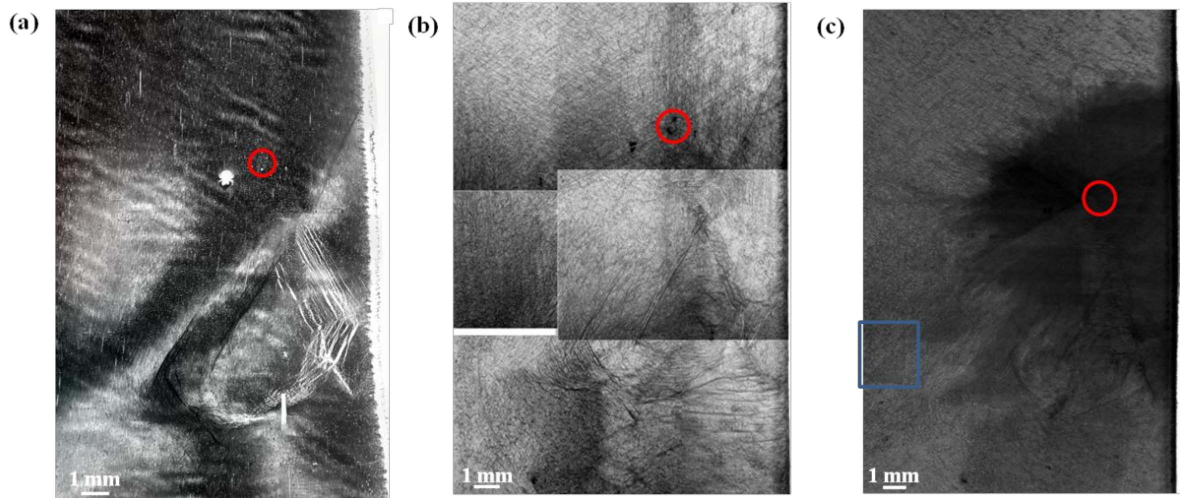

Figure 6.9. (a) SMBXT of facet a, (b) SWBXT of facet a for g = 11-20, and (c) g = 1-101. Note red circle correspond to pits associated with micropipe at center of cross feature and blue rectangle shows isolated triangular stacking fault.

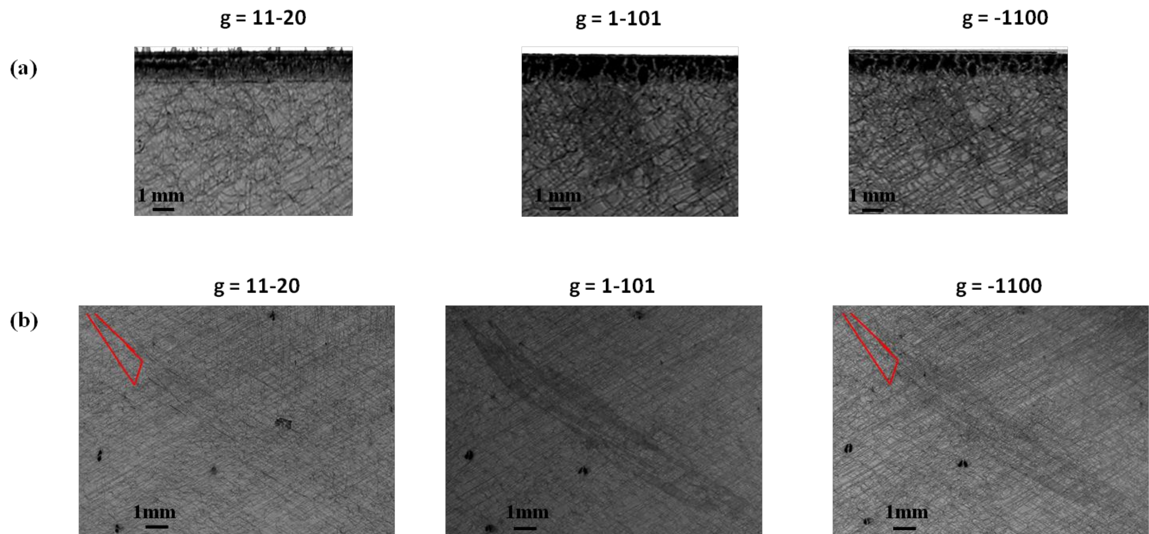

Figure 6.10. SWBXT transmission topographs for SF1 (a) and SF2 (b). Notice the red triangle in (b) highlighting the Franck fault

Similarly, SWBXT and SMBXT topography images were recorded for sample 2. These images are shown in Figures 6.11 and 6.12, respectively. The overall microstructure of this sample can be divided into two regions, an inner central region and an outer peripheral region, as delineated by a curvilinear beadlike morphological defect.

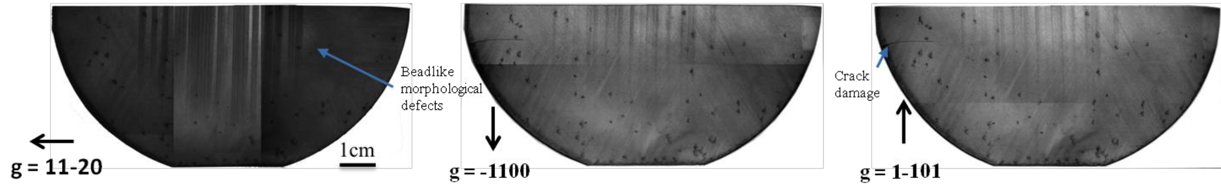

Figure 6.11. SWBXT of sample 2 for three different reflection vectors. The scale is identical for all three reflections

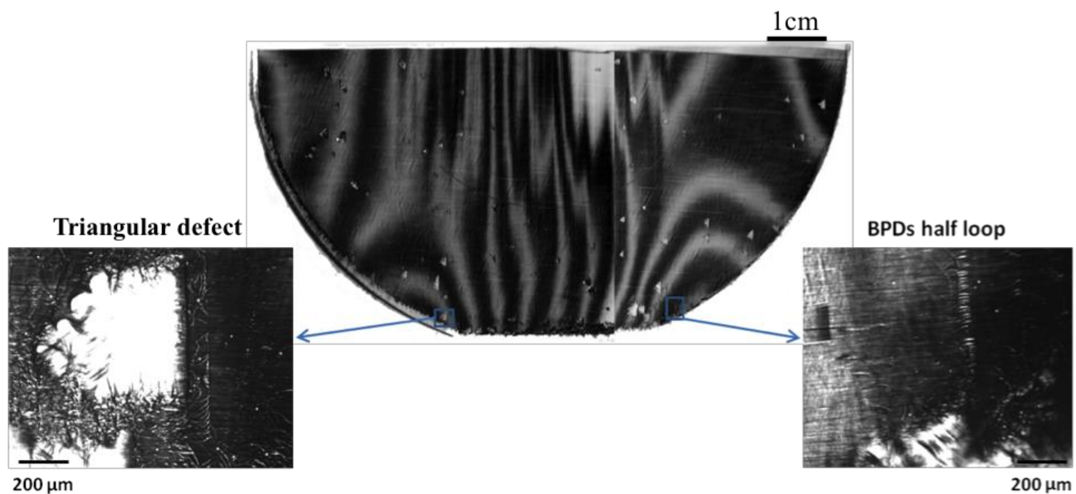

Figure 6.12. SMBXT of sample 2 for (11-28) reflection vector. Note the triangular defects and BPD half loops highlighted near the edge

In the central region, linear defects and short BPD segments connecting TEDs and propagating along the direction perpendicular to the step flow, i.e. <1-100>, dominated the microstructure. These linear defects and short BPD segments connecting TEDs were found to be interfacial dislocations (IDs) and half-loop arrays (HLAs), respectively. The IDs and HLAs were associated with the presence of morphological defects (mainly triangular defects). Similar observation has been reported by Huanhuan et al. [33, 34]. In their studies, IDs and HLAs were observed to propagate along the direction perpendicular to the step flow direction. They further described the formation of these defects using a three-step process:

I. First, pair of opposite sign basal plane dislocations in the substrate intersect the substrate surface in screw orientation
II. Then glide in opposite direction in the epilayer once a critical thickness is reached
III. Finally, side-glide of screw-type BPDs inside the epilayer.

Step I and II correspond to the formation of IDs, and step III is associated with the formation of HLAs. A diagram illustrating the formation mechanism of IDs and HLAs for the case described in step 1 through 3 as well as the special case of a 3C-SiC inclusion is shown in Figure 6.13.

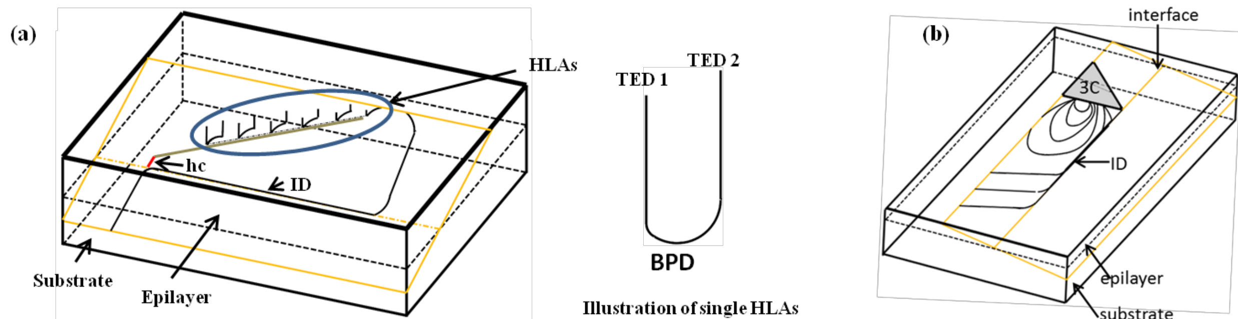

Figure 6.13. Diagram describing formation of IDs and HLAs along with illustration of single HLAs (a), and schematic of IDs and HLAs originating from 3C inclusion. Note that h_c correspond to critical thickness at which screw type BPD (straight line from substrate) is forced to glide sideways at epilayer-substrate interface

IDs typically form in epilayer to accommodate the misfit strain between substrate and epilayer, which could possibly originate from difference in doping concentration. Matthews-Blakeslee proposed a model that explains the underlying structural mechanism that takes place in the epilayer to accommodate this misfit strain [35]. According to the model, glide of substrate

BPD into the epilayer occurs once the epilayer reaches a critical thickness. While it has been shown that the main forces, i.e. the line tension and its opposing shear force, acting on the BPD segment extending into the epilayer are balanced [36, 37], Huanhuan et al. [34] revealed the contribution of the attractive force between pair of opposite sign threading BPDs to the onset of glide and thus the formation of IDs. Huanhuan et al. further showed that the separation between the pair of opposite sign BPD influence the critical thickness, where larger critical thickness are achieved for greater separation between opposite sign threading BPDs. Measurement of the critical thickness was also determined [34]. Its value was extrapolated from the position of the first half-loops in the HLAs or by extending the line direction of the HLA, in case of short glide of substrate dislocation near its surface, to the line direction of the original substrate BPD extended into the epilayer. Since the IDs and HLAs observed in our studies originated from triangular inclusions, we can extrapolate from Huanhuan's studies that the separation between the pair of opposite sign BPDs is determined by the length of the side of the triangular defect perpendicular to the step flow direction. This suggests that the larger the size of the triangular defects, the bigger the critical thickness. Detailed studies on the formation mechanism and origins of IDs and HLAs can be found in references [33, 34].

As for the peripheral region, triangular defects (3C inclusions) with highest density at the edges along with microcracks make up the microstructure of the sample. We also observed a scatter of various shapes of morphological defects distributed across the epiwafer. A Nomarski optical image of observed morphological defects is shown in figure 6.14. The difference in shape, size and core of these morphological defects suggest they originate from different sources. Several studies have reported on the formation of morphological defects in silicon carbide homoepitaxial layers [38-40]. J. Powell and D. J. Larkin reported that defect in the substrate bulk, polishing and cutting damage in the substrate surface as well as tilt angle of the wafer surface contributed to the formation of morphological [38]. Das et al found that triangular defects in 4H-SiC were not due to substrate defects, but rather caused by disturbances during the epitaxial growth [39]. Furthermore, T. Rana et al reported that the use of a different type of precursor, specifically tetrafluorosilane (SiF4) can eliminate Si gas phase nucleation and prevent the formation of Si parasitic deposition morphological type defects during epitaxial growth [40]. It is important to note that morphological defects can cause the formation of structural defects.

For instance, carrot and comet defects have been associated with stacking faults [41]. As such, morphological defects are not desirable.

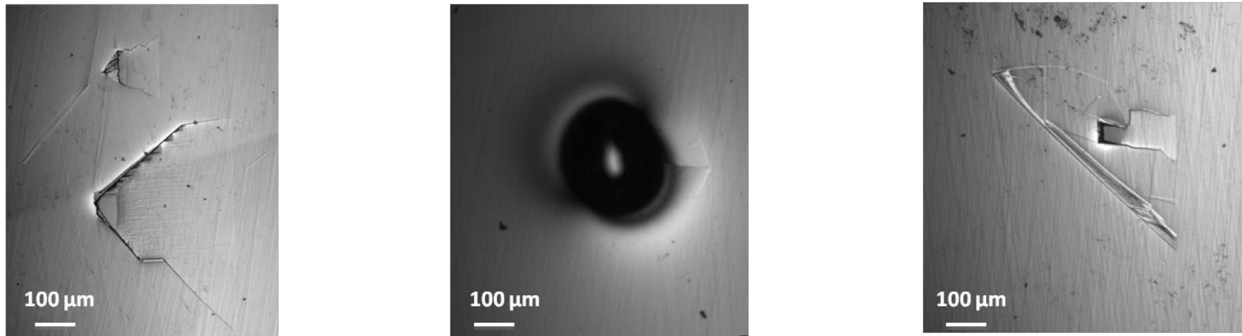

Figure 6.14. Morphological defects of various size and shape.

VI.4.3 Effect of structural and morphological defects on carrier lifetimes

While certain extended defects are more deleterious to carrier lifetime, others are not. Jawad et al. reported that stacking faults in 4H-SiC epilayers are lifetime limiting defects [7]. In our studies, comparison of the µPCD maps with the SMBXT and SWBXT allowed us to correlate extended defects with lifetime and quantify their effect. In sample 1, we observed a direct relationship between reduction in lifetime and stacking faults. The lifetimes associated with SF_1, SF_2 and SF_3 are reduced to ~1.1 µs, 1.7 µs and 1.1 µs while their surrounding regions varying from 2.2 µs to 2.8 the farther away from the core of the faults (Fig.6.15). These results are comparable to those reported by Jawad et al [7], who observed a lifetime below the detection limit of the µPCD technique. Besides stacking faults, low angle grain boundaries (LAGBs) in facet a were seen to contribute to a decrease in lifetime. It is important to notice the peculiarity of facet a. In fact, facet a is filled with overlapping stacking faults (SF), LAGBs, a pit associated with a micro-pipe at the center of a cross feature. The peculiarity of this facet does not enable us to resolve the specific impact of each one of these defects. Nonetheless, it is apparent that the combine effect of these defects is very detrimental to the carrier lifetimes.

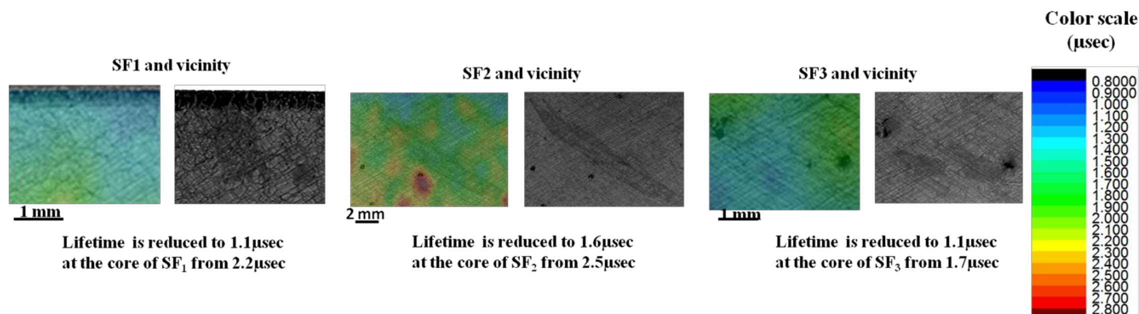

Figure 6.15. Correlation between stacking faults SF_1, SF_2, SF_3 and their µPCD map. Note that the µPCD map is overlaid on top of the SWBXT for each region encompassing the stacking faults

Stacking faults and LAGBs were not the only extended defects that negatively impacted the carrier lifetime in sample 1. BPD half loop pinned to TSDs also contributed to reduction in carrier lifetime. These BPDs half loops became pinned by TSD as they glided on the basal plane during epilayer growth. The lifetime associated with those BPD half loops pinned by TSDs was found to decrease to 1.1µs from about 2.5µs in their immediate surroundings. Another factor that influenced carrier lifetime is the density of structural defects. Regions of different defect density exhibited different carrier lifetimes. SWBXT images for (11-20) reflection vector corresponding to four regions with different BPD density are shown along with their corresponding lifetime map in Figure 6.16. This is consistent with the inverse relationship between lifetime and dislocation density described in references [29] and [30].

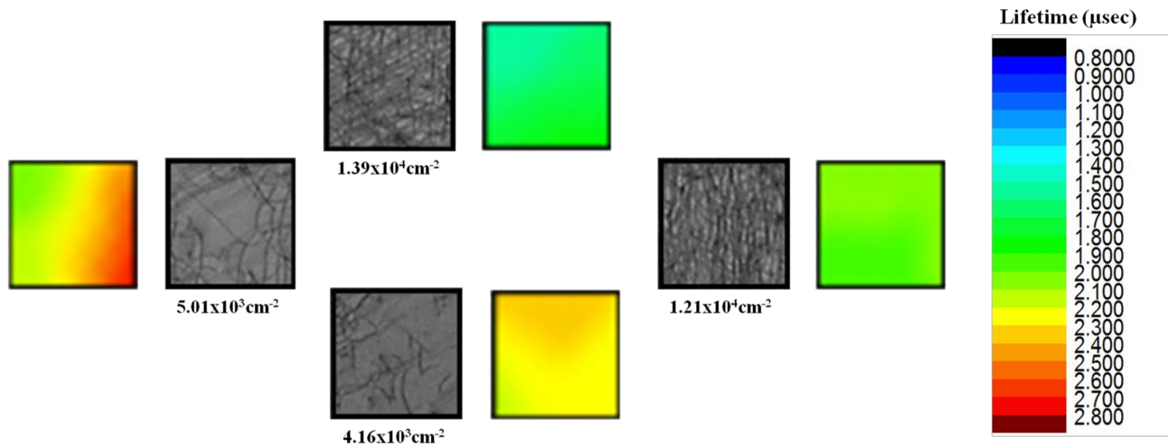

Figure 6.16. (11-20) SWBXT transmission image of four regions from sample 1 along with their corresponding µPCD map

The influence of parasitic depositions (PaDs) and microcracks on the carrier lifetimes was also assessed. A high density of microcracks as well as BPD half loop dominated the edges of sample 1. These microcracks and BPD half loops are related to very small triangular defects, and could be due to lattice mismatch between the high density of small triangular defects and the epilayer/substrate. It is important to note that the non-uniform temperature distribution across sample 1 could be the source of the triangular defects. It has been reported that triangular defects form easily at the edges of an epiwafer under certain growth conditions when the adatom

diffusion length is shorter than the terrace width. As to the parasitic depositions, their influence was mitigated. While some were associated with lower lifetime, others were not. The reason to this variability in influence could be explained by the difference in size, shape and most likely core structure of the PaDs. Illustration of the mitigating effect of PaDs is shown in Figure 6.17.

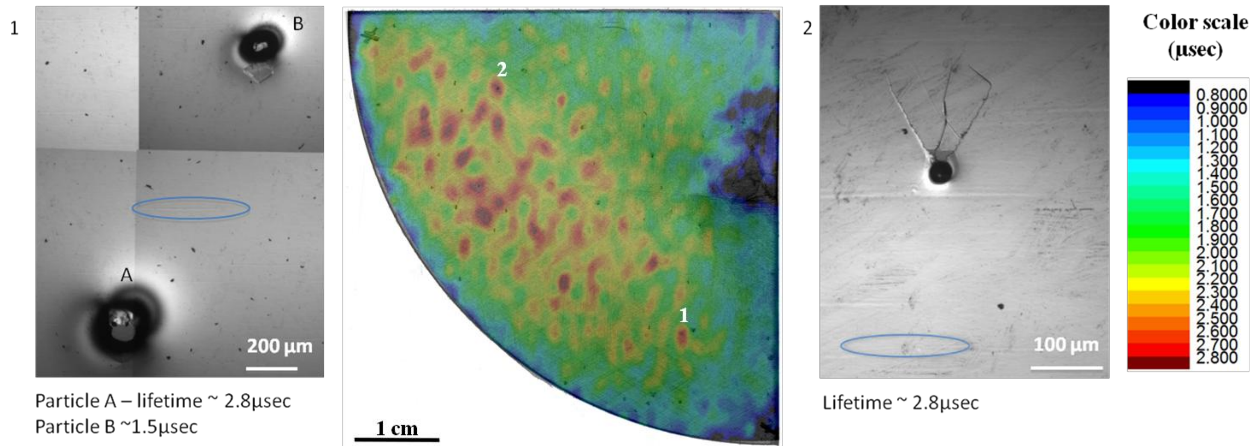

Figure 6.17. Effect of parasitic particulates (PaDs) on carrier lifetime. Blue circles highlight linear defects that correspond to obtuse triangular defects at the apex of which lies wavy pit associated with micropipe

By comparison, sample 2 exhibited a high density of microcracks and BPD half loops associated with a high density of triangular defects. Their origin is the same as the one described for sample 1. In addition to microcracks and BPD half loops associated with a high density of triangular defects, we observed morphological defects, interfacial dislocations and half loop arrays. These microcracks and BPD half loop along with their associated triangular defects corresponded to regions of very low carrier lifetimes. No stacking faults and LAGBs of the types observed in sample 1 were seen. Triangular defects were the most common observed morphological defects. R. Hattori and coworkers reported these types of defects to be in-grown stacking faults (IGSFs) [42].

The triangular defects in sample 2 had a mitigating effect on carrier lifetimes. Some were associated with a very high lifetime while others were not. The morphology and core of the triangular defects suggest that these defects most likely do not have the same structure. M. Abadier et al observed the IGSFs to have an 8H-SiC structure [43]. In contrast, K. Konishi et al reported two types of triangular defects; each associated with 3C-SiC and (4, 2) fault structure [44]. They further found that the 3C type triangular defects was associated with an increase in leakage current at a reverse bias voltage as well as forward current at low bias voltage, whereas

the (4, 2) type of triangular defect did not cause any degradation of device performance. These studies [43, 45] further support that the difference in structure among the triangular defects observed in sample 2 could explain their mitigating impact on carrier lifetimes. Illustration of the effect of morphological defects and microcracks on carrier lifetimes is shown in Figure 6.18 for sample 2.

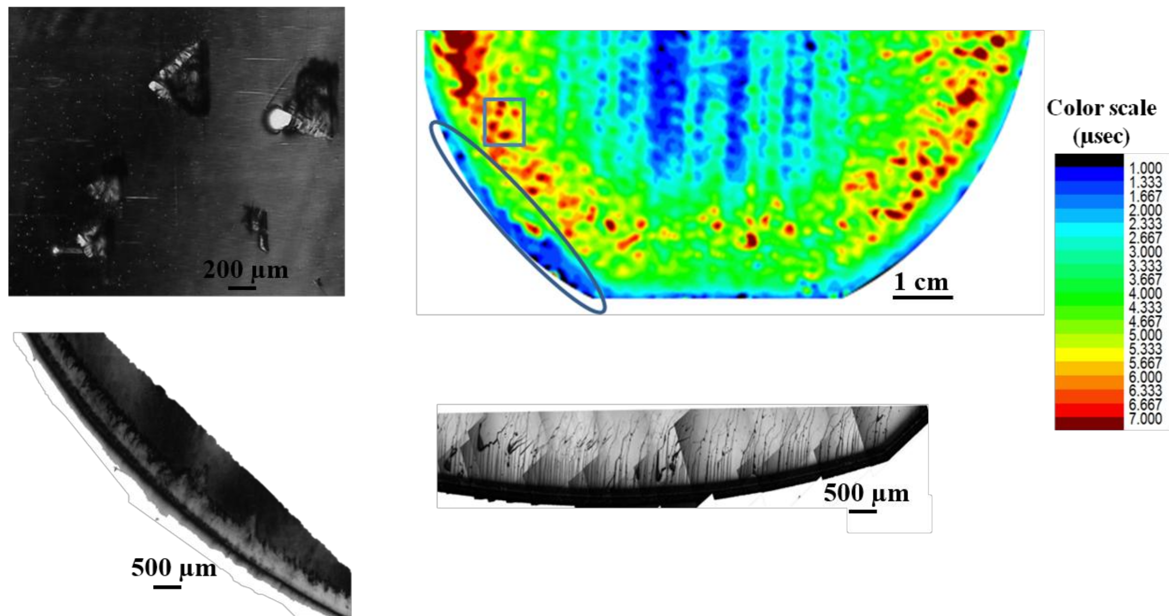

Figure 6.18. Effect of triangular defects, microcracks associated with triangular defects at edge of sample. Note the corresponding SMBXT images of highlighted regions from the µPCD map as well as optical micrograph of a region along the edges of sample 2. Also, the individual triangular defects appear to have no negative effect on lifetime

Unlike the triangular defects, the IDs and HLAs have an unmitigated effect. They have been associated with very low carrier lifetimes (Fig. 6.19). The µPCD measure lifetime associated with the IDs and HLAs varied from ~1 µs to 1.3 µs, a factor of about 7 lower than the highest measured lifetimes. Likewise, the microcracks and BPD half loops associated with triangular defects along the edges of sample 2 were associated with lower carrier lifetimes. Though the carrier diffusion length has been reported to decrease near dislocation and micropipes in SiC, the effect of individual dislocation such as BPDs, TEDs and TSDs could not be assessed due to the relatively high density of these defects in the material. In region of high BPD density, carrier lifetimes were reduced compared to their surroundings. In regions where TEDs and TSDs aligned along grain boundaries (sample 1) as well as IDs and HLAs (sample 2), carrier lifetimes

were found to drastically decrease. It is likely that these TED and TSD defects contributed to the reduced carrier lifetime.

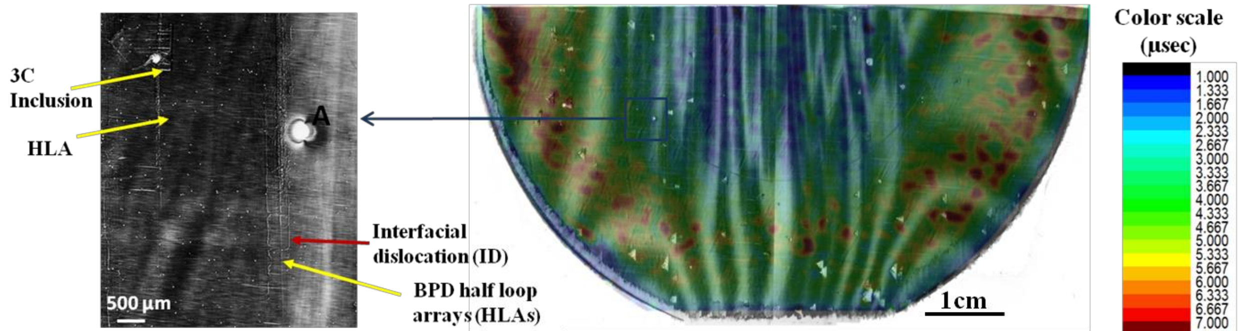

Figure 6.19. Illustration of the effect of IDs and HLAs on carrier lifetimes. Note the HLA originating from a 3C inclusion. Also, the µPCD lifetime map is overlaid on top of the SMBXT image.

VI.5 Conclusion

Optical measurement of carrier lifetimes of 4H-SiC homoepitaxial layers have been performed using a combination of photoluminescence decay and µ-wave photoconductive decay. The measured lifetime values were seen to differ between the two measurement methods. While these techniques are well suited to measure the minority carrier lifetimes, they do have a different sensitivity. For instance, µPCD is sensitive to surface recombination effect, whereas PL decays is more sensitive to bulk effect. This explains the difference in value of the measured lifetimes.

Besides, the measured lifetime values were seen to vary across the samples. This variation in measured lifetimes was related to structural defects in the samples. One to one correlation between µPCD maps and SWBXT and SMBXT distribution maps of structural defects for samples 1 and 2 revealed these structural defects either replicated from the substrate, formed at the substrate-epilayer interface or in the epilayer during epitaxial growth. Defects replicated from the substrate that reduced carrier lifetimes were low angle grain boundaries and stacking faults. Those that formed at the substrate-epilayer interface or in the epilayer during growth were interfacial dislocations, half-loop arrays, morphological defects including triangular defects and parasitic particulates, and microcracks. The aforementioned results demonstrate that SWBXT and SMBXT are powerful tools to trace the sources of the reduction in minority carrier lifetime observed in optical carrier lifetime maps.

References

1. M. Östling, S. –M Koo, M. Domeij, E. Danielsson and C. –M Zetterling, "SiC Device technologies", in Encyclopedia of RF and Microwave Engineering: John Wiley & Sons, Inc., p 4613-4619 (2005)
2. Philip G. Neudeck, Mat Sci. Forum 338-342, p 1161-1166 (2000)
3. M. T. Azar, S. M. Hubbard and C. M. Schnabel, J. Appl. Phys. 84, p 3986 (1998)
4. Paul Klein, J. Appl. Phys. 103, p 033702 (2008)
5. B. Kallinger, P. Berwian, J. Friedrich, M. Rommel, M. Azizi, C. Hecht and P. Friedrichs, Mat. Sci. Forum 740-742, p 633-636 (2013)
6. L. Lija, J. Ul Hassan, I. Booker, P. Bergman and E. Janzén, Mat. Sci. Forum 740-742, p 637-640 (2013)
7. J. Hassan and J. P. Bergman, J. Appl. Phys. 105, p 123518 (2009)
8. N. A. Mahadik, R. E. Stahlbush, J. D. Caldwell, M. O'Loughlin and A. Burk, Mat. Sci. Forum 717-720, p 297-300 (2012)
9. J. A. Powell and D. J. Larkin, Phys. stat. sol. (b) 202 (1), p 529-548 (1997)
10. T. Kimoto, A. Itoh, and H. Matsunami, Phys. stat. sol. (b) 202, (1), p 247-262 (1997)
11. P. G. Neudeck, https://sic.grc.nasa.gov/files/CRCChapterRev.pdf
12. Cree, "Silicon Carbide: Physical & Electronic Properties." http://www.cree.com/Products/sic_index.asp.
13. T. S. Sudarshan, T. Rana, H. Song and M. V. S. Chandrashekhar, ECS J. Solid State Sci. Technol. 2 (8), p N3079-N3086 (2013)
14. T. Rana, M. V. S. Chandrashekhar and T. S. Sudarshan, Phys. Status Solidi (a) 209 (12), p 2455-2462 (2012)
15. T. A. Kuhr, J. Q. Liu, H. J. Chung and M. Skowronski, J. Appl. Phys. 92 (2002)
16. P. Pirouz, M. Zhang, H.McD. Hobgood, M. Lancin, J. Douin and B. Pichaud, Phil. Mag. 86, (2006)
17. P. B. Klein, R. Myers-Ward, K. –K Lew, B. L. VanMil, C. R. Eddy jr., D. K. Gaskill, A. Shrivastava and T. S. Sudarshan, J. Appl. Phys. 108, p 033713 (2010)
18. P. B. Klein, J. D. Caldwell, A. Shrivastava and T. S. Sudarshan, Mat. Sci. Forum 600-603, p 489-492 (2008)

19. R. A. Bardos, T. Trupke, M. C. Schubert and T. Roth, Appl. Phys. Letter. 88, p 053504 (2006)
20. L. Nogueira Vázquez, "Experimental Setup for Carrier Lifetime Measurement Based on Photoluminescence Response", Master Thesis Work, 20 July 2009
21. Z. Zhang, A. Shrivastava and T. S. Sudarshan, Mat. Sci. Forum 527-529, p 419-422 (2006)
22. H. Tsuchida, I Kamata and M. Nagano, J. Cryst. Growth 306 (2), p 254-261 (2007)
23. G. S. Sun, X. F. Liu, Q. C. Gong, L. Wang, W. S. Zhao, J. Y. Li, Y. P. Zeng, J. M. Li, Mat. Sci. Semiconductor Processing 9, p 275-278 (2006)
24. Simon M. Sze, Physics of semiconductor devices (2nd ed), Wiley, New York (1981)
25. J. Hassan, L. Lija, I. D. Booker, J. P. Bergman and E. Janzén, Mat. Sci. Forum 717-720, p 157-160 (2012)
26. J. P. Bergman, O. Kordina and E. Janzén, Phys. Status Solidi A 162, p 65 (1997)
27. De-Sheng Jiang, De-Gang Zhao and Hui Yang, Phys. Stat. Sol. (b) 244 (8), p 2878-2891 (2007)
28. D. L. Meier, Jeong-Mo Hwang and Robert B. Campbell, IEEE Transactions on Electron Devices 35 (1), p 70-79 (1988)
29. P. McKelvey, Phys. Rev. 106 (5), p 910-917 (1957)
30. G. K. Wertheim and G. L. Pearson, p 694-698 (1957)
31. M. J. Marinella, D. K. Schroder, G. Chung, M. J. Loboda, T. Isaacs-Smith and J. R. Williams, IEEE Transactions on Electron Devices 57 (8), p 1910-1923 (2010)
32. F. Wu, Huanhuan Wang, S. Byrappa, B. Raghothamachar, M. Dudley, P. Wu, X. Xu and I. Zwieback, J. Electronic Materials 42 (5), p 787-793 (2013)
33. Huanhuan Wang, M. Dudley, F. Wu, B. Raghothamachar, J. Zhang, G. Chung, B. Thomas, E. K. Sanchez, S. G. Mueller, D. Hansen and M. J. Loboda, J. Electronic Materials 44 (5), p 1268-1274 (2015)
34. Huanhuan Wang, F. Wu, M. Dudley, B. Raghothamachar, G. Chung, J. Zhang, E. K.. Sanchez, S. G. Mueller, D. Hansen and M. J. Loboda, Mat. Sci. Forum 778-780, p 328 (2014)
35. J. W. Matthews, A. E. Blakeslee, J. Cryst. Growth 27, p 118 (1974)

36. H. Jacobson, J. Birch, C. Hallin, A. Henry, R. Yakimova, T. Tuomi and E. Janzen, Appl. Phys. Lett. 82, p 3689 (2003)
37. J. W. Matthews, S. Mader and T. B. Light, J. Appl. Phys. 41, p 3800 (1970)
38. J. A. Powell and D. J. Larkin, Phys. Stat. Sol. (b) 202, p 529 (1997)
39. H. Das, G. Melnychuk and Y. Koshka, Mat. Sci. Forum 615-617, p 121-124 (2009)
40. T. Rana, M. V. S. Chandrashekhar and T. S. Sudarshan, 209 (12), p 2455-2462 (2012)
41. T. Okada, T. Kimoto, H. Noda, T. Ebisui, H. Matsunami and F Inoko, Jpn. J. Appl. Phys. 41, p 6320-6326 (2002)
42. R. Hattori, R. Shimizu, I. Chiba, K. Hamano and T. Oomori, Mat. Sci. Forum 615-617, p 129-132 (2009)
43. M. Abadier, R. L. Myers-Ward, N. A. Mahadik, R. E. Stahlbush, V. D. Wheeler, L. O. Nyakiti, C. R. Eddy Jr., D. K. Gaskill, H. Song, T. S. Sudarshan, Y. N. Picard and M. Skowronski, J. Appl. Phys. 114, p 123502 (2013)
44. K. Konishi, S. Nakata, Y. Nakaki, Y. Nakao, A. Nagae, T. Tanaka, Y. Nakamura, Y. Toyoda, H. Sumitani and T. Oomori, Jpn. J. Appl. Phys. 52, p 04CP05 (2013)
45. T. Yamashita, K. Momose, D. Muto, Y. Shimodaira, K. Yamatake, Y. Miyasaka, T. Sato, H. Matsuhata and M. Kitabatake, Mat. Sci. Forum 717-720, p 363-366 (2012)

Chapter VII: Characterization of CZT Single Crystals Grown by Vertical Bridgman Method under Different Cadmium Overpressures

VII.1 Introduction

In melt growth of cadmium zinc telluride (CZT) single crystals, the control of the melt stoichiometry remains one of the most outstanding challenges. A deviation from ideal stoichiometry promotes the formation of native point defects, which include vacancies, antisites and interstitials [1]. These native point defects affect the chemical homogeneity, the type of conductivity, absorption behavior and dopant incorporation in the grown crystal. Deviation from stoichiometry also favors the formation of tellurium (Te) secondary phase particles, i.e. inclusions and precipitates. Visually, Te precipitates have a nanometer (nm) size compared to a micrometer size for Te inclusions [2-4].

Aside from the physical difference between Te inclusions and precipitates, these two secondary phases can be differentiated based on how they form. Te inclusions form during growth from the trapping of Te-rich droplets at the growth interface when cadmium (Cd) evaporates out of the melt. More specifically, Te inclusions are occasioned by the formation of *pockets* associated with morphological instabilities, which capture Te-rich droplets at the growth interface. By comparison, Te precipitates form as Te-rich droplets re-solidify during cooling down phase of CZT crystal ingot. This re-solidification during cooling down is explained from a solubility point of view. At high growth temperature, Te-rich droplets are highly soluble. This solubility decreases as the crystal is quenched from growth temperature. As the solubility of the Te droplets decrease, they become supersaturated and precipitate in the CZT matrix. Therefore, Te precipitates are said to form from the retrograde solid solubility effect in CZT during rapid cooling from high temperature. It follows from the formation process of Te precipitates that low temperature growth can lead to a drastic reduction of their concentration. This is supported by the temperature-composition projection of the CZT solidus, described in chapter 1 (Figure 1.9), where the solidus is 0.05% wide on the Te side in excess of stoichiometric value at 900˚C and 0.02% wide at 800˚C.

The impact these Te secondary phase particles have on wafer and device quality has been investigated [5, 6]. According to A. E Bolotnikov et al the extent of the influence of tellurium (Te) inclusions on CZT detectors' energy resolution strongly depends on their concentration and

size [5]. While Te inclusion/precipitates are detrimental to CZT based detectors, other defects such as subgrain boundaries and dislocations can also limit their performance. J. Butcher and coworkers [6] reported a direct correlation between subgrain boundaries and reduction in charge collection, underlining the influence of the density of dislocations comprising the subgrain boundaries.

In order to eradicate these defects or mitigate their influence, two main approaches have been considered. The first one consists in growing CZT crystals using alternative growth techniques such as physical vapor transport (PVT) and travelling heater method (THM) [7, 8]. These alternative techniques have been presented in chapter 1. The reader can consult references [7, 8] for further details. On the other hand, the second approach consists in optimizing the widely used vertical Bridgman technique. In this paper, we investigates the second approach in light of studies carried out by C.H. Su and S.L. Lehoczky [9] on the measurement of the Cd reservoir temperature at which stoichiometric growth conditions are maintained. Several CZT single crystal boules were grown under different Cd overpressures in order to compensate for the evaporation of Cd during growth. These crystals were then characterized using a combination of synchrotron white beam x-ray topography (SWBXT) and transmission infrared (IR) microscopy. The broader aim of this experiment is to understand the influence of this growth modification on the crystalline quality of the grown crystals. By crystalline quality, we refer to the presence/absence of defects such as dislocations, subgrain/grain and twin boundaries as well as inclusions/precipitates.

VII.2 Experiment

Several cadmium zinc telluride single crystal boules of size ranging between 20 and 40 mm were grown under different Cd overpressures by vertical directional solidification of Bridgman technique at the Materials and Process Laboratory at NASA/Marshall Space Flight Center. The temperature of the Cd reservoir for each growth was varied between 717°C and 865°C. Two set of specimen, set 1 and 2, were cut from each boule, polished, and then characterized using synchrotron white beam x-ray topography and transmission infrared microscopy. The IR transmission microscopy system had optical resolution limit of 1μm. Set 1 specimen are recorded in Table 7.1, and set 2 in Table 7.2. For the boule corresponding to sample 2g-36/1, two axial slices (2g-36/2 and 2g-36/3) were cut and the evolution of structural defects as well as Te secondary phase particles along the vertical growth direction was also investigated. Schematic

diagram of the boule from which samples 2g-36/1, 2 and 3 were cut along with corresponding directions of cut is shown in Figure 7.1.

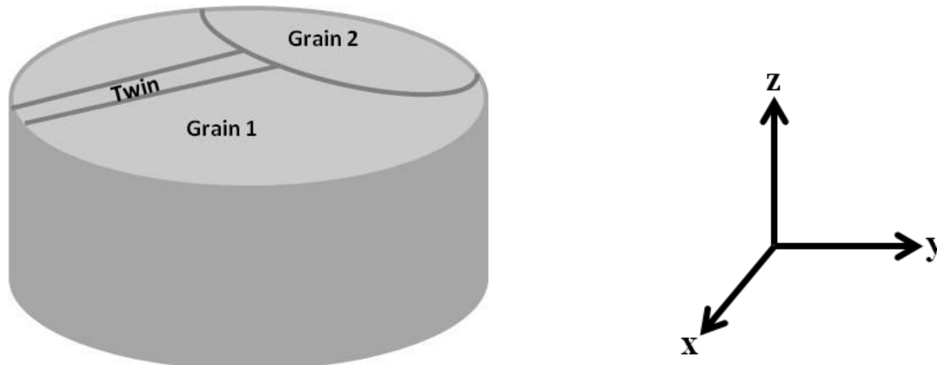

Figure 7.1. Schematic diagram showing boule from which sample 2g-36/1, 2g-36/2 and 2g-36/3 were cut. Direction of cut of axial slices is perpendicular to x-axis and direction of cut for transverse slices in perpendicular to z-axis.

Table 7.1. Sample Id and corresponding Cd reservoir temperature for set 1

Sample Id	2g-30	2g-31	2g-34	2g-36	2g-36/1	2g-38
T (°C) (Cd reservoir)	785	800	840-845	785	785	810

Table 7.2. Sample Id and corresponding Cd reservoir temperature for set 2

Sample Id	1g-30	1g-31	1g-32	1g-33	1g-34	1g-35	1g-36
T (°C) (Cd reservoir)	717	747	754	800	825	843	865

VII.3 Results and discussion

Effect of Cd-overpressures on crystalline quality

In a typical vertical directional solidification Bridgman growth, there is chemical inhomogeneity in the composition of the growing crystal. This compositional non-uniformity can be associated with a local variation in lattice parameters and thermal expansion coefficient during growth. The consequence of this variation in lattice parameters and thermal expansion coefficient is the generation of a thermoeleastic stress that favors the formation, multiplication and glide of dislocations. It should be noted that the compositional non-uniformity can arise because of deviation from stoichiometry during growth. Hence, maintaining stoichiometry can

potentially ensure compositional uniformity and improve the structural quality of the growing crystal.

Several Cd-overpressures were used to compensate for the evaporation of cadmium during growth, and maintain melt stoichiometry. Investigation of crystalline quality for each of the grown boules was performed for samples in set 1 (Table 7.1), using synchrotron white beam x-ray topography. Overall, the samples were characterized by networks of subgrain boundaries with some regions of inhomogeneous strains (Fig. 7.2). These inhomogeneous strains caused lattice distortions near certain regions along the periphery of the samples. It is likely that contact between the ampoule walls and the growing crystal is the source of these strains causing lattice distortions. This is consistent with observation made by B. Raghothamachar and coworkers who investigated the effect of ampoule wall contact on crystalline quality [10]. According to their study, "hoop" stresses generated at the surface of the boule by wall contact lead to the formation of structural defects such as slip bands and twin lamellae.

From the details characteristics of the grain size, defect distribution and types of each sample under investigation shown in Figure 7.2, the samples were qualitatively ranked. The best crystalline quality (Figures 7.2d and 2e) was obtained for samples 2g-36 and 2g-36/1, grown using the Cd reservoir temperature at 785 ^{o}C. Despite being grown using the same Cd reservoir temperature as 2g-36 and 2g-36/1, sample 2g-30 exhibited a much lower crystalline quality. This was due to the high density of microcracks confirmed through the transmission infrared micrographs shown in Figure 7.6. The microcracks most likely occurred during lapping and polishing. Another likely cause is the higher rate of cooling of the Cd reservoir for sample 2g-30. Studies by U. N. Roy et al. on the effect of the rate of crystal cooling on the size and distribution of Te inclusions in traveler heater method growth of CZT wafers suggest that a slower cooling rate is associated with a reduction in size and density of Te inclusions, and hence improved crystalline quality [11]. Because it has been observed that a dense field of dislocations surrounds Te inclusions [12], a poor crystalline quality can be used as an indication of an increase in size and density of Te inclusions. Consequently, we can safely extend U. N. Roy's observation to our case, and posit that the rate of cooling of the Cd reservoir affects crystalline quality.

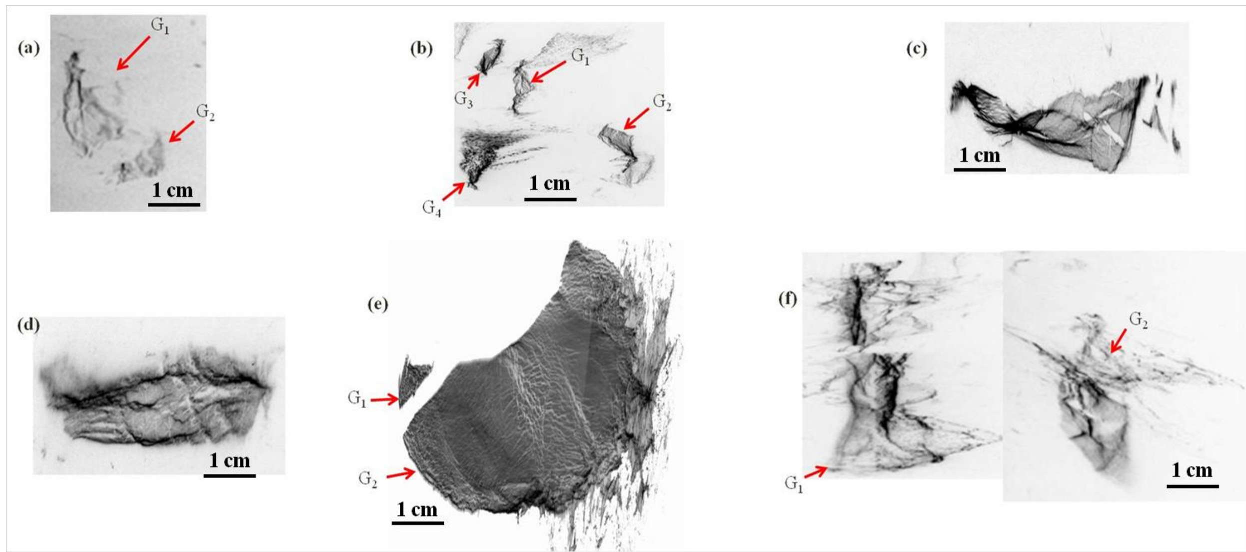

Figure 7.2. SWBXT reflection topograph for samples grown using various Cd reservoir temperatures. Sample 2g-30 grown using 785 °C (a), sample 2g-31 grown using 800 °C (b), sample 2g-34 grown using 840-845 °C (c), sample 2g-36 grown using 785 °C (d), sample 2g-36/1 grown using 785 °C (e), and sample 2g-38 grown using 810 °C (f)

The next best crystalline quality was observed for a Cd reservoir temperature at 840-845 °C, albeit with a large strain in the main grain and several highly distorted small grains. It is probable that the increase in Cd reservoir temperature lead to an increase in Cd atoms in the CZT crystal lattice. This increase in Cd atoms, in turn, resulted in a strained lattice, which explains the severely distorted small grains and large strain in the main grain. Two other samples, 2g-31 and 2g-38 were of very poor crystalline quality. Sample 2g-31 was characterized by four grains with a relatively small strain, and a high lattice distortion near the edges of grain four (G_4). In contrast, sample 2g-38 was characterized by two severely distorted grains due to a large inhomogeneous strain. Observation of smaller strains in sample 2g-31 with a Cd reservoir temperature of 800 °C is consistent with the hypothesis that an increase in Cd reservoir temperature results in an increase in the magnitude of strain. However, it should be emphasized that the temperature of the Cd reservoir cannot solely account for the magnitude of the strain as observed in samples 2g-34 and 2g-38. Three possible sources can contribute to this magnitude. One source of strain is the contact between the surface of the boule and the ampoule walls described in reference [10, 13]. Another source is axial temperature gradient, which can generate an excess strain during solidification and cooling down phases [12, 14]. The third possible

contribution can come from the shape of the solid-melt interface as suggested by Chao and Hung [15].

While all the investigated samples consisted of two or more grains, only 2g-36/1 exhibited twinning in its largest grain (G_1). This is seen in Figure 7.3 for the reflection topographs recorded on both face of the said sample. The orientation of the twin was found to be (2-10) as shown in Figure 7.4. Further, the depth of propagation of the twin boundary in the boule corresponding to sample 2g-36/1was investigated. For two additional samples, two axial slices (2g-36/2 and 2g-36/3) cut from the same boule below 2g-36/1, no twinning was observed as seen in Figures 7.6. This reveals that the twining in the boule corresponding to sample 2g-36/1 was as wide as 2mm, which is the thickness of sample 2g-36/1. It is possible that as the CZT melt solidifies the shear stress in the crystal decreases to below the critical value at which twinning occurs. This could explain why the twin boundary does not extend across the whole length of the boule.

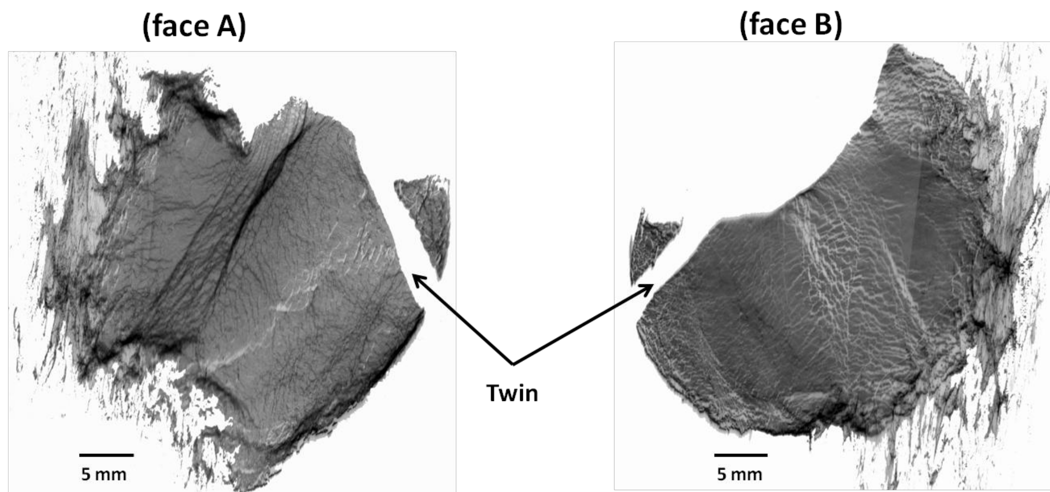

Figure 7.3. SWBXT reflection topograph of both faces of sample 2g-36/1. Note the change in contrast of the subgrain boundaries indicating the nature of the stress on each face

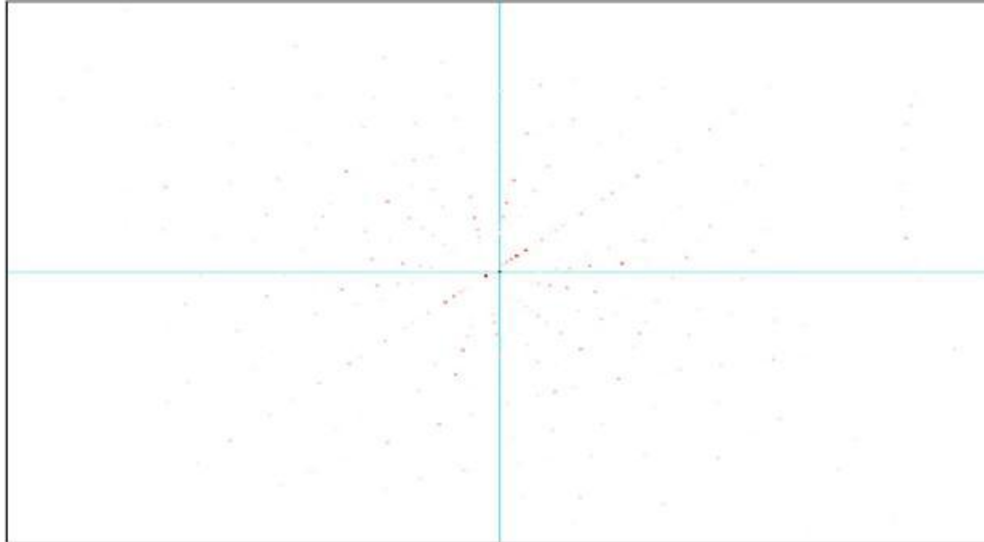

Figure 7.4. Back reflection Laue pattern showing the (2-10) surface orientation of the twin region, which is rotated 180o to the (111) plane normal with respect to the main grains

Because of their thickness, the topographs of samples 2g-36/2 and 2g-36/3 were recorded in reflection geometry. This geometry allows for a limited penetration depth of the X-ray beam, and thus inclusions that are below the depth limit of the beam will not be imaged. Analysis of these topographs, shown in Figure 7.5, reveals the distribution of structural defects along the axial growth direction. Defects such as subgrain boundaries and dislocations are seen to propagate along the growth direction and extend radially. This is expected during the Vertical Bridgman growth, where axial temperature gradient causes stresses that induce formation of dislocations. When the dislocations align themselves to lower their energy, they form subgrain boundaries. The lack of clear contrast from Te inclusions is most likely due to the Te inclusions being buried into the sea of subgrain boundaries observed in the X-ray topography images. As for the Te precipitates, their nanometer size falls below the detection limit of the synchrotron topography X-ray technique. It should be noted that the Cd reservoir temperatures used in this study are within ± 35 ^{o}C of the 818 ^{o}C value predicted by partial pressure data for stoichiometric melt [9].

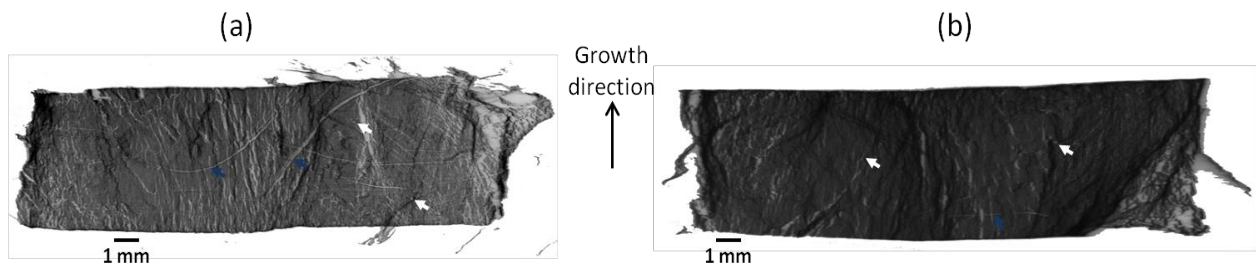

Figure 7.5. SWBXT reflection topograph of sample 2g-36/2 (a), and sample 2g-36/3 (b). The blue arrows indicate surface scratch from polishing, and the white arrows indicate Te inclusions.

Effect of Cd-overpressures on Te secondary phase particles

While the relative strain and dislocation density in the samples of set 1 prevented unambiguous resolution of Te inclusions, Te precipitates could also not be observed because their size (<1μm) is below the detection limit of SWBXT technique. Consequently, to evaluate the influence of Cd-overpressure on Te inclusions and precipitates, infrared (I.R) transmission microscopy technique was used. Figure 7.6 shows the size, distribution and shapes of Te inclusions for all samples in set 1. For set 1, the average size of Te inclusions ranged between 2 and 20 μm. All samples except sample 2g-36 were characterized by cracks, which were attributed to a combination of polishing and thermo-mechanical stresses at the ampoules wall. In fact, the high brittleness of CZT crystal makes it prone to cracking [16].

Two observations transpire from the analysis of the I.R images shown in Figure 7.6. First, Te inclusions were uniformly distributed in samples 2g-36 and 2g-36/1. In sample 2g-31, the Te inclusions were found to concentrate near the center around the cracks, whereas in samples 2g-30, 2g-34 and 2g-38, they concentrated near the periphery. This difference in inclusion distributions between samples 2g-31, 2g-30, 2g-34 and 2g-38 could be linked to the origin of the crack present on them. It is probable that the cracks present in 2g-31 occurred during growth or cool down process because of excess thermal stress. This excess thermal stress, which cause a high pressure build up, draws Te inclusions to the crack regions. In contrast, samples 2g-30, 2g-34 and 2g-38 did not exhibit the same Te inclusion distribution because the cracks present in them resulted from polishing damaging, and could not have thus influenced the formation/distribution of Te secondary phase particles. The second observation relates to the size and density of Te inclusions with respect to the variation in Cd overpressure. Overall, the density of Te inclusions appears to follow a second-degree polynomial function. Sample 2g-31 has the highest density and smallest size of Te inclusions. The fact that sample 2g-31 has a denser concentration of Te inclusions is predictable most likely because it exhibits a higher density of microcracks, whose onset during growth as a result of excess thermal stress cause instability of the growth front and increase tendency to trapping of Te inclusions. The observed smaller Te inclusion size could be attributed to the effect of the Cd overpressure. We hypothesize that while

the addition of Cd vapor during growth potentially reduces/prevents the formation of Te secondary phase particles [17], the actual prevention/annihilation of Te inclusions occurs via a mechanism of size decrease. This implies that the size and density of Te inclusions can be tailored as a function of Cd overpressure.

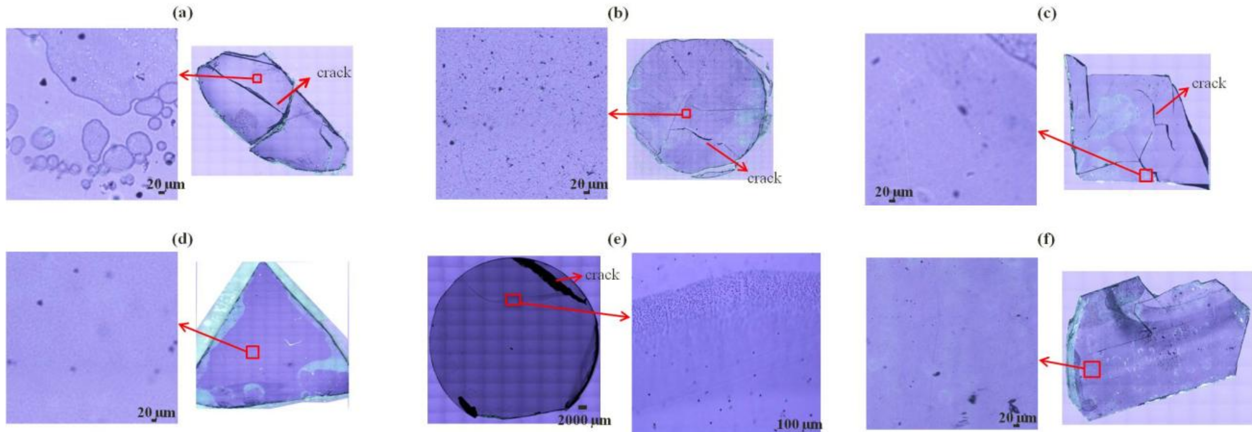

Figure 7.6. Distribution of Te inclusions with respect to Cd overpressure for sample 2g-30 with a Cd reservoir temperature of 785 ^oC (a), sample 2g-31 with a Cd reservoir temperature of 800 ^oC (b), sample 2g-34 with a Cd reservoir temperature of 840-845 ^oC (c), sample 2g-36 with a Cd reservoir temperature of 785 ^oC (d), sample 2g-36/1 with a Cd reservoir temperature of 785 ^oC (e), and sample 2g-38 with a Cd reservoir temperature of 810 ^oC (f). Note the bed of Te inclusions and the thin strip of Te inclusions respectively indicating the grain and the twin boundary in (e).

In a similar manner, investigation of samples from set 2 was carried out. Figure 7.7 shows the size, density and distribution of the Te inclusions observed in these samples. These Te inclusions had a circular or triangular shape like those observed in samples from set 1, with an average size in the range ~ 10µm to 45µm. The density of these inclusions as well as their average size, taken across the range of Cd overpressures, was seen to mimic the pattern of a periodic function. The lowest amounts of inclusions were obtained for Cd reservoir temperature at 815°C±15°C. This result corroborates with partial pressure data for stoichiometric melt [9]. This suggests that there exists an optimum Cd overpressure at which formation of Te inclusions can be mitigated/prevented by maintaining a stoichiometric melt. In other words, as we move away either to the left side or right side of this value, density of Te secondary phases will most certainly increase. Thus, we can anticipate a decrease in the size of the Te inclusions the closer the Cd reservoir temperature is to that value.

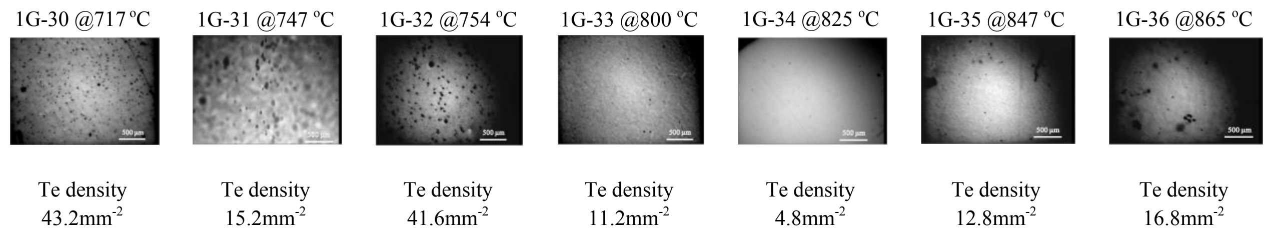

Figure 7.7. Variation in Te inclusions size and concentration with respect to Cd overpressure

A variation in the density and distribution of Te secondary phase particles can be used as an indication of the quality of the CZT crystals because extended defects tend to encompass inclusions. Hence, regions of crystals with low to none Te secondary phase particles are regions of high structural quality. We have observed a uniform concentration of Te secondary phase particles toward the center of the samples under investigation from both sets and away from the ampoule walls. This is highlighted in the infrared micrographs of samples 2g-36/2 and 2g-36/3 in Figure 7.8. It follows then that the samples under investigation are of very high quality away from their center toward the ampoule walls. This could be attributed to the shape of melt-liquid growth interface. According to Kuppurao et al. [18] and Derby et al. [19] a concave interface shape promotes the propagation of extended defects toward the bulk of growing crystal. Conversely, a convex interface minimizes the potential for the propagation of extended defects toward the bulk as these are pushed toward the periphery during growth. These results seem consistent with ours, where the melt-solid interface was concave during growth.

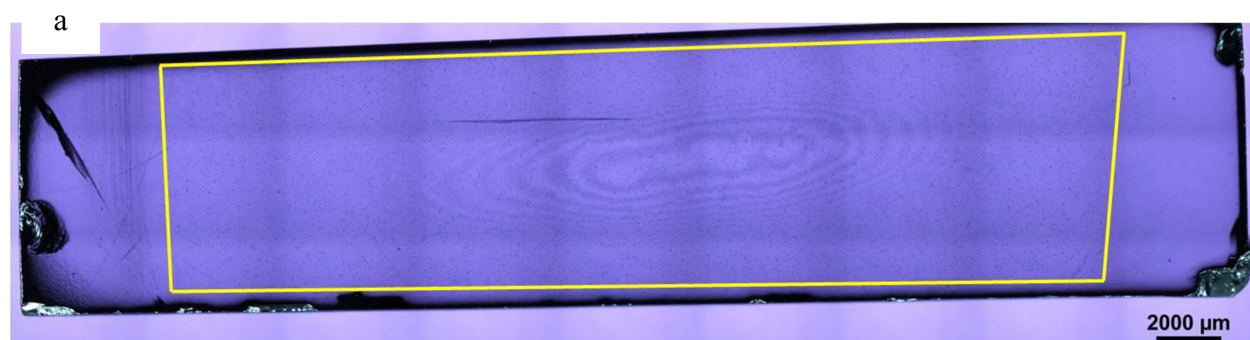

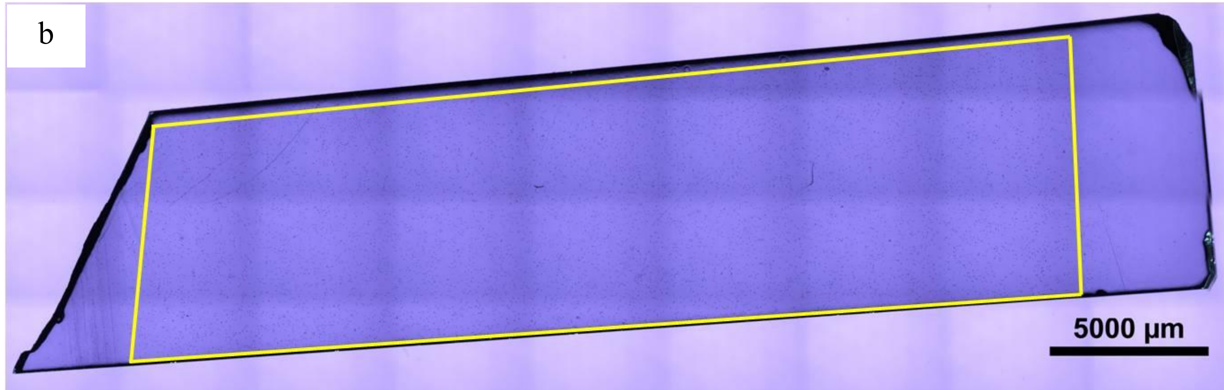

Figure 7.8. Transmission infrared micrograph highlighting in yellow box the concentration of Te secondary phase particles near center of samples (a) for sample 2g-36/2 and (b) for sample 2g-36/3

VII.4 Conclusion

The influence of Cd overpressure on CZT crystalline quality was evaluated for two sets of samples using synchrotron white beam x-ray topography and infrared transmission microscopy. Though the non-linear variation of crystalline quality with respect to Cd overpressure reveals a set of Cd reservoir temperatures at which crystal quality is improved, no strict correlation could be established between crystalline quality (i.e. extended defects, Te inclusions size and density) and the Cd overpressure. It should be noted, however, that the set of Cd reservoir temperature at which crystal quality has improved is within five percent of the predicted 818 ^{o}C by partial pressure data for stoichiometric melt [9]. Other factors such as rate of cooling of the Cd reservoir and formation of cracks during growth/cool down phases (see sample 2g-31) appear to also influence the formation of Te inclusions.

Because all samples in both sets exhibited Te secondary phase particles, it seems apparent that sole use of Cd overpressure to maintain melt stoichiometry does not guarantee complete annihilation of these Te particles. For instance, a combination of effective mixing of the melt with Cd overpressure may decisively reduce the density of Te secondary particles. This has been suggested by P. Rudolph and coworkers [3]. C. Szeles and coworkers also proposed the use of electro-dynamic gradient (EDG) in combination with an active control of the Cd partial pressure in the ampoule as a solution to preventing the formation of Te inclusions and achieving ingots with high structural perfection [12]. Other groups have also proposed alternative method to tackle the issue of Te secondary phase particles. Such methods include the rate of cooling and annealing [20-22].

References

1. P. Rudolph, Cryst. Res. Technol. 38 (7-8), 542-554 (2003)
2. K. Durose, in CdTe and Related Compounds; Physics, Defects, Hetero- and Nano-structures, Crystal Growth, Surfaces and Applications **1**, Eds R. Triboulet and P. Siffert, Elsevier Ltd., p 171-227 (2010)
3. P. Rudolph, A. Engel, I. Schentke and A. Grochocki, J. Cryst. Growth 147 (3-4), p 297-304 (1995)
4. P. Rudolph, M. Neubert and M. Muhlberg, J. Cryst. Growth 128 (1-4), p 585-587 (1993)
5. A.E. Bolotnikov, N.M. Abdul-Jabbar, O.S. Babalola, G.S. Camarda, Y. Cui, A.M. Hossain, E.M. Jackson, H. C. Jackson, J.A. James, K.T. Kohman, A.L. Luryi and R.B. James, IEEE Trans. Nucl. Sci. 55 (5), p 2757 (2008)
6. J. Butcher, M. Hamade, M. Petryk, A. E. Bolotnikov, G. S. Camarda, Y. Cui, G. De Geronimo, J. Fried, A. Hossain, K.H. Kim, E. Vernon, G. Yang and R.B. James, IEEE Trans. Nucl. Sci. 60 (2), p 1189 (2013)
7. Choubey, P. Veeramani, A.T.G. Pym, J.T. Mullins, P.J. Sellin, A.W. Brinkman, I. Radley, A. Basu and B.K. Tanner, J. Cryst. Growth 352 (1), p 120-123 (2012)
8. U.N Roy, A. Burger and R.B James, J. Cryst. Growth 379, p 57-62 (2013)
9. C.H Su and S.L. Lehoczky, J. Cryst. Growth 319, p 4-7 (2011)
10. B. Raghothamachar, H. Chung, M. Dudley and D. J. Larson Jr., J. Electron. Mater. 27 (6), p 556-563 (1998)
11. U. N. Roy, S. Weiler, J. Stein, A. Hossain, G. S. Camarda, A. E. Bolotnikov, R. B. James, J. Cryst. Growth 332 (1), 34-38 (2011)
12. C. Szeles, S. E. Cameron, J. O. Ndap and W. Chalmers, IEEE Trans. Nucl. Sci. 49 (5), 2535-2540 (2002)
13. K. Mandal, S. H. Kang, M. Choi, A. Kargar, M. J. Harrison, D. S. McGregor, A. E. Bolotnikov, G. A. Carini, G. C. Camarda and R. B. James, IEEE Trans. Nucl. Sci. 54 (4), p 802-806 (2007)
14. T. Asahi, O. Oda, Y. Taniguchi and A. Koyama, J. Cryst. Growth 149 (12), p 23-29 (1995)
15. C. K. Chao and S. Y. Hung, J. Cryst. Growth 256 (12), p 107-115 (2003)
16. Cs. Szeles and E.E. Eissler, Proc. MRS Fall meeting, Boston (1997)

17. K. G. Anand, I.J.E.M.S 4 (2), p 113-120 (2013)
18. S. Kuppurao and J. J. Derby, J. Cryst. Growth 172 (3-4), p 350-360 (1997)
19. J. J. Derby, D. Gasperino, N. Zhang and A. Yeckel, in Nuclear Radiation Detection Materials – 2009, Eds. D. L. Perry, A. Burger, L. Franks and M. Schieber, 1164-L05-02, Mater. Res. Soc. Symp. Proc. 1164, Pittsburgh, PA (2009)
20. S. U. Egarievwe, A. L. Adams, M. L. Drabo, M. D. Ashford, R. Pinder, D. E. Jones, A. Kassu, W. Chan, G. Yang, G. S. Camarda, A. E. Bolotnikov and R. B. James, IEEE Nucl. Sci. Symp. Med. Imag. Conf. Record (NSS/MIC), p 4226-4228 (2012)
21. G. Yang, A. E. Bolotnikov, P. M. Fochuk, G. S. Camarda, Y. Cui, A. Hossain, K. Kim, J. Horace, B. McCall, R. Gul, L. Xu, O. V. Kopach and R. B. James, Proc. SPIE 7805, Hard X-ray. Gamma-Ray, and Neutron Detector Physics XII, 780507, (2010)
22. G. Yang, A.E. Bolotnikov, P.M. Fochuk, G.S. Camarda, Y. Cui, A. Hossain, K. Kim, J. Horace, B. McCall,R. Gul, L. Xu, O.V. Kopach and R.B James, Proc. SPIE 7805, (2010)

Chapter VIII: Summary and Future Work

Understanding the issues related to the development and optimization of crystal growth techniques of will help produce large high quality single crystal boules, and potentially reduce the cost of compound semiconductor materials. Similarly, knowledge of the influence of structural defects, be they growth or process related, on material properties will help engineer solutions to tailor suitable defects and/or eradicate unwanted defects. The findings herein published revolve around three parts:

- development of the Large Tapered Crystal (LTC) growth technique for producing large high quality silicon carbide (SiC) single crystal boules;
- investigation of the influence of structural defects on minority carrier lifetime in silicon carbide epitaxial layers;
- investigation of the effect of cadmium (Cd) overpressure on the growth of large high resistivity and high quality cadmium zinc telluride single crystal boules.

Development of the Large Tapered Crystal (LTC) growth technique: This technique is based on a two-step approach: growth of a long seed crystal by solvent laser heated floating zone (Solvent-LHFZ) followed by lateral expansion in hot wall chemical vapor deposition (HWCVD) environment. First, Solvent-LHFZ) growth was carried out to grow long SiC seed crystal. The growth rate was observed to vary proportionally with carbon concentration and growth temperature. While growth rates of 4–135 µm/h were achieved, it was found that the carbon content of the feed rod could potentially influence the formation of a stable melt during growth. The growth of a long single crystal fiber suitable as a seed crystal for implementation of the lateral expansion step of the LTC process requires the formation and control of a much more uniform growth front. The optimum process window was determined to be between T_m and T_m+300C for a carbon concentration of 8% at a high silicon ratio (Fe/Si ~0.35).

For the lateral expansion by HWCVD method, 6H-SiC a/m-plane fibers were used. The as-grown boules were found to replicate the polytype of the underlying fiber. SWBXT revealed the existence of strain at the seed/epilayer interface, and the presence of bands of edge dislocations extending from the seed in a/m axis lateral directions. These bands of dislocations were confirmed by µRS and HRTEM to be regions of different polytypes and found to originate from macrosteps observed on the as-grown surface. This is consistent with previous results reported

by Takahashi et al, whose proposed model can explain the formation of stacking fault/polytypes observed in our experiment.

One limitation toward wide scale implementation of the LTC technique is the growth of a long seed crystal containing a single screw dislocation. For our experiments, the seed fibers used for lateral expansion were of poor quality, containing high density of micropipes and voids. This resulted in the instability of the growth front with the formation stacking faults. A solution to mitigate the generation of stacking faults will be to use a high quality single crystal seed and to optimize the growth conditions. Nonetheless, these results are somehow useful as they open a venue for the growth of SiC nanobands (or nanorods), leading to potential application in heterojunction devices. More work need be done to see the limit of the LTC technique, optimize it, and make it more viable.

Correlation of structural defects with minority carrier lifetime: The measured minority carrier lifetime varied across the samples as a function of defect types and density. One to one correlation between μPCD maps and SWBXT and SMBXT distribution maps of structural defects revealed these structural defects either replicated from the substrate, formed at the substrate-epilayer interface or in the epilayer during epitaxial growth. Defects replicated from the substrate that reduced carrier lifetimes were low angle grain boundaries and stacking faults. Those that formed at the substrate-epilayer interface or in the epilayer during growth were interfacial dislocations, half-loop arrays, morphological defects including triangular defects and parasitic particulates, and microcracks. The usefulness of these results is two-fold. First, they demonstrate the power of SWBXT and SMBXT to non-destructively trace the sources of the reduction in minority carrier lifetime observed in optical carrier lifetime maps. Finally, these results provide a measure to efficiently assess the reliability of epitaxial wafers for use in applications where either low or high carrier lifetimes are required.

Effect of Cd overpressure on the growth of cadmium zinc telluride single crystal boules: While boules of high resistivity were achieved, we observed a non-linear effect of the Cd reservoir temperature on the quality (i.e. structural defects and Te inclusions) of the as-grown boules. Other factors such as rate of cooling of the Cd reservoir and formation of cracks during growth/cool down phases (see sample 2g-31) appear to also influence the formation of Te inclusions. The set of Cd reservoir temperatures at which crystal quality has improved is within five percent of the predicted 818 ^{o}C by partial pressure data for stoichiometric melt. It seems

apparent that the sole use of Cd overpressure to maintain melt stoichiometry does not guarantee complete annihilation of Te secondary phase particles. Possible solutions would be as follow:

- Combination of effective mixing of the melt with Cd overpressure.
- Use of electro-dynamic gradient (EDG) in combination with an active control of the Cd partial pressure in the ampoule.
- Post growth annealing of either individual wafer cut from the as-grown boules or the entire boule in a Cd vapor environment.
- Controlling the rate of cooling.